Synthesis of Novel Molecules for Applications in Material Science

Zur Erlangung des akademischen Grades eines

DOKTORS DER NATURWISSENSCHAFTEN

(Dr. rer. nat.)

von der KIT-Fakultät für Chemie und Biowissenschaften

des Karlsruher Instituts für Technologie (KIT)

genehmigte

Dissertation

von

M. Sc. Julian Brückel

aus Karlsruhe

1. Referent: Prof. Dr. Stefan Bräse
2. Referent: Prof. Dr. Christof Wöll

Tag der mündlichen Prüfung: 08.05.2025

This document is licensed under a Creative Commons Attribution-NonCommercial-ShareAlike 4.0 International License (CC BY-NC-SA 4.0):
https://creativecommons.org/licenses/by-nc-sa/4.0/deed.en

“All we have to decide is what to do with the time that is given us.”

– *Gandalf* from *The Lord of the Rings* –

Declaration of Honesty

This work was carried out from January 2022 through March 2025 at the Institute of Organic Chemistry, Faculty of Chemistry and Biosciences at the Karlsruher Institute of Technology (KIT) under the supervision of Prof. Dr. Stefan Bräse.

Die vorliegende Arbeit wurde im Zeitraum von Januar 2022 bis März 2025 am Institut für Organische Chemie, Fakultät für Chemie und Biowissenschaften des Karlsruher Instituts für Technologie (KIT) unter der Leitung von Prof. Dr. Stefan Bräse durchgeführt.

Hereby I, JULIAN ALEXANDER BRÜCKEL, declare that I completed this work independently, without any improper help and that all material published by others is cited properly. This thesis has not been submitted to any other university before.

Hiermit erkläre ich, JULIAN ALEXANDER BRÜCKEL, dass ich diese Arbeit selbstständig, ohne unzulässige Hilfe, angefertigt und alle fremden Quellen ordnungsgemäß zitiert habe. Diese Arbeit wurde bisher an keiner anderen Universität eingereicht.

Karlsruhe, March 26th, 2025

German Title of this Thesis

Synthese Neuartiger Moleküle und deren Anwendungen in den Materialwissenschaften

Table of Contents

Kurzzusammenfassung

Eine bedeutende Klasse funktionaler Materialien bilden poröse Netzwerke, zu denen metallorganische Gerüstverbindungen (*engl*. metal-organic frameworks, MOFs), kovalente organische Netzwerke (*engl.* covalent organic frameworks, COFs) und Polymere mit intrinsischer Mikroporosität (*engl.* polymers with intrinsic microporosity, PIMs) zählen. Diese Materialien finden Anwendung in verschiedenen Bereichen, darunter die Katalyse chemischer Reaktionen, der zellspezifische Transport von Pharmazeutika sowie die Speicherung und Trennung von Gasen aus Gasgemischen. Ihre charakteristische hohe spezifische Oberfläche in Verbindung mit definierter Porengrößenverteilung prädestiniert poröse Materialien für den Einschluss von Wirkstoffen zum Zwecke des zielgerichteten Transports, die Adsorption von Kohlendioxid (CO_2) zur Reduktion der Treibhausgaskonzentration sowie die Speicherung von neuartigen Energieträgern wie Wasserstoff (H_2) und Methan (CH_4). Die additive Fertigung umfasst eine Klasse von Fertigungsprozessen, bei denen Materialien schichtweise aufgetragen werden, um dreidimensionale (3D) Objekte zu erzeugen. Die laserbasierte additive Fertigung stellt eine Subkategorie innerhalb dieser Verfahren dar. Zu den etablierten Techniken zählen unter anderem die Stereolithografie sowie die Zwei-Photonen-Lithografie, deren Wirkungsweise auf dem Prinzip der Zwei-Photonen-Absorption basiert. Ein neuer kürzlich publizierter Mechanismus ersetzt das Konzept der Zwei-Photon Absorption durch die Zwei-Stufen-Absorption. Die vorliegende Arbeit verfolgt das Ziel, neuartige Moleküle zu synthetisieren und deren potenzielle Anwendungen im Bereich der Materialwissenschaften zu evaluieren. Im Rahmen dieser Studie wurde ein neuartiges aromatisches Diamin auf Basis des [2.2]Paracyclophans synthetisiert und als Baustein für die Herstellung poröser Materialien, einschließlich eines PIM sowie verschiedener COFs, verwendet. Des Weiteren wurde ein Nitroxid-modifiziertes Peptid synthetisiert, das zur Funktionalisierung der Oberfläche von MOF-Nanopartikeln mittels Nitroxid-Austauschreaktion eingesetzt wurde. Ein weiteres Forschungsprojekt konzentrierte sich auf die Synthese neuartiger Azid-funktionalisierter Linker und deren Anwendung in der Herstellung oberflächenverankerter metallorganischer Gerüstverbindungen. Der Einbau der Azid-funktionalisierten organischen Linker soll die photochemische Zersetzung und anschließende Analyse der resultierenden Produkte in einer kristallinen Umgebung ermöglichen. Abschließend wurden Initiatoren für die Anwendung in der laserbasierten additiven Fertigung mittels Zwei-Stufen-Absorption synthetisiert. Die erhaltenen Photoinitiatoren wurden auf ihre Eignung für den 3D Laserdruck evaluiert und in Druckexperimenten getestet.

Abstract

A significant class of functional materials is formed by porous networks, including metal-organic frameworks (MOFs), covalent organic frameworks (COFs), and polymers with intrinsic microporosity (PIMs). These materials find application in various fields, including the catalysis of chemical reactions, cell-specific delivery of pharmaceuticals, and the storage and separation of gases from gas mixtures. Their characteristic high specific surface area, combined with a defined pore size distribution, makes porous materials ideal for the encapsulation of active pharmaceuticals for targeted delivery, the adsorption of carbon dioxide (CO_2) to reduce greenhouse gas concentrations and the storage of novel energy carriers such as hydrogen (H_2) and methane (CH_4).

Additive manufacturing includes processes in which materials are deposited layer-by-layer to create three-dimensional (3D) objects. Laser-based additive manufacturing represents a subcategory within these processes. Established techniques include stereolithography and two-photon lithography, which are based on the two-photon absorption principle. A new, recently published mechanism replaces the concept of two-photon absorption with two-step absorption.

The present work aims to synthesize novel molecules and evaluate their potential applications in the field of materials science. Within this study, a novel aromatic diamine based on [2.2]paracyclophane was synthesized and used as a building block for preparing porous materials, including a PIM and various COFs. Furthermore, a nitroxide-modified peptide was synthesized and used to functionalize the surface of MOF nanoparticles *via* nitroxide exchange reaction. Another research project focused on synthesizing novel azido-functionalized linkers and their application in the fabrication of surface-anchored metal-organic frameworks. Incorporating the azide-functionalized organic linkers enables the photochemical decomposition and subsequent analysis of the resulting products in a crystalline environment. Finally, initiators for application in laser-based additive manufacturing *via* two-step absorption were synthesized. The obtained photoinitiators were evaluated for their suitability for 3D laser printing and tested in printing experiments.

1 Introduction

Materials are the foundation of our modern society, from steel and concrete that shape our cities[1] to the silicon-based chips in our smartphones[2] and the polymers in nearly every modern device.[3] Every technological innovation, from renewable energy solutions to space exploration, is based on the discovery and development of new functional materials with novel and intriguing properties.

Materials science is a rapidly growing field that continues to push the boundaries of the current state of the art (Figure **1**). Researchers are advancing the development of customized three-dimensional (3D) laser-printed nanomaterials to engineer stronger and lighter objects and create materials with novel and counterintuitive properties.[4-5] Additionally, significant efforts are focused on synthesizing highly porous materials for applications such as gas storage and gas separation, particularly to reduce rising carbon dioxide (CO_2) emissions.[6-8] Moreover, these advanced porous frameworks are being explored for pharmaceutical drug delivery, enhancing precision and efficiency in medical treatments.[9-12]

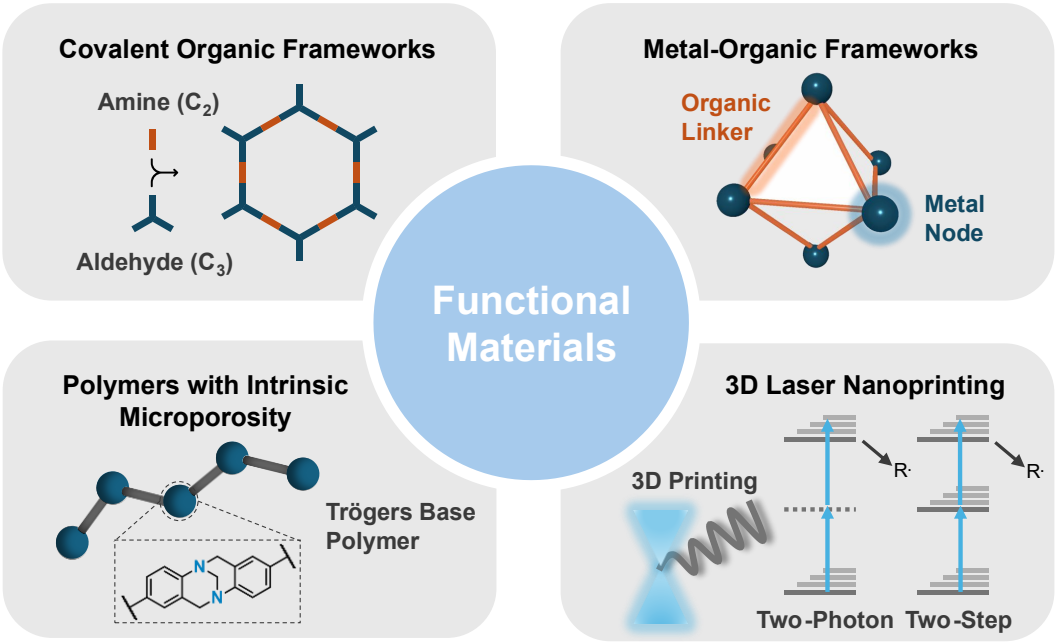

Figure 1: Overview of functional materials and techniques applied in material science; including porous materials such as covalent organic frameworks, metal-organic frameworks, polymers of intrinsic microporosity and 3D laser printing employed for the fabrication of tailored objects.

The precise shaping of materials into well-defined structures is fundamental for the development of advanced functional materials. Additive manufacturing techniques, such as 3D Laser Nanoprinting, have demonstrated significant potential in fabricating structures in the micro- or even nanoscale.[4, 13] These printed structures can exhibit unique physical, chemical, and mechanical properties, enabling novel applications in various scientific and technological fields. Metamaterials, fascinating 3D printed objects, can have negative refractive indices, enabling the manipulation of electromagnetic waves around an object, effectively making the object invisible to certain wavelengths.[14] Additionally, they can exhibit negative elastic modules, meaning they expand when a compressive force is applied, a behavior counterintuitive to conventional material properties.[15]

Carbon capture and storage (CCS) is an emerging research field. The primary target of CCS is the reduction of CO_2 emissions into the atmosphere, which is one of the main contributors to the ongoing climate crisis.[16] It is expected that CO_2 separation from the combustion of fossil fuels can significantly reduce atmospheric CO_2 concentrations by up to 85%.[17] However, several critical issues must be addressed when considering the geological storage of captured CO_2. The accidental release of stored gas can have several serious consequences. The released gas can displace saltwater from deeper rock formations, which results in the upward migration, and ultimately freshwater aquifers near the surface get contaminated. The saltwater intrusion into freshwater sources can lead to soil salinization, making it unsuitable for agriculture.[17] Highly porous materials like Metal-Organic Frameworks (MOFs) and Porous Polymer Networks (PPNs) offer significant potential to address the safety concerns associated with geological CO_2 storage.[16, 18] By effectively adsorbing and storing CO_2 within their porous structures, these materials can minimize the risk of accidental releases and reduce the potential for severe environmental consequences.[7-8] However, applications of porous compounds like MOFs are not only limited to gas storage and separation. Their ability to encapsulate a wide range of therapeutic molecules, including small drugs,[19-20] proteins,[21-22] and nucleic acids,[23-24] has made them potent candidates of modern drug delivery research. Recent advancements in drug delivery are shifting away from traditional oral medications towards more precise and efficient therapeutic approaches.[25] This shift involves the development and application of innovative materials, designed to target diseased cells within the body selectively.[26] In this context, MOFs have emerged as a highly promising class of materials in pharmaceutical drug delivery. Their intrinsic properties make them ideal candidates for enhancing drug solubility, facilitating controlled drug release, and enabling targeted delivery within the body.[25, 27-31]

Bio-compatible MOFs, such as those based on zinc (*e.g.*, **ZIF-8**)[32-33] and iron (*e.g.*, **MIL-100**)[34-36], have shown promising results in preclinical research. However, more *in vivo* studies and clinical trials are needed to fully investigate their safety and efficacy in human drug delivery applications.

1.1 Synthetic Frameworks: A Class of Functional Materials

Chemistry is a fundamental driver in developing novel materials, crucial in continuous scientific and technological progress. Synthetic transformations enable researchers the design and synthesis of building blocks for all kinds of materials with precisely tailored properties.

The linking and combination of different building units allows the precise synthesis of purely organic materials or inorganic-organic hybrid-materials with distinct properties, tailored for specific applications.[37] Inorganic-organic hybrid materials, such as MOFs, are extensively utilized in research and industrial applications.[38-39] Surface-mounted Metal-Organic Frameworks (SURMOFs) have been developed to address the drawbacks associated with bulk or powdered MOF materials, which can limit their practical applications. This approach enables the controlled growth of MOFs on a functionalized substrate using a layer-by-layer method, allowing precise control of the thickness and structure of the SURMOF. In contrast to MOFs, this controlled synthesis improves their suitability for applications that are not doable with conventional powdered MOF materials, extending their usability in novel technologies.[40-42]

In contrast amorphous networks composed entirely of organic building blocks to form synthetic polymers, such as poly(vinyl chloride) (PVC),[43] and polyurethane (PU),[44] have diverse applications across nearly all manufactured products.[45] Additionally, organic polymers can naturally occur as macromolecules essential for life on Earth. Deoxyribonucleic acid (DNA) encodes the genetic information that regulates biological processes. In contrast, ribonucleic acid (RNA) is an intermediate transcribing and translating genetic construction plans for protein and enzyme synthesis.[46-47] Enzymes or proteins catalyze all biochemical reactions in the human body and are also biopolymers, highlighting their fundamental role in sustaining life.[48-50]

Covalently linked porous organic materials can be categorized into two subclasses based on their structural organization. Amorphous porous materials such as polymers with intrinsic microporosity (PIM), hyper crosslinked polymers (HCP), and porous aromatic frameworks (PAF) lack in crystalline long-range order.[51-53] Unlike amorphous networks, Covalent Organic Frameworks (COFs) possess a long-range crystalline order, which enables precise control over their structural and functional properties. The careful selection of molecular building blocks

allows for fine-tuning of key characteristics, such as pore size and surface chemistry, making COFs highly adaptable for various applications.[54-55] An overview of porous materials is illustrated in Figure **2**.

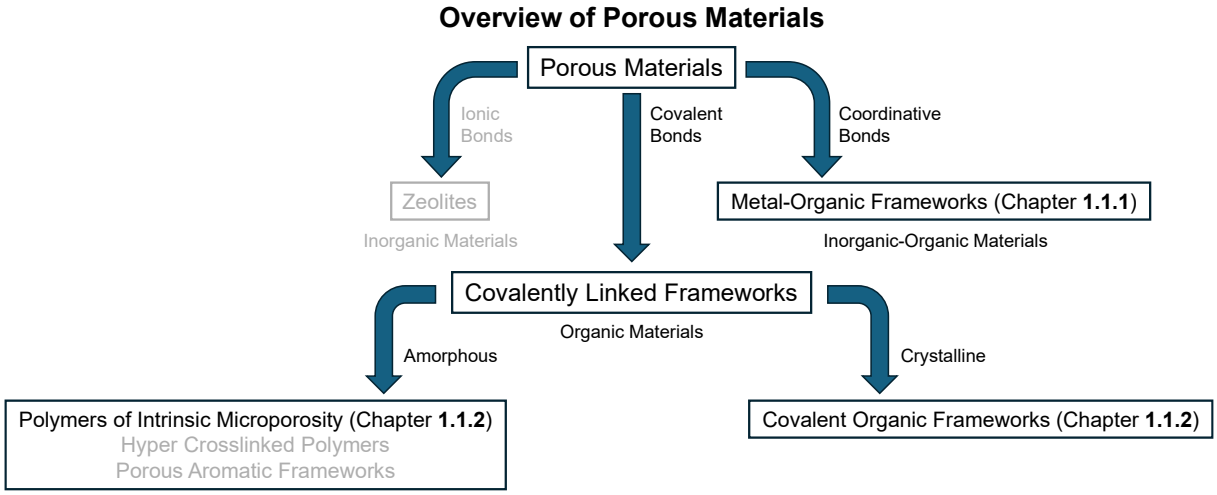

Figure 2: Overview of different subclasses of porous materials, including inorganic materials such as Zeolites, inorganic-organic materials like metal-organic frameworks (MOFs), and covalently linked frameworks - divided into amorphous and crystalline materials, including polymers of intrinsic microporosity (PIMs) and covalent organic frameworks (COFs).

1.1.1 Inorganic-Organic Hybrid Materials

Metal-Organic Frameworks. In 1989, HOSKINS and colleagues reported the first copper-based framework, in which the acetonitrile ligands in tetrakis(acetonitrile)copper(I) tetrafluoroborate complex were replaced by the rod-like organic connector 4,4',4'',4'''-tetracyanotetraphenylmethane, resulting in the formation of a diamond-shaped polymeric 3D network.[56] The term "metal-organic framework", to describe such inorganic-organic hybrid materials, was introduced six years later, in 1995, by YAGHI and co-workers.[57] Since their initial description, research on MOFs has grown substantially with 127.286 publications by 2025 (Sci-Finder search for "metal-organic frameworks", Figure **3**). The diverse range of potential applications for MOFs drives this increase in interest. The tunable nature of MOFs, facilitated by the combination of different metal ions or clusters and organic ligands, which are connected *via* coordinative bonds (so-called Secondary Building Units, SBUs),[58] along with their intrinsic properties such as high surface areas reaching up to ~6200 m^2/g,[59] porosity, and crystallinity, makes them suitable for a wide range of applications. These applications include catalysis,[60] drug delivery,[35] gas storage and separation and sensing technologies.[25, 61]

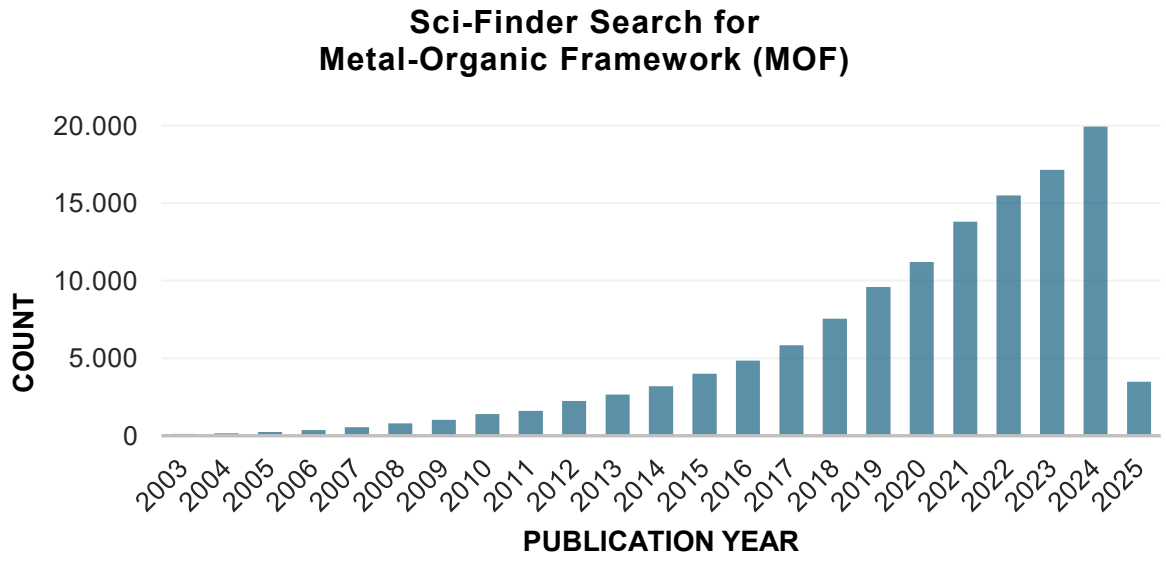

Figure 3: Sci-Finder search for "metal-organic framework" (MOF) by 2025.

Commonly used linkers for MOF synthesis mainly feature carboxylic acid functional groups.[62] However, nitrogen-containing units, such as pyridine- or imidazole-based molecules,[63-64] have also been reported as effective linker components for MOF fabrication. The geometry of the ligand is primarily dictated by its core structure, with several examples in the literature employing two-dimensional ligands that exhibit linear, bent, or star-like geometries.[65] Additionally, three-dimensional linkers have been utilized in MOF design, further expanding the structural diversity of these materials.[66] The topology of a MOF is determined by both the geometry of the linker and the coordination geometry of the SBU.[67] By modifying the length and functional groups attached to the linkers, and adjusting the number of SBUs, a wide variety of MOFs with tailored structures and properties can be synthesized. Furthermore, the fine-tuning of existing MOFs can be achieved through the principles of reticular or isoreticular chemistry, allowing for precise modifications to enhance their functionality.[68] For example, elongating the organic linker of a MOF while preserving its original geometry enables the tuning of the pore size of the resulting framework.[69]

Several methods for the synthesis of MOFs have been described in the literature. These include solvothermal synthesis,[70-71] which involves the use of high temperatures; microwave-assisted approaches,[71-73] which offer rapid synthesis; and the synthesis at ambient temperature and pressure, allowing the formation of MOFs without the need for elevated temperatures, offering a more straightforward and energy-efficient synthesis route.[74-75] The incorporation of modified organic linkers enables post-synthetic modification (PSM), allowing further functionalization and fine-tuning of the MOF after its synthesis.[76-78]

In 2008, a zirconium-based MOF was first described by LILLERUD and colleagues at the University of Oslo.[79] This cubic framework was named after the university, where it was discovered: UiO – Universitat I Oslo. UiO MOFs consist of a cationic zirconium cluster, $[Zr_6O_4(OH)_4(CO_2)_{12}]^+$, combined with three different negatively charged carboxylate linkers 1,4-benzene dicarboxylate (**BDC**, **1**), 4,4′-biphenyl dicarboxylate (**BPDC**, **2**), and terphenyl dicarboxylate (**TBC**, **3**). The nomenclature of these frameworks was assigned based on the applied linker: **UiO-66** containing **BDC**, **UiO-67** incorporating **BPDC**, and **UiO-68** utilizing the **TBC** linker (Figure **4**).

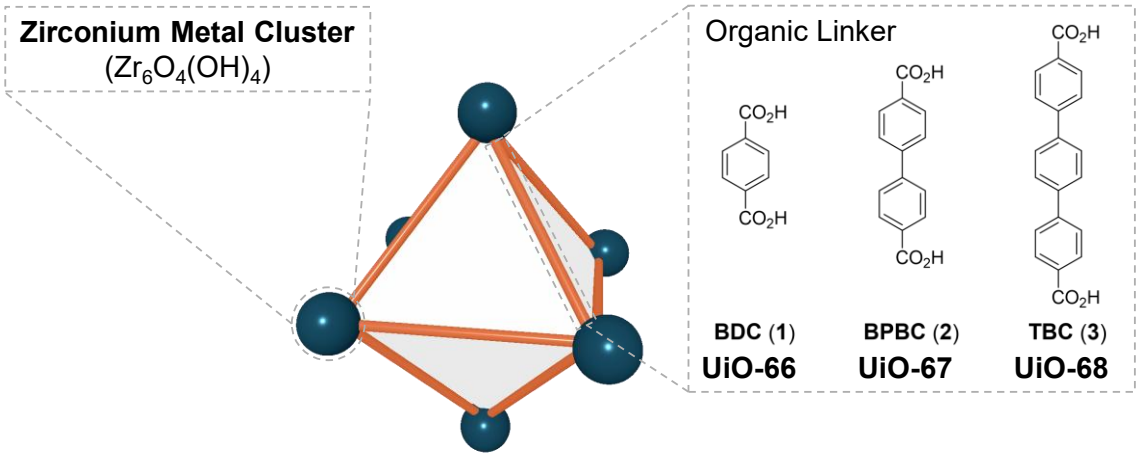

Figure 4: Schematic illustration of metal-organic framework (MOF) **UiO-66**, **-67**, and **-68**.

The thermal stability of most MOFs is generally limited, common frameworks exhibit decomposition temperatures between 350 and 400 °C. Only the aluminum-containing **MIL-53** MOF has been reported with decomposition temperatures of approximately 500 °C.[80] However, due to the strong zirconium–oxygen bond, UiO-MOFs exhibit remarkable properties. **UiO-66** and its derivatives not only have exceptional thermal stability, with decomposition temperatures up to 540 °C, they also exhibit high mechanical (modulus of rigidity of G_{min}=13.7 GPa)[81] and exceptional chemical stability under acidic and basic conditions.[82] Furthermore, surface area measurements revealed remarkably high values, with **UiO-67** exhibiting a surface area of up to 4170 m²/g. These features make UiO-based MOFs highly robust materials for various applications.[83]

Surface Mounted Metal-Organic Frameworks. Thin films of MOFs are synthesized using different techniques and are divided in solution- and vacuum-based approaches. Solution-based techniques include liquid phase epitaxy (LPE) and substrate-seeded heteroepitaxy (SSH), whereas examples of vacuum-based methods involve electrochemical deposition or chemical vapor deposition (CVD).[84] In the LPE approach, thin films of MOFs are prepared on modified substrates like gold, glass, or silicon. In this approach, the MOF is grown in a layer-by-layer (LbL) technique. In contrast to the conventional bulk synthesis of MOFs, the synthesis on a modified surface results in materials with well-defined crystalline structure, low defect density, and controlled film thickness.[84-85]

The LPE technique is one of the most widely used methods for SURMOF fabrication, originally established by WÖLL and colleagues.[86] Two key factors are essential in this approach. First, the substrate surface is functionalized with a self-assembled monolayer (SAM), as an anchoring layer for MOF growth.[84, 87] The SAM is introduced onto the surface to initiate the deposition of the first metal node or organic linker. This monolayer contains functional groups such as -NH_2,[88] -CO_2H, or -OH,[89-90] which facilitate the nucleation and growth of the MOF thin film, ensuring strong adhesion and controlled structural formation.[40, 86] Secondly, unlike traditional solvothermal MOF synthesis, where all precursors are mixed in a single solution, in SURMOF synthesis the metal and linker precursors are applied in separate solutions,[71] allowing for controlled LbL growth and improved structural precision. The different substrate solutions are sequentially applied to the functionalized surface using dipping or spin-coating techniques, with intermediate rinsing steps between each application to remove excess of starting material.[91] This controlled deposition process allows precise regulation of the SURMOF film thickness, which can be customized by varying the number of application and rinsing cycles (Figure **5**).[92] Compared to bulk MOF synthesis, the LPE approach significantly reduces the formation of interpenetrated networks. These interpenetrating networks arise when multiple identical frameworks form simultaneously during the bulk synthesis, co-existing with the targeted MOF. Their presence drastically decreases pore size and reduces the available void space within the framework. Moreover, interpenetration can ultimately lead to the collapse of the framework upon solvent removal.[93-94] However, it is important to note that the fabrication of SURMOFs using the LPE approach is primarily restricted to paddlewheel-structured SBUs, such as those derived from copper(II) and zinc(II) acetates. Despite this limitation, the variety of possible organic linkers, including carboxylate- and nitrogen-containing ligands, allows structural diversity and functional tunability of the resulting SURMOFs.[84]

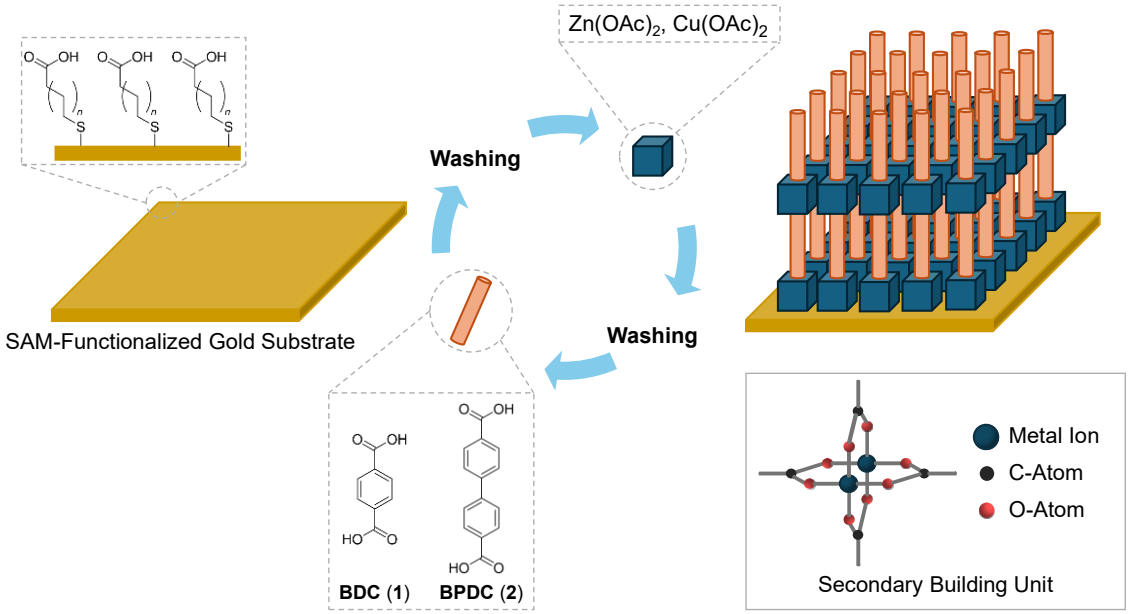

Figure 5: Schematic illustration of **SURMOF-2** fabrication *via* Liquid Phase Epitaxy (LPE).

A specific example of SURMOFs is **SURMOF-2**, which is derived from one of the simplest known MOFs, **MOF-2** first described by YAGHI and co-workers in 1998.[95] The secondary SBU of **MOF-2** consists of four dicarboxylate ligands coordinated to either two zinc(II) or copper(II) ions, forming a two-dimensional lattice.[95-97] The stacking of these two-dimensional **MOF-2** layers in bulk leads to the formation of a three-dimensional structure, where the planes are stabilized by intermolecular hydrogen bonds between the adjacent carboxylic acid moieties. However, the interactions between these stacked planes induce distortions within the lattice. In contrast, thin films derived from **MOF-2** exhibit a completely different structural arrangement. **SURMOF-2**, when grown on a carboxylate-terminated surface, adopts an architecture in which the two-dimensional planes are oriented perpendicular to the substrate. This orientation results in a perfectly stacked lamellar structure, without the distortions observed in the bulk material.[97]

The successful fabrication of SURMOFs is highly dependent on optimizing reaction parameters. Crucial factors such as substrate concentration, temperature, and reaction time significantly influence the structure, crystallinity, and overall properties of the framework.[98] With the rapid advancement of artificial intelligence (AI) and machine learning (ML), current research efforts are focused on developing automated screening methods for reaction parameters.[99-101] These approaches aim to systematically identify the optimal conditions for MOF growth, enhancing the discovery of novel frameworks with tailored properties.

Applications of Inorganic-Organic Materials. In recent years the interest in MOFs and SURMOFs increased drastically within the scientific community and in the industrial sector. This increase is based on their diverse applications across various fields, including gas storage and drug delivery.[102] The exceptional potential of MOFs has found its way into commercial application,[103] demonstrating their impact on economic growth and research efforts.[38, 104] MOFs possess an exceptionally large surface area, with examples reaching up to several thousand of m^2/g,[59] making them ideal candidates for gas storage and separation applications.[8, 105] MOFs are actively investigated in the CO_2 capturing process to reduce atmospheric CO_2 concentrations, and the storage of potential fuels such as methane (CH_4) and hydrogen (H_2). For instance, the copper-based MOF **HKUST-1** has been investigated as a candidate for storing CH_4 at ambient temperature, with an uptake of 270 cm^3 at 65 bar pressure.[106-107] More challenging is the storage of molecular H_2. Since H_2 is discussed as a potential fuel in transportation, the need for materials capable of storing large amounts of H_2-gas is omnipresent. Different MOFs were tested showing outstanding performances. MOFs, *e.g.*, **MOF-177** consisting of a zirconium cluster and 1,3,5-benzenetribenzoate (BTB) can store up to 7.5 wt% of H_2 at 70 bar and 77 K.[38, 105]

A critical challenge in modern drug delivery is the precise targeting of therapeutics to specific cells within the body. MOFs emerge as promising candidates to address this challenge due to their exceptional modifiability.[30, 108] Precise modification either of the organic linkers or the metal nodes within the MOF structure allows researchers to specifically adjust their properties, like the pore size, enabling the encapsulation of various biologically active compounds.[109-111] This tunability enables the fabrication of surface-functionalized MOFs with targeting moieties enabling selective binding to cells and allowing the controlled drug release, which minimizes off-target effects and thereby enhancing drug safety. However their inherent toxicity in living cells due to the presence of heavy metal ions and organic ligands remains a challenge.[112-114] In a recent study, TSOTSALAS and colleagues demonstrated the successful surface modification of **UiO-66** nanoparticles using the Nitroxide-Exchange Reaction (NER). This approach enabled the surface modification of the nanoparticle with the integrin-targeting RGD-sequence.[109] However, applications of MOFs exceed drug delivery and gas storage. These versatile materials are also extensively investigated as heterogeneous catalysts and in sensing applications, highlighting their impact across various scientific disciplines.[37]

1.1.2 Porous Organic Materials

Covalent Organic Frameworks. In contrast to MOFs, which incorporate both organic and inorganic components, Covalent Organic Frameworks (COFs) are crystalline and highly porous materials entirely composed of organic building blocks. This compositional difference often translates to significantly lower densities for COFs compared to MOFs.[54, 115] The formation of linkages between monomers *e.g.*, in polymer chemistry typically involves kinetically controlled reactions, resulting in the formation of irreversible covalent bonds. While kinetically controlled polymerizations often result in amorphous materials, the irreversible nature of the reactions employed in COF synthesis favors the formation of the thermodynamically most stable structure, leading to the construction of highly crystalline materials.[116-117] Based on the geometry of the employed building units, COFs can be classified as either two-dimensional (2D) layers or 3D frameworks. Using monomers with linear, trigonal-planar, or rectangular geometries typically results in the formation of planar 2D sheets; stacking each layer ultimately forms the 3D structure. Vice versa, incorporating monomers with 3D geometries, such as those containing sp^3-hybridized carbons with a tetrahedral geometry or silanes, leads to the construction of non-planar 3D frameworks.[118-119]

A significant milestone in the research field occurred in 2005, when YAGHI and colleagues reported the synthesis of the first COF, marking a decade after the initial description of MOFs. **COF-1** and **COF-5** were synthesized *via* self-condensation reaction of 1,4-benzene boronic acid (**BDBA**, **4**) and the reaction of **BDBA** with 2,3,6,7,10,11-hexahydroxytriphenylene (**HHTP**, **5**), resulting in the formation of a boron-based framework exhibiting both micro- and mesopores with surface areas of ~700 m^2/g (**COF-1**) and ~1600 m^2/g (**COF-5**).[120] The structure of both COFs is shown in Figure **6**.

Similar to MOFs, the successful construction of COFs requires the utilization of building blocks that meet specific criteria, including symmetric connectivity and structural rigidity. Aromatic building units primarily fulfill these criteria, offering facile functionalization and tunability to suit specific applications.[119, 121] Currently, several reversible reactions are employed successfully for the construction of COFs.

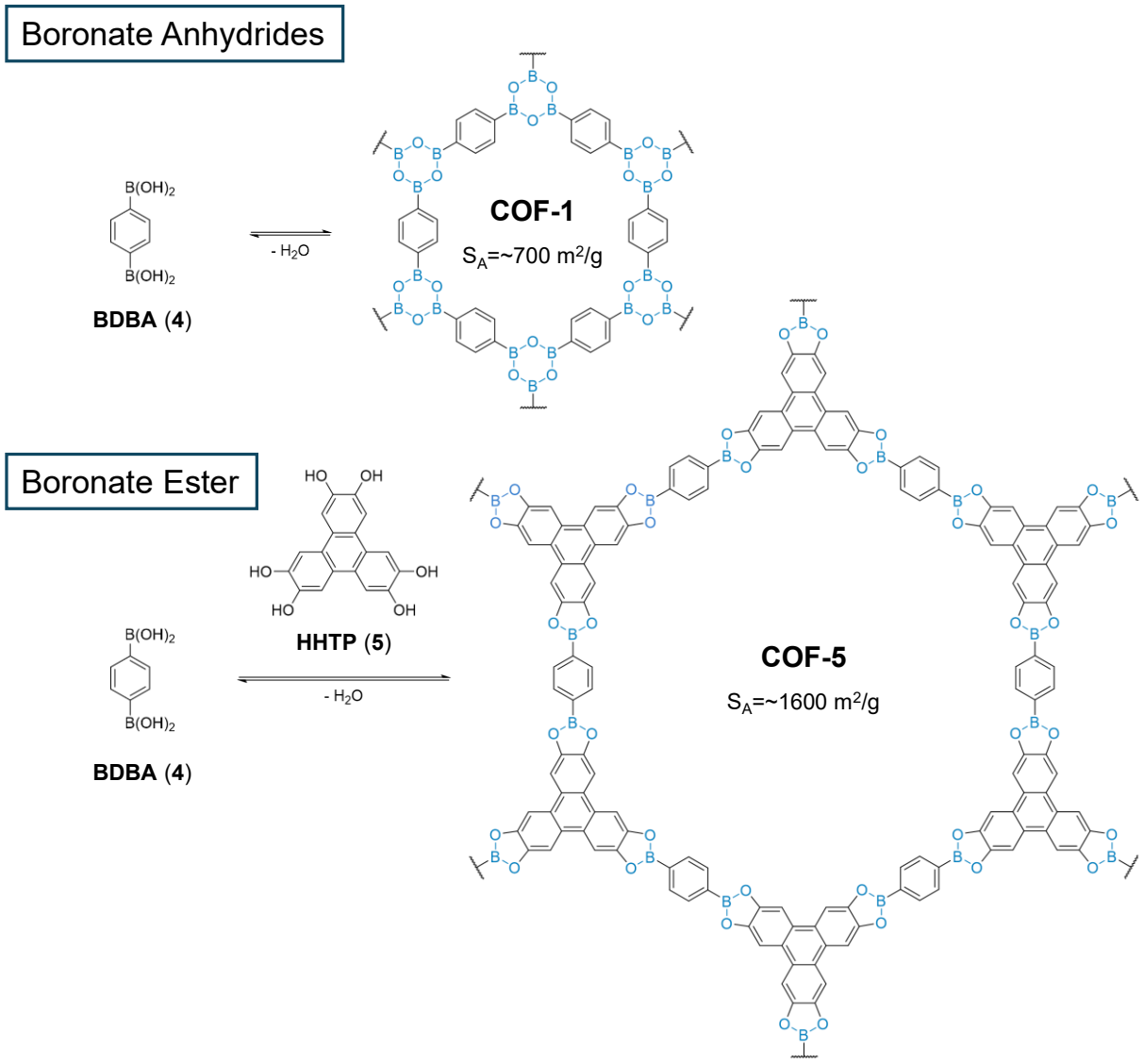

Figure 6: Structure of **COF-1** and **COF-2** as examples for boron-based covalent organic frameworks (COFs).

Self-condensation of boronic acids leads to the formation of boronic anhydride-linked frameworks. Further synthetic strategies involve condensing boronic acids with aromatic alcohols or ketals, resulting in the formation of boronic ester-linked frameworks. Finally, boronic acids can react with silanols to form frameworks connected *via* borosilicate linkages. Due to their linkages, boron-based frameworks are susceptible to hydrolysis in the presence of water or high humidity.[122] Significant research efforts have been undertaken since the initial report of boron-based COFs. These efforts have yielded remarkable advancements, with several frameworks now exhibiting exceptional surface areas exceeding 4000 m^2/g and remarkably low densities.[123]

Triazine-based COFs are synthesized *via* the cyclotrimerization of aromatic nitriles. In 2008, the first representative **CTF-1** was synthesized *via* cyclotrimerization of 1,4-dicyanobenzene (**6**) (Figure **7**).[124] Compared to condensation reactions, cyclotrimerization typically requires elevated temperatures, often exceeding 400 °C, which can limit the incorporation of thermolabile functional groups. Furthermore, the irreversibility of the trimerization reaction often leads to the formation of frameworks with lower crystallinity compared to those synthesized *via* reversible reactions.[117, 125] Despite these challenges, triazine-based frameworks exhibit several desirable properties, including high surface areas, low densities, and exceptional thermal and chemical stability. Their remarkable thermal stability, with decomposition temperatures up to 600 °C, can be attributed to the formation of the ultra-strong aromatic *C=N* bonds within the triazine units.[126]

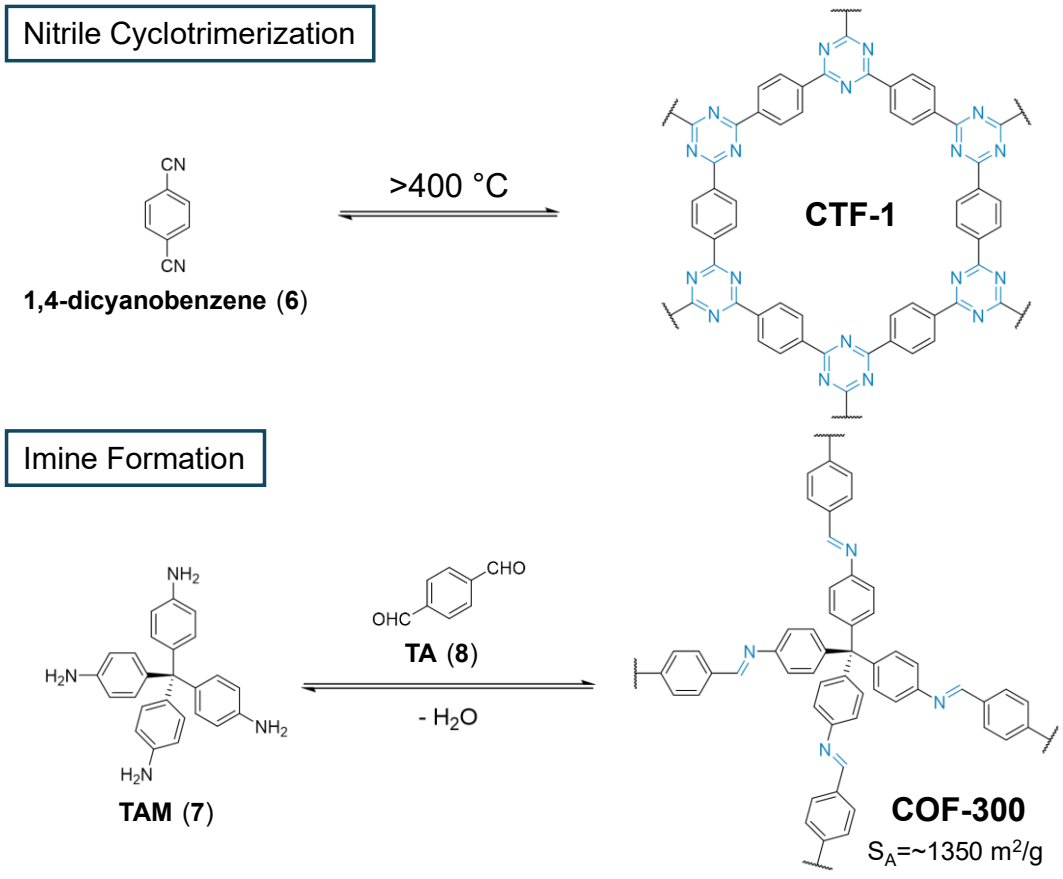

Figure 7: Overview of triazine- and imine-based covalent organic frameworks (COFs). **CTF-1** is an example of a triazine framework synthesized *via* nitrile cyclotrimerization of 1,4-dicyanobenzene (**6**). As an example of an imine-linked framework synthesized *via* condensation of **TAM** (**7**) and **TA** (**8**), the repeating unit of **COF-300** is visualized.

The third class of COFs includes imine-based frameworks. These frameworks are synthesized through the reversible condensation reaction of aldehydes with either aromatic amines or aromatic hydrazines. The condensation of an aldehyde with an amine results in the formation

of a Schiff-base-type framework, while the reaction with hydrazines yields hydrazone-based networks.[115, 127] Compared to boron-based frameworks, which exhibit susceptibility to hydrolysis, and triazine-based COFs, which often show lower crystallinity, imine-linked frameworks demonstrate enhanced stability against hydrolysis compared to boron-based frameworks and typically exhibit high crystallinity.[115, 128-129] In 2009, YAGHI and co-workers reported the condensation reaction of terephthalaldehyde (**TA**, **8**) with tetrakis(4-aminophenyl)methane (**TAM**, **7**), resulting in the formation of the first imine-based organic framework, namely **COF-300** (Figure **7**). This diamond-shaped COF showed exceptional properties including thermal stability up to ~500 °C and a surface area of ~1350 m^2/g.[128]

In recent years, advancements in the synthesis of COFs have been made to enhance the stability of the formed imine-bond. BANERJEE and colleagues used 1,3,5-triformylphloroglucinol (**TP**) and diamines to form crystalline enol-imine COFs (**TpPa-1** and **TpPa-2**) as seen in Figure **8**. Subsequent, irreversible keto-enol tautomerization resulted in the formation of a *ß*-ketoamine-connected COF. Notably, they demonstrated that this tautomerization process did not influence the crystallinity of the material, while significantly enhancing its chemical stability against both acidic as well as basic hydrolysis.[130] Another representative of COFs linked *via* imine-bonds is **TUS-64**. This 3D framework was prepared by condensation of aldehyde 2,3,6,7,14,15-hexakis(4'-formylphenyl)triptycene (**HFPTP**, **10**) with the amine 5,10,15,20-tetrakis(4-aminophenyl)porphyrin (**TAPP**, **9**) and exhibits remarkable properties, most notably the lowest density reported for any organic framework to date, with a value of 0.106 g/cm^3 (Figure **8**).[131]

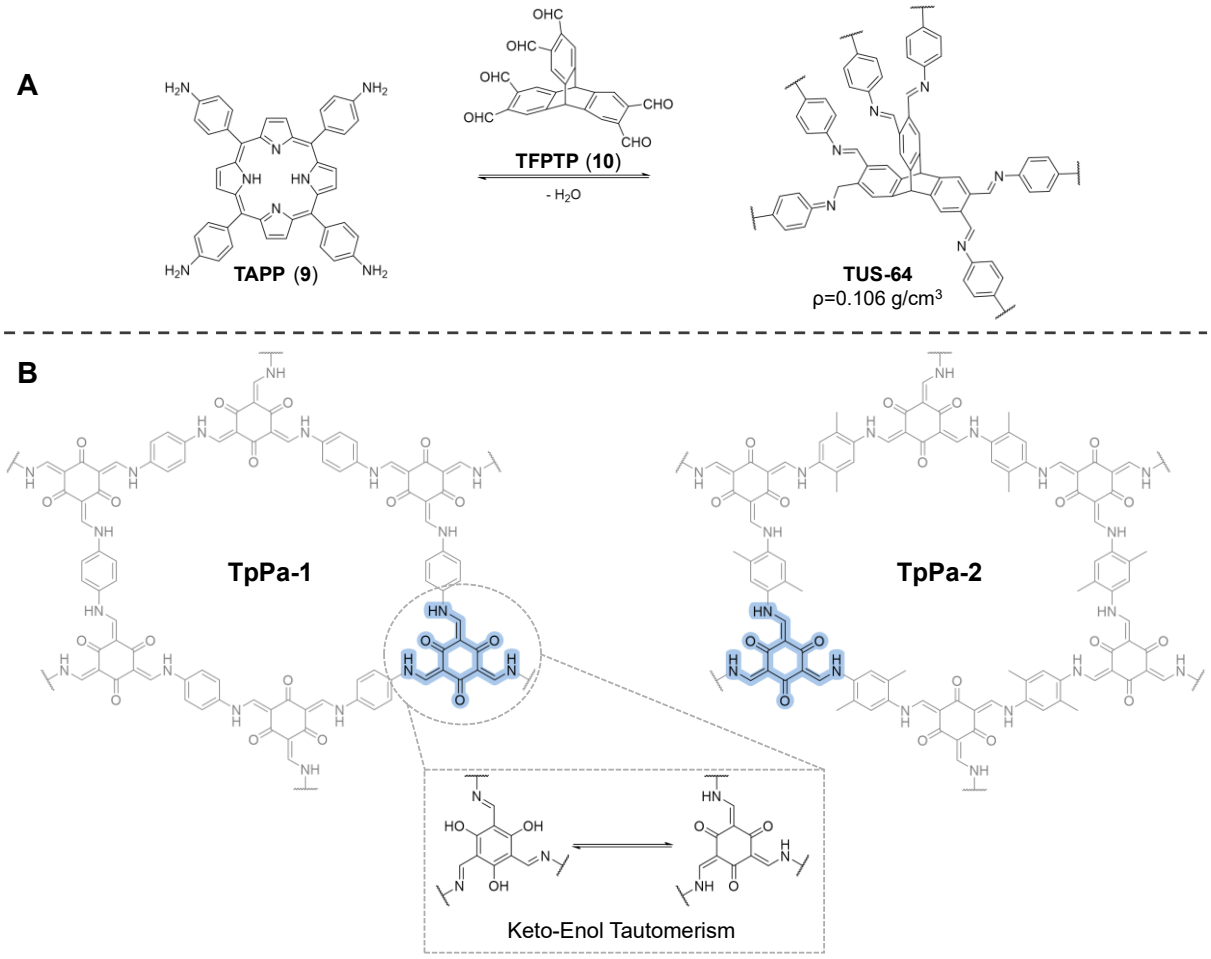

Figure 8: Examples of covalent organic frameworks (COF). A) Synthesis of the imine-linked framework TUS-64 from amine **TAPP** (**9**) and aldehyde **TFPTP** (**10**). **TUS-64** holds the record for an organic framework with the lowest density with a value of 0.106 g/cm^3. B) The structure of COFs **TpPA-1** and **TpPA-2**, keto-enol tautomerism results in a stable framework against acidic and basic conditions.

Polymers of Intrinsic Microporosity. In recent years, there has been a significant increase in interest in porous materials due to their diverse applications in catalysis, gas storage, and separation. This growing interest has driven extensive research efforts, leading to the development of numerous novel porous materials.[132] Polymers with intrinsic microporosity (PIMs) are a sub-class of porous materials that have been developed recently. The first PIM (**PIM-1**) was reported in the literature in 2004 by McKweon and colleagues. Step-growth polymerization *via* nucleophilic aromatic substitution of catechol-based monomers with electron-deficient aromatic systems resulted in the formation of this novel class of macromolecules. A combination of different building blocks gave excess to several PIMs. The determination of the surface revealed highly porous materials with micropores in the range of 0.4-0.8 nm, remarkable thermostability (decomposition at 300 °C), and surface areas up to 850 m^2/g.[133]

The term "intrinsic microporosity" arises from the fact that the porosity of PIMs originates solely from their inherent molecular structure and is not influenced by external factors such as processing techniques. However, the successful construction of PIMs relies on the reasonable selection of monomers. The incorporation of rigid monomers into the polymer backbone results in the formation of rigid and contorted polymer units and prevents efficient chain packing, ultimately leading to the formation of micropores and nanopores within the formed polymer.[132, 134] PIMs have emerged as promising candidates for various applications due to their remarkable properties,. Recent studies have demonstrated the high efficiency of PIMs in separating CO_2 from other gases. These results have considered PIMs as potential state-of-the-art materials for gas separation applications.[135-137]

A recently reported subclass of PIMs possesses the TRÖGER'S base (TB) moiety in their backbone. TB was first synthesized by J. TRÖGER in 1887 *via* condensation of formaldehyde (**12**) with *p*-toluidine (**11**) in an acidic environment and resulted in the formation of a non-polymeric product containing the bridging bicyclic diamine (Figure **9A**).[138] In 1935, the unknown product was identified as TB.[139] Structural investigations conducted in 1944 by PRELOG and WIELAND, employing chromatographic resolution techniques, revealed the chiral nature of the bridging unit within the TB molecule.[140]

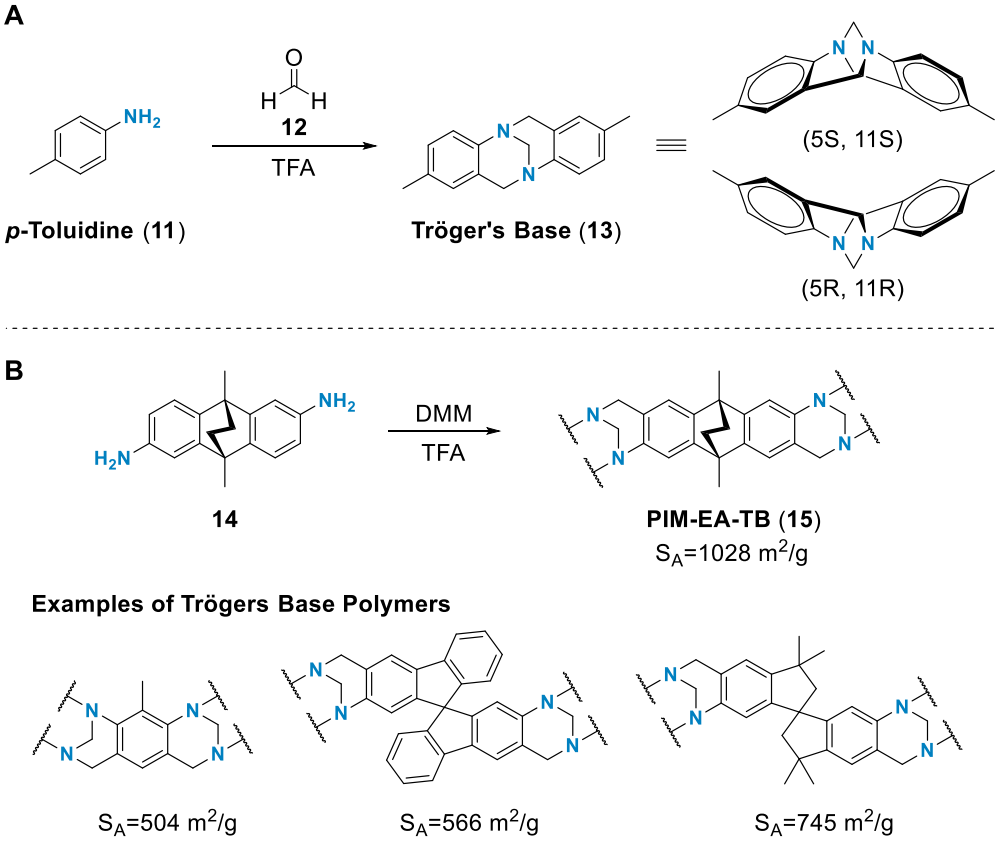

Figure 9: A) Synthesis of TRÖGER's Base (**13**) *via* condensation reaction of *p*-toluidine (**11**) with formaldehyde (**12**) under acidic conditions. B) Synthesis of **PIM-EA-TB** (**15**) *via* TRÖGER's base formation with a surface area of S_A=1028 m^2/g and examples of TB polymers with their respective surface area.

Although TB-containing molecules have a long history in organic synthesis, applications of TB chemistry in the synthesis of polymeric materials have remained relatively unexplored.[141-143] In 2014, MCKEOWN and colleagues reported the synthesis of several PIMs utilizing a novel approach. This approach involved the incorporation of the TB motif into the polymer backbone by reacting various aromatic diamines with dimethoxymethane (DMM) under acidic conditions, leading to the formation of TB-linked polymeric chains (Figure **9**). These TB-based PIMs exhibited remarkable properties, including high surface areas (up to 1030 m^2/g for **PIM-EA-TB**, **15**) and excellent thermal stability with decomposition temperatures reaching 350 °C (Figure **9B**).[144] While their surface areas are much lower compared to those reported for MOFs or COFs, the ease of synthesis and their ability to effectively separate gases make TB-based PIMs an intriguing class of porous materials.[145-146]

Applications of Porous Organic Materials. The modifiability of pore size and shape, combined with their crystallinity, large surface areas, low densities, and excellent thermo- and chemical stability, makes porous organic materials promising candidates for a wide range of applications, including optoelectronics, catalysis, gas storage and separation.[116, 118, 127, 129]

The significant increase in global CO_2 emissions, primarily driven by the combustion of fossil fuels, and the need for novel energy storage systems have intensified the need for materials with excellent gas separation abilities or high gas storage capacities.[147-148] Porous materials are extensively investigated for gas storage applications, including the storage of H_2 and CH_4 for energy purposes and CO_2 capture for reduction of greenhouse gases in the atmosphere.[55] High storage capacities are needed for both applications, but the desired material properties differ significantly. For CO_2 capture, materials should exhibit strong adsorption of CO_2 to remove it from gas streams effectively.[149-150] In contrast, for energy storage applications involving H_2 or CH_4, materials should exhibit weak VAN-DER-WAALS interactions with the stored gas to facilitate efficient desorption and subsequent energy release.[6] In this context, 3D COFs are generally favored over 2D COFs for gas storage applications due to their typically higher surface areas and pore structures, which can enhance gas adsorption and storage capacity.

The U.S. Department of Energy (DOE) established criteria for H_2 storage in vehicles, setting a target storage capacity of 5.5 wt% at an operating pressure of 100 bar by 2017. Since then, COFs have been intensively studied to fit the targeted criteria defined by DOE. The highest H_2 uptake was found for **COF-102** with 7.24 wt%, comparable to uptake capacities demonstrated for MOF-based materials (see Chapter **1.1.1**, **MOF-177**). While theoretical studies have demonstrated the potential for H_2 storage within COF systems at ambient temperatures, experimental studies have primarily focused on H_2 uptake measurements at 77 K, significantly lower than the targeted operating temperature range of –40 to 60 °C for practical on-board H_2 storage applications. Furthermore, the CH_4 storage capacity of COF-based materials has also been investigated. The DOE has defined a target CH_4 storage capacity of 180 mg/g at 35 bar pressure. COF systems, such as 3D **COF-102**, have demonstrated CH_4 uptake capacities exceeding this target, reaching even 187 mg/g. However, the often-tedious synthesis procedures and the relatively high cost of producing such materials remain significant challenges for their industrial application.[54, 115, 118, 151]

Membrane gas separation has emerged as a promising strategy for capturing and separating CO_2 and has gained significant interest within the scientific community. Since 2013, TB-based polymers were extensively studied for their application in gas separation.[152-153] BRÄSE and

co-workers recently reported the incorporation of different amino-functionalized [2.2]paracyclophane building blocks into TB-polymers. While the surface areas of these newly synthesized PIMs may not compete with those of established materials such as **PIM-EA-TB** (see Figure **8**), the determination of their CO_2/N_2 selectivity of the materials, demonstrated their potential as candidates for effectively separating CO_2 from flue gas streams. The synthesized TB-polymer were reported to have CO_2 over N_2 selectivities in the range of 47 to 70. These selectivity values are comparable to those reported for nitrogen-containing materials with similar surface areas that were investigated and employed in gas separation applications.[154-156]

1.2 3D Printing of Functional Materials

Additive Manufacturing (AM), commonly known as 3D printing, was defined by the American Society for Testing and Materials (ASTM) in 2009 as a process of joining materials to create objects from 3D digital models (computer-aided design, CAD), typically using layer-by-layer methods.[157] Initially, AM techniques have been widely applied across various industry sectors, enabling the rapid and cost-effective fabrication of prototypes,[158] the construction of highly complex geometries, and significantly reducing production waste. Furthermore, 3D printing has facilitated the production of highly customized parts with minimal tooling requirements.[159]

The first AM technique, introduced by C. HULL in the late 1980s, is known as Stereolithography (SLA). In SLA, a UV light source initiates the polymerization of acrylate- or epoxide-based inks, resulting in the construction of the 3D printed object.[160-161] Since then, several printing technologies have been introduced and some of them are already utilized in industry. Today, 3D printing has become an essential tool in industry and research such as automotive, aerospace and aircraft manufacturing, as well as robotics and tissue engineering.[158-159, 162]

According to the 2009 ASTM standards, 3D printing technologies can be classified into subclasses based on the manufacturing processes employed. These subclasses include examples like binder jetting (BJT), inkjet printing (IJP), vat photopolymerization (VPP), direct energy deposition (DED, and fused deposition molding (FDM) (Figure **10**). This classification provides a standardized framework for categorizing and understanding the diverse 3D printing technologies available.[157]

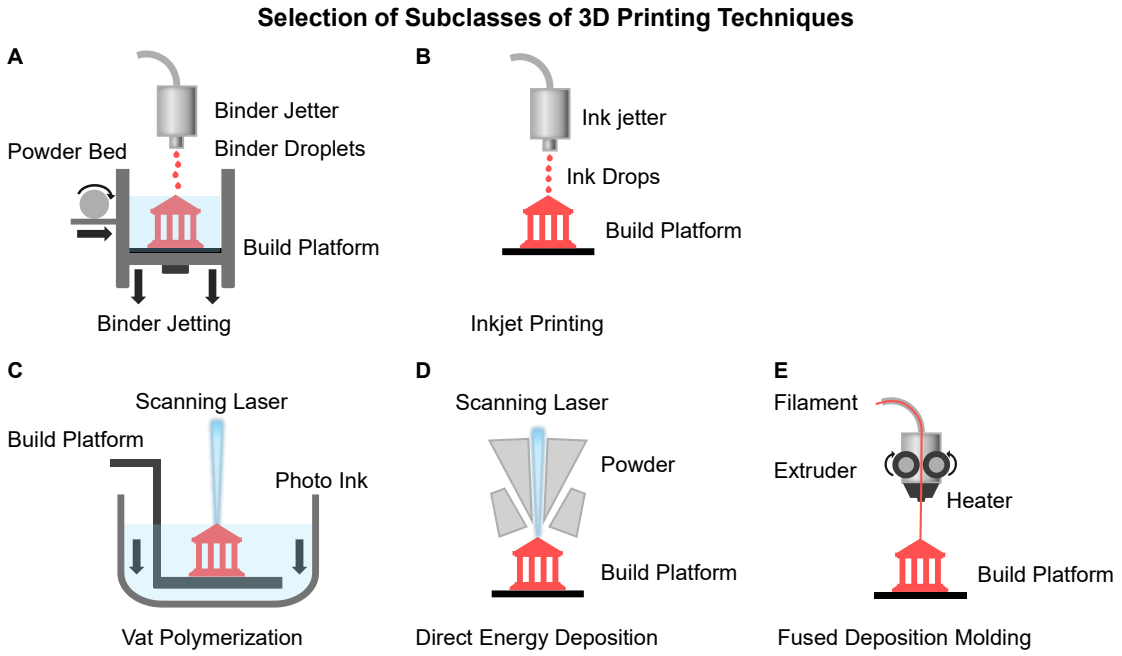

Figure 10: Selection of subclasses of 3D printing. A) Binder Jetting, B) Inkjet Printing, C) Vat Polymerization, D) Direct Energy Deposition, and E) Fused Deposition Molding. Adapted from literature.[163]

Based on the ASTM standards, SLA is classified as a photopolymerization process. In contrast, FDM, characterized by its ease of access and cost-effectiveness, falls under material extrusion systems. In FDM, a thermoplastic material, such as polylactic acid (PLA), is extruded layer-wise onto a build platform. Each successive layer is deposited on top of the previously printed layer, gradually building up the three-dimensional object.[164]

Direct Laser Writing (DLW) is classified as a photopolymerization-based printing technique and utilizes nonlinear photon absorption to solidify a photopolymerizable ink.[165] While the SLA and FDM techniques fabricate objects in a layer-by-layer fashion,[161, 164] DLW directly solidifies the ink within the material volume. This eliminates the need for a layer-by-layer approach and allows for the fabrication of 3D structures with sub-100 nm resolution.[165-166]

1.2.1 Light-Driven Additive Manufacturing Techniques

3D Printing by Photopolymerization. In photopolymerization-based AM techniques, such as SLA, DLW, and Digital Light Processing (DLP), a liquid photo ink is irradiated with light, inducing the solidification of the exposed areas.[167] The photo ink typically consists of a monomer and a photoinitiator (PI). However, adding various additives can further enhance the performance of the printed materials.[168] The absorption of a photon by the PI generates reactive species such as radicals or cations. These reactive species then initiate the polymerization process, leading to the solidification of the ink.[169] While PIs are commonly

employed in photopolymerization processes, examples of photoinitiator-free inks have been reported in the literature. The polymerization mechanism in these systems is based on thermally forbidden cycloaddition reactions, such as [2+2] or [4+4] cycloadditions, which can be carried out photochemically.[170-172]

Since the initial development of SLA, several improvements have been made to optimize the performance of the technique. Nowadays, sophisticated objects can be printed using a variety of different kinds of materials. Laser scanning lithography (first-generation) utilizes a moving laser beam in the x- and y-axis to trace. In contrast, the control of the z-axis is realized by the vertical movement of the platform. The photosensitive ink is irradiated in a layer-by-layer approach, which results in the construction of the printed structure (Figure **11**). This process is known for producing highly detailed and accurate parts with smooth surface finishes, making it a widely applied technology in industrial applications to fabricate complex components. Further developments resulted in the introduction of the second-generation SLA system called projection SLA. In contrast to the first-generation system, projection SLA enables the simultaneous printing of an entire layer through a single exposure of the build platform using a photomask.[160, 173]

In contrast to the SLA technique in which a single laser beam prints the object, in DLP a field of light is applied to the resin vat. The main mechanical component in DLP-based 3D printers is a so-called Digital Micromirror Device (DMD). This device consists of an array of micromirrors, each mirror has two distinct states, the ‘on’ state in which the mirror reflects the light, and the ‘off’ state, where no light is reflected. The printing process is controlled by switching the state of each mirror, generating a spatially controlled light pattern projected onto the photosensitive resin within the vat. This pattern defines the areas exposed to light, initiating the photopolymerization process and forming the desired 3D object (Figure **11**).[173-174]

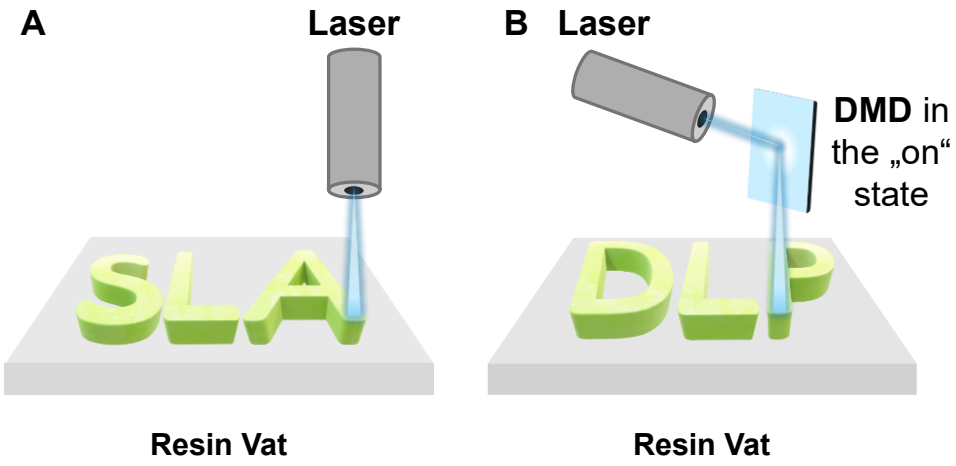

Figure 11: Schematic illustration of Stereolithography (SLA) and Digital Light Processing (DLP) 3D printing.

The printing technique DLW can be categorized into two subclasses based on the underlying photopolymerization mechanism. Pioneering work in the early 1990s led to the development of one-photon absorption (1PA) DLW.[175] Subsequently, in 1997, DLW by multi-photon absorption was introduced.[165] The theoretic base of multi-photon absorption was first described by Maria Goeppert-Mayer in her 1931 doctoral thesis, titled "*Über Elementarakte mit zwei Quantensprüngen*" ("About Elementary Acts with Two Quantum Jumps"). This process involves the simultaneous absorption of two photons, where the sum of the energy of both photons is equal to the transition energy required to excite the electron of the molecule to a higher energy state and is therefore termed two-photon absorption (2PA). In contrast to 1PA, where the absorption of a single photon excites an electron from the ground state to a higher electronic and vibrational energy state, 2PA involves a sequential two-step process. In 2PA, the absorption of the first photon by an electron induces excitation from the ground state into a virtual excited state. This intermediate state is short-lived and only exists within the focal region of the laser beam. Subsequent absorption of a second photon by the electron in this virtual state excites it to a higher electronic and vibrational energy state.[176-179] A schematic illustration of the DLW printing process is shown in Figure **12**.

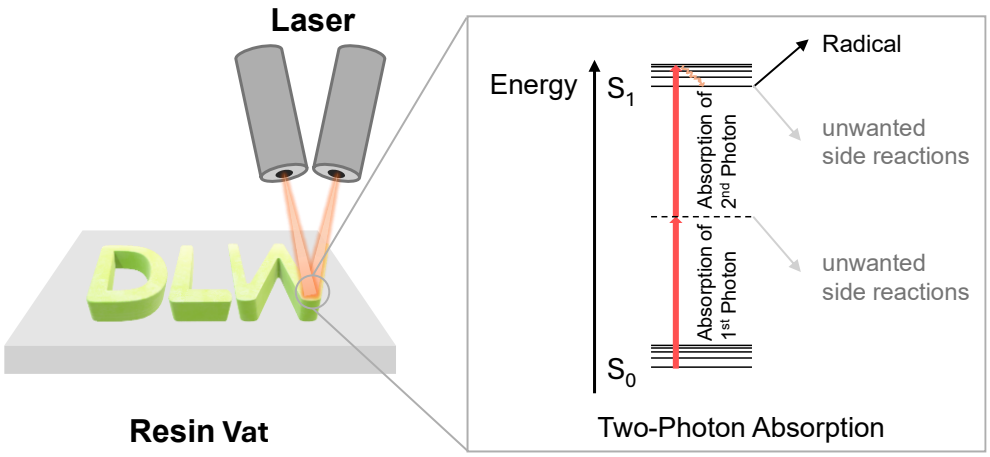

Figure 12: Direct Laser Writing (DLW) *via* Two-Photon Absorption (2PA).

In the context of photopolymerization, the PI gets excited from its ground state to an excited state by the simultaneous absorption of two photons. From this excited state, the PI typically generates reactive species, such as radicals, which subsequently initiate the polymerization process, leading to the solidification of the resin.[178]

Two-Step 3D Laser Nanoprinting. 2PA-DLW typically utilizes femtosecond lasers operating in the near-infrared region, around 800 nm. In contrast, 2SA typically employs one or two continuous-wave (cw) lasers with wavelengths of 405 nm and 640 nm.[180] Although 2PA was successfully applied in widespread applications such as cell biology[181] or photonics,[182] its practical implementation faces significant challenges. The femtosecond lasers employed in 2PA systems are voluminous and expensive, significantly increasing the overall cost and complexity of such printing systems. These factors have hindered the 2PA-based 3D printing of being a widely applied technology.[183] In 2021, WEGENER and colleagues reported a novel 3D printing method that replaces the 2PA mechanism with two-step absorption (2SA). In their study, benzil (**16**), a 1,2-diketone, was successfully utilized as PI for this innovative approach.[184]

In the 2SA approach, the virtual existing state is replaced by a real electronic state that exists independently of the excitation. Non-radiative processes typically determine the lifetime of this real existing state and can be significantly longer than femto- or picoseconds. Following excitation to the real existing excited state, the absorption of the second photon induces the generation of reactive species and subsequently initiates the polymerization process.[185] The PI can be excited using laser systems with operating wavelengths of 405 nm and 640 nm. Two 1,2-diketones, **16** and biacetyl (**17**), have been reported as PIs in 2SA 3D printing. For both

compounds, two excitation approaches can be distinguished: **16** can be used in two-step one-color 3D printing, excitation *via* the sequential absorption of two photons of the same wavelength (405 nm) results in the formation of the reactive species. In contrast, **17** was used in two-step two-color, in which the PI is excited *via* the sequential absorption of two photons with different wavelengths (405 nm and 640 nm).[184, 186] A simplified illustration of the mechanism of 2PA absorption is visualized in Figure **13**.

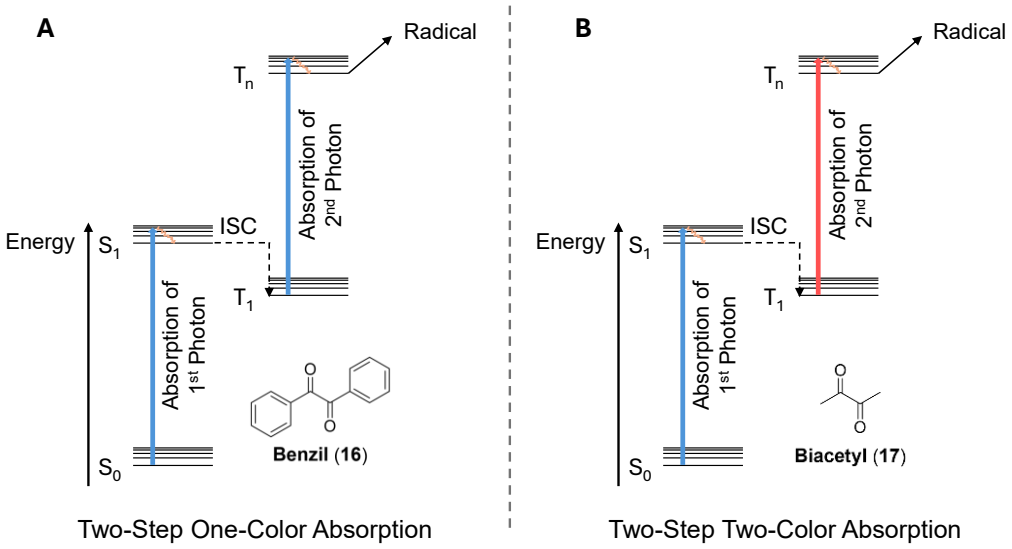

Figure 13: Simplified mechanisms of A) Two-Step One-Color Absorption using benzil (**16**) and B) Two-Step Two-Color Absorption using biacetyl (**17**).

Recently, WEGENER and co-workers demonstrated the application of **17** in a two-step two-color printing. In this novel 3D printing technique, a light-sheet-based approach is employed. This method significantly enhances printing speeds, resulting in fabrication times comparable to traditional injection molding processes.[187] Furthermore, 2SA systems are more compact and affordable laser sources compared to 2PA systems offering significant advantages in 3D laser printing technologies.[184]

2 Objective

Materials science has experienced significant growth in recent years, enabling the design and fabrication of novel materials with precisely tailored properties. Researchers are actively advancing the development of customized 3D-printed nanostructures to engineer materials with enhanced properties, such as increased strength or reduced weight.[4-5] Additionally, significant research efforts are dedicated to the synthesis of highly porous materials for applications in gas storage and separation, specifically to target the increase in atmospheric CO_2 concentration.[6-8] Furthermore, these advanced porous frameworks are being investigated for their potential in drug delivery applications, offering enhanced precision and efficiency in medical treatments.[9-12] This thesis includes five projects, each targeting the synthesis and characterization of novel molecules and their potential applications in materials science to contribute to the growing demand for advanced materials.

The first project aimed to develop a novel porous material incorporating the structurally unique [2.2]paracyclophane building block. To this end, a novel extended mono- and diamino-[2.2]paracyclophane should be synthesized from readily available [2.2]paracyclophane. The mono-functionalized paracyclophane derivative will serve as a model compound for optimizing polymerization conditions, while the diamino-functionalized derivative should be employed as a building unit for synthesizing TRÖGER's base-containing polymers of intrinsic microporosity. The synthesized materials will be characterized by CO_2 and N_2 adsorption-desorption measurements, with their surface areas and pore size distributions determined using the Non-Linear Density Functional Theory (NLDFT) and BRUNAUER-EMMETT-TELLER (BET) theory. Finally, the gas separation performance of these materials should be evaluated *via* theoretical determination of the CO_2/N_2 selectivity.

The novel diamino-functionalized [2.2]paracyclophane building block, synthesized in the previous project, should be utilized in the second project to prepare imine-linked covalent organic frameworks (COFs). These COFs will be synthesized *via* acid-catalyzed reactions at ambient temperature, employing a variety of aldehydes. These aldehydes should be synthesized from commercially available starting materials or purchased from commercial suppliers. The successful formation of the targeted COFs should be confirmed by Fourier-Transform Infrared (FT-IR) spectroscopy and elemental analysis (EA).

The third project investigated the surface functionalization of metal-organic framework nanoparticles (**MOF NPs**) utilizing the nitroxide-exchange reaction (NER). NER represents a

promising strategy for site-selective surface modification of **MOF NPs**, enabling the exchange of an alkoxyamine moiety within the MOF with a synthetically accessible nitroxide radical. In this context, **MOF NPs** should be functionalized with a peptide sequence containing the nitroxide moiety. The successful functionalization of the **MOF NP** surface should be confirmed by Time-of-Flight Secondary Ion Mass Spectrometry (ToF-SIMS) analysis.

Preliminary investigations by WÖLL and colleagues demonstrated the photochemical decomposition of an azide-functionalized stilbene linker within a surface-mounted metal-organic framework. However, these studies revealed an undesired side reaction: the nitrene generated *via* azide photolysis undergoes intramolecular *C-H* insertion into the nearby *C=C* bond of the stilbene linker, resulting in the formation of a five-membered nitrogen-containing ring. To prevent the intramolecular ring formation, the stilbene linker should be replaced by a tolan linker, thereby eliminating the *C-H* bonds in close proximity to the azide group. In the context of this thesis, mono- and diazido-functionalized tolan linkers should be synthesized from readily available starting materials. These newly synthesized linkers should then be employed in the preparation of SURMOFs *via* a layer-by-layer approach. Finally, the successful formation of the fabricated SURMOFs and the photochemical decomposition of the incorporated azide groups should be investigated.

Lastly, the fifth project investigates benzil-based photoinitiators as suitable candidates for 3D laser nanoprinting *via* two-step absorption. To enhance solubility within the photo ink formulation, containing pentaerythritol triacrylate (**PETA**) and 2,2,6,6-tetramethylpiperidine-1-oxyl (**TEMPO**), three benzil derivatives will be synthesized. The synthesized photoinitiators should be systematically evaluated regarding their two-step two-color absorption properties through point exposure and dose test experiments. Finally, the printing performance of these novel photoinitiators will be tested in 3D printing experiments, with a particular focus on comparing their printing behavior to the benchmark initiator, benzil.

3 Results and Discussion

3.1 Polymers of Intrinsic Microporosity containing [2.2]Paracyclophane as Monomer

Preface. In the following chapter parts are already evaluated and discussed in "Polymers of Intrinsic Microporosity Containing [2.2]Paracyclophane Moieties: Synthesis and Gas Sorption Properties (https://doi.org/10.1002/adfm.202401957)" published in 2024 in Advanced Functional Materials. Part of the discussion will be the monomer synthesis conducted during the framework of this thesis. If results from collaborators are used to compare or draw conclusions, the respective parts are mentioned in the text.

Introduction. The unique structure of [2.2]paracyclophane (PCP) is formed by two parallel aligned benzene moieties connected by ethylene bridges at the *para*-position of the respective aromatic ring. The short ethylene bridges in PCP induce ring strain, preventing the benzene rings from adopting their preferred planar geometry and leading to distorted bond angles. Consequently, one would initially expect reduced stability of this compound.[188]

Nevertheless, PCP is remarkably stable due to the restricted rotation of the two rings. Due to this inherent stability, PCP represents a promising monomer for diverse applications in materials science and has been studied extensively in MOFs and polymers.[189-191]

A relatively novel class of polymers are the so-called polymers of intrinsic microporosity (PIM), first introduced in 2004.[133, 135] A class of PIMs can be synthesized from rigid monomers *via* an acid-catalyzed condensation reaction of an amine and an aldehyde. This condensation reaction is known as the TRÖGER's reaction and results in the formation of a chiral nitrogen-containing bridging unit the TRÖGER's Base (TB).[144-145, 192] The rigidity hinders efficient packing of the polymer chains, resulting in the formation of micro- and nano-pores.[134, 193] PIMs are predestined for applications like gas storage, gas separation, water purification and catalysis due to their porous surface.[136, 152-153, 194]

Based on its unique properties, including its rigidity, PCP was selected as a promising structure for preparing PIMs. This project aimed to combine the concept of PIMs with the unique properties of [2.2]paracyclophane to synthesize a novel PCP-based polymer of intrinsic microporosity (Figure **14**).

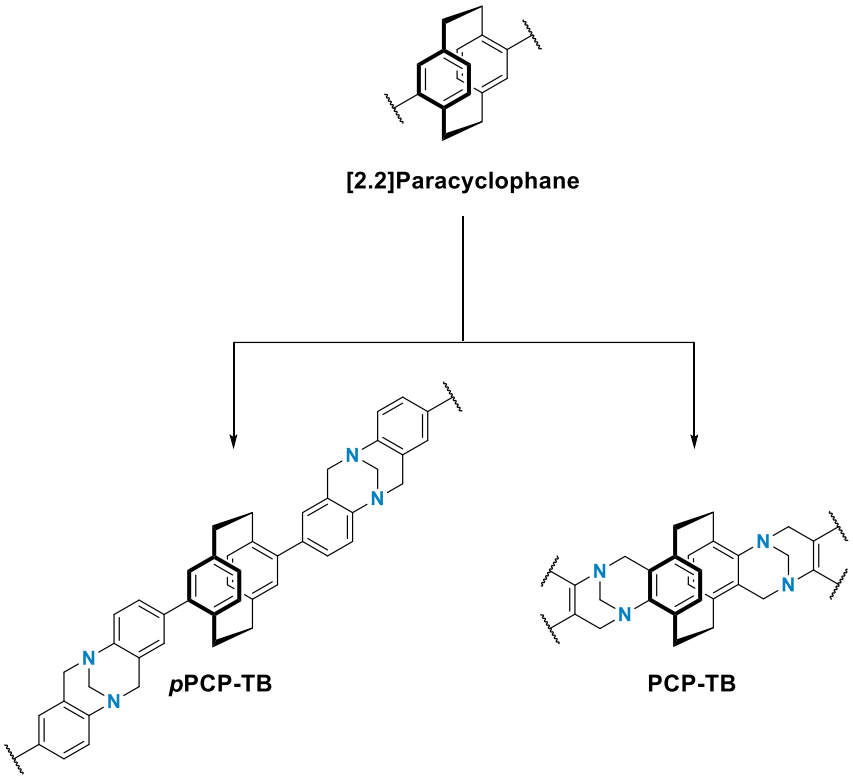

Figure 14: Overview of the targeted polymers with intrinsic microporosity (PIMs) ***p*PCP-TB** and **PCP-TB** containing the PCP-core.

The synthesis of the diamino-PCP **20** monomer was carried out in collaboration with the JEREB group at the University of Ljubljana. Since the compound preparation was not part of this thesis, analytical data and the detailed synthesis route can be found in supporting information of the respective publication. However, to compare and draw conclusions, the macroscopic appearance, adsorption properties, and gas selectivity of both polymers will be included and evaluated in the respective chapters.

Primary arylamines are prone to oxidation by molecular oxygen under basic conditions.[195] Hence, the synthesis of the extended diamino-PCP **18** was targeted to investigate the potential enhancement of oxidative stability and possible beneficial impacts of the phenylene bridge on the targeted PIM. For initial optimization of the polymerization conditions, racemic 4-(4'-amino)phenyl[2.2]paracyclophane (**19**) was aimed at as a model compound. An overview of PCP derivatives prepared in this project is shown in Figure **15**.

The following chapters will detail the monomer synthesis of **PCP-PA** (**19**), the extended pseudo-para building block ***p*PCP-PA** (**18**), and PIM formation, along with the characterization of the respective polymers.

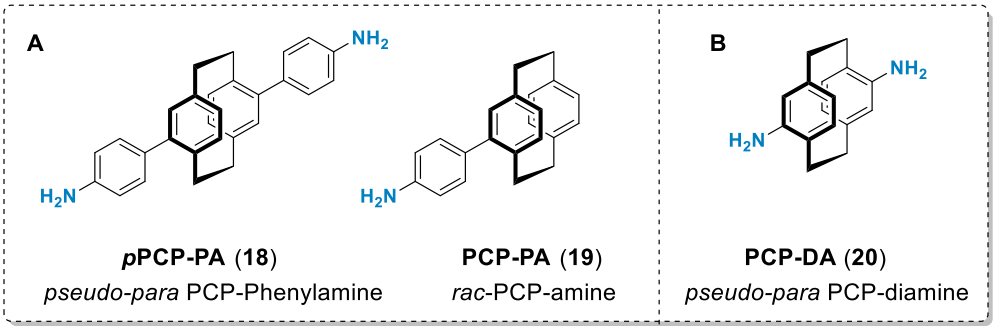

Figure 15: A) Targeted amino-functionalized PCP derivatives ***p*PCP-PA** (**18**) and **PCP-PA** (**19**). B) **PCP-DA** (**20**) synthesized in the working group of Prof. JEREB, University of Ljubljana.

3.1.1 Synthesis of an Extended [2.2]Paracylophane Derivative as Model Compound for TRÖGER'S Base Formation

Model compound 4-(4'-Amino)phenyl[2.2]paracyclophane (**18**) was prepared in a three-step synthesis route, starting from *rac*-bromo[2.2]paracyclophane (**20**). In the first step, [2.2]paracyclophane was reacted with molecular bromine and iron as catalyst in dichloromethane (DCM) according to a literature-reported procedure.[196] Quenching of the orange reaction mixture with aqueous sodium thiosulfate resulted in the isolation of racemic bromine **22** in 99% yield. The bromination of starting material **21** is illustrated in Scheme **1**.

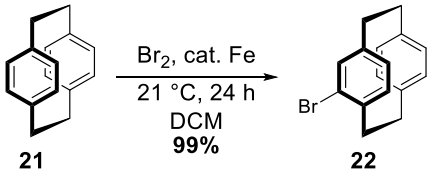

Scheme 1: Synthesis of *rac*-bromo[2.2]paracyclophane (**22**).[196]

The *tert*-butyloxycarbonyl (Boc-group) protected PCP **24** was synthesized from the brominated precursor **22** *via* SUZUKI-MIYAURA cross-coupling (Scheme **2**). Therefore, 4-(*N*-boc-amino)phenylboronic acid (**23**) was reacted with the brominated precursor **22** under palladium catalysis for 24 hours. Purification of the crude product *via* column chromatography afforded the desired *N*-Boc protected PCP **24** in 66% yield.

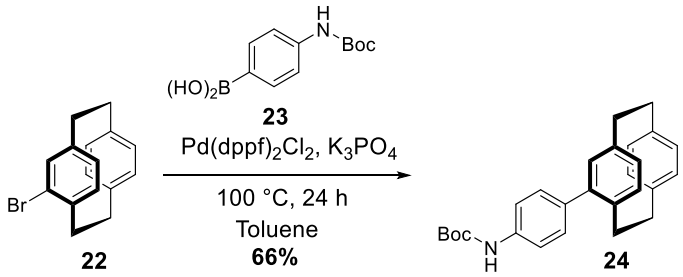

Scheme 2: Synthesis of racemic *N*-Boc-protected PCP **24** *via* SUZUKI-MIYAURA cross-coupling.

The acidic-labile Boc-protecting group was removed by treating the Boc-protected PCP derivative **24** with trifluoroacetic acid (TFA) in DCM for 24 hours. Purification of the crude product resulted in the isolation of the racemic extended mono-amino PCP (**PCP-PA**, **19**) in a yield of 65% (Scheme **3**).

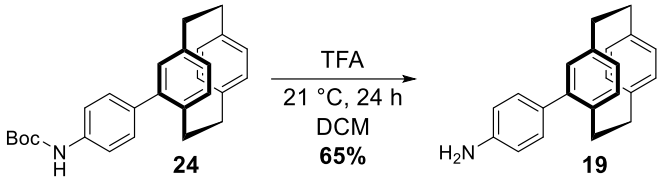

Scheme 3: Synthesis of **PCP-PA** (**19**) *via* deprotection of the Boc-protecting group under acidic conditions.

3.1.2 Synthesis of Model Compound Containing TRÖGER'S Base

To investigate the feasibility of the TB generation, amine **19** was converted into TB using typical TRÖGER's base formation conditions reported in literature.[144-145] Therefore, dimethoxymethane (DMM, **25**), used as methylene precursor, was added to a solution of **18** in DCM and TFA for 24 hours. The isolated solid was dried under a high vacuum to afford model compound **25** as shown in Scheme **4**.

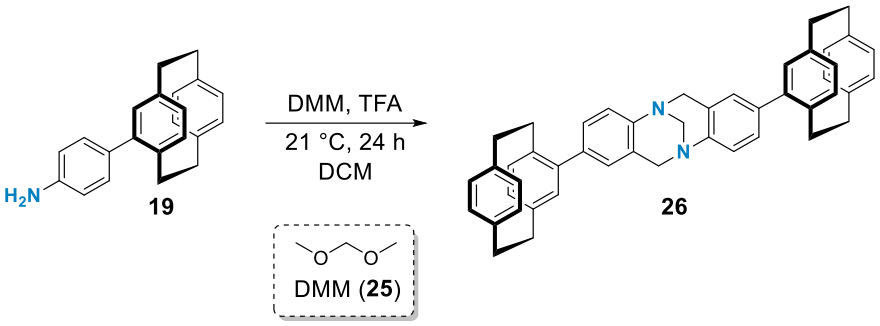

Scheme 4: Test reaction for implementing the TB formation conditions using model compound **PCP-PA** (**19**).

FT-IR spectroscopy was used to characterize the isolated TB-containing model compound **26**, focusing on identifying characteristic absorption bands of the TB core. In addition, the infrared spectrum of the monomer **PCP-PA** (**19**) was compared to the spectrum of **26**. The investigation of the infrared spectrum obtained from amine **19** revealed the typical asymmetric absorption band of primary amines in the region 3445–3356 cm^{-1} (Figure **17**). Compared to the spectra of the TB-containing model compound **26**, both prominent *N-H* stretching vibration bands in this region are absent, indicating the successful conversion of the primary amine. Furthermore, characterization of the isolated solid *via* FT-IR revealed the *C-N* absorption band at 1297 cm^{-1}, anticipated for the TB in the region 1300–1200 cm^{-1}. This finding is in line with examples of TB polymers reported in the literature.[197] The combined infrared spectra of the mono-amino PCP **19** and the model compound **26** are illustrated in Figure **17**. Based on these findings, the synthesis of the targeted extended diamino derivative **18** was aimed at in the next step.

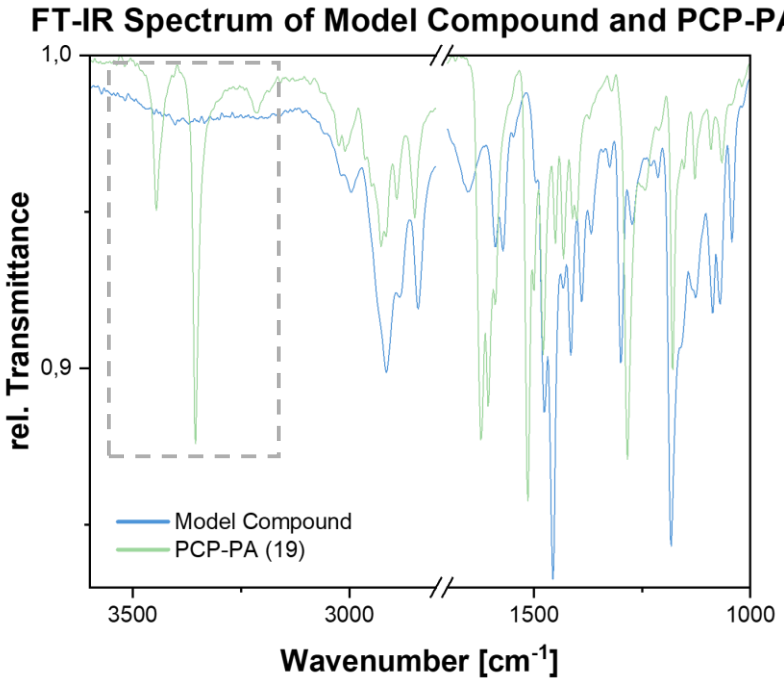

Figure 16: Combined FT-IR spectra of model compound **26** and **PCP-PA** (**19**). The missing *N-H* stretching vibration in the region between 3500 and 3300 cm^{-1} in the model compound is highlighted.

3.1.3 Synthesis of an Extended [2.2]Paracyclophane as Monomer for the Synthesis of Polymer with Intrinsic Microporosity

The *pseudo-para* dibrominated PCP precursor **27** was synthesized in a one-pot reaction according to a well-established protocol reported in the literature.[198]

Therefore, [2.2]Paracyclophane (**21**) was treated with molecular bromine and iron as the catalyst. After purification by recrystallization from hot toluene the desired *pseudo-para*-brominated PCP **27** was isolated with a yield of 29%. The bromination of the starting material is illustrated in Scheme **5**.

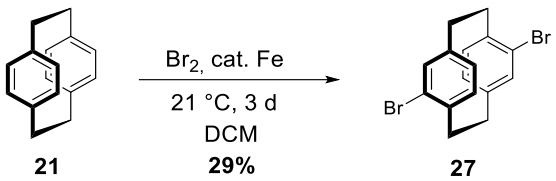

Scheme 5: Synthesis of dibromo[2.2]paracyclophane (**27**) *via* bromination of [2.2]paracyclophane (**21**).[198]

In contrast to the straightforward bromination of aromatic systems utilized in organic chemistry, which typically affords high yields,[199-201] the bromination of paracyclophane results a mixture of brominated by-products like the *pseudo-meta* derivative. This product distribution significantly contributes to the observed low yield of the desired product.[202]

Subsequently, **27** was converted into the extended Boc-protected diamine **28** using SUZUKI-MIYAURA cross-coupling with the *N*-protected boronic acid **23**. Although, cross-coupling reactions like the well-established SUZUKI-MIYAURA coupling usually proceed with excellent yields up to 98%,[203] examples of cross-coupling reactions of *pseudo-para* PCP-derivatives, including SUZUKI-MIYAURA couplings, have been reported with reduced yields.[204-205] In the present case, purification *via* column chromatography followed by recrystallization from toluene afforded the *N*-protected diamine **28** a yield of 44% (Scheme **6**).

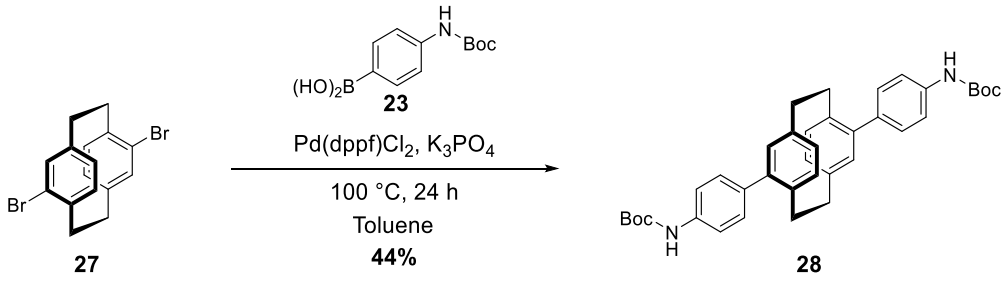

Scheme 6: Synthesis of the *N*-protected intermediate **28** *via* SUZUKI-MIYAURA cross-coupling reaction.

Considering that the reaction occurs at individual reaction centers simultaneously, a yield per reaction center can be calculated according to equation **1**, where 'n' represents the number of reaction centers involved and 'yield' represents the isolated overall yield.

$$Yield_{per\ reaction\ center} = \sqrt[n]{yield} \qquad (1)$$

The reaction yielded 66% per reaction center, identical to the isolated yield obtained for **PCP-PA** (**19**). Compared to well-known mono-couplings, the reduced isolated yield may be attributed to the fact the coupling proceeds at multiple positions simultaneously and the substantially lower solubility of the highly symmetrical starting material 27 and the formed product **28**.

Conditions for the deprotection were adapted from the synthesis of the model compound. The desired primary amine was obtained *via* deprotection of the Boc-group under acidic conditions. Therefore, **28** was treated with TFA in DCM for 24 hours. After purification of the crude product, the desired extended diamino-PCP (***p*PCP-PA**, **18)** was isolated in a yield of 62%. To

summarize, the targeted final structure **18** bearing the primary amine in *pseudo-para* position was obtained *via* a three-step synthetic route with an overall yield of 8%. The structure and planarity of ***p*PCP-PA (18)** was confirmed *via* single crystal analysis. The synthesis route of the described deprotection and the crystal structure of **18** are shown in Scheme **7**.

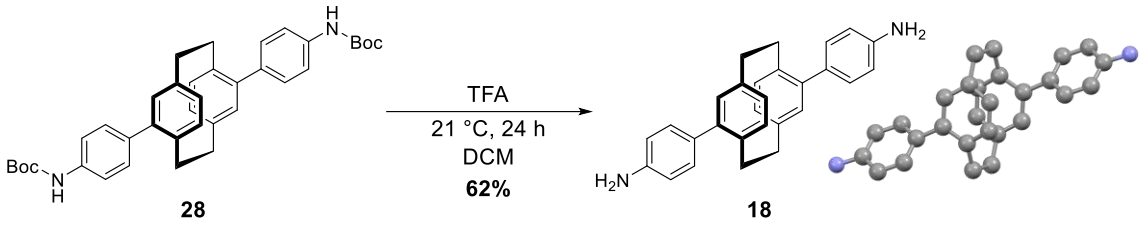

Scheme 7: Deprotection of Boc-protected diamino-PCP **28** to afford the ***p*PCP-PA** (**18**). The crystal structure of **18** is illustrated on the right. Hydrogen atoms have been removed for visual simplicity.

In contrast to the diamino-PCP **20** synthesized by JEREB and colleagues, the extended PCP monomer **18** exhibits significantly enhanced stability against oxidation. Initial attempts to synthesize **20** *via* reduction of diazido-PCP resulted in the formation of a dark-colored solid. Isolation and analysis of the solid by mass spectroscopy revealed the formation of the oxidized amine.

The synthesis of the ***p*PCP-PA** (**18**) gave access to a bench stable off-white solid that could be stored for days without oxidation of the primary amine. This enhanced stability translates into several practical benefits compared to the non-extended counterpart, such as simplified handling during synthesis and storage, avoiding the requirement for inert conditions throughout the synthesis.

3.1.4 Synthesis of Polymer with Intrinsic Microporosity *via* TRÖGER's Base Formation

PIM containing ***p*PCP-PA** (**18**) as monomer unit was synthesized by employing typical conditions discussed in Chapter **3.1.2** to form TRÖGERs base.[144]

Therefore, **18** was treated for 24 hours with DMM (**25**) and TFA as the solvent and acid catalyst (Scheme **8**). In addition, DCM was added to the reaction mixture to support the solubilization of **18**. Due to its low solubility in the reaction mixture, the formed polymer precipitated and was subsequently isolated by filtration. The crude product was washed with water and refluxed with acetone, tetrahydrofuran (THF), DCM and methanol. Drying the collected precipitate at 80 °C under vacuum gave ***p*PCP-TB** (**29**) in a yield of 53%.

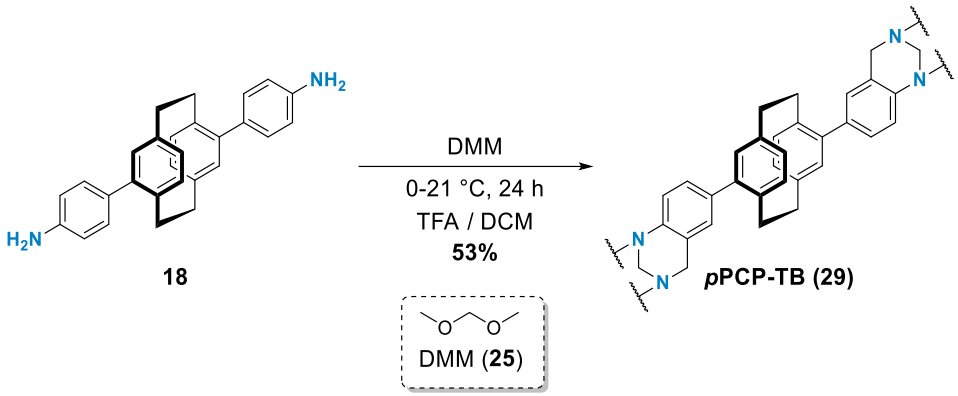

Scheme 8: Synthesis of ***p*PCP-TB** (**29**) *via* acid-catalyzed polymerization of ***p*PCP-PA** (**18**) and DMM (**25**).

3.1.5 Characterization of Polymer with Intrinsic Microporosity

In collaboration with A. Zupanc from the University of Ljubljana, structural characterization and investigation of the polymer's properties were conducted.

Initial observations during the synthesis revealed that ***p*PCP-TB (29)** was formed more smoothly compared to the polymer obtained from the non-extended monomer **20**. As already mentioned, enhanced stability towards oxidation significantly simplified the handling and therefore its synthesis. For ***p*PCP-TB** an off-white colored solid was isolated which is expected for TB polymers. The **PCP-TB** polymer obtained from the non-extended PCP derivative **20** gave a darker-colored polymer. The color difference may arise from the fact that the oxidated monomer is still present in the polymer and could lead to the darker appearance of the solid. Successful TB core formation was confirmed by ^{13}C and ^{15}N solid-state NMR and FT-IR spectroscopy.

^{13}C solid-state NMR analysis exhibited aromatic resonances in the 120–150 ppm region, attributable to the PCP core and the phenylene bridge. Theoretical considerations predicted downfield shifts for the PCP ethylene bridge and TB methylene (CH_2) groups. The ^{13}C-solid-state NMR spectrum displayed signals at approximately 49.1–67.5 ppm and 33.9 ppm. Given the typical chemical shift range for methylene carbons (20–70 ppm), signals at 49.1–67.5 ppm were assigned to the TB methylene groups. In comparison the signal at 33.9 ppm was attributed to the PCP ethylene bridge. These spectroscopic data confirm the successful formation of the TB core and, consequently, the successful polymerization. Moreover, ^{15}N solid-state NMR spectroscopy revealed a single nitrogen resonance at 41.9 ppm, which is expected for a successfully formed TB core. The ^{13}C- and ^{15}N-solid-state NMR spectra of ***p*PCP-TB** are illustrated in Figure **17**.

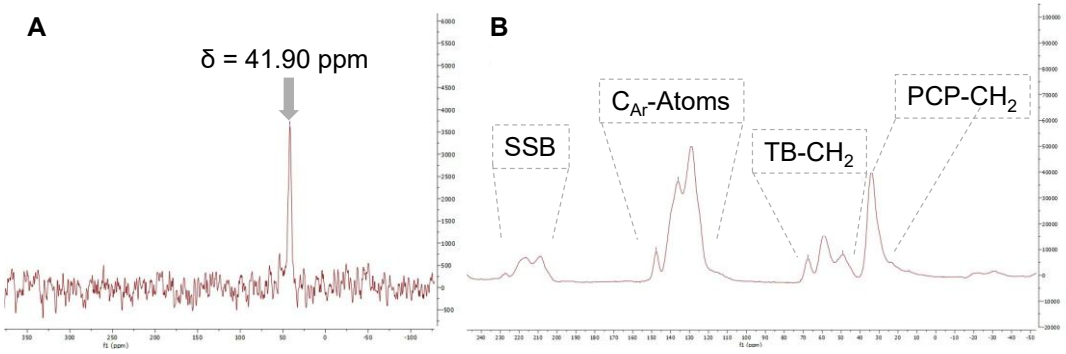

Figure 17: A) ^{15}N-solid-state NMR of ***p*PCP-TB**, the chemical shift of the TB nitrogen is at 41.9 ppm. B) ^{13}C-solid-state NMR of ***p*PCP-TB**, highlighted signals are marked: Spinning side bands (SSB), the *C*-Atoms of the aromatic core and the TRÖGERs base CH_2-signals and the CH_2-signals originated from PCP core. Data provided by A. ZUPANC (University of Ljubljana).

FT-IR spectroscopy was carried out to confirm successful polymerization and TB formation. It is important to note that the chemical environment surrounding a functional group can significantly influence its vibrational frequencies. Consequently, the observed IR absorption bands for a particular functional group may show slight variations compared to literature values. To draw conclusions, the spectra of the PCP-monomer and the polymer were compared. The monomer and the polymer spectra exhibit an absorption band at approximately 3000 cm^{-1}. These vibration bands can be attributed to the absorption of aromatic *C-H* bonds present in the starting material and the PIM. Furthermore, characteristic *C–N* stretching vibrations are observed in the polymer spectrum within the 1300–1200 cm^{-1} region (Figure **18**), consistent with examples found in the literature.[197]

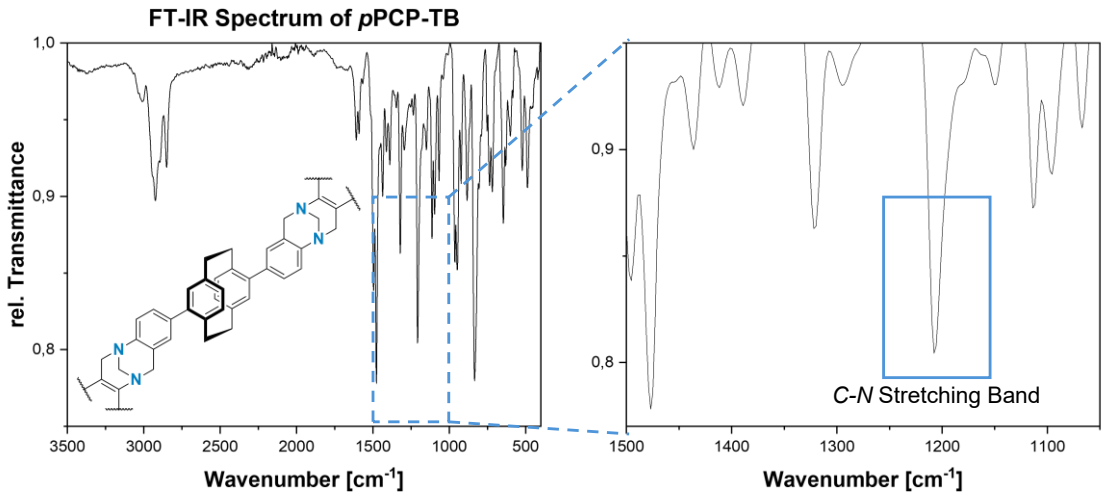

Figure 18: FT-IR spectrum of ***p*PCP-TB**. The *C-N* stretching vibration, characteristic of the TRÖGERs base core in the region of 1300–1200 cm^{-1} is highlighted. Data provided by M. CARTA (University of Swansea)

Porosity of the sample was investigated by Scanning Electron Microscopy (SEM). Figure **19** depicts the images of ***p*PCP-TB** in different magnifications. The SEM images revealed a porous structure of the sample which was anticipated for the structure of the PIM. The appearance of the polymer is characterized by the presence of pores with diameters ≤ 1 µm.

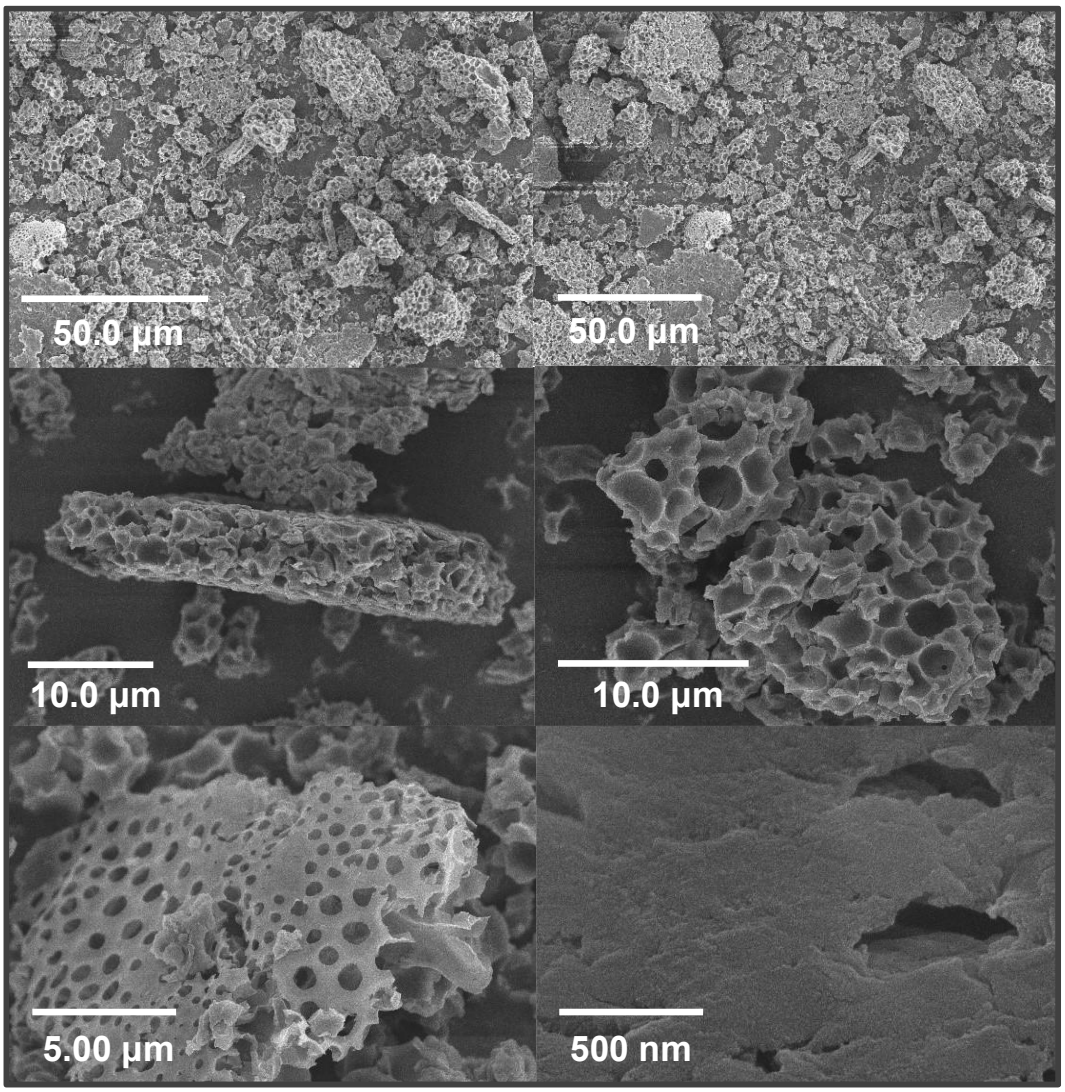

Figure 19: SEM images of ***p*PCP-TB**. Images were provided by A. ZUPANC (University of Ljubljana).

3.1.6 Gas Adsorption Properties and Thermal Stability

Gas adsorption properties and thermal stability of the polymer were done in collaboration with M. CARTA University of Swansea.

After the successful ***p*PCP-TB** polymer formation was confirmed, its gas adsorption properties and thermal stability were investigated. As their name indicates, polymers with intrinsic microporosity possess micro- and nano-pores with high surface areas. To examine the porosity and surface area (SA) of the polymer, adsorption isotherms of CO_2 and N_2 at 77 K, 273 K and 298 K, respectively, were determined and compared to the **PCP-TB** synthesized from the ***p*PCP-PA (18)**.

Values for the surface areas were calculated using the BRUNAUER-EMMETT-TELLER (BET) theory. In addition, the CO_2/N_2 selectivity using the Ideal Adsorbed Solution Theory (IAST) was determined to study possible applications as materials for gas storage and gas separation.

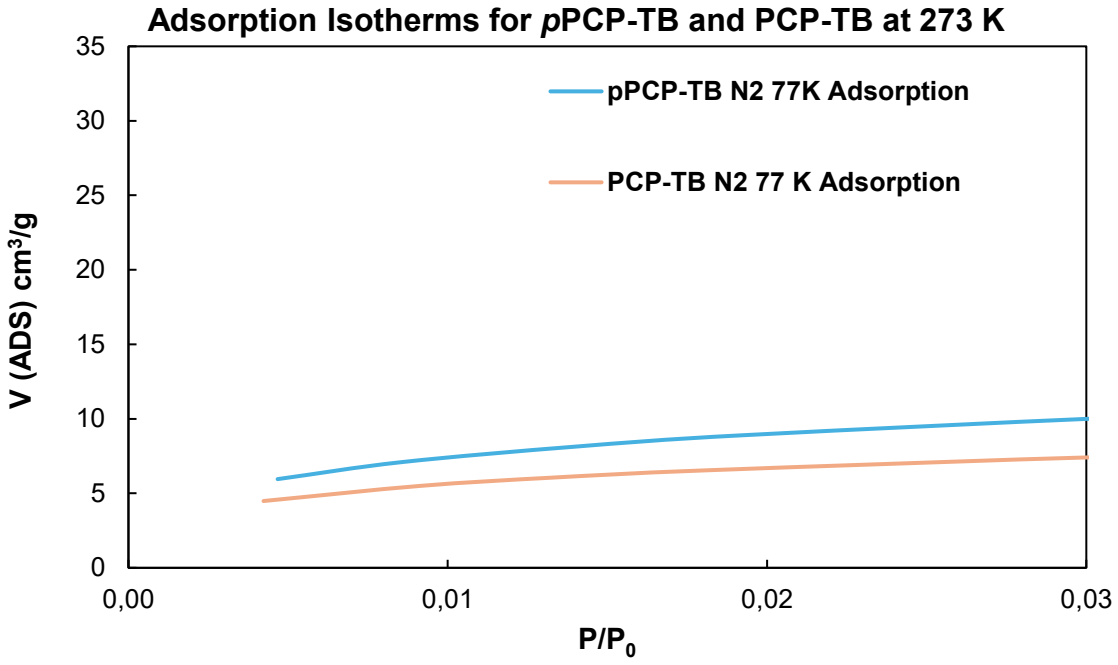

Figure 20: Adsorption and Desorption curves for N_2 at 77 K for ***p*PCP-TB** and **PCP-TB**. Data provided by M. CARTA (University of Swansea).

BET analysis using N_2 adsorption-desorption isotherms at 77 K were carried out to assess the SA of ***p*PCP-TB** and **PCP-TB**. The results showed a low surface area of 62.1 m^2/g for ***p*PCP-TB** and 43.5 m^2/g for **PCP-TB** (Figure **20**). This observation is unexpected considering the high porosity typically exhibited by TB polymers reaching values up to 1000 m^2/g as reported for **PIM-EA-TB**.[144] Single x-ray diffraction (XRD) analysis of the extended PCP

monomer **18** revealed a slight rotation between the *C*-*C* bond of the PCP core and the phenylene bridge and linear molecular structure (Scheme **7**). This geometry likely facilitates efficient packing within the polymer chains, minimizing the pores and restricting probe gas diffusion at 77 K. Therefore, the observed low porosity and SA are assumed to be attributed to the efficient packing of the polymer chains at this temperature.

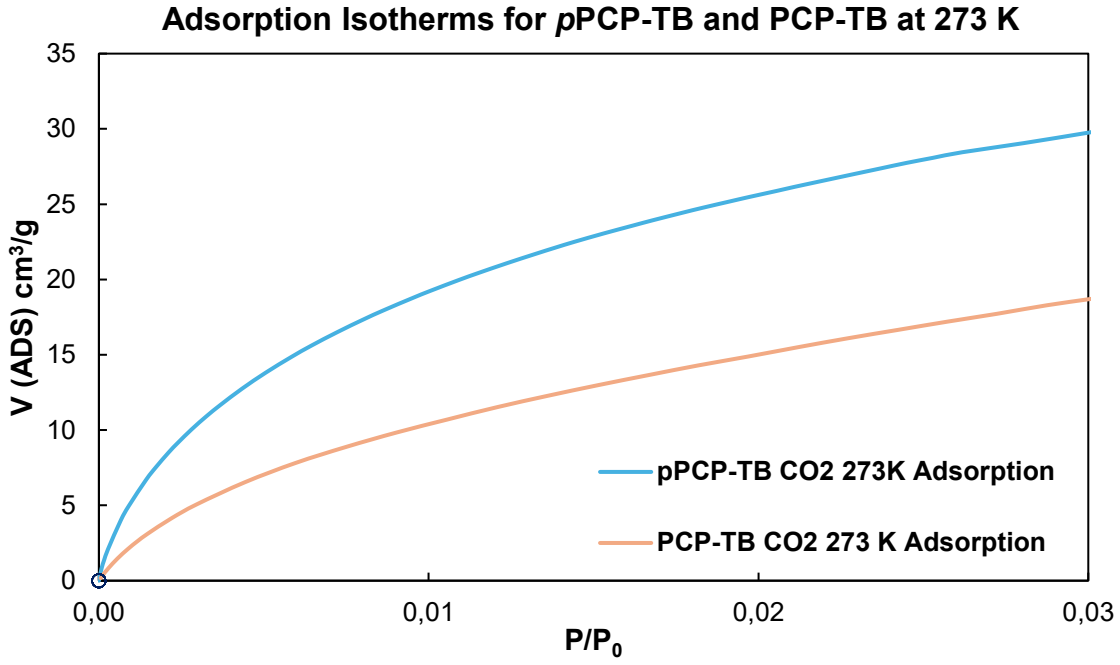

Figure 21: Adsorption-desorption graph for ***p*PCP-TB** and **PCP-TB** determined for CO_2 at 273 K. Data provided by M. CARTA (University of Swansea).

BET analysis is typically conducted using N_2 as the adsorbate at 77 K. However, as already noted, applying these standard conditions yielded a very low surface area for ***p*PCP-TB**. Given that similar results can be obtained with CO_2 adsorption-desorption isotherms at 273 K, the SA of ***p*PCP-TB** was determined using the alternative conditions. Measurements of the SAs for ***p*PCP-TB** and **PCP-TB** gave values of 233 m^2/g and 197 m^2/g, respectively (Figure **21**). SA values of PIMs reported in literature for rigid monomers (see Chapter **1.1.2**, Figure **9**) typically range from 504–1028 m^2/g[144] and are higher than the value obtained. However, it should be noted that the synthesized ***p*PCP-TB** and **PCP-TB** polymers are the first reported in literature containing PCP as a monomer and further projects should aim to optimize the monomer structure to enlarge the SA and achieve better gas adsorption properties.

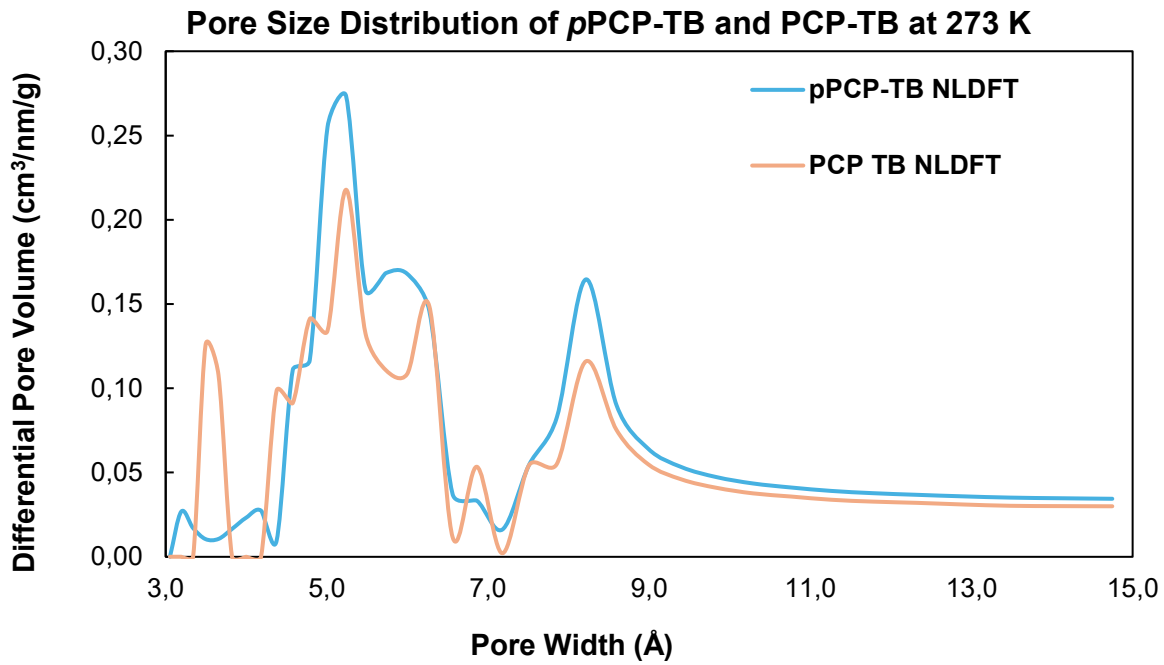

Figure 22: Pore size distribution for ***p*PCP-TB** and **PCP-TB** determined by non-local density functional theory (NLDFT). Data provided by M. CARTA (University of Swansea).

The pore size distribution of ***p*PCP-TB** was determined using the NLDFT method. Evaluation of the data revealed a microporous material with pores mainly in the region between 5 and 9 Å (Figure **22**). Compared to the non-extended monomer, no pore size change is present. The **PCP-TB** synthesized from the non-extended monomer revealed pores in the order of magnitude from 3 to 9 Å, which is similar to ***p*PCP-TB** containing the extended monomer. In addition. for **PCP-TB** ultra-micropores with a diameter of approximately 3.5 Å are observed. This finding supports the hypothesis that the extended monomer creates a more elastic polymer, leading to more efficient packing and therefore smaller pores are blocked. By extending the PCP core, a *C*-*C* bond between the aromatic ring of the PCP and the phenyl bridge is formed. Even though rotation should be restricted around this bond, single XRD structure analysis revealed a small rotation around the *C*-*C* bond with a deviation from the planar structure leading to this flexible structure.

Table 1: Gas adsorption properties and surface areas of ***p*PCP-TB** and **PCP-TB**.

Polymer	$SA_{BET, CO2}$ [$m^2\ g^{-1}$]	[a] $V_{ADS, CO2}$ [mmol g^{-1}]	[b] $V_{ADS, CO2}$ [$mmol^3\ g^{-1}$]	Q_{ST} [kJ mol^{-1}]	CO_2/N_2 (IAST)
PCP-TB	197	0.835	0.701	27.8	69.4
***p*PCP-TB**	233	1.325	0.616	32.6	47.5

[a] CO_2 uptake at 273 K at 1 bar; [b] CO_2 uptake at 298 K at 1 bar.

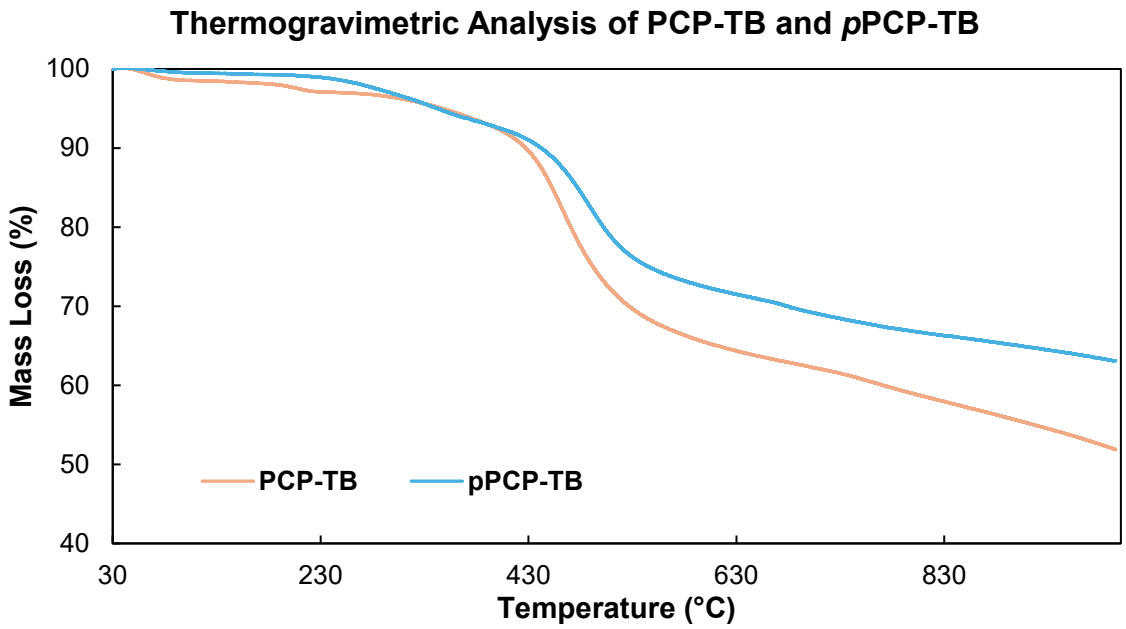

Figure 23: Decomposition graphs obtained by thermogravimetric analysis (TGA) for ***p*PCP-TB** and **PCP-TB**. Data provided by M. CARTA (University of Swansea).

Additionally, the thermal stability was assessed by thermogravimetric analysis (TGA). PIMs reported in literature show a very high thermal stability with values >400 °C.[51] In accordance with the data found in literature, ***p*PCP-TB** is characterized by a high thermal stability. Decomposition of the sample occurred at 456 °C. TGA data obtained for **PCP-TB** containing the non-extended monomer shows decomposition at a lower temperature at 435 °C. The respective decomposition curves are depicted in Figure **23**. The slightly higher decomposition temperature of ***p*PCP-TB** could be explained by a higher degree of polymerization. To support this hypothesis, gel permeation chromatography (GPC) should be performed to compare the degree of polymerization of both samples.

3.1.7 Application of Polymers in Selectivity Studies

Flue gas, a ubiquitous by-product of fossil fuel combustion (coal, oil, and natural gas), is a complex mixture primarily comprising N_2, CO_2, water, and O_2. However, it also contains significant concentrations of hazardous compounds, including CO, SO_x, and NO_x. Considering the annual substantial amount of flue gas produced, it exerts a major impact on global warming and air pollution quality.[16, 206-207] Therefore, a main goal is purification of flue gas, which can be effectively achieved through gas separation. By separating harmful combustion by-products from relatively inert gas components, a purified gas stream can be obtained. In recent years several polymers were synthesized and tested on their ability to selectively separate CO_2 from N_2 in flue gas.[208-209] To investigate whether the novel ***p*PCP-TB** polymer is capable of separating gases, CO_2/N_2 selectivity studies were conducted.

Flue gas separation, specifically the separation of CO_2 from N_2 typically is performed at 298 K to optimize the performance of the used materials.[210] To study the gas adsorption property of the polymers, CO_2 and N_2 adsorption at 298 K were measured. Initial measurements of CO_2 adsorption at 273 K showed a moderate adsorption of 1.325 mmol/g for ***p*PCP-TB** and 0.835 mmol/g for **PCP-TB** (Table **1**). However, measurements at 298 K revealed a lower CO_2 adsorption for both polymers, for ***p*PCP-TB** the adsorption decreased significantly to 0.616 mmol/g and for **PCP-TB** only slightly to 0.701 mmol/g. In comparison both polymers only show a very low N_2 adsorption at 298 K (Figure **24**).

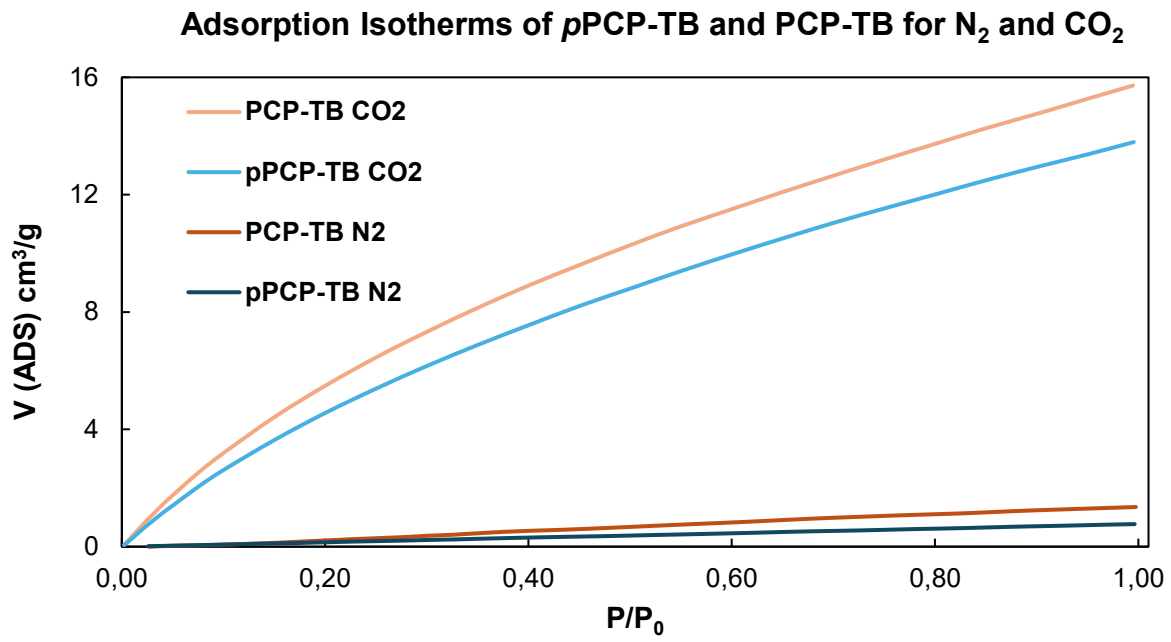

Figure 24: Adsorption curves of N_2 and CO_2 at 298 K for ***p*PCP-TB** and **PCP-TB**. Data provided by M. CARTA (University of Swansea).

Considering the primary application, these results are very promising. At typical flue gas separation temperatures (298 K), CO_2 can be adsorbed at the polymer surface, thus facilitating its retention. In contrast, the ability of the polymer to absorb N_2 is much lower, enabling the unhindered passage of the N_2 gas stream through the polymer. Gas selectivities for ***p*PCP-TB** and **PCP-TB** were determined using IAST. For both polymers a high CO_2/N_2 selectivity was calculated (Figure **25**). As depicted in Table 1, **PCP-TB** exhibits a selectivity of 69.4, while ***p*PCP-TB** has a lower selectivity of 47.5. The gas separation performance of both ***p*PCP-TB** and **PCP-TB** is comparable to previously reported materials with similar surface areas and CO_2 adsorption capacities. The selectivity of state-of-the-art materials for gas separation incorporating nitrogen in their backbone typically ranges from 53 to 77.[155-156, 211]

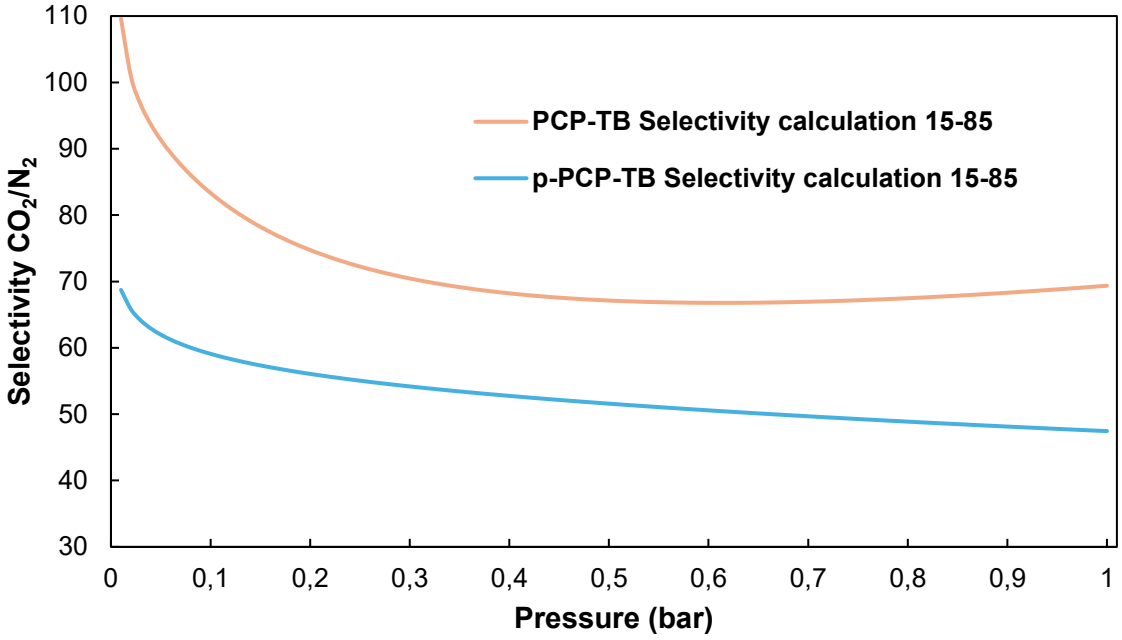

Figure 25: Selectivity of ***p*PCP-TB** and **PCP-TB** for CO_2 over N_2 (IAST, 298 K for a 15/85 CO_2/N_2 composition). Data provided by M. CARTA (University of Swansea).

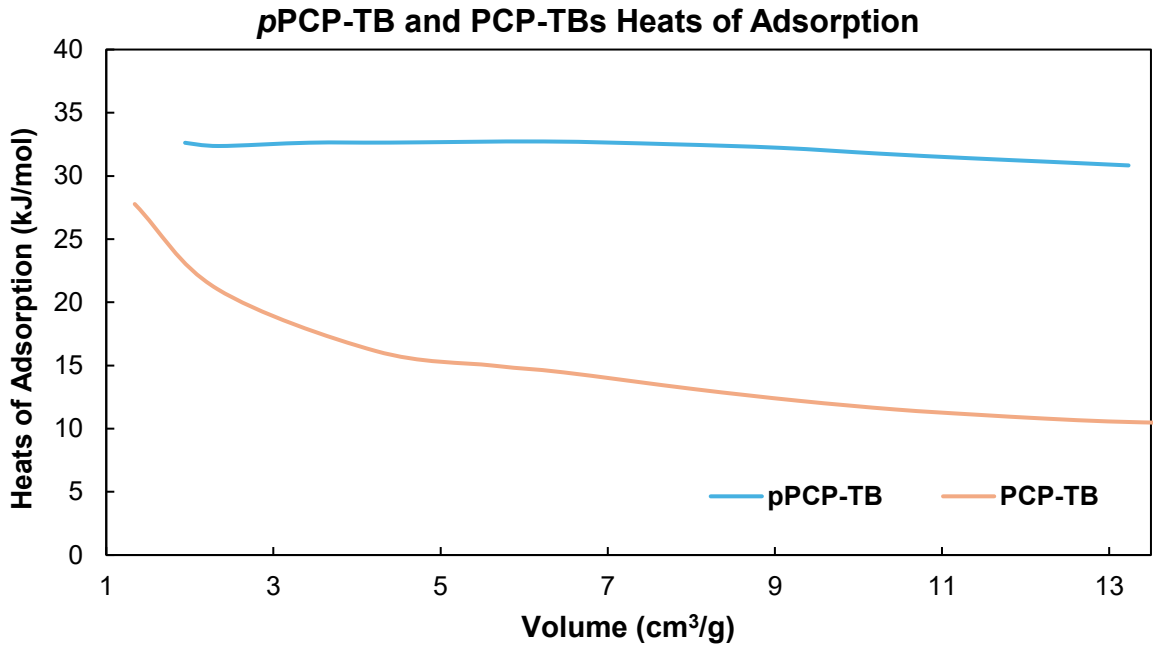

Figure 26: Isosteric heats of adsorption (in kJ/mol^{-1}) calculated for ***p*PCP-TB** and **PCP-TB** for isotherms measured at 273 K and 298 K for the respective gas. The values are fitted with the LANGMUIR-FREUNDLICH equation and calculated *via* CLAUSIUS-CLAPEYRON equation. Data provided by M. CARTA (University of Swansea).

In addition, the adsorption mechanism of the gas onto the material surface was studied using heats of adsorption (Q_{ST}) analysis (Figure **26**). To remove the adsorbed gas from the polymer, physisorption of the gas is advantageous compared to chemisorption. Q_{ST} values indicating chemisorption are typically ≥ 50 kJ mol^{-1}.[212] The Q_{ST} values obtained for ***p*PCP-TB** and **PCP-TB** are 32.6 kJ mol^{-1} and 27.8 kJ mol^{-1}, respectively (Table **1**). These findings imply a physisorption mechanism for both polymers, meaning CO_2 molecules are weakly interacting with the polymer surface, primarily physically entrapped within the pores and the adsorption is mainly driven by VAN-DER-WAALS forces. As previously discussed, this characteristic is beneficial as CO_2 desorption from the surface does not require harsh conditions, such as high pressure or temperature to remove the trapped CO_2, in contrast to chemisorption processes. Since the obtained results are preliminary and gas adsorption/desorption behavior can differ significantly under practical application conditions, further investigations are necessary. These studies should include experiments employing flue gas to evaluate the suitability of both polymers for practical gas separation applications.

In conclusion, a novel PCP-base TB polymer was prepared *via* acid-catalyzed polymerization. Subsequently, the successful polymer formation was confirmed by solid-state NMR and FT-IR spectroscopy. Furthermore, the gas adsorption properties were determined revealing low surface area compared to PIMs reported in literature. However, it was demonstrated that the material is suitable as a potential candidate for applications such as gas separation.

3.2 Covalent Organic Frameworks containing Paracyclophane

Introduction. In 2005, the synthesis of the first covalent organic framework (COF) marked the emergence of a novel class of highly porous materials. Early reports described the synthesis of COFs through the condensation of two boronic acids.[120] A key advantage of COFs over metal-organic frameworks (MOFs) lies in their robust covalent linkages between building blocks and their composition, which is primarily comprised of light elements resulting in a low density of the formed framework.[131, 213-214] Application of COFs range from gas storage, vapor sorption, catalysis, chemical sensing and electronic conduction.[118-119, 215] Since COFs and their synthesis are a novel research field, exploration and optimization need to be done.

Several synthetic strategies are employed for the preparation of COFs, including those based on boron, triazine, and imine linkages. Boron-based COFs can be obtained *via* different approaches like condensation of the respective boronic acid, reaction of an alcohol with the respective boronic acid or by condensation of boronic acid with silanols to form the respective borosilicates.[115, 213, 215] COFs containing triazine linkages are synthesized *via* cyclotrimerization of aromatic nitriles, exhibiting a high chemical stability and are very stable against heat and mechanical pressure. Triazine-based COFs are characterized by high surface areas and low framework densities. However, their synthesis typically requires elevated temperatures, often exceeding 400 °C, which excludes the incorporation of thermally sensitive functional groups.[124-125, 216] Furthermore, the inherent irreversibility of the cyclotrimerization reaction often leads to limited crystallinity in the resulting COFs. Imine-based COFs firstly introduced by YAGHI and co-workers in 2009 can be synthesized using two distinct approaches.[128, 217] They are either prepared by condensation of an aldehyde with an amine[128] or by reacting hydrazines with aldehydes to form hydrazones.[218] Imine-linked COFs exhibit excellent thermal and chemical stability. However, limitations in crystallinity and porosity remain significant challenges and must be addressed in further investigations.[115, 214]

Up to date several examples were reported where [2.2]paracyclophane was utilized for the construction of porous materials such as MOFs.[219-220] However, until now only one example is reported in literature, in which a tetra-substituted [2.2]paracyclophane was used for the preparation of a covalent organic framework.[221] This project aimed to extend the successful results obtained of the previous project discussed in Chapter **3.1**, employing [2.2]paracyclophane as monomer in the synthesis of porous materials. Therefore, the previously reported extended diamino [2.2]paracyclophane (**18**) was reacted with various aldehydes to

prepare novel PCP-based COFs. Successful framework formation was confirmed by FT-IR spectroscopy and elemental analysis.

3.2.1 Synthesis of Aldehydes as Monomers in the Covalent Organic Framework Synthesis

Since the synthesis of the ***p*PCP-PA** (**18**) is already part of chapter 2.1.1, only the aldehyde synthesis will be discussed in detail. The aldehydes selected for COF synthesis are well-established in literature and have been widely employed in previous studies for the synthesis of porous materials.[222-226] The targeted structures of the aldehydes are illustrated in Figure **27**. The aldehydes were synthesized according to literature procedures, unless otherwise noted. They include tris(4-formylphenyl)amine (**TFPA, 30**), 4,4',4"-benzene-1,3,5-trityltris(ethyne-2,1-diyl))tribenzaldehyde (**BTT**, **31**), 1,3,5-tris(4-formylphenyl)benzene (**TFPB**, **32**) and 1,3,5-tris(4-formylphenyl)triazine (**TFTA**, **33**) which were synthesized by N. ERIC during a research internship - conducted in the BRÄSE group[227] and commercially available 1,3,5-triformylphloroglucinol (**TP**, **34**) (Figure **27**).

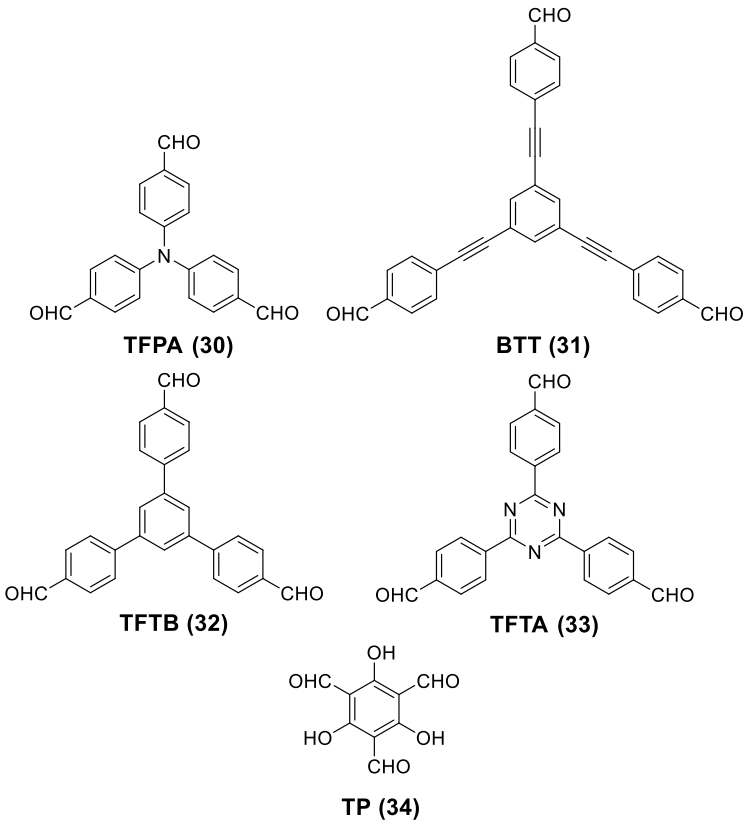

Figure 27: Chemical structure of aldehydes **TFPA** (**30**), **BTT** (**31**), **TFTB** (**32**), **TFTA** (**33**) and **TP** (**34**) as linking compounds for COF.

TFPA (**30**) was synthesized from the commercially available starting material triphenylamine (**35**). Therefore, amine **35** was subjected to a VILSMEIER-HAACK reaction by treating it with phosphorus oxychloride and dimethylformamide. Electron-rich arenes like triphenylamine (**35**) react with the *in-situ* generated VILSMEIER-HAACK reagent formylating the benzene moiety.[228]

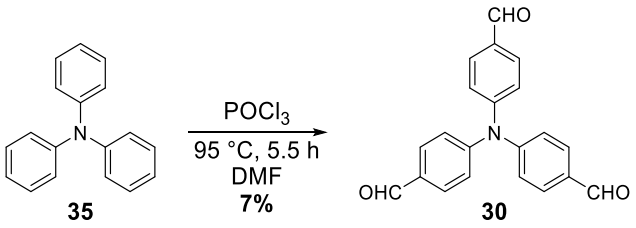

Scheme 9: Synthesis of **TFPA** (**30**) *via* VILSMEIER-HAACK formylation of triphenylamine (**35**).[229]

The initial attempt to synthesize **TFPA** (**30**) involved the reaction of triphenylamine (**35**) with 3.00 equivalents of phosphorus oxychloride ($POCl_3$) at 95 °C for 16 hours. This reaction primarily yielded the monosubstituted arene, with approximately 10% of the disubstituted triphenylamine and only trace amounts of the desired trisubstituted product **30**. In order to prepare **30**, the reaction conditions were optimized based on the methodology reported by MALLEGOL and co-workers.[229] By increasing the excess of phosphorus oxychloride and

shortening the reaction time to 4 hours while maintaining the temperature, the formation of the disubstituted aldehyde was favored (Scheme **9**). Subsequently, the crude product was subjected to a second reaction with an excess of phosphorus oxychloride for 1.5 hours at 95 °C, ultimately affording **TFPA** (**30**) in a yield of 7%.

BTT (**31**) was synthesized following an adapted literature-known procedure reported by ZHOU and colleague.[222] However, employing the reported conditions did not result in the formation of **31**. Consequently, the protocol was adapted and shifted to copper-free SONOGASHIRA-conditions. Therefore, the procedure was modified by changing the palladium source (palladium acetate instead of solely $PdCl_2(PPh_3)_2$) and adding XPhos as ligand as well as utilization of acetonitrile instead of THF. Adapting the used solvent allowed to increase the reaction temperature from 60 °C to 95 °C, which ultimately resulted in the formation of **BTT** (**31**). XPhos was employed as the ligand to facilitate copper-free conditions. 1,3,5-Triethynyl benzene (**36**) was reacted with 4-bromobenzaldehyde (**37**) in the presence of palladium acetate as catalyst and cesium carbonate for 16 hours. Aldehyde **31** was isolated after purification of the crude product in a yield of 12% (Scheme **10**).

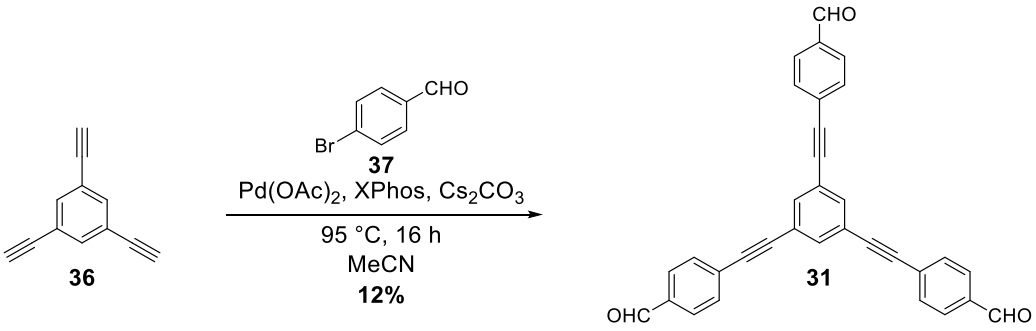

Scheme 10: Synthesis of BTT (31) *via* SONOGASHIRA cross-coupling using 1,3,4-triethynyl benzene (36) and 4-bromobenzaldehyde (37).[222]

The isolated yield of **BTT** (**31**) (12%) was drastically lower compared to the yield reported in the literature (56%).[222]

The synthesis of **TFPB** (**32)** was achieved by applying an adapted SUZUKI-MIYAURA cross-coupling protocol reported by JIANG and co-workers.[224] 4-Formylboronic acid (**39)** was coupled with 1,3,5-tribromobenzene (**38**) in the presence of palladium acetate as a catalyst for 16 hours at 75 °C. Subsequent purification of the crude product *via* column chromatography yielded **TFPB** (**32**) in a yield of 75% (Scheme **11**).

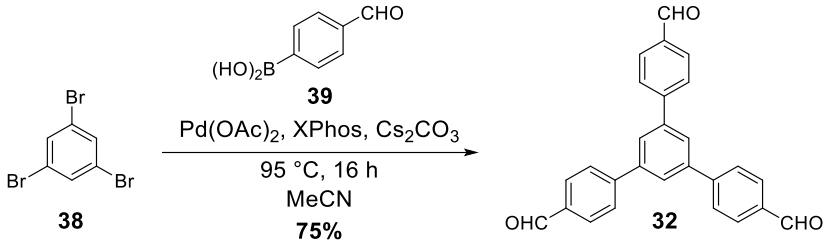

Scheme 11: Synthesis of TFPB (32) *via* SUZUKI-MIYAURA cross-coupling using 1,3,5-tribromo benzene (38) and 4-formylboronic acid (39).[224]

TFTA (**33**) was synthesized from bromine **41** which was prepared according to a literature-known procedure *via* cyclotrimerization of 4-bromobenzonitrile (**40**) under acidic conditions using trifluoromethanesulfonic acid (TfOH).[230] After neutralization of the reaction mixture the crude product was recrystallized from ethanol to yield 1,3,5-tris(4-bromophenyl)triazine (**41**) as a colorless solid in a yield of 92%. To prepare **TFTA** (**33**), precursor **41** was treated with *n*-butyllithium (*n*-BuLi) at -78 °C in dry THF according to a reported protocol.[231] Subsequently, the lithiated intermediate was quenched with dimethylformamide (DMF) and hydrolyzed under acidic conditions. The formed precipitate was filtered off to yield **33** as a colorless solid in a yield of 13%. **TFTA** (**33**) was prepared in a two-step synthesis sequence with an overall yield of 12%. The synthesis route to prepare **33** is visualized in Scheme **12**.

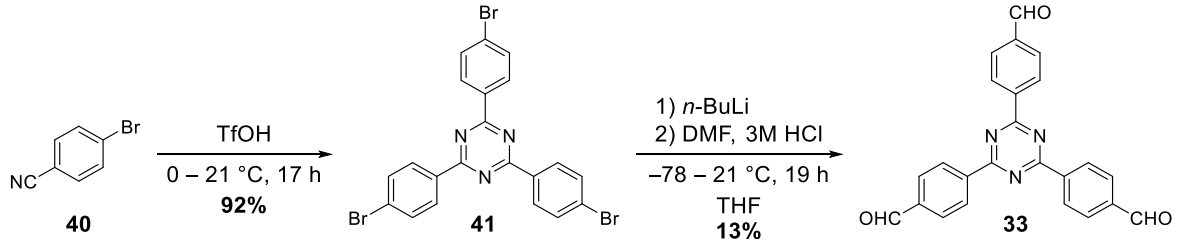

Scheme 12: Synthesis of **TFTA** (**33**) *via* cyclotrimerization of 4-bromobenzonitrile (**40**)[230] followed by formylation of bromine **41** *via* lithiation with *n*-butyllithium.[231]

3.2.2 Preparation of Covalent Organic Frameworks

The following covalent organic frameworks (**COFs 42**–**46**) were prepared *via* acid-catalyzed room temperature synthesis by combining the ***p*PCP-PA** (**18**) with the respective aldehyde (**30**-**34**) in a ratio of 3:2 in 1,4-dioxane (Scheme **13**). Acetic acid (AcOH) was added, whereupon precipitation immediately occurred, and the resulting suspension turned yellow to light orange. The resulting suspension was allowed to stand undisturbed for three days. After completion, the precipitate was filtered off and washed with DCM, ethyl acetate, ethanol, water, and methanol to remove residues of acetic acid and traces of unreacted starting materials. The

obtained insoluble solid was dried under high vacuum at 21 °C to yield the corresponding COF as yellow to light orange powder. Since all COFs are constructed with ***p*PCP-PA** (**18**) the nomenclature was based on the respective aldehyde used in the synthesis. An overview of all prepared COFs and their respective designation is shown in Figure **28**.

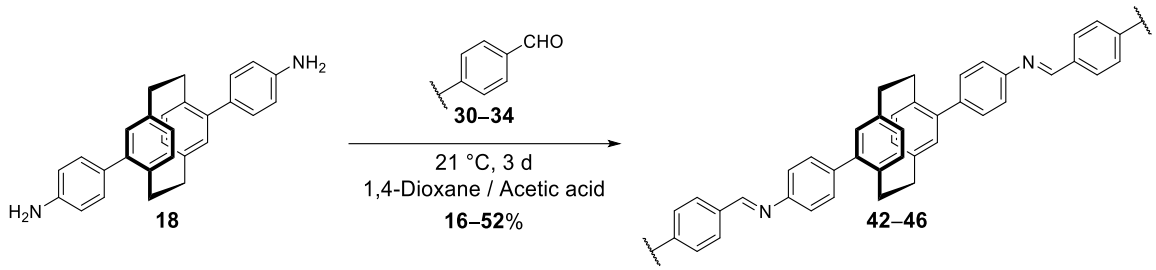

Scheme 13: Preparation of COFs *via* acid-catalyzed room temperature synthesis using acetic acid as catalyst.

The insolubility of the precipitate in various organic solvents already hinted a successful framework formation. The isolated yields of the COFs ranged from 16–52%, which are drastically lower than those reported in literature. For instance, solvothermal as well as acid-catalyzed room temperature synthesis have been reported with high yields up to 90%.[226, 232-233] However, it is crucial to note that these reactions were preliminary investigations to demonstrate the feasibility of preparing COFs using [2.2]paracyclophane as building unit. Therefore, the obtained yields should be considered initial values and serve as a foundation for further optimization efforts.

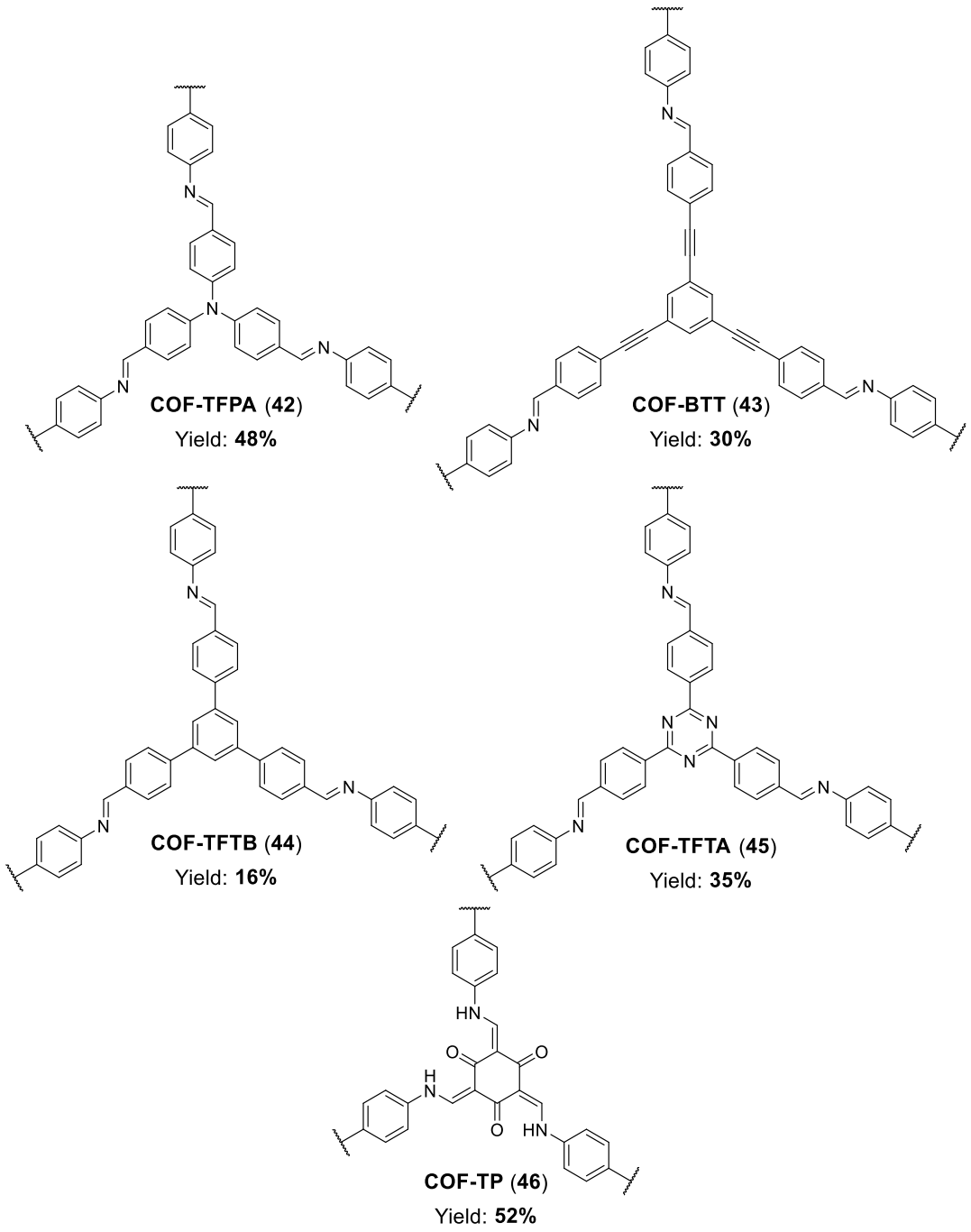

Figure 28: Overview of synthesized COFs. The repeating aldehyde unit is visualized, whereas the paracyclophane unit is not depicted.

3.2.3 Characterization of the Covalent Organic Framework

The successful formation of the framework was confirmed *via* analysis of their infrared spectra. Therefore, the infrared spectra recorded from the starting material and the respective COF were compared and evaluated. In addition, elemental analysis was performed to investigate the chemical composition of the frameworks.

Starting materials and their corresponding COFs exhibit distinct functional groups. The formyl group, characterized by a *C=O* and *C-H* bond, shows characteristic infrared absorptions. The *C-H* stretching vibration typically appears as a doublet in the region of 2830–2720 cm^{-1} with medium intensity, while the *C=O* stretching vibration exhibits a strong absorption band in the range of 1820–1660 cm^{-1}. Primary amines are typically characterized by their strong *N-H* stretching vibration within the 3500 – 3400 cm^{-1} region of the infrared spectrum.[234-235] This characteristic peak arises from the symmetric and asymmetric stretching vibrations of the two *N-H* bonds present in primary amines. The observation of the absence of both distinct *N-H* bands as well as the strong absorption band of the carbonyl group in the region of 1740–1720 cm^{-1}[235] in the infrared spectrum is a strong indicator for the conversion of the starting materials. To confirm the successful COF formation, these distinct regions of the starting materials were compared to those of the prepared frameworks.

The successful formation of the framework can be confirmed by the presence of the imine group which represents the most significant functionality in the COF. The *C=N* stretching vibration typically appears within the 1690–1640 cm^{-1} region of the infrared spectrum with medium intensity. It is crucial to acknowledge that the chemical structure, in particular, the presence of conjugation with aromatic systems and hydrogen bonding, can significantly influence the position of the absorption bands. Therefore, the observed values may deviate slightly from the typical ranges.[234-235]

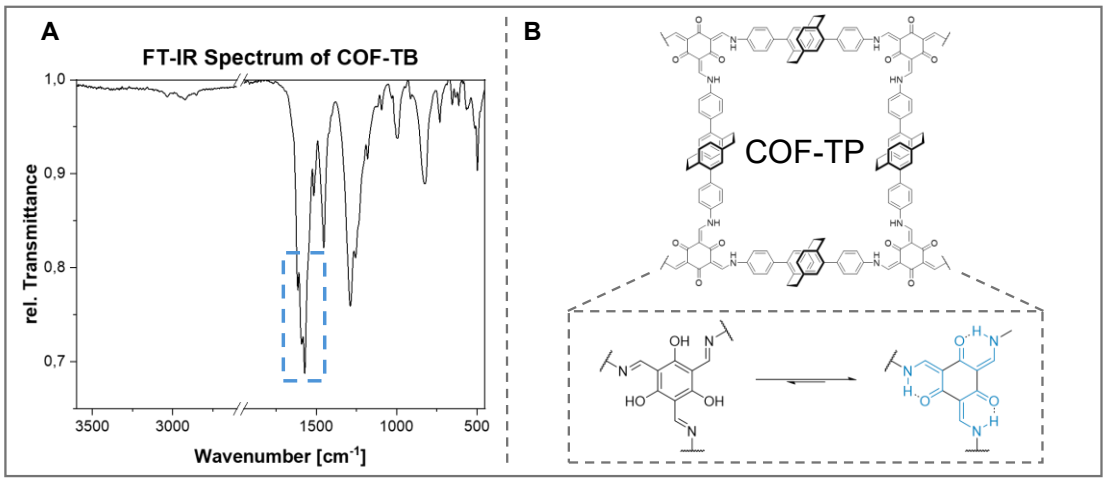

Figure 29: A) FT-IR spectrum of **COF-TP**; B) Iminol-ketoenamine tautomerization of **TP** (**34**) building block in **COF-TP**.

The infrared spectrum of **COF-TP** depicted in Figure **29** shows the absence of the typical formyl *C-H* stretching vibration in the region around 1700 cm^{-1} and the prominent *N-H* vibration of the primary amine in the region between 3500–3000 cm^{-1}. The absence of both absorption bands clearly indicates a complete conversion of the starting material and hints the successful framework formation. Furthermore, the broad *O-H* stretching vibration of the hydroxyl group corresponding to the starting material as well as the *C=N* vibration of the imine bond is absent This finding can be attributed to the iminol-ketoenamine tautomerization, a unique characteristic for **TP** (**34**) as illustrated in Figure **30**. This tautomerization has two significant consequences for the formed covalent organic framework. Firstly, the aromatic hydroxyl groups undergo tautomerization to form carbonyl groups. Secondly, the linkage between monomer units occurs through enamine bonds rather than the expected imine bonds. This explanation is in line with **TP**-containing COFs reported in literature.[236-238] In the distinct region, a strong absorption at 1571 cm^{-1}, accompanied by two shoulders at 1616 and 1590 cm^{-1} can be seen. In literature absorption bands of the *C=C* and *C-N* bonds of the enamine are reported in the region around ~1600 cm^{-1} for COFs containing **TP** (**34**). This finding already hints the successful formation.[226] Furthermore, the vibration at 1616 cm^{-1} could arise from the *C=O* vibration of the carbonyl group present in **COF-TP**. Usually, carbonyl vibrations can be observed in the region between 1720–1708 cm^{-1}. However, conjugation with the formed α, ß-unsaturated system and intramolecular hydrogen bonding the absorption band is likely shifted to lower wavenumbers.

The same finding can be concluded for the absorption band of the enamine. Due to conjugation and intramolecular hydrogen bonding, the characteristic *N-H* stretching vibration observed in

enamines within the 3400–3400 cm^{-1} region is absent. In contrast, this conjugation leads to a strong absorption band in the 1700–1600 cm^{-1} region, which arises from the *C-N* vibration.[234] As previously discussed for the carbonyl group, conjugation and intramolecular hydrogen bonding results in a significant shift to lower wavenumbers, compared to values reported in literature.

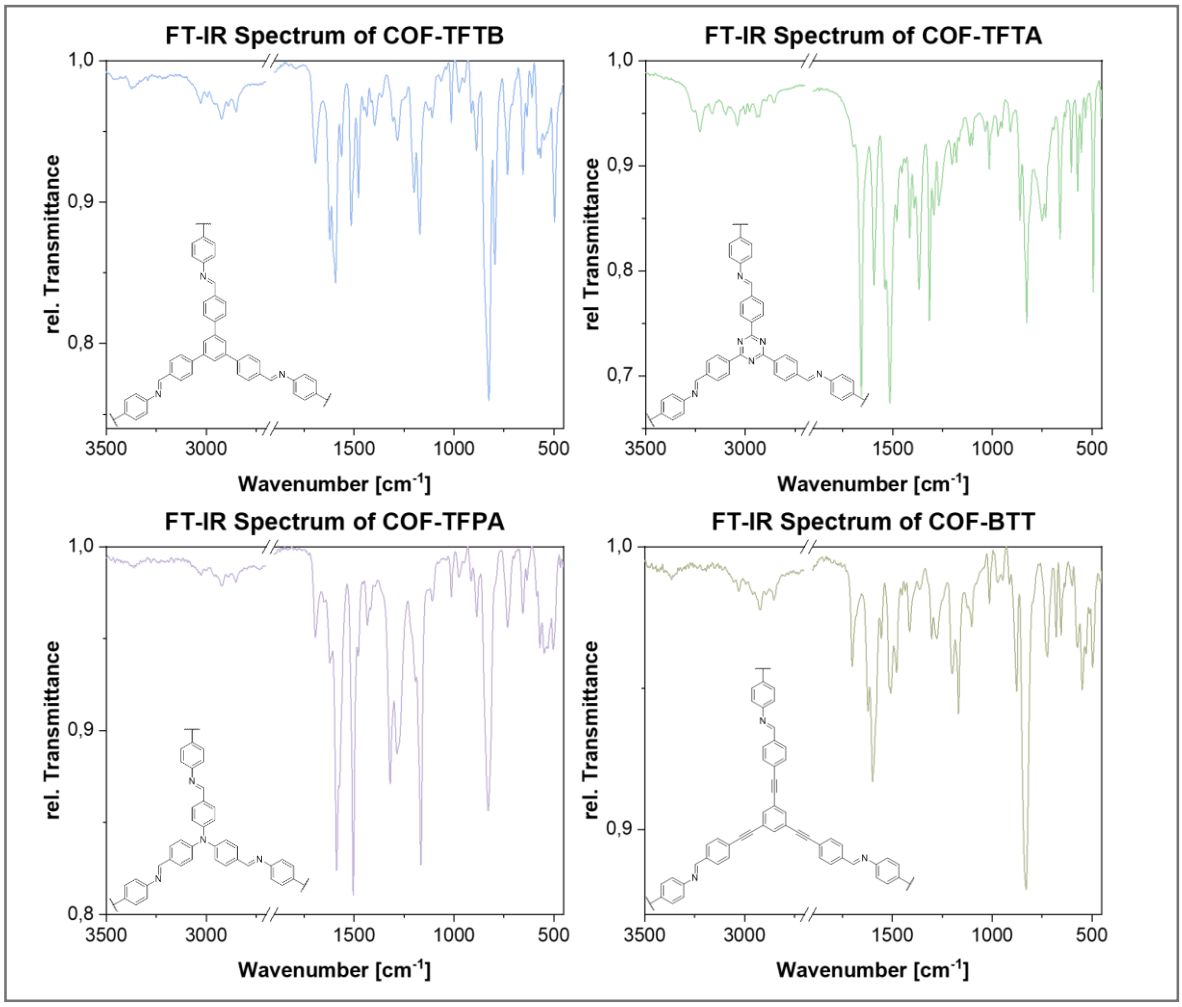

Figure 30: FT-IR spectra of COF-TFTB, COF-TFTA, COF-TFTA and COF BTT.

Figure **30** depicts the infrared spectrum of **COF-TFPA**, **COF-BTT**, **COF-TFPB** and **COF-TFTA**. Like **COF-TP**, no absorption bands of the aldehyde nor the amine groups can be seen.

Investigation of the IR spectrum of **COF-TFPA** revealed only the three bands in the region of the significant bands ranging from 1650–1000 cm^{-1}. At 1585 cm^{-1} a strong absorption band with a shoulder at 1622 cm^{-1} can be observed. Both bands are in the region of aromatic *C=C* stretching vibrations (1600–1450 cm^{-1}). Since both, the starting materials and COFs possess aromatic cores, no confirmation of the successful framework formation can be made from these bands. In addition, a medium intense absorption band appears at 1694 cm^{-1}. This band is most

likely attributed to *C=N* stretching vibration of the imine linkage, which appears in the region of 1690–1640 cm^{-1}.

Analysis of **COF-BTT** revealed the same findings as already discussed. The spectrum shows the absence of the prominent formyl and amine absorption bands. However, examination of the significant region shows two distinct absorption bands at 1699 cm^{-1} and at 1598 cm^{-1} with a shoulder at 1622 cm^{-1}. The vibration band at 1699 cm^{-1} is likely due to the *C=N* stretching vibration band which appears in the region, hinting the successful framework formation. Absorption bands at 1622 – 1598 cm^{-1} much likely originate from the aromatic *C=C* stretching vibrations. Similar to the previously discussed infrared spectra of **COF-TFPA** and **-BTT**, the spectrum of **COF-TFPB** exhibits characteristic absorption bands in the typical region for imine bonds (1690–1640 cm^{-1}), while simultaneously lacking the vibrational stretching modes of the formyl and amine functionalities. A strong band appears at 1594 cm^{-1}, accompanied by a neighboring medium-intensity band at 1622 cm^{-1}. Given that the medium-intensity band falls within the expected region for the vibrational stretching of conjugated imine bonds, the successful formation of the framework can be concluded. The infrared spectrum of **COF-TFTA**, was also investigated. The findings align with the results obtained for **COF-TP**, **-TFTP**, **-BTT** and **-TFPB**. The spectrum notably lacks the characteristic absorption bands of the formyl and amine groups. A very strong absorption band is observed at 1658 cm^{-1}. This band can be attributed to the vibrational stretching mode of the imine bond, thus confirming the successful formation of the framework. Furthermore, signals observed at 1539 cm^{-1} and 1316 cm^{-1} are characteristic of the triazine building unit and are also present in the starting material providing additional evidence for the successful formation of the framework. In addition, all prepared COFs exhibit absorption bands in the region 3200–2800 cm^{-1}. These bands arise from the *C–H* vibration, typical for aromatic compounds.

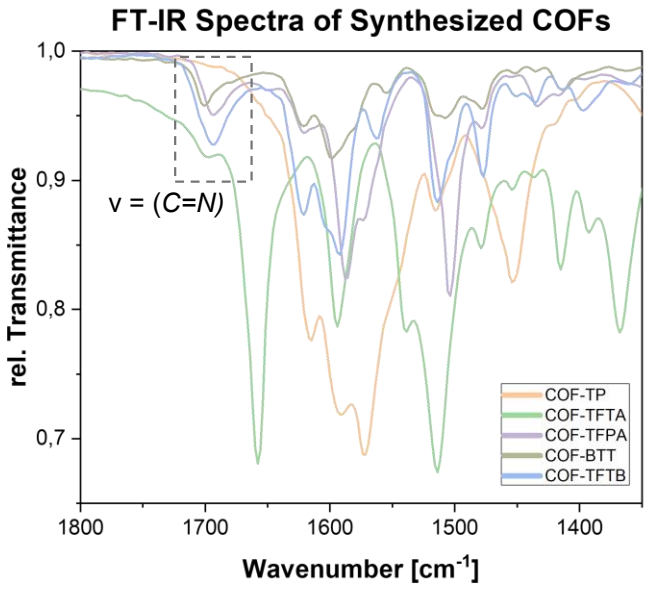

Figure 31: FT-IR spectra of all COFs in the range 1850 to 1350 cm^{-1}. The *C=N* stretching vibration of **COF-TFTA**, **COF-TFPA**, **COF-BTT**, and **COF-TFTB** is highlighted.

Figure **31** presents a magnified view of the infrared spectra of all synthesized COFs within the range of 1850–1350 cm^{-1}. In addition to the previously discussed imine linkage, absorption bands located between 1690 and 1640 cm^{-1} can be seen for all COFs except **COF-TP**. This observation further supports the iminol-ketoenamine tautomerization resulting in the loss of the imine absorption band.

However, a detailed analysis of the fingerprint region for each COF was not conducted due to the novelty of these frameworks and the lack of literature data for comparison.

Elemental analysis was performed to get a deeper understanding of the chemical composition of the prepared frameworks. It must be noted that the chemical composition determined by elemental analysis may not perfectly reflect the actual chemical composition of the COF. This discrepancy arises from unreacted end-groups within the framework, which can significantly influence the elemental analysis results. Furthermore, COFs can readily adsorb water from the atmosphere.[239-241] This presence of water molecules within the COF framework effectively lowers the carbon content of the material. Resulting in a lower overall carbon percentage in the elemental analysis, even if the framework itself has the expected carbon composition. Therefore, the removal of trapped water from porous COF structures to analyze their chemical composition remains a significant challenge.

In Table **2** the calculated and found values are depicted. For all COFs the experimental carbon and nitrogen values are much lower than the theoretical ones, with the highest discrepancy seen for the carbon values. The most significant deviation was found for **COF-TP**, with a value of 6.89%. The presence of the carbonyl groups within **COF-TP** could explain this finding. Atmospheric water could readily interact *via* hydrogen bonding with the hydrophilic COF surface resulting in a water-storing effect in the framework. Similar incidences for TP-containing COFs have already been reported in literature and could explain the deviation from the anticipated carbon value.[241]

However, only moderate deviations were found for the nitrogen content, with **COF-TFTA** exhibiting the most significant discrepancy at 2.10%. In contrast, the hydrogen values were generally in good agreement with the expected

Table 2: Results of the Elemental Analysis of COFs.

COF	***C*-Atoms found (calc.)**	***N*-Atoms found (calc.)**	***H*-Atoms found (calc.)**
COF-TP ($C_{93}H_{75}N_6O_3$)	77.44 (84.33)	5.28 (6.34)	5.08 (5.71)
COF-TFPA ($C_{105}H_{84}N_7$)	81.66 (87.66)	6.30 (6.79)	5.54 (5.86)
COF-BTT ($C_{117}H_{87}N_6$)	84.26 (89.11)	4.50 (5.33)	5.17 (5.56)
COF-TFTA ($C_{108}H_{84}N_9$)	85.24 (88.59)	4.80 (5.58)	5.74 (5.83)

3.3 Biofunctionalization of Metal-Organic Framework Surface *via* Nitroxide-Exchange Reaction

Preface. In the following chapter, parts are already evaluated and discussed in "Biofunctionalization of Metal-Organic Framework Nanoparticles *via* Combined Nitroxide-Mediated Polymerization and Nitroxide Exchange Reaction (https://doi.org/10.1002/mame.202300048)" published in 2023 in Macromolecular Materials and Engineering. Part of the discussion will be the peptide synthesis conducted during the framework of this thesis. If results from collaborators are used to compare or draw conclusions, the respective parts are mentioned in the text.

Introduction. Metal-Organic Frameworks (MOFs) are highly porous and crystalline materials with large surface areas fabricated by combining organic linker molecules with metal ions or clusters. The shape and size of created pores can be tuned and modified by varying the metals and organic linkers.[242] This approach can tailor MOFs for specific applications like gas storage and separation, drug delivery and catalysis.[37, 61, 242-243] Nanoparticles of metal-organic frameworks (**MOF NPs**) represent a growing class of MOFs characterized by a well-defined crystalline lattice, porosity and pore size distribution. In recent years, **MOF NPs** have been used in a diverse array of biomedical applications such as therapeutics, imaging and drug-delivery systems.[244-245] Surface chemistry modulation is crucial for these applications. Modifications can be achieved *via* post-synthetic modification (PSM), a technique that allows the incorporation of different functional groups to tailor the properties of the **MOF NPs** specifically.[77-78] Several methods to modify the surface area are reported in literature, including the functionalization of the metal ion or cluster by coordination chemistry or directly at the organic linker.[244]

This study utilized the nitroxide-mediated polymerization (NMP) for surface modification. NMP employs a persistent nitroxide radical, which initiates the polymerization by thermal decomposition of an alkoxyamine. The nitroxide radical is both mediator and initiator of the polymerization and reacts with the growing polymer chain end, forming a stable, but reversible bond and thus can "cap" the chain, preventing it from reacting further. With this approach, well-defined polymers are obtained under mild conditions. In combination with the nitroxide exchange reaction (NER) the "capped" polymer can be modified to specifically tailor the surface of the **MOF NP**.[246] In this approach the alkoxyamine capping the end can be exchanged by an external nitroxide enabling the precise functionalization of the polymer end.

In this project, a nitroxide-functionalized peptide was used to modify the MOF surface *via* NER. Therefore, a well-defined peptide sequence consisting of lysine, arginine, glycine and glutamic acid was synthesized. Post-synthetic modification of the peptide using a five-membered nitroxide ring led to the targeted compound, which was employed for **MOF NP** functionalization.

Since the peptide was utilized to modify the surface, the synthesis of the nitroxide and of the targeted peptide were part of this thesis and will be discussed in the following chapters. MOF fabrication and post-synthetic modification *via* NMP were performed by I. WAGNER from the TSOTSALAS research group at the Institute of Functional Interfaces (IFG) at Karlsruhe Institute of Technology (KIT) and are therefore excluded from the discussion. If data generated by collaborators is used for comparative analysis or to support conclusions, the respective part is mentioned within the text.

3.3.1 Nitroxide Synthesis

The five-membered nitroxide ring was synthesized in a four-step synthesis route starting from triacetonamine (**47**). According to a reported protocol, amine **47** was reacted with molecular bromine in acetic acid for one hour at 21 °C.[247] The crude product was purified by recrystallization from hot ethyl acetate to isolate the brominated intermediate **48** in a yield of 59% (Scheme **14**).

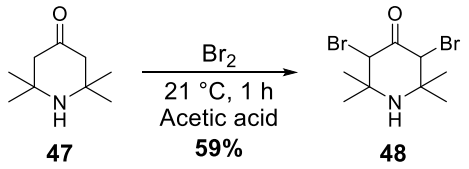

Scheme 14: Synthesis of the dibrominated precursor 48 *via* bromination with molecular bromine of triacetonamine (**47**).[247]

Subsequently, the brominated intermediate **48** was subjected to a FAWORSKI rearrangement by treating it with sodium hydroxide in aqueous ammonia for two hours at 21 °C.[248] Purification of the crude product by recrystallization from hot toluene yielded the five-membered ring 2,2,5,5-3-pyrroline-3-carboxamide (**TPC**, **49**) with a yield of 35% (Scheme **15**).

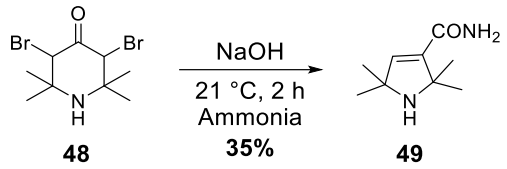

Scheme 15: Synthesis of the carboxylic amid **TPC** (**49**) *via* FAWORSKI rearrangement of dibromine **48**.[248]

Nitroxides are easily synthesized by oxidation of a nitrogen precursor. Most applied precursors for nitroxide synthesis are secondary amines or hydroxyl amines which are treated with oxidizing reagents like hydroxy peroxide or peroxy acids (*e.g.*, *meta*-chlorperoxybenzoic acid (***m*CPBA**, **51**)). The secondary amine of intermediate **49** was reacted with **51** in DCM for 16 hours at 21 °C.[249] Straightforward purification of the crude product yielded 2,2,5,5-tetramethyl-3-pyrroline-3-carboxamide radical (**TPCR**, **50)** with a yield of 69% (Scheme **16**).

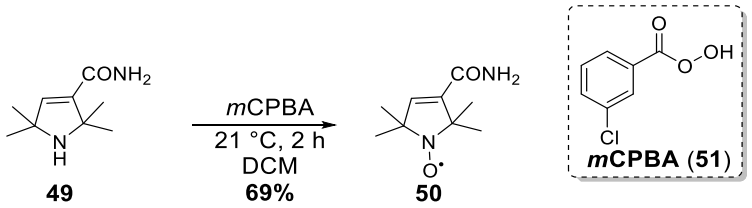

Scheme 16: Synthesis of the nitroxide containing five-membered ring **TPCR** (**50**) *via* oxidation of the secondary amine **TPC** (**49**) with ***m*CPBA** (**51**).[249]

Characterization *via* nuclear magnetic resonance (NMR) spectroscopy of the synthesized compound was not performed due to the presence of the nitroxide moiety. Nitroxides possess an unpaired electron on the oxygen atom and exhibit paramagnetic properties. This paramagnetic character results in significant line broadening in NMR spectra. This broadening effect originates from the interaction between the magnetic moment of the unpaired electron and the magnetic moments of the NMR-active nuclei (*e.g.*, protons), leading to a loss of spectral resolution. Electron Paramagnetic Resonance (EPR) spectroscopy confirmed the successful conversion into the nitroxide radical. While NMR probes the magnetic properties of atomic nuclei, EPR detects unpaired electrons by exciting their spin with microwave irradiation. Investigations of the spectrum showed a resonance with a *g* value of 2.00603, which is very similar to the *g* value reported for (2,2,6,6-tetramethylpiperidin-1-yl)oxidanyl (**TEMPO**) with a *g* value of 2.0056).[250] EPR measurement of the nitroxide radical at room temperature revealed a spectrum with three narrow lines. These three lines result from the hyperfine coupling between the nitrogen (I_N=1) and the unpaired electron. The Hyperfine coupling

constant to the nitrogen atom was 40 mHz (A=1.43 mT). The cw-EPR spectrum of nitroxide **TPCR** (**50**) is illustrated in Figure **32**.

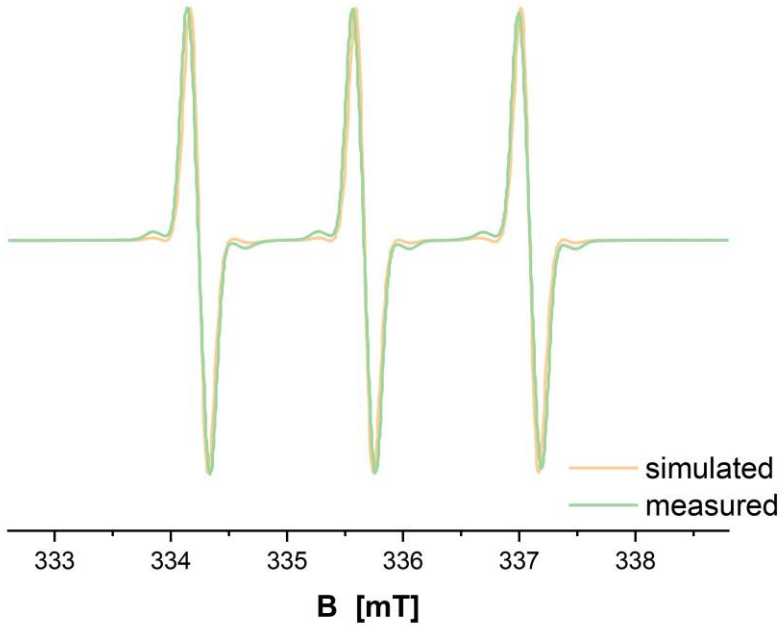

Figure 32: Cw-EPR spectrum of TPCR (50) in toluene (0.1 mM, modulation amplitude: 1.00 G, 9.424612 GHz, ambient temperature, 1 scan, *g*=2.00603).

In addition, mass spectrometry and FT-IR spectroscopy were conducted to support the successful radical formation further.

Several strategies to modify peptide side chains are reported in literature. For instance, copper-catalyzed azide-alkyne cycloaddition (CuAAC).[251] In this approach the incorporation of an azide moiety into a side chain is needed. Furthermore esterification of a serine side chain or the attachment of a carboxylic acid to a lysine side chain *via* peptide coupling is possible.[252-253] Since the targeted peptide was designed to exhibit a lysine with a terminal primary amine functionality in its side chain, peptide coupling was performed to conjugate the nitroxide to the targeted peptide-sequence. To obtain the needed carboxylic acid, **TPCR** (**50)** was subjected to hydrolysis under basic conditions using aqueous sodium hydroxide under reflux for 16 hours until no ammonia was released anymore. Subsequent purification of the crude reaction mixture *via* column chromatography afforded 2,2,5,5-tetramethyl-3-pyrroline-3-carboxylic acid radical (**TPAR**, **52**) in a yield of 52% (Scheme **17**).

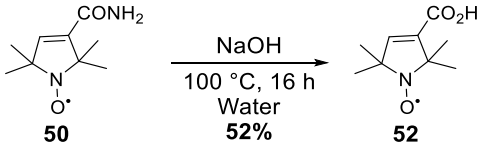

Scheme 17: Synthesis of carboxylic acid **TPAR** (**50**) *via* hydrolysis of **TPCR** (**52**) under basic conditions.

3.3.2 Peptide Synthesis for Surface Functionalization

To assess the efficiency of MOF surface modification *via* NER for biomedical applications, the arginine-glycine-aspartic acid sequence, abbreviated with RGD corresponding to the one-letter code of the respective amino acid, was chosen as a model target. The RGD motif, first reported in 1970,[254] contains the amino acids arginine, glycine, and aspartic acid. It is a crucial cell adhesion motif and can be utilized in drug delivery to target specific cell types in particular tumor cells.[255] The presence of lysine within the peptide sequence facilitates subsequent modification. Lysine, a basic amino acid featuring a primary amine group in its side chain, enables the coupling of carboxylic acid **52** *via* standard peptide coupling protocols, yielding the desired modified RGD peptide.

Synthesis of the targeted peptide was carried out on solid phase; therefore, *N*-Fmoc-protected aspartic acid (**54**) was firstly attached to 2-chlorotrityl chloride resin (**53**) under basic conditions using diisopropylethylamine (DIPEA) (Scheme **20**). Subsequently, deprotection of the base sensitive fluorenylmethoxy carbonyl (*N*-Fmoc, **56**) protecting group using 20% piperidine in DMF resulted in the formation of the resin bond amino acid **55**. Afterward, *N*-Fmoc glycine (**58**) was coupled to the loaded resin using *O*-(7-azabenzotriazol-1-yl)-*N*,*N*,*N*,*N*-tetramethyluronium-hexafluorophosphate (HATU) as coupling reagent. *N*-Fmoc deprotection and coupling of the respective amino acids (**61** and **61**) was repeated until the side-chain protected peptide (**62**) was obtained (Scheme **18**).

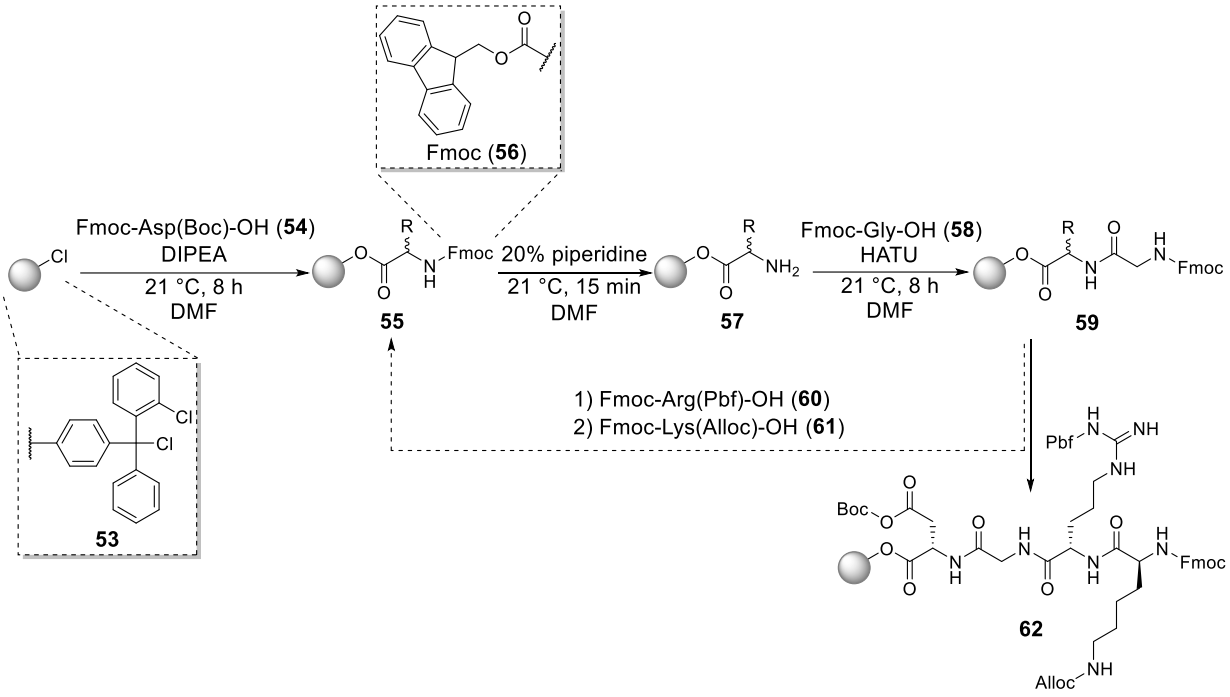

Scheme 18: Synthesis of the resin bond peptide **62** *via* sequential coupling and deprotection of the respective amino acids (**54**, **58**, **60** and **61)**.

N-Allyloxy carbonyl (*N*-Alloc, **63**) protecting group was removed using palladium catalysis. Therefore, the resin bond peptide (**62**) was mixed with tetrakis(triphenylphosphine) palladium as catalyst and phenylsilane (**64**) in dry DCM at 21 °C for 20 minutes. Phenylsilane (**64**) was added as scavenger to trap the highly reactive carbocation intermediate formed during the deprotection. This prevents the unwanted side reaction between the primary amine and the formed carbocation, which could otherwise occur due to the nucleophilic nature of the amine. The palladium-catalyzed deprotection of peptide **62** is illustrated in Scheme **19**.

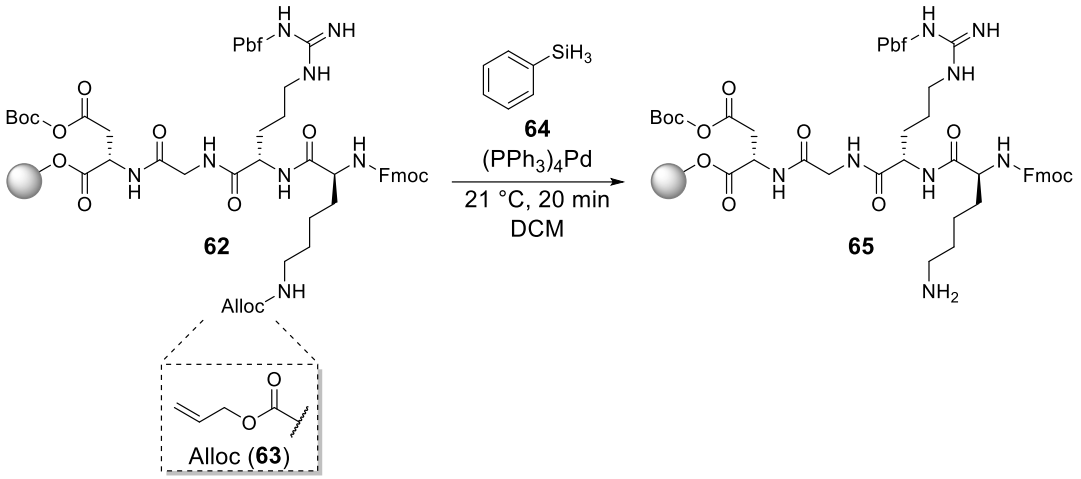

Scheme 19: Palladium-catalyzed deprotection of the Alloc-protecting group of the resin bond peptide **60**.

Attachment of nitroxide **52** was achieved by reacting the resin-bond peptide **65** with **TPAR (52)** using HATU as coupling reagent and DMF as solvent for 24 hours (Scheme **20**). The resin bound nitroxide-functionalized peptide **63** was obtained *via* coupling of nitroxide **52** to the *N*-terminal lysine side chain.

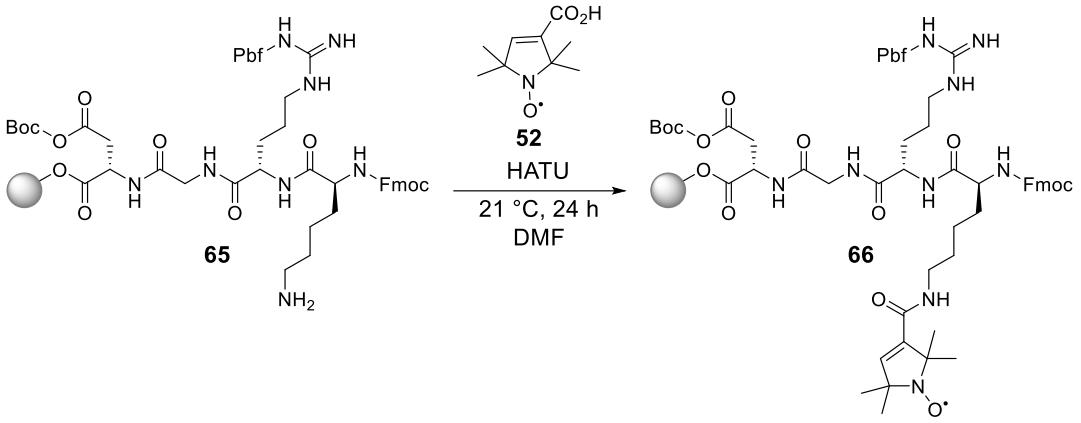

Scheme 20: Synthesis of the nitroxide functionalized peptide **63** employing peptide coupling conditions.

Subsequently, the removal of the *N*-terminal Fmoc protecting group was accomplished by incubation of **66** under basic conditions at 21 °C for 15 minutes. Afterwards, the *N*-terminal deprotected peptide was cleaved from the resin under acidic conditions. Therefore, **66** was treated with hexafluoro isopropanol (HFIP) at 21 °C for two hours (Scheme **21**).

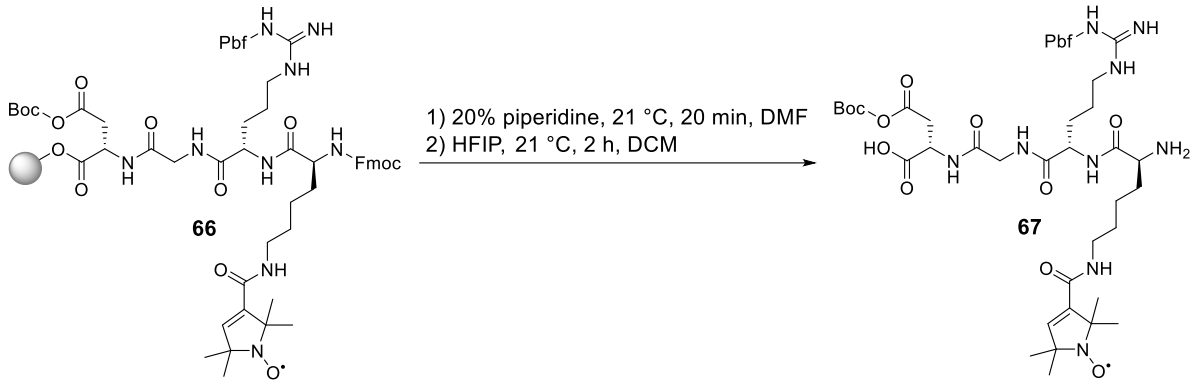

Scheme 21: 1) Deprotection of the *N*-terminal Fmoc-protecting group of peptide **66** using 20% piperidine. 2) Cleavage of the deprotected peptide **67** from the resin using HFIP.

To remove the acid sensitive *tert*-butyloxy carbonyl (*N*-Boc, **68**) and 2,2,4,7-pentamethyl dihydrobenzofurane-5-sulfonyl (*N*-Pbf, **69**) protecting groups from the crude linear peptide **67**, the peptide **67** was treated with TFA, phenol and triisopropylsilane (TIPS) in water at 21 °C for three hours (Scheme **22**). Phenol and TIPS were added to the reaction mixture as scavengers to trap reactive intermediates such as cations formed during the deprotection of the side chains.

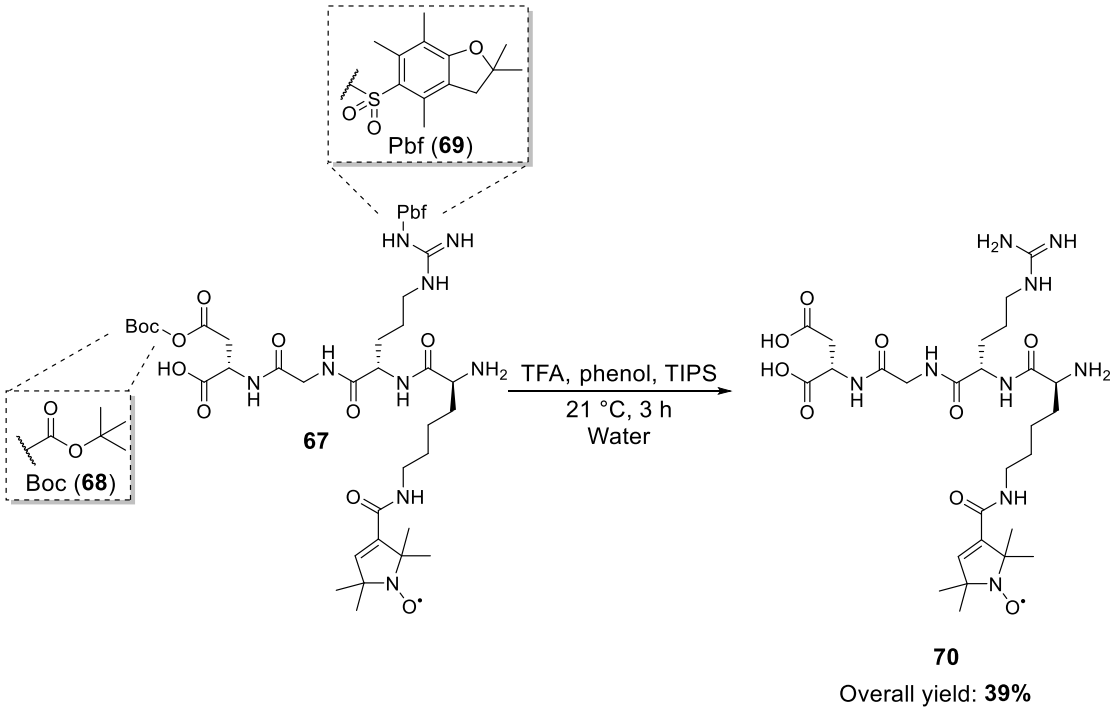

Scheme 22: Removal of the acid labile *N*-Pbf- and *N*-Boc-protecting group using TFA.

After completion, the targeted peptide **70** was obtained by precipitation from cold diethyl ether as a colorless solid in an overall yield of 39% starting from **53**. Cleavage from resin and the successful peptide formation was confirmed by matrix-assisted laser desorption-ionization (MALDI) spectrometry. It is important to note that the reported yield represents the overall yield of the entire synthetic route. Individual yields for each step of the reaction sequence were not determined.

3.3.3 Surface Modification *via* Nitroxide Exchange Reaction

MOF NP surface modification *via* NMP and NER experiments and evaluation of the results was conducted by I. WAGNER from the research group of M. TSOTSALAS at the IFG at KIT. The successful NER with the synthesized nitroxide containing RGD-Sequence was confirmed by Time-of-Flight Secondary Ion Mass Spectrometry (ToF-SIMS) conducted by A. WELLE at IFG at KIT. **MOF NPs** of the type UiO-66-NH_2 were employed for all experiments.

Initially, the **MOF NP** surface was modified using NMP. Consequently, the alkoxyamine (AA, **72**) was coupled to the amine-functionalized MOF **71** using standard coupling reagents 1-ethyl-3(3-dimethylaminopropyl)carbodiimide (EDC) and the *N*-hydroxysulfosuccinimide sodium salt (sulfo-NHS) in ethanol. NMP was initiated by thermally induced homolytic cleavage of the weak *C-O* bond within the UiO-66-AA (**73**), generating two radical species: a carbon-centered radical and the persistent oxidanyl TEMPO radical. Subsequently, radical polymerization was carried out using the styrene derivative PEO-methyl-*p*-vinylbenzyl-ether (SPEGA, **74**) as monomer. The polymerization was terminated *via* capping of the growing polymer chain with TEMPO, resulting in the formation of the TEMPO-"capped" **MOF NP** (**75**), which was subsequently utilized in the NER (Scheme **23**).

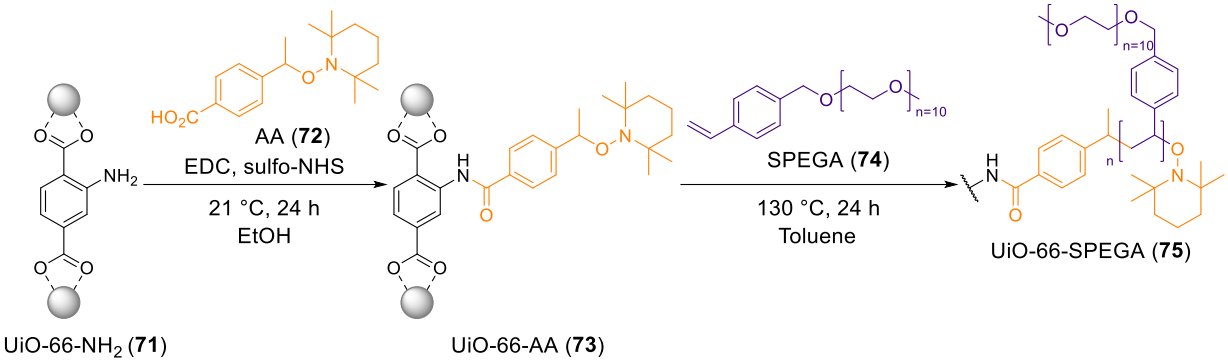

Scheme 23: Coupling AA (**70**) to MOF NP using EDC and sulfo-NHS and subsequent surface modification *via* NMP with SPEGA (**74**) as a monomer. Surface modification of the **MOF NP** was carried out by I. WAGNER (IFG, KIT).

Exchanging the alkoxyamine amine cap *via* NER offers a useful tool to tune the **MOF NP** surface specifically. Surface modification of **MOF NP** with the synthesized RGD-Peptide **70** was carried out in *N*,*N*-dimethylformamide as solvent for 1 day at 100 °C. Scheme **24** depicts a schematic overview of the NER.

Like in the already discussed NMP, the NER is initiated thermally by cleaving the relatively weak *C-O* bond of the alkoxyamine **75**. The homolytic *C-O* bond cleavage results in the formation of two radical species: a carbon-centered radical localized at the MOF linker and the persistent **TEMPO** (**76**) radical. Recombination of the carbon-centered radical with the nitroxide-functionalized RGD-peptide (**70)**, results in the formation of a new alkoxyamine namely the RGD-modified **MOF NP 73**. Since the reaction is completely controlled thermodynamically, the exchange ultimately results in the thermodynamically most stable product. In the six-membered ring structure of TEMPO, the *N-O* functional group exhibits a non-planar geometry, wherein the oxygen atom is sterically shielded by the adjacent methyl substituents. This structural arrangement ultimately results in the formation of a thermodynamically stable radical species. In contrast, studies of the five-membered proxyl ring have revealed a planar configuration of the *N-O* functional group, leading to greater exposure of the oxygen atom. The reduced steric shielding of the oxygen results in a radical species that is thermodynamically less stable.[256]

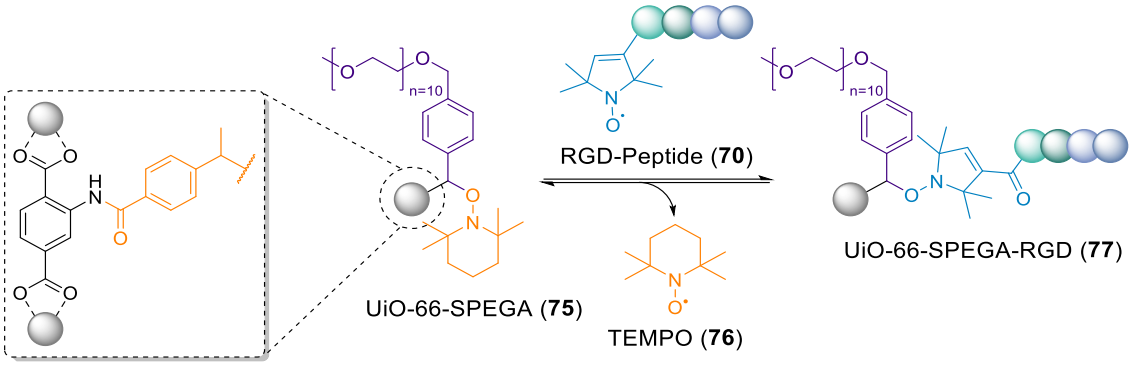

Scheme 24: Schematic illustration of the nitroxide-exchange reaction (NER) in which the TEMPO end-cap of **UiO-66-SPEGA** (**75**) is exchanged by the nitroxide-functionalized RGD-peptide (**70**). End-group exchange was carried out by I. WAGNER (IFG, KIT).

The successful surface modification was confirmed by comparing the recorded mass spectra before and after the nitroxide-exchange reaction. Mass spectrum of the **MOF NP** shows a concise signal at *m/z* 156.14 which can be assigned to the $[TEMPO]^+$ fragment. This fragment originates from the alkoxyamine end group and can be used as an indicator of the exchange reaction (Figure **33**).

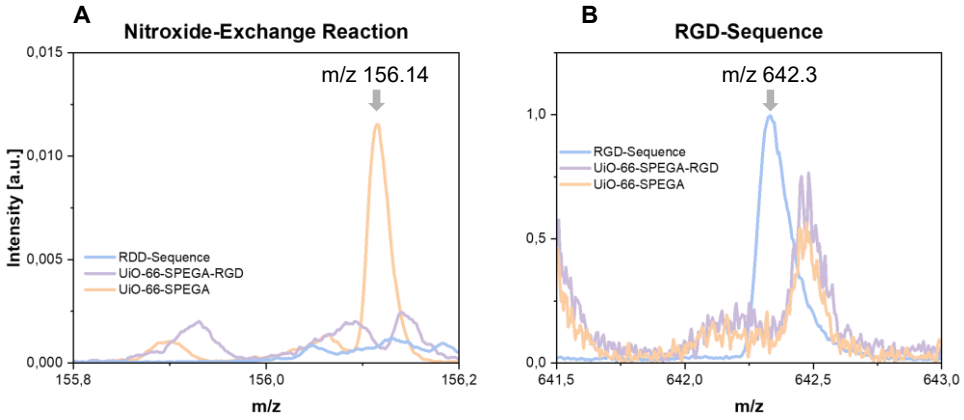

Figure 33: Time-of-Flight Secondary Ion Mass Spectra (ToF-SIMS) of A) the nitroxide-exchange reaction (NER), the $[TEMPO]^+$ fragment with m/z 156.4 is marked and B) the RGD-Sequence with m/z 642.3. Data provided by A. WELLE (IFG, KIT).

A significant reduction in the $[TEMPO]^+$ fragment signal was observed. This indicates the loss of the alkoxyamine end group and, consequently, confirms the successful exchange with the RGD-peptide **70**. MS analysis of the RGD-sequence revealed a signal at *m/z* 642.3 originating from the $[M]^+$, confirming the presence of the intact RGD-sequence (Figure **33**). In addition, characteristic fragment ions originating from arginine were observed at *m/z* 43.03 ($CH_3N_2^+$), 100.09 ($C_4H_{10}N_3^+$), and 127.01 ($C_5H_{11}N_4^+$) (Figure **34**).[257]

Analysis of the MS spectrum of the modified **MOF NP** reveals the absence of the RGD-sequence signal, while the presence of signals originating from arginine fragments provides further evidence of successful surface modification.

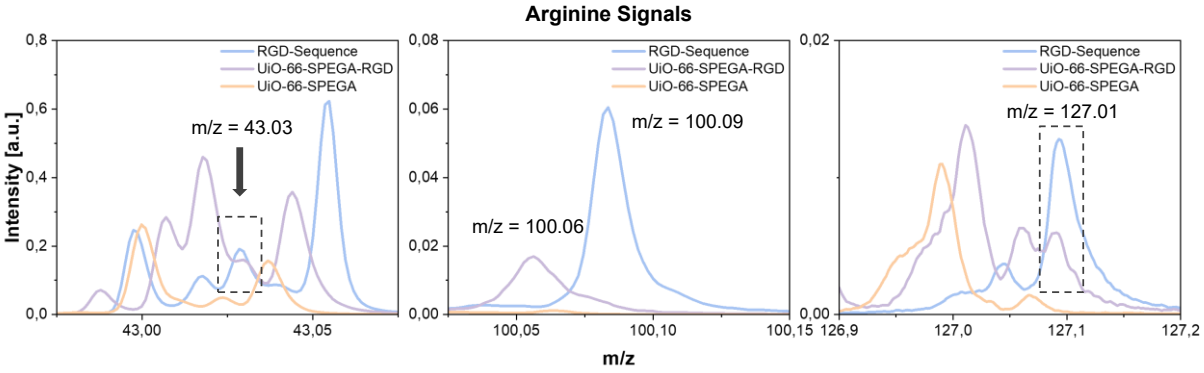

Figure 34: Prominent arginine fragments observed in the RGD-sequence and in UiO-66-SPEGA-RGD (**73**). Data provided by A. WELLE (IFG, KIT).

3.4 Organic Azides as Linker for Metal-Organic Frameworks

Introduction. MOFs are a class of crystalline materials prepared by combining an organic linker and metal ions. MOFs are renowned for their exceptionally high surface areas and pore volumes, which arises from the crystalline nature.[100, 258] Furthermore, the tunability of MOFs represents a significant advantage. The selection of the metal ion and organic linker allows researchers to tailor the properties of MOFs for specific applications. Pore sizes can be adjusted to host guest molecules or ions. Introducing specific functional groups within the MOF provides chemical properties for applications like catalysis or selective adsorption.[41, 61, 102, 259] In addition, MOFs can be engineered with enhanced stability against chemical degradation or mechanical stress to improve the durability and longevity of the material.[260-262]

While MOF powders have shown promising results in various fields, their applications are limited.[38-39, 263] Due to their appearance, MOF powders are difficult to handle and to process. In addition, diffusion of molecules within the MOF material is possible, leading to irregular composition. Surface-mounted MOFs (SURMOF) thin films were developed to overcome these limitations. SURMOFs are grown on solid substrates in liquid phase and exhibit only low defect densities with well-defined surface morphology.[40-41]

Organic azides represent a versatile class of compounds characterized by the unique azide functional group. This functional group has received considerable attention recently due to its diverse potential applications in pharmaceuticals, bioactive molecules, and energetic materials.[264] A wide range of transformation reactions of the azide group are known. The application of thermal energy or irradiation with light initiates decomposition of the azide group, resulting in the expulsion of elemental nitrogen and the formation of a highly reactive intermediate known as nitrene. Chemically analogous to carbenes, nitrenes exhibit a diverse reactivity profile, participating in various transformations, including the formation of nitriles, azobenzenes, azepines, and secondary amines (Scheme **25**).[265]

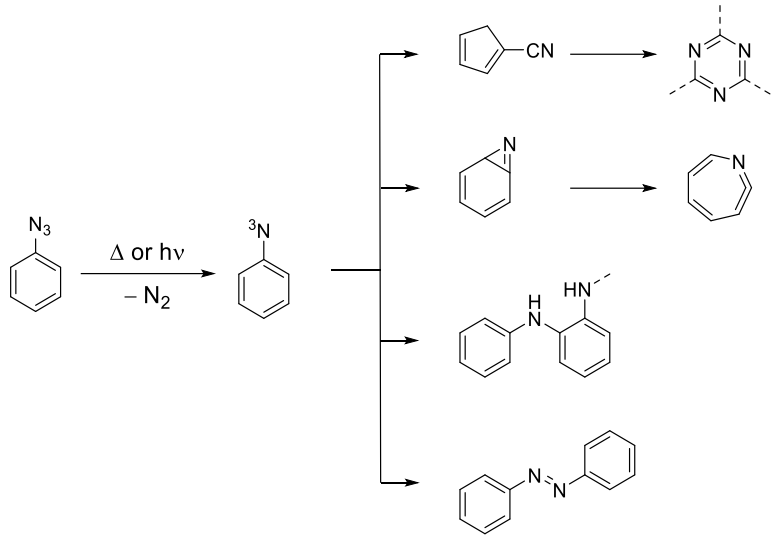

Scheme 25: Decomposition of an aromatic azide and follow-up reactions of the generated nitrene.[265]

Transformation reactions of azides are widely applied in organic chemistry, such as the renowned and Nobel prize-awarded CuAAC discovered by B. SHARPLESS and M. MELDAL.[266-267] However, insights in the mechanism of their photochemical decomposition are lacking. In comparison to decomposition experiments carried out in solvent-based approaches leading to unwanted side reactions, MOFs have the potential to investigate the decomposition mechanism in an ordered environment to get an in-depth view in a controlled manner.

Preliminary studies on the photochemical decomposition of azides within a SURMOF framework were previously carried out by WÖLL and co-workers.[258] In their work, an azido-functionalized stilbene linker (**78**) was employed. However, the decomposition of the azide resulted in the formation of unwanted side products originating from the intramolecular reaction of the generated nitrene with the adjacent *C*=*C* bond as illustrated in Figure **35**.

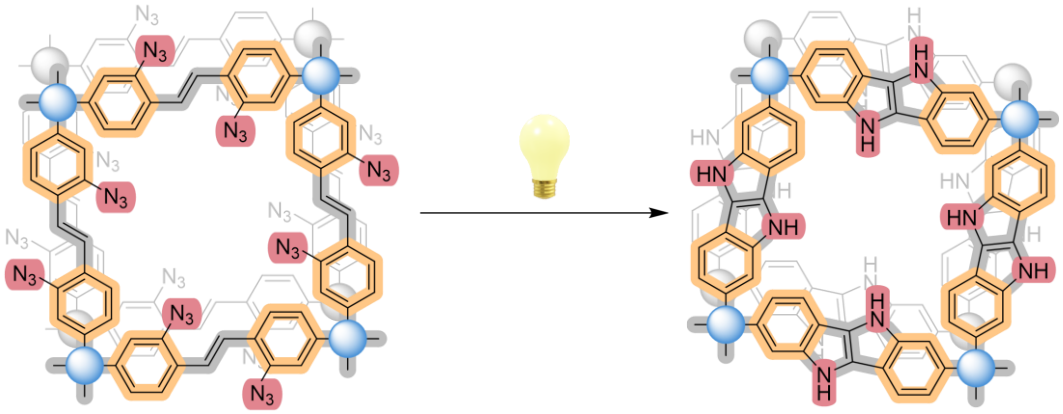

Figure 35: Photochemical decomposition of azido-functionalized stilbene linker DASDC (**75**) within SURMOF. Adapted from literature.[258]

In this project, the stilbene linker should be replaced by two novel azido-functionalized tolan-based MOF linker **MATDC** (**79**) and **DATDC** (**80**) (Figure **36**). The design of the linker molecules was chosen to allow the decomposition of the azide in the SURMOF and simultaneously prevent the nitrene from reacting in unwanted side reactions. Therefore, the synthesis of tolan-based MOF linker containing the dicarboxylic acid for MOF fabrication and the azide moiety were targeted to investigate its photochemical decomposition.

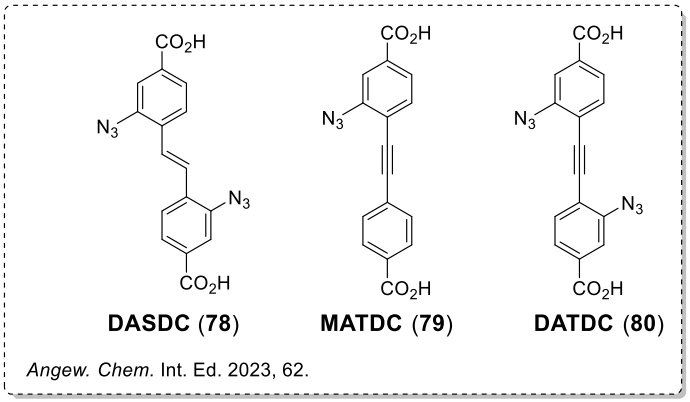

Figure 36: Overview of the literature reported stilbene linker **DASDC** (**78**) (left) and the novel mono- and diazido tolan linker **MATDC** (**79**) and **DATDC** (**80**) (right) for applications in SURMOF fabrication.

3.4.1 Synthesis of Monoazido Tolan Linker

The mono-azido MOF linker was synthesized from commercially available starting materials. Initially, attempts were made to introduce the azide moiety at the beginning of the synthetic sequence before conducting further transformations on the resulting intermediate.

The literature describes several synthetic strategies for the preparation of aromatic azides. One approach involves converting aromatic halides into their corresponding lithiated intermediates using *n*-butyllithium. The lithiated species can then react with azide transfer reagents such as tosyl azide (*p*TsN$_3$, **81**) or trimethylsilyl azide (TMS-N$_3$, **82**) to yield the desired aromatic azides (Method A). An alternative approach involves the transformation of an aromatic amine into the corresponding azide. This typically involves a two-step process, firstly, the amine compound is subjected to diazotization using common reagents such as *para*-toluenesulfonic acid (*p*TsOH) and *tert*-butyl nitrite (*t*BuONO). Subsequently, the resulting diazo-compound is then reacted with sodium azide to form the targeted aromatic azide (Method B).[251] Both synthetic approaches for the synthesis of aromatic azides are illustrated in Scheme **26**.

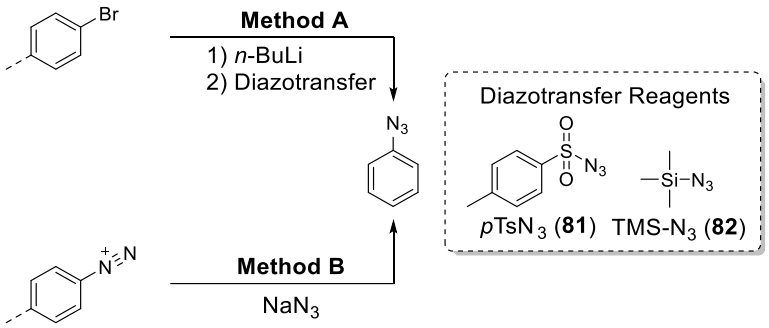

Scheme 26: Synthesis of aromatic azides *via* lithiation and diazo transfer (**Method A**) or diazotization followed by treating the diazonium salt with sodium azide (**Method B**).[251]

Given the availability and affordability of methyl 3-amino-4-iodobenzoate (**83**) in multi-gram quantities, Method B was selected for the synthesis of precursor **84**. To prepare **84**, amine **83** was subjected to diazotization. Therefore, the amine was treated with sulfonic acid and sodium nitrite at 0 °C to generate the diazonium salt *in situ*. The progress of the diazotization reaction was monitored by thin-layer chromatography (TLC) until complete consumption of the starting amine was observed, which typically occurred within 30 minutes. After complete conversion of the starting material, an aqueous sodium azide solution was added to transform the diazonium salt into the organic azide. Purification of the crude product *via* column chromatography afforded **84** in a yield of 88% (Scheme **27**).

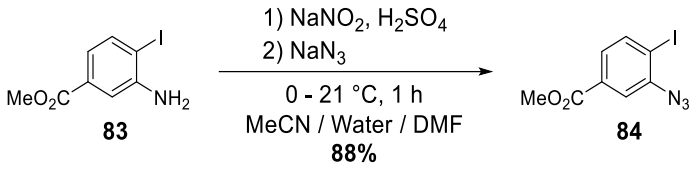

Scheme 27: Synthesis of azide **84** *via* diazotization-azidation of methyl 3-amino 4-iodobenzoate (**83**).

Based on the design of the linker molecule, SONOGASHIRA cross-coupling was selected as the most useful tool for the synthesis. However, two major drawbacks of cross-coupling reactions in this specific context should be addressed. Typically, SONOGASHIRA conditions employ copper(I) salts as co-catalysts to simplify the proton abstraction of the terminal alkyne. As mentioned, the renowned CuAAC reaction also utilizes both copper(I) salts and alkynes which could result in the formation of unwanted side products. In this context, the azide could react with the alkynes, forming nitrogen-containing 5-membered triazoles. However, significant advancements have been made in recent years, leading to the development of copper-free methods for the SONOGASHIRA cross-couplings. These advancements involve the utilization of sophisticated phosphine-based ligands like XantPhos or XPhos that enable palladium-catalyzed cross-coupling reactions to proceed efficiently in the absence of copper.[268] Furthermore, it should be noted that azides are known to react with organic phosphines in the STAUDINGER reaction, which would result in the reduction of the azide to the corresponding organic amine.[269-270] Nevertheless, transformations of azide-functionalized organic molecules utilizing cross-coupling conditions and employing triphenylphosphine and other widely used organic phosphines as ligands are reported in literature.[271]

Consequently, intermediate **84** was reacted with methyl 4-ethynyl benzoate (**85**) utilizing copper-free SONOGASHIRA conditions (Scheme **28**). However, the desired transformation did not proceed as anticipated, and the target compound could not be isolated successfully.

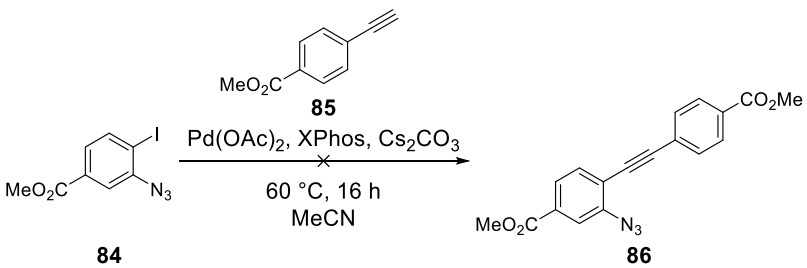

Scheme 28: Synthesis approach for synthesizing tolan **86** *via* copper-free SONOGASHIRA cross-coupling.

The synthetic approach for the target compound was further modified to address this. Instead of forming the azide prior to the cross-coupling reaction, the conversion of the aromatic amine

into the azide should be carried out after the preparation of the tolan core. Therefore, methyl 3-amino-4-iodobenzoate (**83**) was coupled with methyl 4-ethynylbenzoate (**85**) using common cross-coupling conditions. Purification of the crude reaction mixture by column chromatography afforded the desired intermediate **87** in a yield of 75% (Scheme **29**).

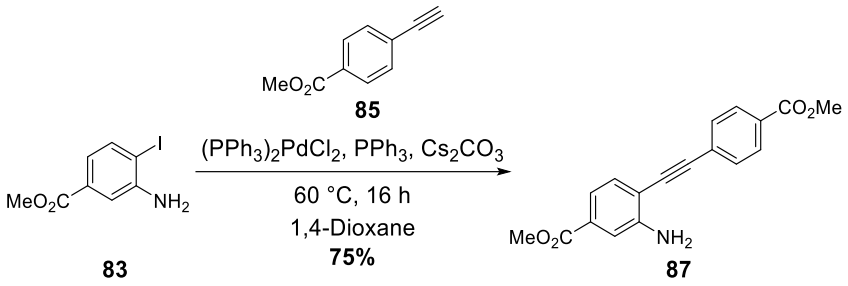

Scheme 29: Preparation of intermediate **87** *via* SONOGASHIRA cross-coupling using methyl 3-amino 4-iodobenzoate (**83**) and methyl 4-ethynylbenzoate (**85**).

Subsequently, amine **87** was subjected to a diazotization-azidation reaction. Intermediate **87** was treated with sulfonic acid and sodium nitrite at 0 °C to generate the diazonium salt *in situ*. Following complete consumption of the starting material, monitored by TLC, an aqueous sodium azide solution was added to convert the generated diazonium compound into the target azide **86**. Purification of the crude product afforded **86** in a yield of 55% (Scheme **30**).

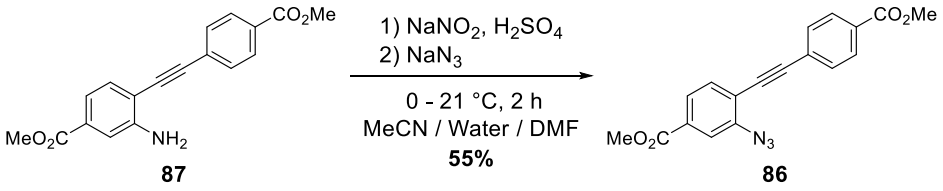

Scheme 30: Diazotization-azidation of amine **87** for the synthesis of azide **86**.

In the next step the methyl ester was saponified to prepare the carboxylic acid for the following MOF synthesis. Intermediate **88** was treated with lithium hydroxide in a mixture of methanol, tetrahydrofuran, and water for 4 days. The formed precipitate was filtered off, and the crude product was purified by several washing steps with water and methanol, resulting in the isolation of the mono-azido tolan dicarboxylic acid (**MATDC**, **79**) in a yield of 81% (Scheme **31**).

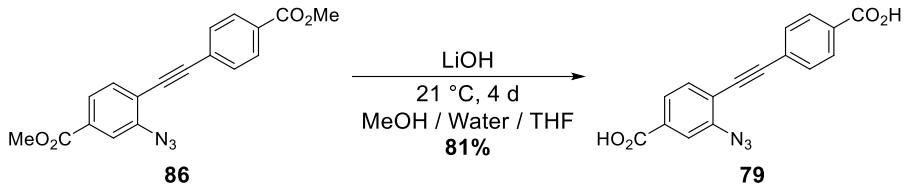

Scheme 31: Saponification of **86** with lithium hydroxide to form **MATDC** (**79**).

3.4.2 Synthesis of Diazido Tolan Linker

Initial investigations into the photochemical-induced decomposition of azide groups were conducted by WÖLL and colleagues, in which a diazido-functionalized stilbene linker (**78**) was employed to fabricate SURMOFs (Figure **35**). It was demonstrated that the nitrene intermediate undergoes intramolecular amination with the adjacent *C=C* bond, leading to the formation of indoles. To prevent this, the synthesis of the diazido tolan linker (**80**) was pursued. In contrast to the stilbene linker, the tolan linker lacks the *C=C* double bond in close proximity to the *in situ* formed nitrene moiety. Because of that, it is anticipated that insights into the azide decomposition process can be gained without unwanted intramolecular side reactions.

DATDC (**80**) was prepared based on the synthetic strategy discussed in Chapter **2.4.1**. The introduction of the azide moiety should be performed after the synthesis of the tolan core structure.

Initially, the TMS-protected alkyne precursor **89** for the tolan synthesis was prepared according to a procedure reported in literature.[272] Commercially purchased 3-amino-4-iodobenzoate (**83**) was coupled with TMS-protected acetylene (**88**) using standard SONOGASHIRA cross-coupling conditions. Straightforward purification of the crude product resulted in the isolation of **89** in a yield of 97% (Scheme **32**).

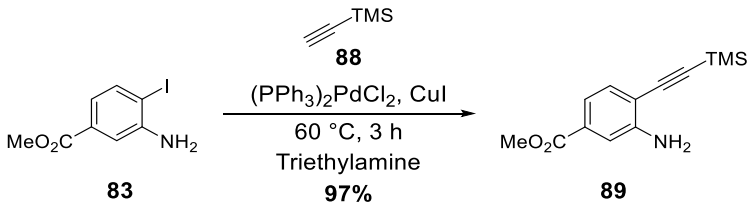

Scheme 32: Preparation of the TMS-protected intermediate **89** *via* SONOGASHIRA cross-coupling using methyl 3-amino 4-iodobenzoate (**83**) and TMS-protected acetylene (**88**).[272]

The TMS-protecting group was removed under basic conditions using potassium carbonate in methanol.[272] Subsequent purification of the crude product *via* column chromatography yielded the deprotected alkyne **90** in 85% (Scheme **33**).

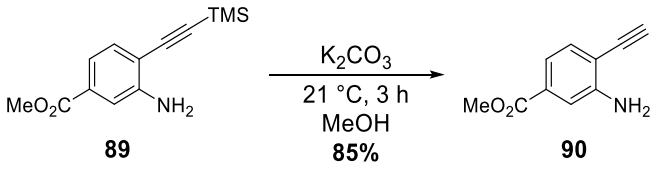

Scheme 33: Deprotection of the TMS-group of **89** to obtain the unprotected precursor **90**.[272]

The synthesized alkyne **90** was subjected to a SONOGASHIRA cross-coupling reaction with methyl 3-amino-4-iodobenzoate (**83**) in triethylamine (Scheme **34**). Due to the low solubility of the product, diamine **91** was readily isolated by filtration of the formed precipitate during the reaction. The use of triethylamine resulted in the formation of the corresponding triethylammonium salt as an impurity which was identified in the NMR spectrum and could not be effectively removed by evaporation of the reaction mixture under reduced pressure. However, it was possible to remove the ammonium salt successfully by co-evaporation of the reaction mixture with toluene, affording **91** in a yield of 58%.

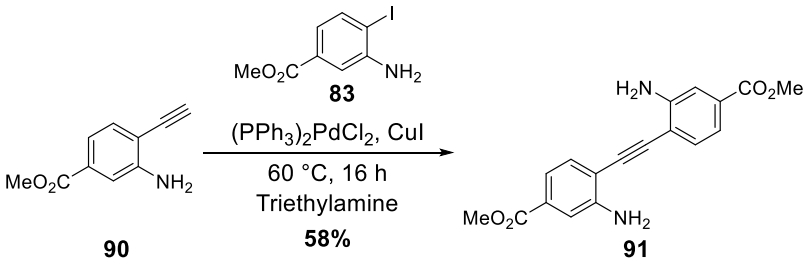

Scheme 34: SONOGASHIRA cross-coupling for the synthesis of diamine **91**.

Azides **84** and **86** were prepared by diazotization of the aromatic amine and subsequent azidation with sodium azide of the *in situ* formed diazonium salt (Scheme **27** and **30**). In contrast to the previously discussed diazotization reactions, adjustments of the employed reagents were made. Initial synthetic attempts were carried out using the established conditions applied in the synthesis of azides **84** and **86**. However, it was observed that even when the diazotization reaction was conducted at 0 °C, rapid decomposition of the diazonium salt occurred for this specific compound, leading to a significant decrease in the isolated yield. The stability of diazonium salts is known to be influenced by the nature of the counterion, which originates from the acid used in the diazotization process. In literature, several examples of diazonium salts are reported, such as tetrafluoroborates and tosylates, which exhibit enhanced thermal stability and even considered to be bench stable.[273-274]

The synthetic procedure was modified to prevent the rapid decomposition of the diazonium salt. Instead of sulfonic acid, *p*TsOH was employed. Furthermore, sodium nitrite was substituted with *t*BuONO. By changing the reagents, diamine **91** was successfully converted. Purification of the crude product afforded the targeted azide **92** in a yield of 38% (Scheme **35**).

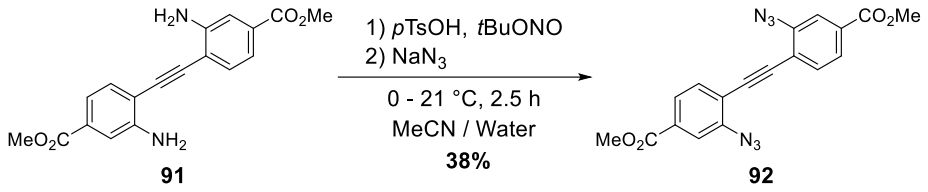

Scheme 35: Synthesis of azide **92** *via* diazotization-azidation of diamine **91**. The diazonium salt was formed *in situ*.

As discussed in Chapter **2.1.1**, chemical conversions simultaneously at more than one reaction center can result in poor overall yields even though the yield per reaction can be drastically better. Calculating the yield for each amine by applying *equation 1* resulted in a yield of 62%.

The carboxylic acid, crucial for the MOF synthesis, was prepared *via* saponification. Therefore, azide **92** was treated with lithium hydroxide for four days in a mixture of water, methanol and THF. The precipitate formed was collected by filtration and the crude product was purified by several washing steps with water and methanol to remove inorganic residue. Drying the product under high vacuum afforded the diazido tolane dicarboxylic acid (**DATDC**, **80)** in a yield of 76% (Scheme **36**).

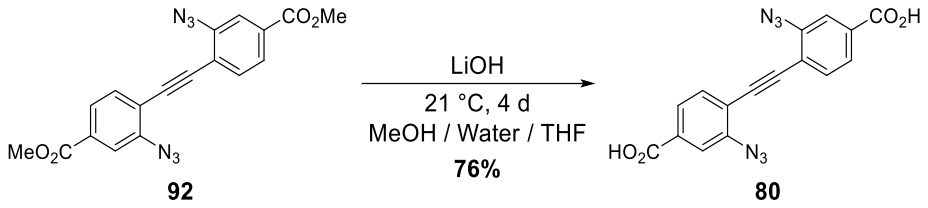

Scheme 36: Saponification of **92** for the synthesis of **DATDC** (**80**).

3.4.3 Preparation of Surface-Mounted Metal-Organic Framework

In a preliminary study, the azide-containing SURMOF was grown on gold substrates. This involved the functionalization of the gold surface with 16-mercaptohexadecanoic acid (MHDA) to form a self-assembled monolayer (SAM). Subsequently, the functionalized surface was sprayed with a methanolic solution of copper acetate followed by a methanolic solution of the azide-functionalized stilbene linker **DASDC** (**78**). Sequential spraying with the copper acetate and stilbene solution resulted in the formation of the SURMOF.[258]

In this chapter only preliminary results are presented. Accordingly, a similar approach for the synthesis of SURMOF in a layer-by-layer approach using LPE is attempted. SURMOF fabrication and characterization was carried out by A. FINGOLO in the WÖLL group at the IFG at KIT. First results could show the successful incorporation of the **DATDC** (**80**) within the SURMOF. Incorporation of the azide-functionalized linker and the crystallinity of the fabricated porous material was confirmed by XRD analysis and FT-IR spectroscopy. The out-of-plane XRD spectrum confirmed the highly crystalline structure of the SURMOF with sharp diffraction reflexes at 5.19°, 10.4° and 15.4°. A schematic illustration of the SURMOF constructed from **DATDC** and the XRD spectrum is shown in Figure **37**. FT-IR spectroscopy revealed a medium intense absorbance band at 2130 cm^{-1} which is in the reported range of the absorbance of the azide group (2160−2120 cm^{-1}) further supporting the successful incorporation of the **DATDC** linker into the SURMOF (Figure **38**).[235]

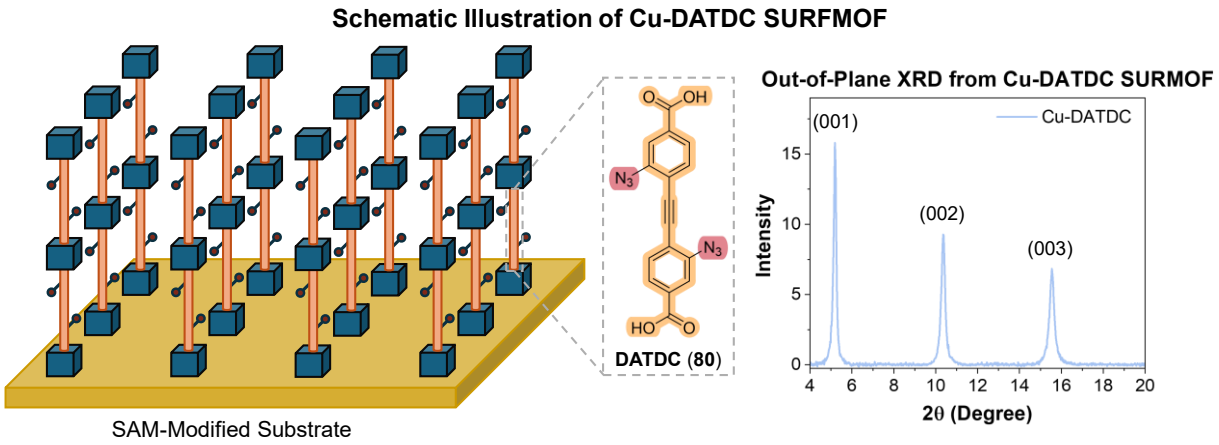

Figure 37: Schematic illustration of the lamella SURMOF structure fabricated from **DATDC** (**80**) (left). Powder XRD of the respective SURMOF (right). Powder XRD data provided by A. FINGOLO (IFG, KIT)

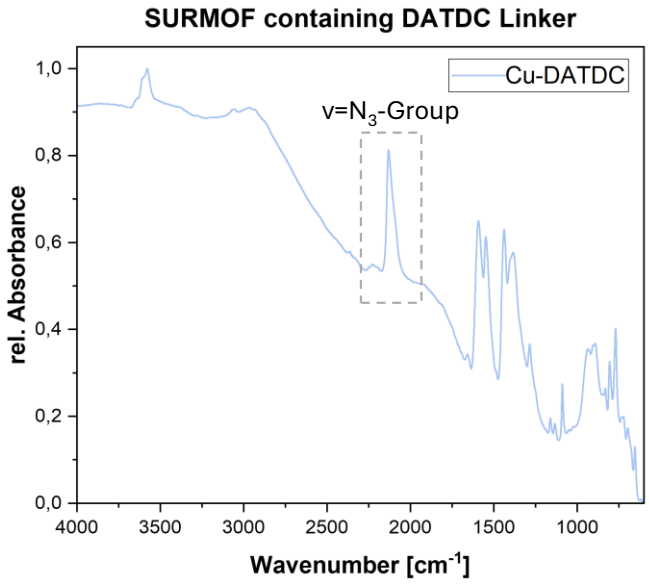

Figure **38**: FT-IR spectrum of SURMOF Cu-DATDC. The absorption band of the azide group is highlighted, confirming the incorporation of the **DATDC** linker. Data provided by A. Fingolo (IFG, KIT).

3.5 Benzil-based Photoinitiators for Applications in 3D Laser Nanoprinting *via* Two-Step-Absorption

Preface. In the following chapter parts have been already evaluated and discussed in "Search for Alternative Two-Step-Absorption Photoinitiators for 3D laser nanoprinting (https://doi.org/10.1002/adfm.202212482)" published in 2022 in Advanced Functional Materials. Part of the discussion will be the photoinitiator synthesis conducted during the framework of this thesis. If results from collaborators are used to compare or draw conclusions, the respective parts are mentioned in the text.

Introduction. Light-induced 3D printing has represented a growing research field in recent years. It is used to print defined three-dimensional objects. 3D laser printing relies on photopolymerization of a monomer and is already widely applied in research fields such as micro-robotics, optics, and life sciences.[275] Currently, several photopolymerizable printing techniques are known, such as stereolithography (SLA),[160] direct laser writing (DLW)[165] and digital light processing (DLP).[174] SLA utilizes a moving laser beam to trace and solidify the desired object's shape within a photosensitive resin bath in a layer-by-layer approach. This process is renowned for producing highly detailed and accurate parts with smooth surface finishes, making it a widely applied technology in industrial applications to fabricate complex components.[160-161] Another method employing a laser beam to print precise objects in a controlled manner is the DLW technique. DLW utilizes a tightly focused laser beam to solidify a photosensitive resin. This technique is known to produce objects with an exceptional resolution, allowing the printing of extremely fine structures in the nanometer range.[276] Unlike other layer-by-layer 3D printing techniques, where solidification of the resin only occurs on the surface, DLW allows the fabrication of 3D objects within the resin material.[165-166, 182] In contrast to the localized laser exposure in SLA and DLW, DLP employs a projected light sheet to cure the entire resin layer simultaneously. 3D objects, printed by DLP can achieve a high resolution, however the resolution of printed objects may not be as precise as objects printed by laser-based SLA or DLW systems.[174, 277-278] While laser printing has found widespread application in industry, a significant drawback lies in the light source itself. Most commercial systems utilize lasers emitting within the ultraviolet (UV) range, typically between 300–400 nm. However, recent research has shifted towards the usage of lasers with wavelengths in the visible light region. Those lasers possess significant benefits compared to systems employing light in the UV range, since they are more eco-friendly due to reduced energy consumption and are generally more cost-effective.[184] Two-Photon-Absorption (2PA)

represents an approach to address the limitations of conventional UV-based 3D printing. 2PA is an optical phenomenon where a molecule simultaneously absorbs two photons, each possessing lower energy than the energy required for a single-photon transition. The absorption of the first photon excites the molecule to a virtual excited state. This virtual state is extremely short-lived and only exists within the focal volume of the laser beam. Simultaneous absorption of a second photon within this localized region excites the molecule further resulting in a real excited state. This unique mechanism enables the precise, three-dimensional fabrication of micro- and nanostructures with exceptional spatial resolution.[179, 279-280] Another method used is two-step absorption (2SA). WEGENER and co-workers first reported 3D laser printing *via* 2SA. They employed **PETA** as monomer and **BZ** as photoinitiator, in addition to a radical scavenger such as **TEMPO** to trap radicals produced from unproductive excited states. In contrast to the previously described 2PA mechanism in 2SA, the virtual excited state is replaced by a real excited state, which not only exists in the focal volume of the laser beam and therefore has a much longer lifetime. Further excitation of the real excited state results in the excited state from which the photopolymerization is initiated. Using 2SA allows the printing of structures with high resolution in the nanometer scale.[4, 13, 184, 187, 281]

Photoprintable inks used in laser printing typically consist of one or more monomers, either inherently photopolymerizable or formulated with a photoinitiator (PI) to initiate the polymerization process. Absorption of a photon with sufficient energy excites the PI to an excited state. This excited state subsequently interacts with the monomer, initiating the photopolymerization reaction through either a radical or cationic mechanism (Figure **39**).[173]

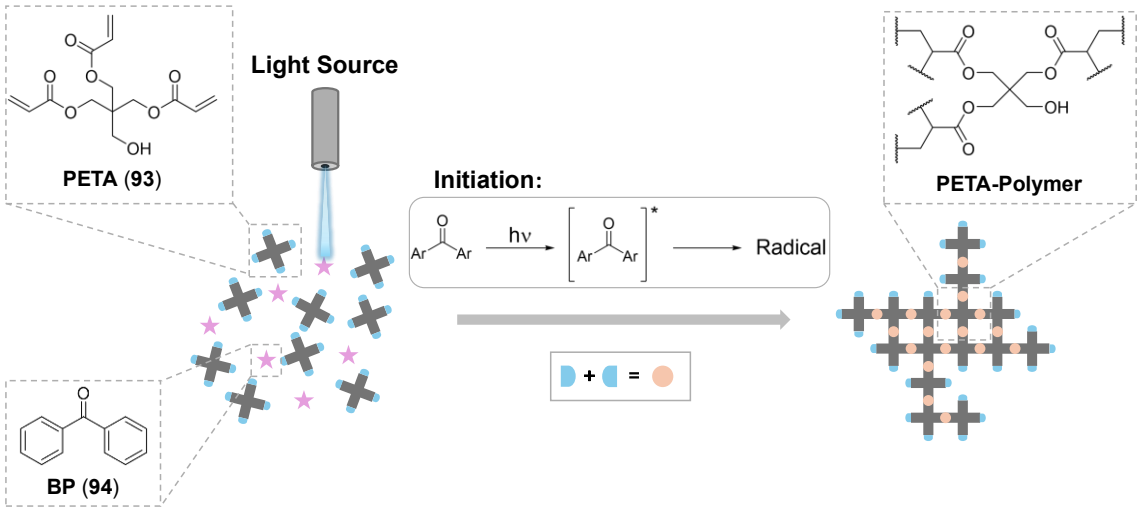

Figure 39: Schematic overview of light-induced radical polymerization. Adapted from literature.[282]

PIs employed in 3D laser printing include diketones such as benzil (**BZ**, **16**) and its derivatives, as well as ketones such as benzophenone (**BP**, **94**) and Irgacure 1733 (**Irg1733**, **95**). Frequently utilized monomers comprise acrylates and methacrylates, such as pentaerythritol triacrylate (**PETA**, **93**) and triethylene glycol dimethacrylate (**TEGDMA, 96**), as well as epoxides such as 3,4-epoxycyclohexylmethyl-3,4-epoxycyclohexanecarboxylate (**EPOX, 97**) (Figure **40**).[173, 185, 282]

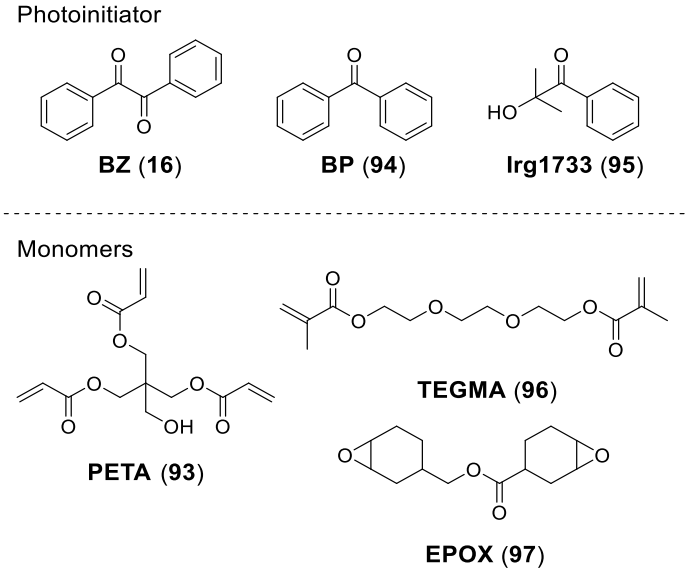

Figure 40: Commonly applied photoinitiators **BZ** (**16**), **BP** (**94**) and **Irg1733** (**95**) (top). Monomers used in photopolymerization include acrylates such as **PETA** (**93**), methyacrylates such as **TEGMA** (**96**) and epoxides like **EPOX** (**97**) (bottom).

Before initiating the printing process, several critical factors concerning the PI must be considered. A crucial parameter is the solubility of the initiator in **PETA** (**94**). Insufficient solubility of the PI within the resin can lead to significant shrinkage of the printed object. This phenomenon arises from uneven distribution and subsequent migration of the PI during the printing and curing process, resulting in variations in the degree of polymerization.

The following project aimed to synthesize benzil-based photoinitiators for application in 3D laser nanoprinting *via* Two-Step-Absorption (2SA) with PETA as a monomer.

3.5.1 Synthesis of Photoinitiators

Symmetrical and asymmetrical PIs were targeted to investigate whether substituents on the **BZ** (**16**) core enhances the solubility in **PETA** (**93**) which could result in the fabrication of structures with higher resolution. Therefore, three different PIs were prepared with polar residues including hydroxyl and carboxyl groups. Asymmetrical PIs were synthesized in a two-or three-step route depending on the PI.

Intermediates **100** and **102** were obtained *via* straightforward SONOGASHIRA cross-coupling reaction using an adapted procedure reported in literature.[283] Therefore, the commercially available starting materials 4-iodophenol (**99**) and methyl 4-iodobenzoate (**101**) were reacted with phenylacetylene (**98**) under palladium catalysis (Scheme **37**). Purification of the crude products yielded the tolan intermediates **100** and **102** in yields of 62 and 82% respectively.

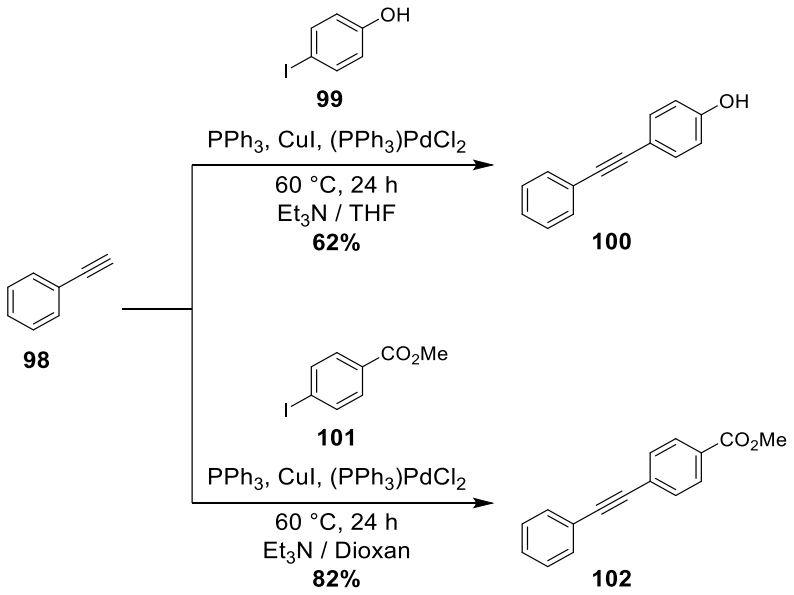

Scheme 37: Synthesis of tolan intermediates **101** and **103** *via* SONOGASHIRA cross-coupling.[283]

Subsequently, the intermediates **100** and **102** were oxidized using palladium dichloride in DMSO (Scheme **38**).[284] Purifying the crudes *via* column chromatography resulted in the targeted PIs 4-hydroxy benzil (**HBZ**, **103**) and methyl ester **104** in yields of 82 and 85%, respectively.

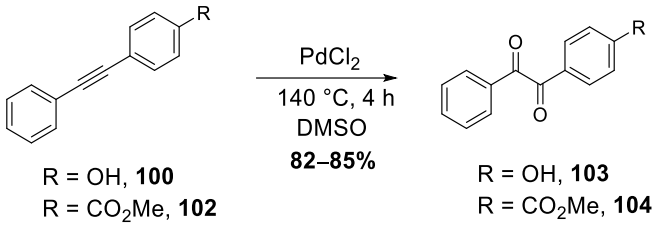

Scheme 38: Palladium catalyzed oxidation to synthesize **HBZ** (**103**) and methyl ester **104**.[284]

Since the target compound possesses the carboxylic acid functionality, methyl ester **104** was subjected to ester hydrolysis under acidic conditions. Therefore, **104** was treated with sulfonic acid in acetic acid for 16 hours (Scheme **39**). The formed precipitate was collected by filtration, washed, and dried under vacuum to isolate **CBZ** (**105**) in a yield of 87%.

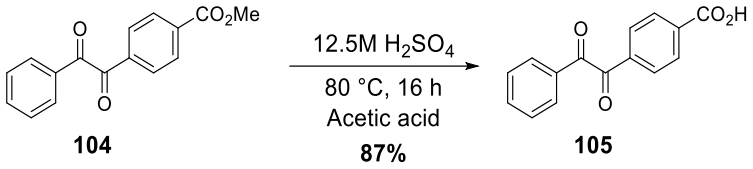

Scheme 39: Hydrolysis of methyl ester **10**4 under acidic conditions to form the **CBZ** (.

The symmetrical 4,4'-dicarboxy benzil (**DCBZ**, **19)** was prepared in a three-step synthesis route according to a protocol reported in the literature.[285] Commercially available methyl 4-formylbenzoic acid (**106**) was subjected to a benzoin condensation employing potassium cyanide. Filtration of the precipitate gave the benzoin **107** in a yield of 58%. Oxidation of **107** to benzil derivative **108** was performed using hydrobromic acid in DMSO, giving **108** in a yield of 84% (Scheme **40**).

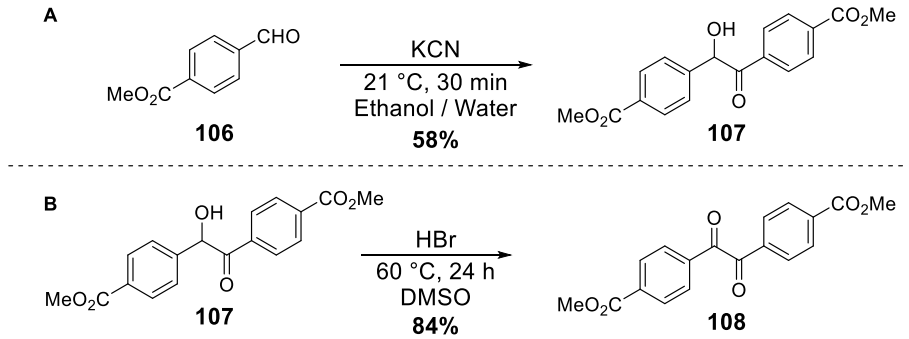

Scheme 40: A) Preparation of benzoin **107** *via* benzoin condensation of aldehyde **107**. B) Oxidation of benzoin **107** to benzil derivative **108** using hydrobromic acid.[285]

Hydrolysis of ester **108** under acidic conditions afforded **DCBZ** (**109**) in a yield of 95% (Scheme **41**).

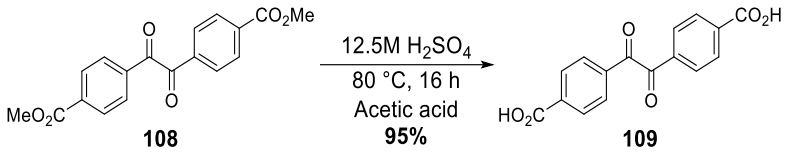

Scheme 41: Hydrolysis of methyl ester **108** to **DCBZ** (**109**) under acidic conditions.[285]

3.5.2 Application of Photoinitiators in 3D Laser Nanoprinting

Printing experiments of the respective PI were conducted by A. VRANIĆ from the BRÄSE research group at the Institute of Organic Chemistry (IOC) at KIT, in collaboration with the facilities provided by the WEGENER group at the Institute of Applied Physics (APH) at KIT.

This project investigated two different absorption mechanisms namely: the two-step one-color and the two-step two-color mechanism. In the two-step one-color mechanism, two photons with identical wavelengths (405 nm) are absorbed, whereas in two-step two-color the absorption of photons with different wavelengths (405 and 640 nm) are involved. At the beginning of this project, only one example for each two-step absorption mechanism was reported, namely benzil (**16**) (two-step one-color) and biacetyl (**17**) (two-step two-color), respectively. Therefore, all synthesized PIs within this study were evaluated for their suitability in 3D laser nanoprinting *via* 2SA.

Inks for 3D printing were prepared by dissolving the respective PIs **103**, **105**, and **109** in **PETA**. As noted, good solubility and an even distribution of the PI within the liquid monomer is crucial for successful printing experiments. Given that **DCBZ** exhibited poor solubility in the printing ink, its evaluation as PI was not feasible. In contrast, both **HBZ** and **CBZ** demonstrated good solubility in **PETA**, prompting further investigations into their suitability as **PIs** for 3D laser nanoprinting applications. Each PI was dissolved in the acrylic monomer, and **TEMPO** was added as scavenger. Standardized ratios for 3D laser printing experiments *via* 2SA were used for the preparation of the inks. In each photo ink, the respective **PI** and **TEMPO** were dissolved in **PETA**, with a concentration of 100 mM for the PI and 50 mM for **TEMPO**.

The printability of the resins was investigated *via* point-exposure experiments. Here, the dependence of the laser power is plotted against the exposure time on a double-logarithmic scale. In this experiment a dot is printed for a specific exposure time and the respective threshold

laser power *p*(405) which leads to the solidification of the resin. After the development of the sample, the printed dots are investigated under a microscope.

Figure **41** depicts the results of the point-exposure experiments for **HBZ** and **CBZ**. The linearity or non-linearity of the graph provides crucial information about the absorption mechanism. A linear relationship characterized by a slope of 1, indicates a one-photon absorption. In this process, the molecule absorbs a single photon, leading to its excitation. If the slope of the graph is equal to 2, it indicates a quadratic relationship. This is characteristic for two-photon absorption, where the simultaneous absorption of two photons is required to excite the molecule. If the relationship shows a non-linear dependency, a 2SA mechanism is often proposed. In the presented data, the observed relationship between laser power and exposure time exhibits a non-linearity. The increase in the exposure time did not result in a linear decrease of the laser power. Hence, this can be interpreted as a two-step absorption mechanism. However, it should be noted that these statements do not constitute proof of the two-step two-photon mechanism; rather, they are assumptions based on existing literature.[184]

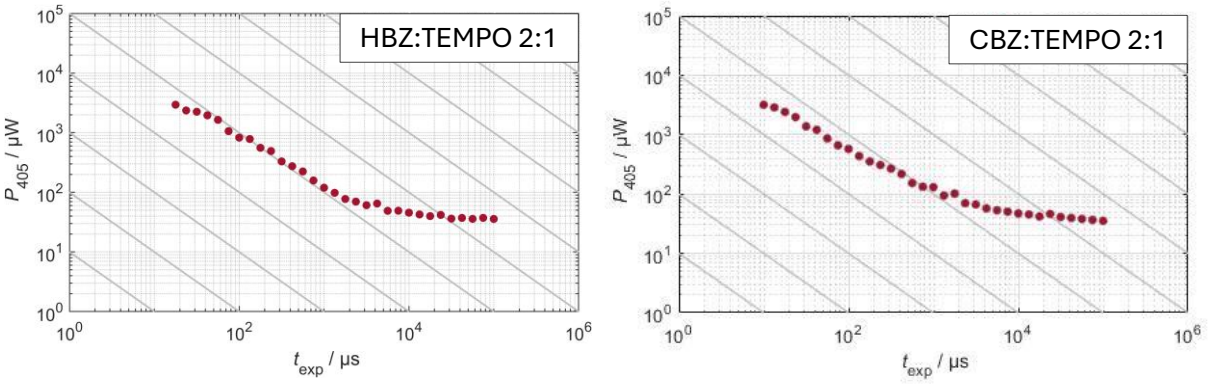

Figure 41: Point-exposure experiments for **HBZ** and **CBZ**. The graphs depict the non-linearity according to two-step absorption. Data provided by A. VRANIĆ (IOC, KIT).

To investigate the feasibility of both PIs in two-step two-color printing, their photoinitiation behavior was evaluated under dual-wavelength irradiation by carrying out a dose test. Results of the dose test for **HBZ** and **CBZ** are visualized in Figure **42**.

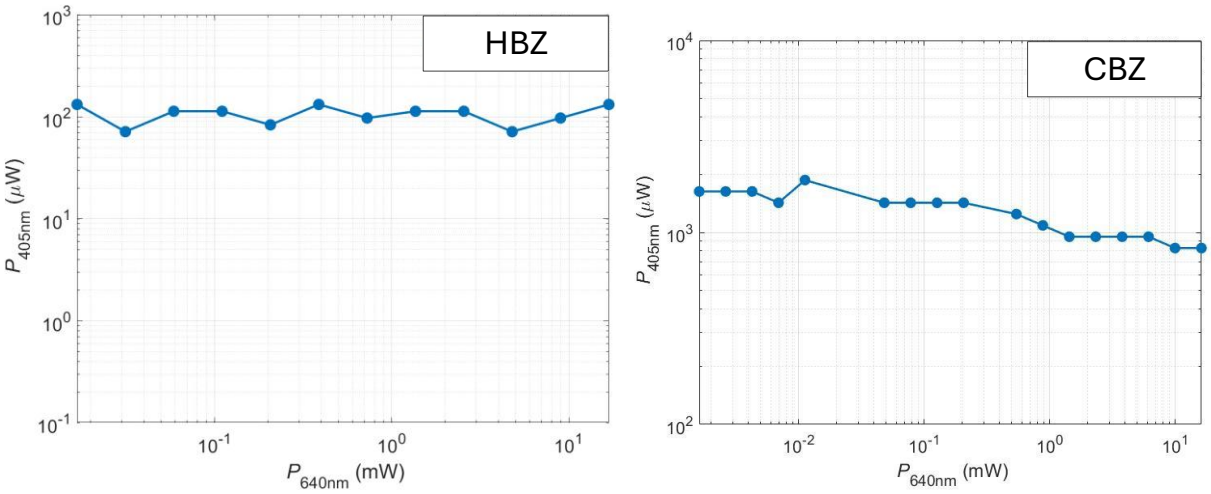

Figure 42: Dose tests of **HBZ** and **CBZ**. The laser power *p*(405) is plotted against *p*(640). Data provided by A. VRANIĆ (IOC, KIT).

Specifically, the printing ink was exposed to two independent laser beams with wavelengths of 405 nm and 640 nm simultaneously, while printing dotted lines with a scan velocity of ν = 100 µm/s. In the experimental setup, multiple job files were printed, in which different laser powers *p*(640) were kept constant and the laser power *p*(405 was increased incrementally in the vertical axis. For each fixed laser power *p*(640), the threshold laser power *p*(405) at which the solidification of the ink occurred was determined by analyzing the printed dotted lines under a dark-field optical microscope using a MATLAB script. The respective laser power *p*(405) and the corresponding red laser power *p*(640) were then plotted on a double logarithmic scale. If the PI can be employed in two-step two-color absorption, the graph should show a decrease of the blue laser power when increasing the red laser power. Figure **42** visualizes the dependency of the blue and red laser power. Both PIs investigated do not show the characteristic dependency between the laser powers expected for two-step two-color absorption. **HBZ** exhibits a rather linear dependency, which suggests a two-step one color absorption. In contrast, **CBZ** shows a slight decrease in the blue laser power, however, the magnitude of this decrease is not sufficient to definitively conclude a two-step two-color absorption mechanism.

Initially, the utilization of **CBZ** and **HBZ** in two-step two-color 3D laser nanoprinting was targeted, based on the results obtained, both PIs do not show the desired two-step two-color absorption behavior. Nonetheless, both PIs are suitable for two-step absorption and tested in 3D laser nanoprinting employing two-step one-color absorption. Therefore, printing

experiments were conducted to compare, whether both PIs perform better than the state-of-the-art PI **BZ**. All structures were printed using a blue laser (λ=405 nm) with a scan velocity of ν = 1 mm/s. The printed structures were cured by immersion of the glass substrate, first in acetone, and second in isopropanol to remove any residual unreacted resin. Subsequently, the structures were investigated *via* SEM analysis. To date, the evaluation of printed structures has primarily relied on subjective optical investigation. Development of standardized analysis procedures is crucial to ensure consistent and reliable evaluation.

Using **HBZ** as initiator resulted in the formation of sharp, well-defined structures without defects. Furthermore, the line thickness was observed to be consistent across the x-, y-, and z-axes, indicating uniform polymerization throughout the structure. Figure **43** shows the image of the structure with the optimal achieved sharpness at a laser power output of 240 µW. The image was captured at a 60° angle of view.

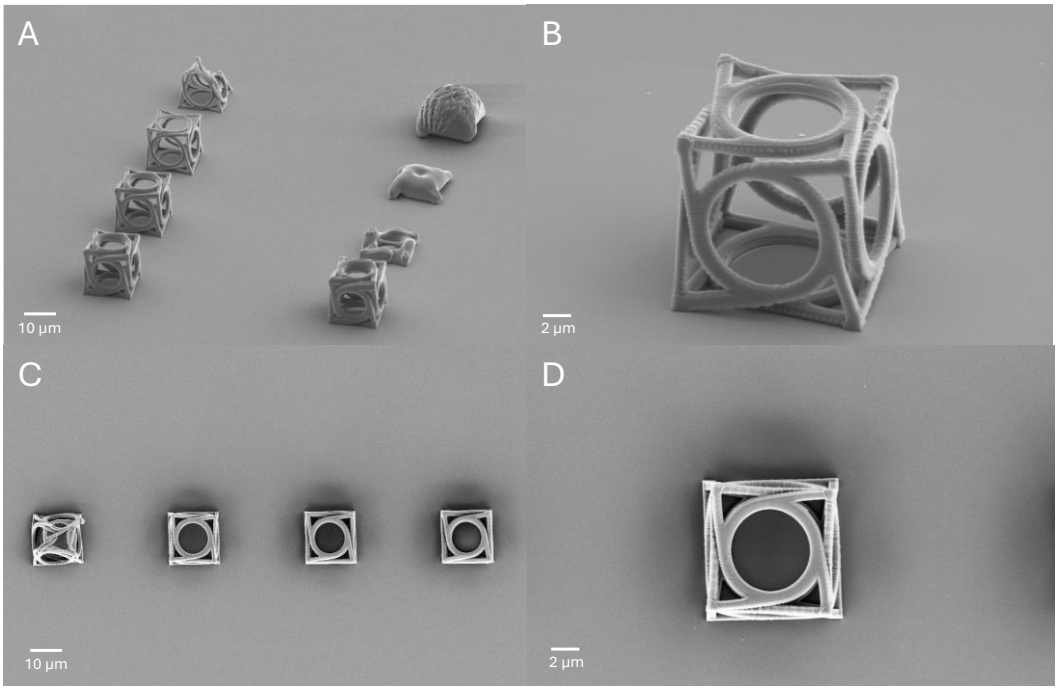

Figure 43: A) SEM-image of printed structures with **HBZ**. The object was printed with *p*(405) = 320, 280, 200, 160 (µW) (top-left to bottom-left) and *p*(405) = 4800, 2400, 800, 400 (µW) (top-right to bottom-right) B) Sharpest print with a power of 240 µW. The SEM images A and B were taken at an angle of 60° C) Top-view of printed structures, printing was performed at *p*(405) = 160, 200, 280, 320 (µW) (left to right) D) Top-view of the sharpest structure printed at 240 µW. Images provided by A. VRANIĆ (IOC, KIT).

Given that both photoinitiators, **CBZ** and **HBZ**, possess *para*-substituted structures and exhibit similar chemical characteristics, it was initially anticipated that they would demonstrate comparable printing performances. However, experimental observations contradicted this expectation. Structures printed using **CBZ** as the initiator showed a significantly lower quality

compared to those printed with HBZ (Figure **44**). These structures exhibited a lack of sharpness and definition, often appearing contorted or incomplete. This behavior suggests potential issues such as overexposure or inconsistent polymerization. Overexposure can occur when the used PI is highly sensitive to the laser power, leading to rapid and uncontrolled polymerization within the focal volume. This overexposure can result in contorted structures, incomplete features, and potentially even damage to the surrounding printing ink. Furthermore, the **CBZ**-initiated polymerization process may exhibit significant spatial variations, leading to inconsistencies in the degree of polymerization in the printed structure. This can result in regions of incomplete polymerization, leading to weakened structures and the observed defects. Further investigations are necessary to investigate the exact cause of these observed differences in printing performance between **CBZ** and **HBZ**.

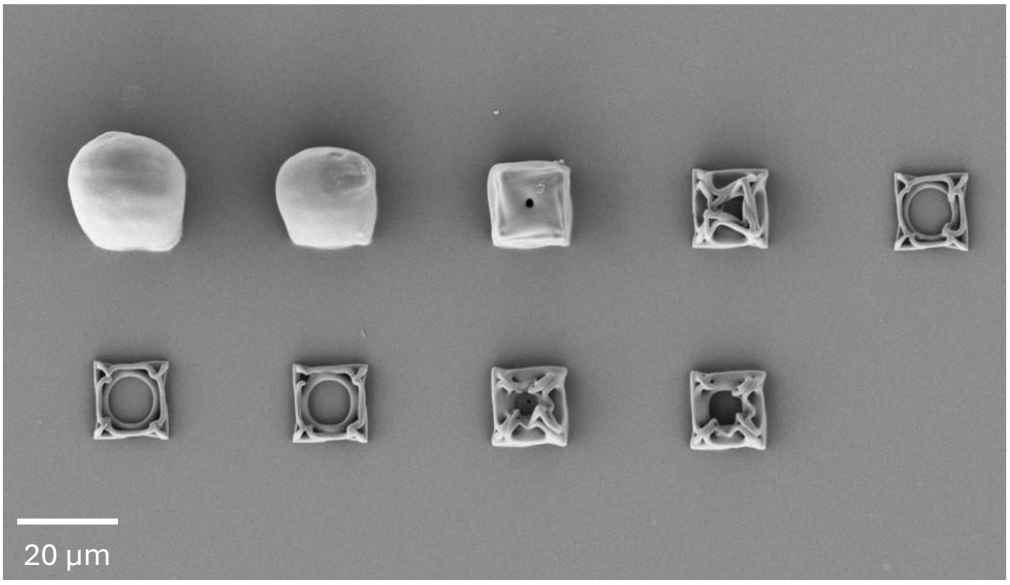

Figure 44: Top-view SEM image of printing attempts with **CBZ**. The image was taken from an angle of 0°. Structures were printed at a power of $p(405)$ = 270, 216, 189, 108, 81, 108, (µW) (top left to right) and $p(405)$ = 135, 162, 175.5 (µW) (bottom left to right). Images provided by A. VRANIĆ (IOC, KIT).

However, as shown in the point-exposure experiment or the dose test, printing in two-dimensional space is not influenced by this occurrence and the initiator would be suitable as PI in two-dimensional printing processes. **HBZ** can be classified as PI comparable to **BZ**, whereas in contrast, **CBZ** is classified as PI not suitable for 3D laser nanoprinting.

4 Conclusion and Outlook

Materials science holds immense potential to address critical challenges facing humanity. The rising global atmospheric CO_2 concentration presents a significant concern among these challenges.[17] Porous frameworks, characterized by their high surface area and exceptional stability, emerge as a highly promising class of materials for reducing this issue.[107, 127, 137, 150, 155] Their unique properties enable applications in gas storage and separation, offering potential solutions for carbon capture and separation.[147-148, 151, 263] Current research has demonstrated the successful employment of inorganic-organic MOFs, as well as purely organic materials like COFs and PIMs, in applications such as storing of CO_2, H_2, and CH_4, and the separation of CO_2 from flue gas generated by the combustion of fossil fuels.[147-149, 155, 286-287]

Additive manufacturing (AM) represents a class of 3D printing techniques enabling the fabrication of tailored objects for specific applications.[157-159] Light-induced 3D printing methods such as stereolithography, direct light processing or direct laser writing which is based on two-photon absorption enabling the printing of structures in die sub-micrometer scale.[160-161, 165, 182, 278] Current research efforts are focused on the development of more cost-effective and environmentally friendlier methods. Recently, WEGENER and colleagues demonstrated the employment of benzil as photoinitiator in a novel printing approach *via* two-step absorption.[184, 288]

During the timeframe of this thesis, five projects were carried out, each aiming for the synthesis and characterization of novel molecules for applications in materials science. In the first project [2.2]paracyclophane was used as building block in the synthesis of PIMs for gas separation applications. The second project aimed to employ this [2.2]paracyclophane derivative to construct several COFs *via* imine-bond formation with aldehydes to examine these novel frameworks. The third project targeted the functionalization of the surface of MOF nanoparticles *via* nitroxide-exchange reaction (NER) as possible approach to selectively modify nanoparticles to improve their suitability in drug delivery applications. Therefore, the integrin recognition RGD-peptide sequence, containing the amino acids arginine, glycine, and aspartic acid was synthesized and subsequently functionalized with a nitroxide to investigate the modification of the nanoparticles. In the fourth project, azido-functionalized tolan linkers for applications in SURMOF fabrication were synthesized to investigate the photochemical decomposition of the azide-groups within the highly structured MOFs environment and lastly, the fifth project targeted the synthesis of benzil-based photoinitiators for applications in 3D laser nanoprinting *via* two-step absorption.

4.1 Polymers of Intrinsic Microporosity containing [2.2]Paracyclophane as Monomer

Summary. Novel mono- and diamino-functionalized [2.2]paracyclophane derviatives were prepared in a three-step synthesis route in reasonable yields ranging from 99% to 29%. The **PCP-PA** (**19**) was utilized in the optimization of the TRÖGERs base formation reaction (Figure **44**). The results obtained were transferred to convert the ***p*PCP-PA** (**18**) into PIMs connected *via* the TB bridging unit to generate the polymeric ***p*PCP-TB** in a reasonable yield of 35% (Figure **45**).

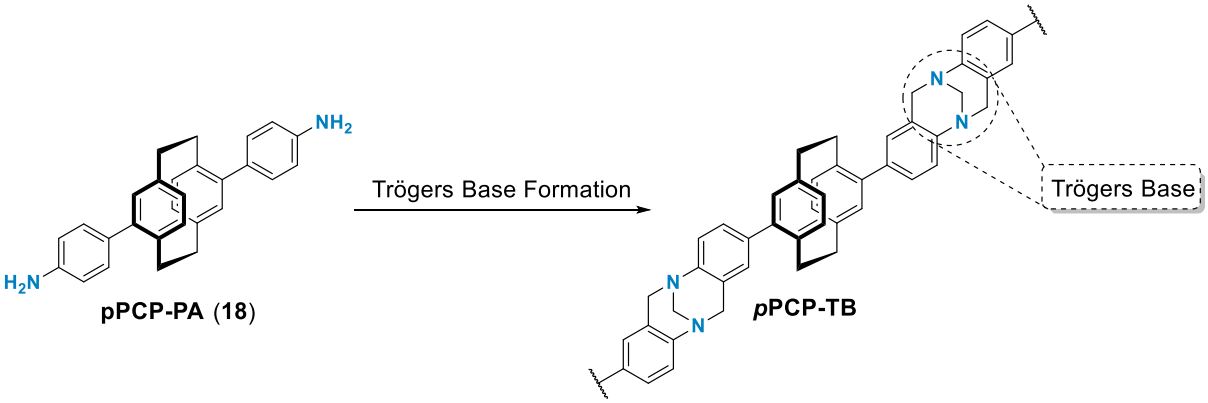

Figure 45: Synthesis of PCP-containing polymer of intrinsic microporosity *via* TRÖGERS base formation.

The successful formation of the polymer was confirmed in collaboration with M. CARTA (University of Swansea) and A. ZUPANC (University of Ljubljana). The polymers were characterized by solid-state ^{13}C and ^{15}N NMR spectroscopy and FT-IR spectroscopy and SEM analysis. ^{15}N NMR analysis revealed a single resonance at 41.9 ppm, indicating the formation of a single nitrogen species, which was anticipated for the successful TB polymer formation. ^{13}C NMR spectroscopy exhibited signals in the range of 49.1–67.5 ppm, characteristic of the CH_2-groups within the TB bridging unit. Additionally, signals observed in the aromatic region (120–150 ppm) and at approximately 33.9 ppm were assigned to the aromatic core and the CH_2-methylene bridge of the [2.2]paracyclophane moiety, respectively, further supporting the successful polymer formation. SEM analysis of the polymers revealed the anticipated microporous surface.

FT-IR analysis confirmed the presence of the characteristic *C-N* stretching vibration in the region between 1300–1200 cm^{-1}, consistent with literature reports for PIMs. The porous nature of the synthesized PIM was confirmed by SEM, which revealed a surface morphology characterized by the presence of pores with diameters ≤ 1 µm.

To evaluate the potential of the prepared polymer for gas storage or gas separation applications, its gas adsorption properties and thermal stability were investigated. Gas adsorption-desorption isotherms of CO_2 and N_2 were measured at 77 K, 273 K, and 298 K, respectively, to determine the porosity and surface area. The surface area of ***p*PCP-TB** was found to be 233 m^2/g which was unexpected since surface areas of existing PIMs like **PIM-EA-TB** (S_A=1028 m^2/g) are an order of magnitude higher. NLDFT analysis provided insights into the pore size distribution, revealing a microporous material with pore diameters predominantly in the range of 3–9 Å. TGA was performed to assess the thermal stability of the polymer, demonstrating a decomposition temperature of 456 °C, which is accordance to reported PIMs. Compared to the non-extended **PCP-TB**, ***p*PCP-TB** showed a slightly higher decomposition temperature.

Furthermore, selectivity studies of ***p*PCP-TB** were performed. Given that ***p*PCP-TB** exhibited a moderate CO_2 adsorption capacity of 0.616 mmol/g at 298 K and negligible N_2 adsorption at this temperature, its potential application in gas separation was investigated. The CO_2/N_2 selectivity was determined using Ideal Adsorbed Solution Theory (IAST), yielding a value of 47.5 for ***p*PCP-TB**, comparable to values reported for materials with similar chemical structures. The adsorption mechanism was further examined using Q_{ST} analysis. For ***p*PCP-TB**, a Q_{ST} value of 32.6 kJ/mol was determined, indicating a physisorption mechanism. This is advantageous for gas separation processes, as the weak interaction between the gas molecules and the polymer surface facilitates the efficient removal of the adsorbed gas without requiring significant energy input. To sum up, it could be demonstrated that ***p*PCP-TB** is a promising candidate in flue gas separation applications.

Outlook. Investigations of the gas separation properties of ***p*PCP-TB** were only determined in theoretical experiments by IAST. Since gas adsorption and desorption behavior can differ under practical application conditions, further investigations such as flue gas separation in a test facility is needed to evaluate the polymer in gas separation applications.

In addition, GPC analysis should be applied to investigate whether the higher decomposition temperature of 456 °C measured for ***p*PCP-TB** is due to a higher degree of polymerization compared to **PCP-TB** (decomp. 435 °C).

From a chemical perspective, future investigations should incorporate different bridging units within the diamino [2.2]paracyclophane building block. A significant limitation of the extended building block was observed to be the free rotation around the aromatic *C-C* bond, which facilitated efficient polymer packing. Incorporating more sterically demanding bridging groups

can restrict this rotational freedom, thereby hindering efficient polymer packing and potentially leading to the formation of polymers with larger pores and enhanced gas adsorption properties.

4.2 Covalent Organic Frameworks containing Paracyclophane

Summary. The diamino [2.2]paracyclophane derivative ***p*PCP-PA** (**18**) was utilized to prepare **COF-TFPA**, **COF-BTT**, **COF-TFTB**, **COF-TFTA** and **COF-TP** were prepared *via* acid-catalyzed ambient temperature synthesis by combining the diamine **18** with the respective aldehydes (**30**-**34**) in yields ranging from 16-52% (Figure **46**). The subsequent addition of acetic acid resulted in the formation of an orange to light yellow solid, which was insoluble in common organic solvents such as dichloromethane, ethyl acetate, ethanol, and water. COFs were isolated in yields ranging from 16-52%. The respective aldehydes **TFPA** (**30**), **BTT** (**31**), **TFTB** (**32**), and **TFTA** (**33**) were prepared according to literature-reported procedures in yields ranging from 7% to 92%. **TP** (**34**) was purchased from a commercial chemical supplier.

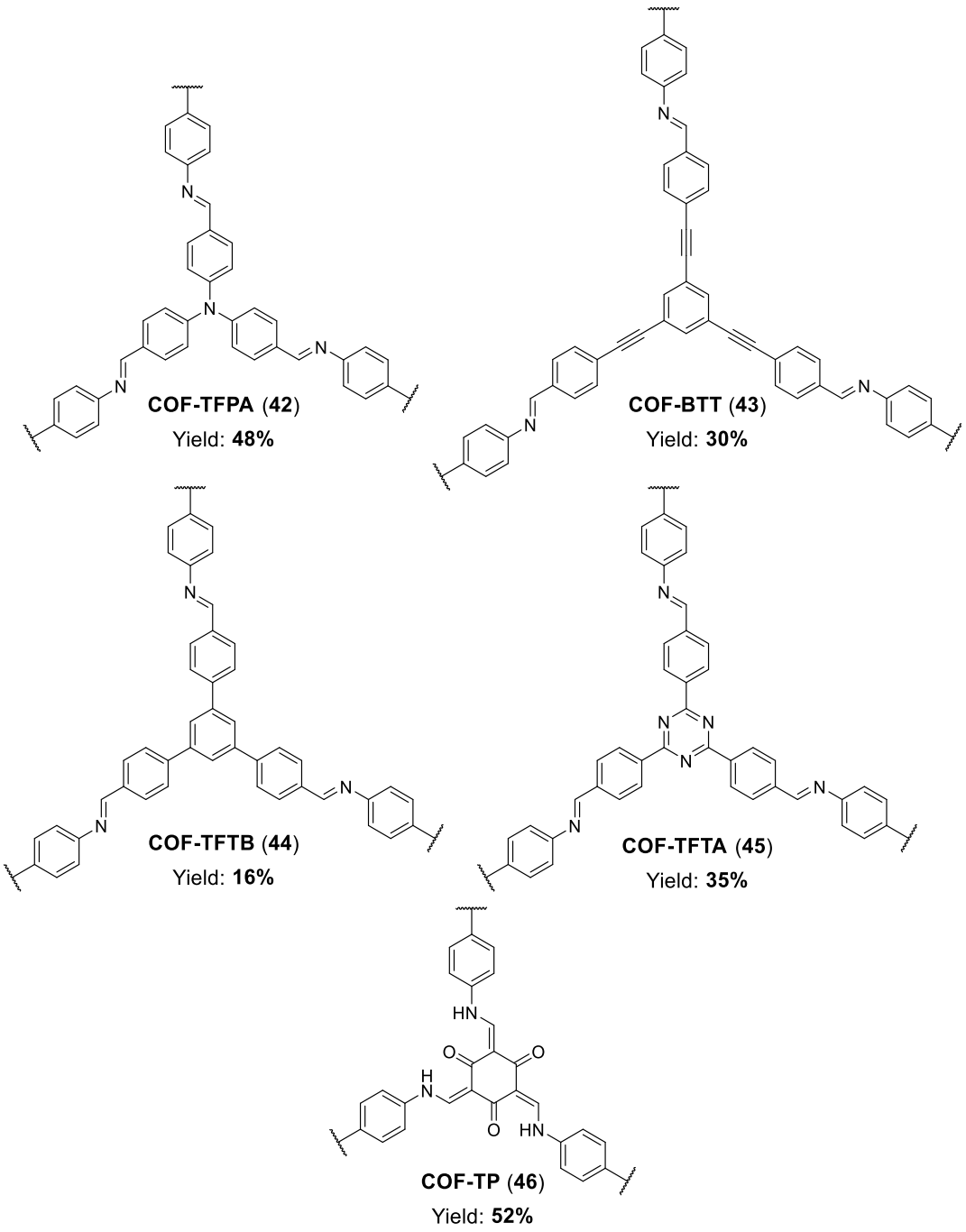

Figure 46: Overview of covalent organic frameworks prepared *via* acid-catalyzed synthesis.

The successful formation of the imine linkages within the COFs was confirmed by FT-IR spectroscopy. The FT-IR spectra of the respective COFs were compared to those of their corresponding monomers. The presence of prominent absorption bands confirmed the successful framework formation. Given that all COFs are connected *via* imine-linkage, the characteristic vibration band of the *C=N* stretching vibration observed within the region of 1690–1640 cm^{-1} was analyzed. Furthermore, the absence of the *C=O* stretching vibration indicative for carbonyl groups, typically found in the range of 1740–1720 cm^{-1}, provided

additional evidence for the successful COF formation. FT-IR analysis of **COF-TFPA**, **COF-BTT**, **COF-TFTB**, and **COF-TFTA** revealed the absence of the characteristic carbonyl absorption band, while the presence of the imine stretching vibration was observed in all cases, indicating the successful framework formation. Furthermore, the absence of the *N-H* stretching vibration of the primary amine in all COF spectra provided further evidence for the successful formation of the imine linkages within the framework structures.

A different interpretation of the FT-IR spectrum could be drawn for **COF-TP**. The anticipated absence of the *C=O* band originating from the carbonyl group and the *N-H* stretching vibration of the primary amine in the FT-IR spectrum of **COF-TP** indicated the complete consumption of the starting materials. However, no absorption band characteristic for the *C=N* imine vibration was observed in the region of 1690–1640 cm^{-1}. Furthermore, the spectrum did not exhibit any broad absorption bands that would be expected for *OH* groups, which are typically present in COFs with significant amounts of hydroxyl groups. These findings can be attributed to the iminol-keto-enamine tautomerism, a unique characteristic of **TP** (**34**). Due to intramolecular hydrogen bonding, the absorption band of the formed carbonyl group is shifted to lower wavenumbers, appearing at approximately 1600 cm^{-1}. Based on these spectroscopic observations, the successful formation of the **COF-TP** framework was confirmed.

Elemental analysis was carried out to gain a deeper understanding of the chemical composition of the formed COFs. The experimentally determined carbon values exhibited deviations from the theoretical values, with the most significant discrepancy observed for **COF-TP**, with a value of 6.89%. This discrepancy can be attributed to the adsorption of atmospheric water within the porous framework, which can lead to a lower carbon content even if the framework is successfully formed. EA revealed moderate deviations in the experimentally determined nitrogen values, with the most significant deviation observed for **COF-TFTA** with a value of 2.10%. These deviations can be attributed to unreacted end-groups within the framework structure. In contrast to the carbon and nitrogen values, the experimentally determined hydrogen values generally showed good agreement with the theoretical values.

Outlook. Isolated yields for the preparation of COFs were reasonable compared to those reported for state-of-the-art COFs. Nevertheless, optimization of reaction conditions remains essential to achieve satisfactory yields for PCP-containing COFs. While preliminary results suggest successful COF formation, further characterization of the solids is required to elucidate the structure. In addition to FT-IR spectroscopy, solid-state ^{13}C and ^{15}N NMR spectroscopy should be employed to confirm imine-bond formation and incorporation of the

[2.2]paracyclophane unit. X-ray powder diffraction (XRD) analysis should investigate whether the samples exhibit a crystalline structure, providing further confirmation of successful COF synthesis. Furthermore, given the potential of porous materials in applications such as gas storage and separation, the gas adsorption and desorption properties of the COFs should be evaluated. Specifically, BET theory should be applied to determine the surface areas and pore volumes.

4.3 Biofunctionalization of Metal-Organic Framework Surface *via* Nitroxide-Exchange Reaction

Summary. To functionalize the MOF nanoparticle surface *via* NER, a nitroxide-functionalized RGD-peptide **70** was synthesized using solid-phase peptide synthesis in a yield of 39%. The nitroxide **TPCR** (**52**) was synthesized separately from readily available starting material triacetonamine (**47**) *via* a four-step synthetic route with yields ranging from 35% to 59%.

Confirmation of nitroxide radical formation was achieved *via* EPR spectroscopy, further supported by FT-IR spectroscopy and mass spectrometry. The EPR spectrum exhibited a resonance at g=2.00603, consistent with the reported g-value for TEMPO (g=2.0056). Hyperfine coupling to the nitrogen nucleus was observed, with a coupling constant of 40 mHz.

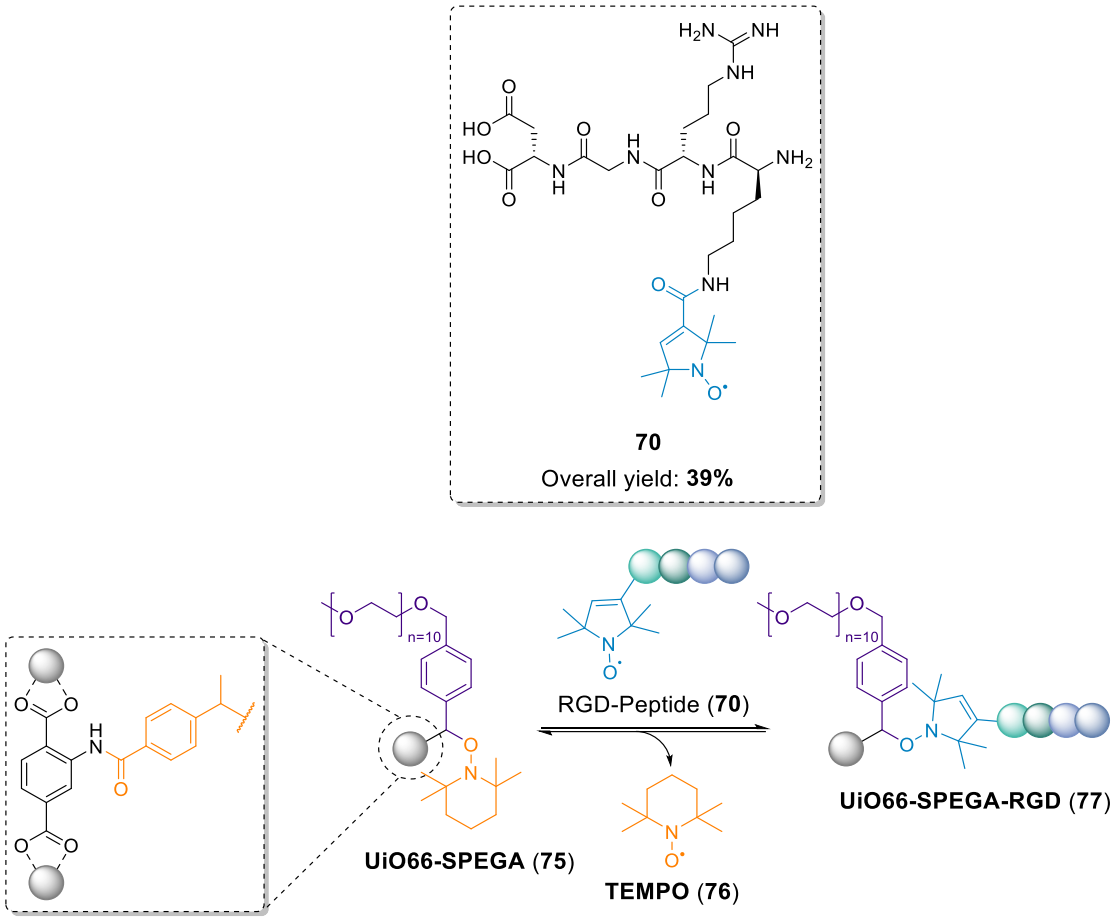

Figure 47: Surface modification of **MOF NP** *via* nitroxide-exhange reaction with the synthesized nitroxide-functionalized peptide **70**. Nitroxide **TPCR** (**52**) attached to the RGD-sequence is colored blue.

The surface modification of the MOF nanoparticles was carried out in collaboration with I. WAGNER of the TSOTSALAS group (Figure **47**). Successful functionalization of the MOF nanoparticles was confirmed by ToF-SIMS. The detection of characteristic RGD-peptide fragments in the ToF-SIMS spectra provided evidence of successful surface modification. In summary, the successful surface modification of MOF nanoparticles with the RGD peptide was achieved. This methodology holds promise for enabling cell-specific delivery of encapsulated small molecules.

Outlook. Preliminary results suggest successful surface modification of the MOF nanoparticles *via* nitroxide exchange reaction (NER). Given the association of integrins with various pathologies, including cancer,[289] future studies should focus on evaluating the efficacy of RGD-functionalized MOF nanoparticles in *in vitro* assays. Specifically, their potential as cell-specific drug delivery vehicles for anti-cancer therapeutics should be investigated.

4.4 Organic Azides as Linker for Metal-Organic Frameworks

Summary. WÖLL and colleagues previously investigated the photochemical decomposition of azides and the characterization of the resulting products within a SURMOF. Utilizing an azido-functionalized stilbene linker for SURMOF synthesis, they observed that photolysis of the azide moiety resulted in the formation of undesired side products due to an intramolecular cyclization reaction between the generated nitrene and the adjacent *C*=*C* bond. In the present thesis, two novel azido-functionalized tolan-based MOF linkers **MATDC** (**79)** and **DATDC** (**80**) were prepared in reasonable overall yields of 33% and 14% as replacements for the already investigated stilbene linker **DASDC** (**78**) (Figure **48**). Both linkers should be incorporated into a SURMOF to investigate the photochemical decomposition of the azide moiety within the highly structured MOF. The unwanted intramolecular cyclization observed during decomposition experiments employing **DASDC** (**78**) as MOF linker is expected to be suppressed by the utilization of both tolan linkers.

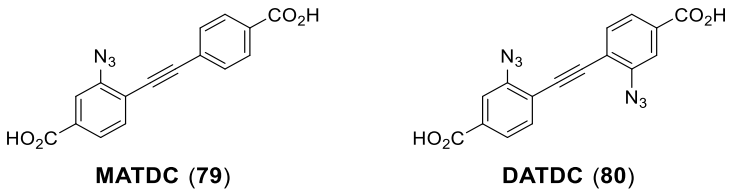

Figure 48: Synthesized azido-functionalized tolan linkers **MATDC** (**79**) and **DATDC** (**80**) for applications in SURMOF fabrication.

Outlook. Currently, the fabrication of SURMOFs is under investigation by A. FINGOLO within the WÖLL group. Preliminary results indicate the successful synthesis of a SURMOF exhibiting a lamellar structure. To reduce undesired side reactions, the incorporation of a second linker is targeted. This co-linker strategy aims to establish a pillar-layer architecture within the SURMOF, thereby increasing the spatial separation between azide functionalities which should support the prevention of the unwanted ring cyclization after the photochemical nitrene formation.

4.5 Benzil-based Photoinitiators for Applications in 3D Laser Nanoprinting *via* Two-Step Absorption

Summary. The synthesis of benzil-based photoinitiators exhibiting enhanced solubility in pentaerythritol triacrylate (**PETA**, **90**) for application in two-photon absorption 3D printing was targeted. Three distinct benzil derivatives **HBZ** (**103**), **CBZ** (**105**) and **DCBZ** (**109**) were synthesized *via* either cross-coupling reactions followed by oxidation or benzoin condensation (Figure **49**).

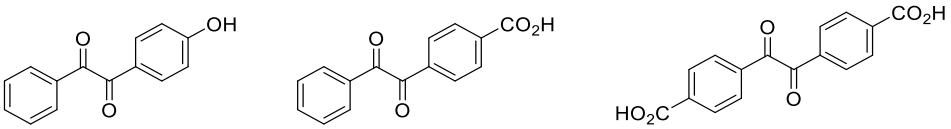

Figure 49: Synthesized photoinitiators **HBZ**, **CBZ** and **DCBZ** for applications in 3D laser printing *via* two-step absorption.

In collaboration with A. VRANIĆ, the synthesized photoinitiators were evaluated in 3D printing experiments. **DCBZ** proved to be insoluble in the resist and was therefore excluded from further testing. **HBZ** and **CBZ** exhibited suitable solubility and were subsequently assessed in printing experiments. Point exposure experiments conducted with both photoinitiators demonstrated a non-linear dependence of polymerization on laser intensity, consistent with the anticipated two-photon absorption mechanism. Dose tests were carried out for both initiators. Evaluation of the results confirmed the suitability of both **HBZ** and **CBZ** for two-photon one-color 3D printing.

Both photoinitiators were further evaluated in 3D printing experiments to assess their performance relative to the benchmark initiator, benzil. Printing experiments were carried out in collaboration with A. VRANIĆ (IOC, KIT). The resulting printed structures were characterized by SEM (Figure **50**). Printing experiments using **HBZ** yielded sharp, well-defined, and defect-free structures. Moreover, consistent line thickness was observed in all directions, indicating a uniform polymerization. Structures printed using **CBZ** showed significantly lower resolution and quality compared to those obtained with **HBZ**. The printed objects exhibited a lack of sharpness and definition. However, as shown in the point-exposure experiment and the dose test, only the printing in 3D is influenced by this occurrence and **CBZ** would be a suitable as photoinitiator in 2D.

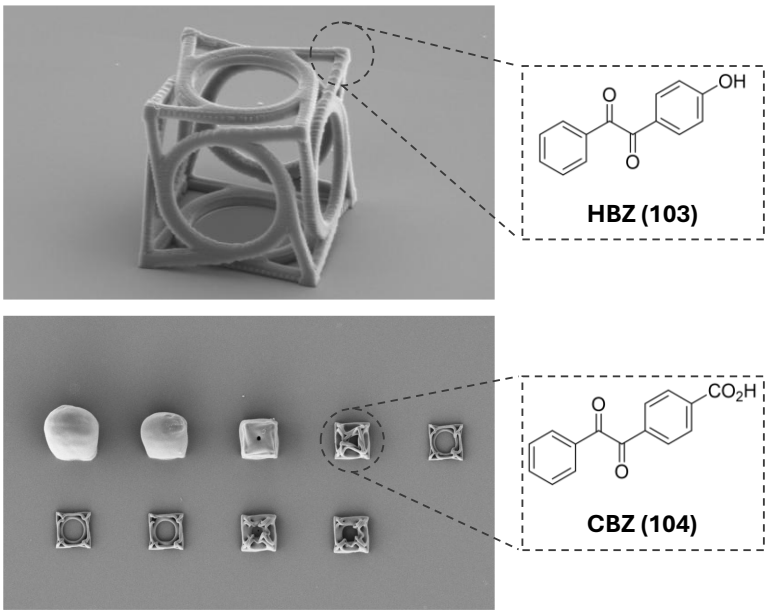

Figure 50: 3D structures printed with synthesized photoinitiators **HBZ** and **CBZ**.

In conclusion, both initiators **CBZ** and **HBZ** can be utilized in photopolymerization printing techniques. The performance of **HBZ** in 3D printing experiments can be compared to the state-of-the-art photoinitiator benzil, whereas **CBZ** can be classified as initiator in 2D printing techniques and is not suitable in 3D laser nanoprinting.

Outlook. The presented results raise several open questions that require further investigations. Specifically, the radical generation mechanism of the initiator remains unclear. Initial investigation suggested radical formation *via* Norrish Typ I fragmentation of **BZ**.[184] However, the actual initiation mechanism is still not fully understood. A combination of theoretical and experimental approaches such as trapping and analyzing of the generated radical is required to investigate the radical generation mechanism following two-photon excitation.

Furthermore, printed structures have been evaluated primarily through subjective optical inspection, the development of standardized analytical procedures based on artificial intelligence is essential for consistent and reliable evaluation. Additionally, the underlying cause of the observed discrepancies in printing performance and quality between **CBZ** and **HBZ** needs further investigation. Employing different acrylates or methacrylates as printing inks could investigate whether the poor solubility of **CBZ** within the ink led to the observed discrepancies in printing quality.

5 Experimental Section

5.1 General information

5.1.1 Materials and Methods

The starting materials, solvents, and reagents were purchased from ABCR, ACROS, ALFA AESAR, APOLLO SCIENTIFIC, CARBOLUTION, CHEMPUR, FLUKA, FLUOROCHEM, MERCK, RIEDEL-DE HAËN, SIGMA ALDRICH, STREM, TCI, or THERMO FISHER SCIENTIFIc and used without further purification unless stated otherwise.

The starting materials, (dry) solvents, and reagents were purchased from ACROS ORGANICS, FISHER SCIENTIFIC, ABCR, ALFA AESAR, MERCK, SIGMA-ALDRICH, ROTH, or RIEDEL-DEHAËN and used without further purification. All solvents were purchased in HPLC grade. Solvents of technical quality were purified by distillation or with the solvent purification system MB SPS5 (acetonitrile, dichloromethane, diethyl ether, tetrahydrofuran, toluene) from MBraun.

All reactions with reagents sensitive to air or moisture were performed under argon with common Schlenk technique. In general, solvents were removed at preferably low temperatures (<50 °C) under reduced pressure with a rotary evaporator. Solvents for solvent mixtures were separately volumetrically measured. If not indicated otherwise, solutions of inorganic salts were used as aqueous, saturated solutions.

For certain reactions, flat-bottom crimp neck vials from CHROMAGLOBE with aluminum crimp cap were used. Liquids were added with a stainless-steel cannula and solids were added in powdered shape.

Reactions at low temperatures were cooled using shallow vacuum flasks produced by Isotherm, Karlsruhe, filled with a water/ice mixture for 0 °C, water/ice/sodium chloride for –20 °C or isopropanol/dry ice mixture for –78 °C. The reaction flask was equipped with a reflux condenser and connected to the argon line for reactions at high temperatures.

Flash column chromatography was performed using MERCK silica 60 (0.040 × 0.063 mm, 230–400 mesh ASTM) and quartz sand (glowed and purified with hydrochloric acid). Reactions in liquid phase were controlled by analytical thin-layer chromatography (TLC) with aluminium silica gel plates from MERCK (TLC Silica gel 60 F_{254}, d = 0.25 mm) with fluorescent quencher. Detection was performed by examination under UV light (λ = 254 nm & λ = 365 nm).

The RAYONET reactor Model RPR-100 with (16) 14W light bulbs (254 nm) was used for the irradiation with UV light.

For the irradiation with a blacklight, an OMNILUX UV lamp (160W, 368 nm) was used.

5.1.2 Devices

Nuclear magnetic resonance spectroscopy

NMR spectra were recorded at 21 °C using the following devices: ^{1}H NMR: BRUKER Avance 400 (400 MHz), BRUKER Avance 500 (500 MHz); ^{13}C NMR: BRUKER Avance 400 (100 MHz), BRUKER Avance 500 (126 MHz).

The NMR spectra were recorded in deuterated solvent from EURISOTOP, SIGMA ALDRICH, or DEUTERO. The chemical shift δ were expressed in parts per million (ppm) and referenced to: chloroform-d_1, DMSO-d_6, and Chemical shifts δ chloroform-d_1 (^{1}H: δ = 7.26 ppm, ^{13}C: δ = 77.0 ppm), DMSO-d_6 (^{1}H: δ = 2.50 ppm, ^{13}C: δ = 39.5 ppm), dichloromethane-d_2 (^{1}H: δ = 5.32 ppm, ^{13}C: δ = 53.8 ppm). Centrosymmetrical signals were characterized through the median point; for multiplet signals the signal range was annotated. The signal structures are described with the following abbreviations: s = singlet, d = doublet, t = triplet, q = quartet, br. s = broad singlet, m = multiplet, dd = doublet of doublets, dt = doublet of triplets. All coupling constants are absolute values and expressed in Hertz (Hz) with the largest values first. The superscript number gives the number of bonds in-between. spectra were measured as broadband, proton decoupled. Characterization of the ^{13}C NMR signals was done by DEPT techniques (distortionless enhancement by polarization transfer or with 2D NMR spectroscopy using ^{1}H-^{13}C-HSQC (HSQC = *heteronuclear single quantum coherence*).

The following abbreviations were used for aromatic proton/carbon signals CH_{Ar} and C_q for quaternary carbon atoms, CH_3 for methyl substituents, CH_2 for alkane units and CH for alkene units.

Solid State Nuclear Magnetic Resonance Spectroscopy

Solid state CPMAS NMR spectra were measured using BRUKER Avance III spectrometer operating at 500 MHz for protons using a double resonance CPMAS probe head. Samples were packed into 4 mm o.d. ZrO_2 rotors, plugged with KEL-F endcaps and spun at spinning frequency of 6, 8 or 10 kHz. In ^{13}C CPMAS measurements the length of the contact time for cross-polarization was 1 ms and a variable amplitude ramped from 70% to a maximum

amplitude during contact time was used. During the acquisition period the protons were decoupled using SPINAL-64 decoupling. The scans were collected with a 5 s relaxation delay and spectra externally referenced to adamantane. For ^{15}N CPMAS the parameters were otherwise similar, but the contact time used was 3 ms and spectra externally referenced to glycine. MALDI-TOF analysis was performed using Shimadzu's Axima Performance MALDI-TOF-MS instrument. Stains were prepared on stainless steel target (DE1580TA) with 384 wells. Matrix used was 2,5-dihydroxybenzoic acid (for MALDI-MS, Sigma-Aldrich) dissolved in trifluoroacetic acid (99%, Fischer Scientific) at a concentration of 10 mg/ml. Sample solutions prepared in TFA had a target concentration of 5 mg/ml, although it was difficult to ascertain complete dissolution. For staining 10 µl of the matrix solution and 5 µl of sample solution were mixed and 1 µl added portion-wise on a well to prevent excess spreading of the solution. Despite this, the spreading of the droplet posed a significant problem rendering most stains useless. The SEM images were acquired with a Hitachi S-4800 field emission scanning electron microscope (FESEM). The polymers were coated with 5 nm of Au-Pd alloy prior to the imaging.

Electron Paramagnetic Resonance Spectroscopy (EPR

Continuous wave EPR spectroscopy (CW-EPR) was performed at X-band on a Bruker EMXplus spectrometer. The field was calibrated using 2,2-diphenyl-1-picrylhydrazine (DDPH) with a g value of 2.0036.[290] CW-EPR simulations were carried out by using the EasySpin implementation in MatLab.

Infrared Spectroscopy (IR)

IR spectra were recorded on a BRUKER *Alpha T* using ATR (attenuated total reflection) for solids. All samples were analyzed at 21 °C. The absorption is given in wave numbers $\bar{\upsilon}$ [cm^{-1}] and was measured in the range from 3600 cm^{-1} to 400 cm^{-1}.

Mass Spectrometry (FAB-MS, EI-MS, ESI-MS)

The mass spectra were measured on a FINNIGAN MAT 95 (70 eV) for EI-MS (Electron ionization mass spectrometry) or FAB-MS (Fast atom bombardment mass spectrometry) (with 3-nitrobenzyl alcohol (3-NBA) as matrix). ESI-MS (Electron spray ionization mass spectrometry) was conducted on a THERMO SCIENTIFIC Q-Exactive Plus. For the interpretation of the mass spectra, the molecular ion $[M]^+$, peaks of pseudo molecules, such as $[M+H]^+$, and characteristic fragments are indicated as mass per charge ratio (*m/z*), and their intensity given

in percent, relative to the main peak (100%). For the high-resolution mass spectroscopy (HR-MS) the following abbreviations were used: calc. = calculated mass, found = mass found in the analysis.

Elemental Analysis (EA)

Elemental analysis (EA) was performed on an ELEMENTAR vario MICRO instrument, with a weight scale from Sartorius M2P. The calculated and found percentage are given for carbon, hydrogen, nitrogen and sulfur in fractions of 100%.

Single Electron Microscopy (SEM)

Single electron microscopy (SEM) images were acquired with a HITACHI S-4800 field emission scanning electron microscope (FESEM). The polymers were coated with 5 nm of Au-Pd alloy prior to the imaging.

IAST Selectivity Calculation

The ideal adsorption solution theory (IAST) of MYERS and PRAUSNITZ[291] is typically used to the selectivity of binary mixtures of gases from the single isotherms. The isotherms were fitted with Dual-Site LANGMUIR-FREUNDLICH using the software IAST++[292] and the selectivity (S) was calculated according to the formula:

$$S = \frac{Q_{CO2}}{Q_{N2}} \times \frac{P_{N2}}{P_{CO2}}$$

Were

P_{CO2} is the partial pressure of CO_2
P_{N2} is the partial pressure of N_2
Q_{N2} is the N_2 uptake
Q_{CO2} is theCO_2 uptake

Melting Point

Melting points were measured on an OptiMelt MPA100 device from the STANFORD RESEARCH SYSTEM.

X-Ray structure analysis

The crystal structure was determined in cooperation with Dr. O. FUHR at the Institute of Nanotechnology (INT) at the Karlsruhe Institute of Technology. Single crystal X-ray diffraction data were collected on a STOE STADI VARI diffractometer with monochromated Ga Kα (1.34143 Å) radiation at low temperature. Using Olex2,[293] the structures were solved with the ShelXT[294] structure solution program using Intrinsic Phasing and refined with the ShelXL[294-295] refinement package using Least Squares minimization. Refinement was performed with anisotropic temperature factors for all non-hydrogen atoms; hydrogen atoms were calculated on idealized positions. The molecular structure as ORTEP representation is shown in Figure **50**. Crystallographic data and refinement details are summarized in Table **3**.

Crystallographic data for compound ***p*PCP-PA** reported in the publication "Adv. Funct. Mater. 2024, 34, 2401957" have been deposited with the Cambridge Crystallographic Data Centre as supplementary information no. CCDC-2329941. Copies of the data can be obtained free of charge from https://www.ccdc.cam.ac.uk/structures/.

Time-of-Flight Secondary Ion Mass Spectrometry (ToF-SIMS)

ToF-SIMS was performed on a ToFSIMS5 instrument (IONTOF GmbH, Münster, Germany). The spectrometer is equipped with a Bi cluster primary ion source and a reflectron type time-of-flight analyzer. UHV base pressure during analysis was $<3\times 10^{-8}$ mbar. For high mass resolution, the Bi source was operated in bunched mode providing short Bi_3^+ primary ion pulses at 25 keV energy, a lateral resolution of approx. 4 μm, a target current of 0.35 pA at 10 kHz repetition rate, and 1.1 ns pulse length. Data acquisition was stopped at the quasi-static limit (2×10^{11} ions per cm^2). Charge compensation was performed by applying a 21 eV electron flood gun and tuning the reflectron accordingly. Mass scale calibration was based on low Mw hydrocarbon signals together with ZrO_2^-, ZrO_3H^-, or Zr^+ signals, respectively. The primary ion beam was rastered across a 500×500 μm^2 field of view on the sample, and 128×128 data points were recorded.

5.2 Synthesis Procedures

5.2.1 Synthesis Procedures for Chapter 3.1

Rac-Bromo[2.2]paracyclophane (22)

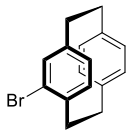

Bromine (3.84 g, 1.23 mL, 24.0 mmol, 1.00 equiv.) was diluted with dichloromethane (40 mL). From this solution, 5.0 mL were added to iron (26.8 mg, 480 µmol, 0.0200 equiv.) and stirred at 21 °C for 1 h. The reaction mixture was diluted with dichloromethane (80 mL), and [2.2]paracyclophane (5.00 g, 24.0 mmol, 1.00 equiv.) was added portion-wise and stirred for further 30 min. The remaining bromine solution was slowly added over a period of 5 h and the mixture was stirred overnight. Aqueous Na_2SO_3 solution (150 mL) was added and stirred until the organic phase was colorless. The phases were separated, and the aqueous layer was extracted with dichloromethane (3 x 100 mL). The combined organic layers were dried over Na_2SO_4, and the solvent was removed under reduced pressure to obtain *rac*-bromo[2.2]paracyclophane (6.82 g, 23.8 mmol, 99% yield) as a colorless solid.

R_f = 0.71 (cyclohexane/ethyl acetate 9:1).

^{1}H NMR (400 MHz, Chloroform-*d* [7.26 ppm], ppm) δ = 7.25–7.20 (m, 1H, CH_{ar}), 6.62–6.59 (m, 1H, CH_{ar}), 6.57–6.55 (m, 2H, CH_{ar}), 6.53–6.48 (m, 3H, CH_{ar}), 3.51 (ddd, *J* = 12.3 Hz, *J* = 10.0 Hz, *J* = 2.0 Hz, 1H, CH_{ar}), 3.28–3.20 (m, 1H, CH_2), 3.18–3.03 (m, 4H, CH_2), 3.01–2.91 (m, 1H, CH_2), 2.89–2.81 (m, 1H, CH_2).

Impurity: Signal at 3.10 ppm due to residues of [2.2]paracyclophane.

^{13}C NMR (100 MHz, Chloroform-*d* [77.2 ppm], ppm) δ = 141.6 (C_q), 139.4 (C_q, 2C), 139.1 (C_q), 137.4 (CH, C_{ar}), 135.1 (*C*H, C_{ar}), 133.3 (*C*H, C_{ar}), 132.9 (*C*H, C_{ar}), 132.3 (*C*H, C_{ar}), 131.5 (*C*H, C_{ar}), 128.7 (*C*H, C_{ar}), 127.1 (C_q), 35.9 (CH_2), 35.5 (CH_2), 34.9 (CH_2), 33.5 (CH_2).

Impurity: Signal at 133.0 ppm and 35.7 ppm due to residues of [2.2]paracyclophane.

MS (FAB, 3-NBA), m/z (%): 288/286 (15/15) $[M]^+$, 184/182 (16/16) $[C_8H_7Br]^+$, 104 (100) $[C_8H_8]^+$.

HRMS (FAB): *m/z* = calcd. for $C_{16}H_{15}{}^{79}Br^{81}Br$ $[M]^+$:286.0352; found 286.0350.

IR (ATR, $\tilde{\nu}$) = 3921 (w), 3900 (w), 3038 (w), 3009 (w), 2952 (w), 2925 (s), 2888 (w), 2849 (m), 2791 (w), 2768 (w), 1585 (w), 1541 (w), 1497 (w), 1475 (m), 1449 (w), 1431 (w), 1409 (w), 1390 (m), 1319 (w), 1237 (w), 1203 (w), 1184 (w), 1156 (w), 1033 (vs), 953 (w), 941 (w), 898 (s), 874 (w), 840 (vs), 792 (s), 718 (s), 708 (vs), 691 (m), 667 (s), 640 (vs), 577 (m), 513 (vs), 473 (s), 458 (w), 439 (w), 431 (w), 404 (w), 381 (w) cm^{-1}.

Additional data supporting the chemical synthesis results is available *via* the Chemotion repository: https://dx.doi.org/10.14272/reaction/SA-FUHFF-UHFFFADPSC-RJOYWTPJYZ-UHFFFADPSC-NUHFF-NUHFF-NUHFF-ZZZ.4

tert-Butyl (4-(1,4(1,4)-dibenzenacyclohexaphane-12-yl)phenyl)carbamate (**24**)

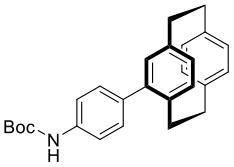

rac-Bromo[2.2]paracyclophane (1.50 g, 5.22 mmol, 1.00 equiv.), [4-(*tert*-butoxycarbonylamino)phenyl]boronic acid (1.86 g, 7.83 mmol, 1.50 equiv.), $Pd(dppf)Cl_2$ (153 mg, 209 µmol, 0.0400 equiv.) and K_3PO_4 (2.22 g, 10.4 mmol, 2.00 equiv.) were dissolved under argon atmosphere in 30 mL of dry toluene. The mixture was heated to 110 °C for 24 h and the reaction mixture was let cool down to 21 °C and then diluted with 40 mL toluene. The crude mixture was hydrolyzed with 10 mL of 10% aqueous NaOH-solution. The phases were separated, and the aqueous layer was extracted with ethyl acetate (3 x 50 mL). The organic layer was dried with $MgSO_4$ and concentrated in under reduced pressure. Subsequently, the residue was purified by flash column chromatography (cyclohexane /ethyl acetate, 20:1) to yield *tert*-butyl (4-(1,4(1,4)-dibenzenacyclohexaphane-12-yl)phenyl)carbamate (1.38 g, 3.45 mmol, 66% yield) as an off-white solid.

R_f = 0.22 (cyclohexane/ethyl acetate (20:1)).

^{1}H NMR (400 MHz, Chloroform-*d* [7.26 ppm], ppm) δ = 7.50–7.48 (m, 2H, CH_{ar}), 7.44–7.42 (m, 2H, CH_{ar}), 6.66–6.63 (m, 1H, CH_{ar}), 6.61–6.57 (m, 4H, CH_{ar}), 6.55–6.50 (m, 3H, CH_{ar}), 3.49–3.44 (m, 1H, CH_2), 3.21–3.11 (m, 3H, CH_2), 3.09–3.02 (m, 1H, CH_2), 2.95–2.84 (m, 2H, CH_2), 2.69–2.63 (m, 1H, CH_2), 1.58 (s, 9H, CH_3).

Impurities: Signals at 1.58 ppm due to water and at 1.43 ppm due to residues of cyclohexane.

^{13}C NMR (100 MHz, Chloroform-*d* [77.2 ppm], ppm) δ = 152.8 (C_q, CO), 141.3 (C_q), 139.8 (C_q), 139.7 (C_q), 139.4 (C_q), 137.2 (C_q), 137.0 (C_q), 136.2 (C_q), 135.8 (*C*H, C_{ar}), 133.1 (*C*H, C_{ar}), 132.6 (CH, C_{ar}), 132.0 (*C*H, 2C, C_{ar}), 132.0 (C_q), 130.3 (*C*H, 2C, C_{ar}), 129.7 (*C*H, C_{ar}), 118.6 (*C*H, 2C, C_{ar}), 80.6 (C_q), 35.5 (CH_2), 35.3 (CH_2), 34.8 (CH_2), 34.2 (CH_2), 28.4 (3C, CH_3)

Impurity: Signal at 26.3 ppm due to residues of cyclohexane.

MS (FAB, 3-NBA), m/z (%): 399 (33) $[M]^+$, 343 (100) $[M–C_4H_9]^+$, 239 (16) $[C_{15}H_{12}NO_2+H]^+$, 238 (24) $[C_{15}H_{12}NO_2]^+$, 105 (14) $[C_8H_8]^+$.

HRMS (FAB): *m/z* = calcd. for $C_{27}H_{29}O_2N$ $[M+H]^+$: 399.2193; found 399.2191.

IR (ATR, ṽ) = 2925 (w), 2850 (w), 1724 (w), 1698 (m), 1609 (w), 1589 (w), 1520 (vs), 1502 (m), 1479 (w), 1451 (w), 1414 (w), 1392 (w), 1366 (m), 1313 (m), 1292 (w), 1227 (s), 1154 (vs), 1092 (w), 1052 (m), 1024 (w), 1014 (w), 901 (w), 839 (m), 795 (w), 768 (w), 755 (w), 737 (w), 717 (m), 700 (w), 669 (w), 649 (m), 632 (w), 613 (w), 586 (w), 555 (w), 516 (m), 490 (m), 460 (w), 380 (w) cm^{-1}.

Additional data supporting the chemical synthesis results is available *via* the Chemotion repository: https://dx.doi.org/10.14272/reaction/SA-FUHFF-UHFFFADPSC-HUSNYROSCU-UHFFFADPSC-NUHFF-NUHFF-NUHFF-ZZZ

4-(4'-Amino)phenyl[2.2]paracyclophane (**19**)

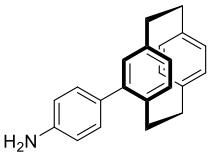

Under an argon atmosphere, *tert*-butyl (4-(1,4(1,4)-dibenzenacyclohexaphane-12-yl)phenyl)carbamate (1.78 g, 4.46 mmol, 1.00 equiv.) was dissolved in 90 mL of dry dichloromethane and 2,2,2-trifluoroacetic acid (102 g, 68.2 mL, 891 mmol, 200 equiv.) was added. The solution was stirred at 21 °C for 18 h. Subsequently, it was concentrated under reduced pressure, the residue was dissolved in ethyl acetate and neutralized with sat. $NaHCO_3$ solution. The mixture was extracted with ethyl acetate (3 x 50 mL). The combined organic layers were washed with sat. NaCl solution, dried over anhydrous $MgSO_4$ and the solvent was removed under reduced pressure. The crude product was dissolved in warm acetonitrile and precipitated as the hydrochloride by adding hydrogen chloride (325 mg, 741 µL, 8.91 mmol, 12.0M, 2.00 equiv.). The white solid was filtered off, washed with acetonitrile and dissolved in water. After addition of sat. $NaHCO_3$

solution, the mixture was extracted with ethyl acetate (3 x 50 mL). The combined organic layers were washed with brine, dried over anhydrous $MgSO_4$ and the solvent was removed under reduced pressure to obtain 4-(4'-amino)phenyl[2.2]paracyclophane (830 mg, 2.77 mmol, 65% yield) as an off-white solid.

^{1}H NMR (400 MHz, Chloroform-*d* [7.26 ppm], ppm) δ = 7.32–7.29 (m, 2H, CH_{ar}), 6.84–6.80 (m, 2H, CH_{ar}), 6.66–6.64 (m, 2H, CH_{ar}), 6.58–6.54 (m, 3H, CH_{ar}), 6.52–6.47 (m, 2H, CH_{ar}), 3.79–3.72 (br. s, 2H, NH_2), 3.53–3.45 (m, 1H, CH_2), 3.20–3.10 (m, 3H, CH_2), 3.08–3.00 (m, 1H, CH_2), 2.94–2.84 (m, 2H, CH_2), 2.75–2.67 (m, 1H, CH_2)

Impurity: Signals at 1.25 ppm, 2.05 ppm and 4.12 ppm due to residues of ethyl acetate.

^{13}C NMR (100 MHz, Chloroform-*d* [77.2 ppm], ppm) δ = 145.3 (C_q), 141.8 (C_q), 139.9 (C_q), 139.6 (C_q), 139.4 (C_q), 136.9 (C_q), 135.7 (*C*H, C_{ar}), 133.1 (*C*H, C_{ar}), 132.5 (*C*H, C_{ar}), 132.0 (*C*H, C_{ar}), 132.0 (*C*H, C_{ar}), 131.8 (*C*H, C_{ar}), 131.5 (*C*H, C_{ar}), 130.7 (*C*H, 2C, C_{ar}), 129.7 (*C*H, C_{ar}), 115.2 (*C*H, 2C, C_{ar}), 35.6 (*C*H_2), 35.3 (*C*H_2), 34.8 (*C*H_2), 34.3 (*C*H_2).

MS (EI, 70 eV, 90 °C), m/z (%): 299 (100) $[M]^+$, 195 (53) $[M–C_8H_8+H]^+$, 194 (87) $[M–C_8H_8]^+$.

Unknown impurities: 331 (10), 319 (21).

HRMS (EI): *m/z* = calcd. for $C_{22}H_{21}N$ $[M]^+$: 299.1669; found 299.1666.

IR (ATR, ṽ) = 3445 (w), 3356 (s), 3305 (w), 3214 (w), 3024 (w), 3009 (w), 2962 (w), 2948 (w), 2925 (w), 2915 (w), 2890 (w), 2849 (w), 1622 (s), 1605 (m), 1589 (m), 1514 (s), 1500 (w), 1479 (m), 1451 (w), 1431 (w), 1411 (w), 1401 (w), 1283 (s), 1247 (w), 1211 (w), 1179 (m), 1153 (w), 1128 (w), 1091 (w), 1065 (w), 960 (w), 952 (w), 941 (w), 901 (m), 880 (w), 853 (w), 832 (vs), 815 (vs), 793 (m), 737 (w), 715 (vs), 700 (m), 683 (w), 653 (s), 635 (s), 606 (w), 589 (m), 569 (m), 552 (s), 513 (vs), 489 (vs), 462 (s), 418 (m), 399 (m), 388 (m), 375 (m) cm^{-1}.

Additional data supporting the chemical synthesis results is available *via* the Chemotion repository: https://dx.doi.org/10.14272/reaction/SA-FUHFF-UHFFFADPSC-ARANCIPPBY-UHFFFADPSC-NUHFF-NUHFF-NUHFF-ZZZ.1

4,16-Dibromo[2.2]paracyclophane (27)

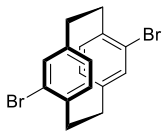

Bromine (32.2 g, 10.3 mL, 202 mmol, 2.10 equiv.) was diluted with dichloromethane (80 mL). Of this solution, 14.0 mL were added to Iron (241 mg, 4.32 mmol, 0.0450 equiv.) and stirred at 21 °C for 1 h. The reaction mixture was diluted with dichloromethane (100 mL) and [2.2]paracyclophane (20.0 g, 96.0 mmol, 1.00 equiv.) was added portion-wise and stirred for further 30 min. The remaining bromine solution was slowly added over 5 h, and the mixture was stirred for 3 d. Aqueous Na_2SO_3 solution (100 mL) was added and stirred until the organic layer turned colorless. The organic phase was filtered, and the residual solid was recrystallized from hot toluene to obtain 4,16-dibromo[2.2]paracyclophane (10.3 g, 28.1 mmol, 29% yield) as colorless crystals.

R_f = 0.87 (cyclohexane/ethyl acetate 9:1).

^{1}H NMR (400 MHz, Chloroform-*d* [7.26 ppm], ppm) δ = 7.20–7.15 (m, 2H, CH_{ar}), 6.56–6.52 (m, 2H, CH_{ar}), 6.49–6.44 (m, 2H, CH_{ar}), 3.55–3.48 (m, 2H, CH_2), 3.22–3.14 (m, 2H, CH_2), 3.01–2.93 (m, 2H, CH_2), 2.92–2.83 (m, 2H, CH_2).

Impurity: Signal at 1.53 ppm due to water.

^{13}C NMR (100 MHz, Chloroform-*d* [77.2 ppm], ppm) δ = 141.2 (C_q ,2C), 138.6 (C_q, 2C), 137.3 (*C*H, 2C, C_{ar}), 134.1 (*C*H, 2C, C_{ar}), 128.3 (*C*H, 2C, C_{ar}), 126.8 (*C*H, 2C, C_{ar}), 35.4 (*C*H_2, 2C), 32.9 (*C*H_2, 2C).

MS (EI, 70 eV, 90 °C), m/z (%): 368/366/364 (23/45/20) $[M]^+$, 184/182 (100/96) $[M–C_8H_7Br]^+$, 103 (70) $[C_8H_7]^+$.

HRMS (EI): *m/z* = calcd. for $C_{16}H_{14}{}^{79}Br^{81}Br$ 365.9436; found 365.9438.

IR (ATR, ṽ) = 2962 (w), 2932 (m), 2888 (w), 2850 (m), 1582 (m), 1534 (m), 1473 (m), 1449 (m), 1432 (m), 1390 (vs), 1313 (w), 1239 (w), 1186 (m), 1105 (w), 1030 (vs), 948 (w), 898 (vs), 887 (s), 856 (vs), 830 (vs), 771 (m), 705 (vs), 698 (vs), 669 (vs), 647 (vs), 599 (w), 585 (w), 523 (vs), 465 (vs), 421 (w), 394 (s) cm^{-1}.

Additional data supporting the chemical synthesis results is available *via* the Chemotion repository: https://dx.doi.org/10.14272/reaction/SA-FUHFF-UHFFFADPSC-QDMAXRJHDM-UHFFFADPSC-NUHFF-NUHFF-NUHFF-ZZZ.6

tert-Butyl-*N*-[4-[11-[4-(*tert*-butoxycarbonylamino)phenyl]-5-tricyclo[8.2.2.24,7]hexadeca-1(12),4,6,10,13,15-hexaenyl]phenyl]carbamate (28)

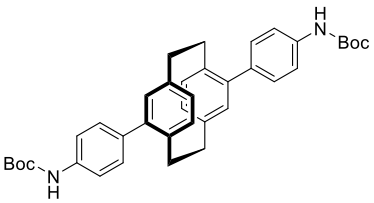

4,16-Dibromo[2.2]paracyclophane (3.00 g, 8.19 mmol, 1.00 equiv.), [4-(*tert*-butoxycarbonylamino)phenyl]boronic acid (5.83 g, 24.6 mmol, 3.00 equiv.), Pd(dppf)Cl_2 (300 mg, 410 µmol, 0.0500 equiv.) and K_3PO_4 (5.22 g, 24.6 mmol, 3.00 equiv.) were dissolved under argon atmosphere in 60 mL of dry toluene. The mixture was heated to 115 °C for 48 h, after completion, the reaction mixture was allowed to cool to 21 °C and was diluted with 40 mL toluene. The crude mixture was hydrolyzed with 30 mL of an aqueous 10% NaOH. The phases were separated, and the aqueous layer was extracted with ethyl acetate (3 x 50 mL). The organic layer was dried over $MgSO_4$ and concentrated in vacuo. Subsequently, the residue was purified by flash column chromatography (cyclohexane/ethyl acetate, 10:1) to obtain *tert*-butyl N-[4-[11-[4-(*tert*-butoxycarbonylamino)phenyl]-5-tricyclo[8.2.2.24,7]hexadeca-1(12),4,6,10,13,15-hexaenyl]phenyl]carbamate (2.13 g, 3.61 mmol, 44% yield) as an off-white solid.

R_f = 0.37 (cyclohexane/ethyl acetate (10:1)).

^{1}H NMR (400 MHz, Dichloromethane-d_2 [5.32 ppm], ppm) δ = 7.59–7.48 (m, 8H, CH_{ar}), 6.76–6.72 (m, 2H, N*H*CO), 6.69–6.66 (m, 4H, CH_{ar}), 6.61–6.59 (m, 2H, CH_{ar}), 3.52–3.45 (m, 2H, CH_{ar}), 3.07–3.00 (m, 2H, CH_{ar}), 2.91–2.84 (m, 2H, CH_{ar}), 2.79–2.72 (m, 2H, CH_{ar}), 1.58 (s, 18H, CH_3).

Impurities: Signals at 7.25, 7.15 and 2.34 ppm due to residues of toluene and at 1.52 ppm due to water.

^{13}C NMR (100 MHz, Dichloromethane-d_2 [53.8 ppm], ppm) δ = 152.7 (C_q, 2C), 141.5 (C_q, 2C), 140.0 (C_q, 2C), 137.5 (C_q, 2C), 136.8 (C_q, 2C), 136.1 (C_q, 2C), 134.8 (*C*H, 2C, C_{ar}), 132.0 (*C*H, 2C, C_{ar}), 130.3 (*C*H, 4C, C_{ar}), 128.9 (*C*H, 2C, C_{ar}), 118.5 (*C*H, 4C, C_{ar}), 80.4 (C_q, 2C), 34.5 (CH_2, 2C), 33.8 (CH_2, 2C), 28.1 (CH_3, 6C).

Impurity: Signals at 129.4 ppm, 128.6 ppm, 125.6 and 21.5 ppm due to residues of toluene.

MS (FAB, 3-NBA), m/z (%): 590 (10) $[M]^+$.

HRMS (FAB): *m/z* = calcd. for $C_{27}H_{30}O_2$ $[M+H]^+$: 590.3139; found 590.3138.

IR (ATR, ṽ) = 3272 (w), 2973 (w), 2922 (w), 2851 (w), 1713 (w), 1686 (s), 1612 (w), 1585 (w), 1523 (vs), 1477 (m), 1455 (w), 1414 (w), 1392 (m), 1367 (m), 1310 (m), 1285 (m), 1242 (s), 1153 (vs), 1113 (m), 1084 (w), 1055 (vs), 1027 (m), 1016 (m), 972 (w), 958 (w), 946 (w), 907 (w), 850 (m), 829 (s), 781 (m), 755 (m), 731 (m), 718 (w), 707 (w), 656 (s), 632 (m), 613 (m), 562 (m), 537 (w), 507 (w), 494 (s), 465 (w), 445 (w), 421 (w), 388 (w) cm^{-1}.

Additional data supporting the chemical synthesis results is available *via* the Chemotion repository: https://dx.doi.org/10.14272/reaction/SA-FUHFF-UHFFFADPSC-VTTAMWKROF-UHFFFADPSC-NUHFF-NUHFF-NUHFF-ZZZ

4-[11-(4-Aminophenyl)-5-tricyclo[8.2.2.24,7]hexadeca-1(12),4,6,10,13,15-hexaenyl]aniline (18)

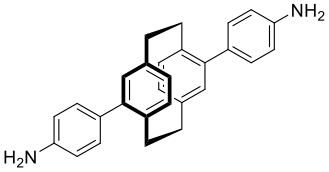

Under an argon atmosphere *tert*-butyl N-[4-[11-[4-[(2-methylpropan-2-yl)oxycarbonylamino]phenyl]-5-tricyclo[8.2.2.24,7]hexadeca-1(12),4,6,10,13,15-hexaenyl]phenyl]carbamate (2.40 g, 4.06 mmol, 1.00 equiv.) was dissolved in 60 mL of dry dichloromethane and 2,2,2-trifluoroacetic acid (92.6 g, 62.2 mL, 813 mmol, 200 equiv.) was added. The solution was stirred at 21 °C for 24 h. Subsequently, the mixture was concentrated under reduced pressure, the residue was dissolved in ethyl acetate and neutralized with sat. aqueous $NaHCO_3$ solution. The layers were separated, and the aqueous layer was extracted with ethyl acetate (3 x 50 mL). The combined organic layers were washed with sat. NaCl, dried over $MgSO_4$ and the solvent was removed under reduced pressure. The crude product was dissolved in warm acetonitrile and precipitated as the hydrochloride by

adding hydrogen chloride (593 mg, 1.35 mL, 16.3 mmol, 12.0M, 4.00 equiv.). The white solid was filtered off, washed with acetonitrile and dissolved in water. After addition of sat. $NaHCO_3$ solution, the mixture was extracted again with ethyl acetate (3 x 50 mL). The combined organic layers were washed with sat. NaCl, dried over anhydrous $MgSO_4$ and the solvent was removed under reduced pressure to obtain 4-[11-(4-aminophenyl)-5-tricyclo[8.2.2.24,7]hexadeca-1(12),4,6,10,13,15-hexaenyl]aniline (982 mg, 2.51 mmol, 62% yield) as an off white solid.

R_f = 0.43 (cyclohexane/ethyl Acetate (2:1)).

^{1}H NMR (400 MHz, Chloroform-*d* [7.26 ppm], ppm) δ = 7.36–7.33 (m, 4H, CH_{ar}), 6.85–6.82 (m, 4H, CH_{ar}), 6.63–6.57 (m, 6H, CH_{ar}), 3.52–3.46 (m, 2H, CH_2), 3.00–2.94 (m, 2H, CH_2), 2.84–2.76 (m, 4H, CH_2).

Missing signals: Amine protons missing NH_2 (4H) due to H/D exchange.

Impurities: Signals at 1.25 ppm and 0.84-0.87 ppm due to H–grease. Signals at 4.12 ppm and 2.05 ppm due to ethyl acetate.

^{13}C NMR (100 MHz, Chloroform-*d* [77.2 ppm], ppm) δ = 145.3 (C_q, 2C), 142.0 (C_q, 2C), 139.9 (C_q, 2C), 136.6 (C_q, 2C), 134.7 (*C*H, 2C, C_{ar}), 132.2 (C_q, 2C), 131.9 (C_q, 2C), 130.8 (*C*H, 4C, C_{ar}), 128.5 (*C*H, 2C, C_{ar}), 115.2 (*C*H, 4C, C_{ar}), 34.7 (*C*H_2, 2C), 34.0 (*C*H_2, 2C)

Impurity: Signal at 29.7 ppm due to H–grease.

MS (EI, 70 eV, 220 °C), m/z (%): 390 (56) $[M]^+$, 196 (70) $[M–C_{14}H_{13}N+H]^+$, 195 (56) $[M-C_{14}H_{13}N]^+$.

HRMS (EI): *m/z* = calcd. for $C_{28}H_{26}N_2$ $[M]^+$: 390.2091; found 390.2092.

IR (ATR, $\tilde{\nu}$) = 3077 (vw), 3040 (w), 3030 (w), 3016 (w), 2993 (w), 2980 (w), 2942 (w), 2922 (w), 2898 (w), 2871 (w), 2853 (w), 2764 (w), 2686 (w), 2655 (w), 2626 (w), 2615 (w), 2608 (w), 1672 (s), 1608 (m), 1565 (w), 1531 (w), 1513 (s), 1482 (w), 1459 (vw), 1422 (w), 1402 (w), 1201 (vs), 1183 (vs), 1129 (vs), 1020 (w), 911 (w), 832 (s), 800 (s), 744 (vw), 722 (vs), 683 (w), 662 (w), 637 (w), 599 (w), 581 (w), 551 (w), 528 (w), 518 (w), 493 (vs), 448 (m), 415 (w), 392 (w) cm^{-1}.

Additional data supporting the chemical synthesis results is available *via* the Chemotion repository: https://dx.doi.org/10.14272/reaction/SA-FUHFF-UHFFFADPSC-YYEYWECUVL-UHFFFADPSC-NUHFF-NUHFF-NUHFF-ZZZ

5.2.2 Synthesis Procedures for Chapter 3.2

4-(4-Formyl-N-(4-formylphenyl)anilino)benzaldehyde (30)

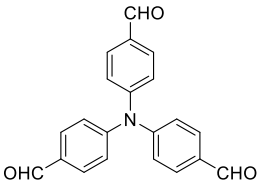

Phosphorus oxychloride (15.6 g, 9.30 mL, 102 mmol, 25.0 equiv.) was added dropwise at 0 °C under argon to *N*,*N*-dimethylformamide (6.85 g, 7.26 mL, 93.8 mmol, 23.0 equiv.) and the reaction mixture was stirred for 1 h. Triphenylamine (1.00 g, 4.08 mmol, 1.00 equiv.) was added, and the resulting mixture was stirred at 95 °C for 4 h. After cooling to 21 °C, the mixture was poured into ice water (200 mL) and basified with 1M NaOH. After extraction with dichloromethane (3 x 50 mL), the organic layer was washed with water (3 x 50 mL), dried over Na_2SO_4 and filtered over a short pad of silica gel. The solvent was then removed under reduced pressure and the residue was added to an ice-cooled mixture of phosphorus oxychloride (15.6 g, 9.30 mL, 102 mmol, 25.0 equiv.) and *N*,*N*-dimethylformamide (6.85 g, 7.26 mL, 93.8 mmol, 23.0 equiv.). The resulting mixture was stirred at 95 °C for 2 h. Subsequently, the reaction mixture was allowed to cool to 21 °C, poured into ice-water (200 mL), and basified with 1M NaOH. After extraction with dichloromethane (3 x 50 mL), the organic layer was washed with water (3 × 50 mL) and dried over Na_2SO_4. After evaporation of the solvent, the crude product was purified by column chromatography (dichloromethane/ ethyl acetate 1:0-9:1) to yield 4-(4-formyl-N-(4-formylphenyl)anilino)benzaldehyde (89.0 mg, 270 µmol, 7% yield) as an off-whit solid.

R_f = 0.56 (dichloromethane).

^{1}H NMR (400 MHz, Dichloromethane-d_2 [5.32 ppm], ppm) δ = 9.90 (s, 3H, C*H*O), 7.85–7.79 (m, 6H, CH_{ar}), 7.27–7.22 (m, 6H, CH_{ar}).

Impurity: Signals at 1.57 ppm due to water.

^{13}C NMR (100 MHz, Dichloromethane-d_2 [53.8 ppm], ppm) δ = 190.4 (*C*HO, 3C), 151.2 (C_q, 3C), 132.6 (C_q, 3C), 131.3 (*C*H, 6C, C_{ar}), 124.5 (*C*H, 6C, C_{ar}).

MS (ESI), m/z (%): 330 (100) $[M+H]^+$, 282 (13), 221 (15).

HRMS (ESI, DCM): *m/z* = calcd. for $C_{21}H_{16}NO_3^+$ $[M+H]^+$: 330.1125, found 330.1123.

IR (ATR, $\tilde{\nu}$) = 3092 (s), 3055 (s), 3044 (s), 2954 (s), 2923 (s), 2834 (s), 2823 (s), 2730 (s), 1698 (vs), 1682 (vs), 1673 (vs), 1585 (vs), 1575 (vs), 1561 (vs), 1501 (vs), 1320 (vs), 1308 (vs), 1267 (vs), 1212 (vs), 1161 (vs), 1121 (s), 1110 (s), 829 (s), 814 (vs), 537 (m), 526 (m) cm^{-1}.

Additional data supporting the chemical synthesis results is available *via* the Chemotion repository: https://dx.doi.org/10.14272/reaction/SA-FUHFF-UHFFFADPSC-YOXHQRNDWB-UHFFFADPSC-NUHFF-NUHFF-NUHFF-ZZZ

4-[2-[3,5-Bis[2-(4-formylphenyl)ethynyl]phenyl]ethynyl]benzaldehyde (**31**)

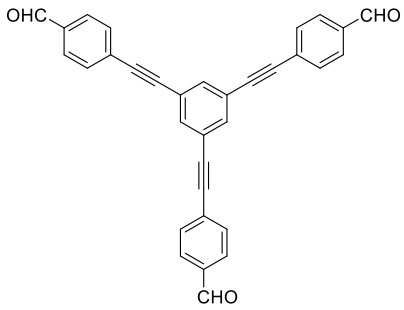

To a vial was added 1,3,5-triethynylbenzene (259 mg, 1.72 mmol, 1.00 equiv.), copper (I) iodide (65.7 mg, 345 µmol, 0.200 equiv.), triphenylphosphine (90.5 mg, 345 µmol, 0.200 equiv.) and 4-bromobenzaldehyde (1.34 g, 7.24 mmol, 4.20 equiv.). The flask was evacuated under vacuum for 10 min, before being refilled with argon thrice. Subsequently, 20 mL of triethylamine was added, and the mixture was degassed for 5 min prior to the addition of bis(triphenylphosphine)palladium chloride (121 mg, 172 µmol, 0.100 equiv.). The resulting suspension was heated at 85 °C for 16 h before being allowed to cool to 21 °C. The reaction was diluted with water (30 mL), extracted with dichloromethane (3 × 50 mL) and dried over Na_2SO_4. The resulting crude product was purified *via* column chromatography using dichloromethane as eluent, to obtain 4-[2-[3,5-bis[2-(4-formylphenyl)ethynyl]phenyl]ethynyl]benzaldehyde (97.9 mg, 212 µmol, 12% yield) as a colorless solid.

R_f = 0.82 (Dichloromethane).

^{1}H NMR (400 MHz, Chloroform-*d* [7.26 ppm], ppm) δ = 10.07 (s, 3H, C*H*O), 7.94–7.91 (m, 6H, CH_{ar}), 7.77 (s, 3H, CH_{ar}), 7.72 (m, 6H, CH_{ar}).

Impurities: Signals at 5.30 ppm due to dichloromethane and at 4.08, 2.00 and 1.26 ppm due to ethyl acetate and 1.56 ppm due to water.

^{13}C NMR (100 MHz, Chloroform-*d* [77.2 ppm], ppm) δ = 191.3 (*C*HO, 3C), 135.8 ($C_{q,}$ 3C), 134.8 (C_{ar}H, 3C), 132.3 (C_{ar}H, 6C), 129.7 (C_{ar}H, 6C), 128.8 (C_q, 3C, C_{ar}), 123.7 (C_q, 3C), 91.2 (C_q, 3C), 90.0 (C_q, 3C).

MS (ESI), m/z (%): 582 (9), 581 (21), 513 (9), 512 (10), 511 (30), 479 (5), 478 (36), 477 (100).

IR (ATR, $\tilde{\nu}$) = 3052 (s), 3039 (s), 2960 (vs), 2925 (vs), 2866 (s), 2848 (vs), 2734 (s), 2209 (m), 1697 (vs), 1599 (vs), 1561 (s), 1458 (w), 1442 (m), 1417 (m), 1389 (m), 1302 (m), 1206 (vs), 1166 (s), 1103 (w), 875 (w), 823 (vs), 722 (m), 679 (w), 526 (w) cm^{-1}.

Additional data supporting the chemical synthesis results is available *via* the Chemotion repository: https://dx.doi.org/10.14272/reaction/SA-FUHFF-UHFFFADPSC-RSQZINMBNW-UHFFFADPSC-NUHFF-NUHFF-NUHFF-ZZZ

4-[3,5-Bis(4-formylphenyl)phenyl]benzaldehyde (32)

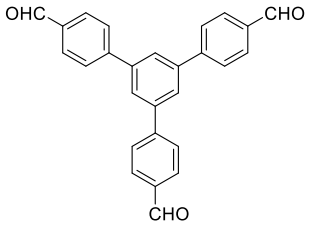

1,3,5-Tribromobenzene (100 mg, 318 µmol, 1.00 equiv.), (4-formylphenyl)boronic acid (143 mg, 953 µmol, 3.00 equiv.), palladium(II) acetate (7.13 mg, 31.8 µmol, 0.100 equiv.), XPhos (30.3 mg, 63.5 µmol, 0.200 equiv.) and Cs_2CO_3 (311 mg, 953 µmol, 3.00 equiv.) were dissolved in 10 mL of dry tetrahydrofuran. The mixture was heated at 75°C for 16 hours. Subsequently, the mixture was cooled to 21 °C and was extracted with dichloromethane (2 × 100 mL). The obtained organic layer was dried over Na_2SO_4. The solvent was removed under reduced pressure. The resulting crude product was purified *via* column chromatography (cyclohexane/ ethyl acetate 7:3-1:1) to obtain 4-[3,5-bis(4-formylphenyl)phenyl]benzaldehyde (89.0 mg, 228 µmol, 72% yield) as an off-white solid.

R_f = 0.90 (*n*-hexane/ethyl acetate (3:1)).

^{1}H NMR (400 MHz, Chloroform-*d* [7.26 ppm], ppm) δ = 10.13 (s, 3H, C*H*O), 8.07–8.04 (m, 6H, CH_{ar}), 7.94 (s, 3H, CH_{ar}), 7.90 (m, 6H, CH_{ar})

Impurities: Signals at 4.12, 2.05 and 1.32 ppm due to ethyl acetate and at 1.56 ppm due to water.

^{13}C NMR (100 MHz, Chloroform-*d* [77.2 ppm], ppm) δ = 191.8 (*C*HO, 3C), 146.3 (C_q, 3C), 141.6 (C_q, 3C), 135.8 (C_q, 3C), 130.4 (*C*H, 6C, C_{ar}), 128.0 (*C*H, 6C, C_{ar}), 126.5 (*C*H, 3C, C_{ar}).

MS (ESI), m/z (%): 202 (5), 152 (32), 151 (7), 150 (100).

IR (ATR, ṽ) = 3352 (m), 3205 (m), 3119 (m), 3060 (s), 3045 (s), 3030 (m), 3010 (m), 2997 (m), 2988 (m), 2981 (m), 2957 (m), 2924 (s), 2808 (s), 2721 (s), 1683 (vs), 1599 (vs), 1567 (vs), 1383 (s), 1308 (s), 1211 (vs), 1169 (vs), 855 (m), 813 (s), 790 (vs) cm^{-1}.

Additional data supporting the chemical synthesis results is available *via* the Chemotion repository: https://dx.doi.org/10.14272/reaction/SA-FUHFF-UHFFFADPSC-ZCJZVMNBJK-UHFFFADPSC-NUHFF-NUHFF-NUHFF-ZZZ

2,4,6-Tris(4-bromophenyl)-1,3,5-triazine (41)

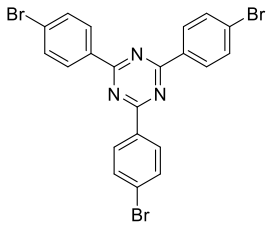

4-bromobenzonitrile (6.00 g, 33.0 mmol, 1.00 equiv.) was added to trifluoromethanesulfonic acid (5.61 g, 3.30 mL, 37.4 mmol, 3.40 equiv) and cooled to 0 °C and stirred for 1 hour, before being stirred at 21 °C for 16 hours. Subsequently, 50 mL of water was added, and the suspension was neutralized with aqueous 10% NaOH. The white precipitate was filtered off, washed with water (3 x 50 mL), ethanol (2 x 50 mL) and dried in airflow. The crude product was recrystallized from hot ethanol to give 2,4,6-tris(4-bromophenyl)-1,3,5-triazine (5.53 g, 10.1 mmol, 92% yield) of a colorless solid.

^{1}H NMR (400 MHz, Chloroform-*d* [7.26 ppm], ppm) δ = 8.62–8.60 (m, 6H, CH_{ar}), 7.72–7.70 (m, 6H, CH_{ar})

Impurities: Signals at 1.55 ppm due to water and unknown impurities at 0.07 and 1.25 ppm.

^{13}C NMR (100 MHz, Chloroform-*d* [77.2 ppm], ppm) δ = 132.0 (*C*H, 6C, C_{ar}), 130.5 (*C*H, 6C, C_{ar}).

Missing Signals: C_q (9C) due to insolubility of the compound.

MS (EI, 70 eV, 210 °C), m/z (%): 543/544/545/546/547/548/549/550 (32/8/100/23/96/23/32/7) $[M]^+$, 181/182/183/184 (43/12/43/10) $[C_7H_4BrN]^+$, 102 (32) $[C_7H_4N]^+$.

HRMS (EI): *m/z* = calcd. for $C_{14}H_{15}N_3O_3$ $[M]^+$: 546.8535; found 546.8533.

IR (ATR, $\tilde{\nu}$) = 1590 (w), 1580 (s), 1543 (w), 1512 (vs), 1485 (s), 1401 (s), 1368 (s), 1351 (s), 1329 (w), 1290 (vw), 1277 (vw), 1170 (m), 1148 (vw), 1100 (w), 1092 (vw), 1068 (s), 1010 (vs), 969 (vw), 858 (w), 841 (s), 829 (w), 802 (vs), 629 (vw), 494 (vs), 475 (s) cm^{-1}.

Additional data supporting the chemical synthesis results is available *via* the Chemotion repository: https://dx.doi.org/10.14272/reaction/SA-FUHFF-UHFFFADPSC-WZYVDGDZBN-UHFFFADPSC-NUHFF-NUHFF-NUHFF-ZZZ

4-[4,6-Bis(4-formylphenyl)-1,3,5-triazin-2-yl]benzaldehyde (33)

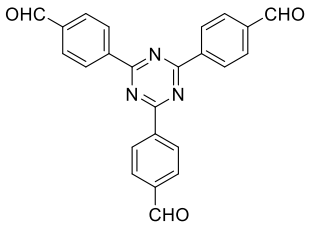

2,4,6-Tris(4-bromophenyl)-1,3,5-triazine (500 mg, 916 µmol, 1.00 equiv.) was dissolved under an inert atmosphere in 70 mL of dry tetrahydrofuran. The obtained solution was cooled to –78 °C under stirring. Subsequently, *n*-BuLi (587 mg, 3.66 mL, 9.16 mmol, 2.50M, 10.0 equiv.) was added dropwise to the stirred solution at –78 °C. After addition, the solution was stirred for 3 h at this temperature. Subsequently, the obtained green solution was treated with anhydrous *N*,*N*-dimethylformamide (1.34 g, 1.42 mL, 18.3 mmol, 20.0 equiv.). The mixture was allowed to warm to 21 °C and stirred for 16 h. The milky opaque mixture was acidified with 17 mL of 3M HCl. A white precipitate appeared, and the mixture was stirred for 1 hour. Then 15 mL of water and 30 mL of petroleum ether were added. The resulting white solid was collected by filtration and washed with water (3 x 50 mL), petroleum ether (3 x 50 mL), and ethanol (3 x 50 mL). The crude product was recrystallized from hot ethanol. After drying under vacuum, the product 4-[4,6-bis(4-formylphenyl)-1,3,5-triazin-2-yl]benzaldehyde (75.0 mg, 191 µmol, 21% yield) was obtained as a colorless solid.

^{1}H NMR (400 MHz, Dichloromethane-d_2 [5.32 ppm], ppm) δ = 10.21 (s, 3H, C*H*O), 8.99 (d, J = 7.9 Hz, 6H, CH_{ar}), 8.14 (d, J = 7.9 Hz, 6H, CH_{ar})

Impurities: Signals at 3.66, 1.33 and 1.19 ppm due to ethanol and at 0.07 ppm due to silicone grease.

^{13}C NMR (100 MHz, Dichloromethane-d_2 [53.8 ppm], ppm) δ = 191.8 (*C*HO, 3C), 171.2 (C_q, 3C), 140.7 (C_q, 3C), 139.4 (C_q, 3C), 129.8 (C_{ar}H, 6C), 129.6 (C_{ar}H, 6C)

Impurities: Signal at 0.81 ppm due to silicon grease.

MS (ESI), m/z (%): 394 (4) $[M+H]^+$, 307 (26), 289 (14) $[C_{17}H_{10}N_3O_2+H]^+$, 155 (21), 154 (72), 147 (24), 138 (24), 137 (46), 136 (100), 91 (35), 90 (32), 89 (25).

IR (ATR, $\tilde{\nu}$) = 2961 (w), 2929 (w), 2817 (w), 2789 (w), 2728 (w), 1694 (vs), 1606 (w), 1581 (s), 1511 (vs), 1504 (vs), 1418 (m), 1373 (m), 1356 (vs), 1298 (s), 1259 (m), 1198 (vs), 1147 (m), 1103 (s), 1052 (m), 1041 (m), 1033 (m), 1013 (s), 866 (m), 863 (m), 803 (vs), 704 (m), 687 (m), 664 (m), 629 (w), 601 (w), 571 (w), 561 (w), 545 (w), 499 (s), 407 (m), 395 (m), 387 (m), 381 (m) cm^{-1}.

Additional data supporting the chemical synthesis results is available *via* the Chemotion repository: https://dx.doi.org/10.14272/reaction/SA-FUHFF-UHFFFADPSC-RXFWPOMAJB-UHFFFADPSC-NUHFF-NUHFF-NUHFF-ZZZ

General Procedure for the Synthesis of Covalent Organic Frameworks

The respective aldehyde (3.00 equiv.) and the amine (2.00 equiv.) were suspended in 2.00 mL of 1,4-dioxane. Subsequently, acetic acid (40.0 equiv.) was added, and an orange precipitate formed immediately. The suspension was let stand still for 3 days at 21 °C. The obtained solid was filtered off and was washed with dichloromethane, ethyl acetate, ethanol, water and methanol. The isolated solid was dried under high vacuum to afford the covalent organic framework.

COF-TP (**42**)

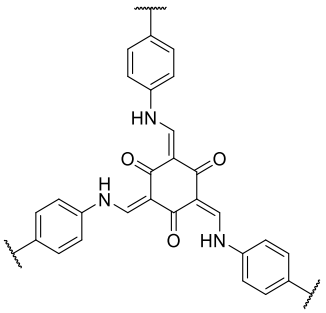

COF-TP was synthesized from 2,4,6-trihydroxybenzene-1,3,5-tricarbaldehyde (4.84 mg, 23.0 µmol, 1.00 equiv.) and 4-[11-(4-aminophenyl)-5-tricyclo[8.2.2.24,7]hexadeca-1(12),4,6,10,13,15-hexaenyl]aniline (6.03 mg, 15.4 µmol, 0.670 equiv.) according to general procedure. The titled compound was afforded as an orange solid (15.8 mg, 52%).

IR (ATR, $\tilde{\nu}$) = 1615 (vs), 1592 (vs), 1571 (vs), 1516 (m), 1454 (s), 1288 (vs), 1255 (s), 1181 (w), 823 (w), 498 (w) cm^{-1}.

EA ($C_{93}H_{75}N_6O_3$): calcd. C 84.33, H 5.71, N 6.34 found. C 77.44, H 5.08, N 5.28.

COF-TFPA (**43**)

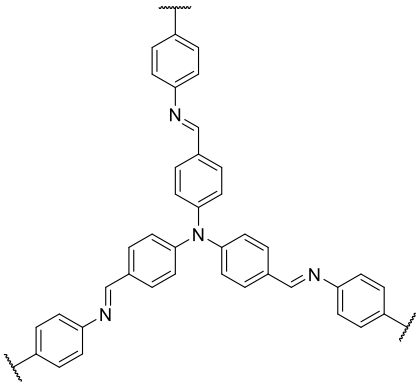

COF-TFPA was synthesized from 4-(4-formyl-N-(4-formylphenyl)anilino)benzaldehyde (8.43 mg, 25.6 µmol, 0.333 equiv.) and 4-[11-(4-aminophenyl)-5-tricyclo[8.2.2.24,7]hexadeca-1(12),4,6,10,13,15-hexaenyl]aniline (30.0 mg, 76.8 µmol, 1.00 equiv.) according to general procedure. The titled compound was afforded as a dark orange solid (17.0 mg, 48%).

IR (ATR, ṽ) = 1588 (vs), 1574 (s), 1504 (vs), 1318 (s), 1286 (s), 1193 (w), 1166 (vs), 829 (vs) cm^{-1}.

EA ($C_{105}H_{84}N_7$): calcd. C 87.66; H 5.86; N 6.79 found. C 81.66; H 5.54, N 6.30.

COF-BTT (**44**)

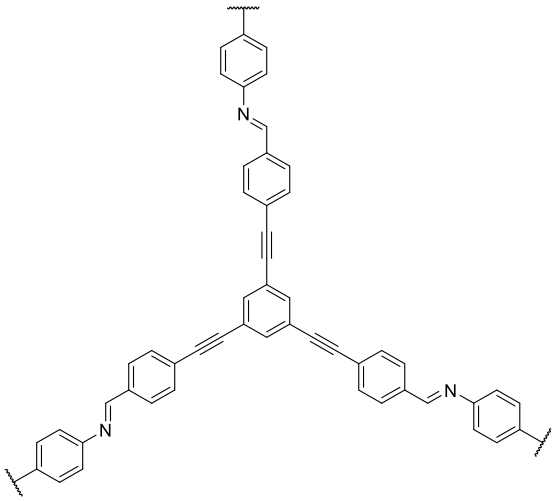

COF-BTT was synthesized from 4-[2-[3,5-bis[2-(4-formylphenyl)ethynyl]phenyl]ethynyl]benzaldehyde (11.8 mg, 25.6 µmol, 1.00 equiv.) and 4-[11-(4-aminophenyl)-5-tricyclo[8.2.2.24,7]hexadeca-1(12),4,6,10,13,15-hexaenyl]aniline (6.70 mg, 17.2 µmol, 0.670 equiv.) according to general procedure. The titled compound was afforded as a yellow solid (12.3 mg, 30%).

IR (ATR, ṽ) = 1623 (m), 1598 (s), 1508 (m), 1168 (m), 878 (m), 829 (vs), 549 (m) cm^{-1}.

EA ($C_{117}H_{87}N_6$): calcd. C 89.11; H 5.56; N 5.33 found. C 84.26; H 5.17, N 4.50.

COF-TFPB (**44**)

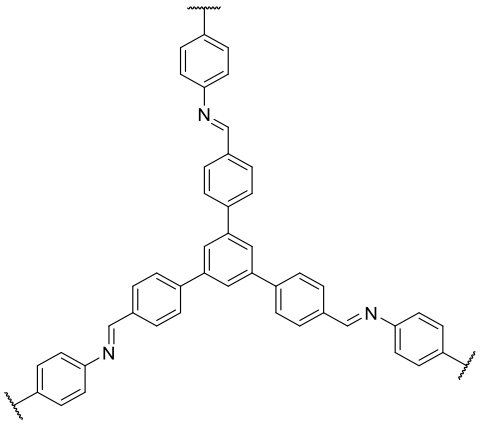

COF-TFPB was synthesized from 4-[3,5-bis(4-formylphenyl)phenyl]benzaldehyde (20.1 mg, 51.5 µmol, 1.49 equiv.) and 4-[11-(4-aminophenyl)-5-tricyclo[8.2.2.24,7]hexadeca-1(12),4,6,10,13,15-hexaenyl]aniline (13.5 mg, 34.5 µmol, 0.670 equiv.) according to general procedure. The titled compound was afforded as a yellow solid (12.8 mg, 16%).

IR (ATR, $\tilde{\nu}$) = 1693 (w), 1621 (m), 1592 (s), 1514 (m), 1477 (m), 1199 (w), 1170 (m), 825 (vs), 794 (s), 730 (w), 654 (w), 496 (m) cm^{-1}.

EA ($C_{111}H_{87}N_6$): cacld. C 88.59; H 5.83; N 5.58 found. C 85.24; H 5.74, N 4.80.

COF-TFTA (45)

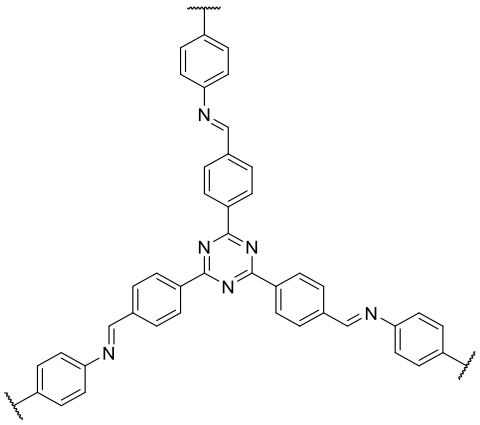

COF-TFTA was synthesized from 4-[4,6-bis(4-formylphenyl)-1,3,5-triazin-2-yl]benzaldehyde (10.1 mg, 25.6 µmol, 1.00 equiv.) and 4-[11-(4-aminophenyl)-5-tricyclo[8.2.2.24,7]hexadeca-1(12),4,6,10,13,15-hexaenyl]aniline (6.70 mg, 17.2 µmol, 0.670 equiv.) according to general procedure. The titled compound was afforded as a dark orange solid (13.5 mg, 35%).

IR (ATR, $\tilde{\nu}$) = 1658 (vs), 1539 (s), 1514 (vs), 1316 (vs), 827 (vs), 494 (vs) cm^{-1}.

EA ($C_{108}H_{84}N_9$): cacld. C 86.02, H 5.62, N 8.36 found. C 79.17, H 6.00, N 6.26.

5.2.3 Synthesis Procedures for Chapter 3.3

3,5-Dibromo-2,2,6,6-tetramethyl-piperidin-4-one (48)

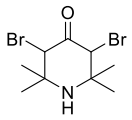

In a solution of molecular bromine (10.3 g, 3.30 mL, 64.4 mmol, 2.00 equiv.) in 6 mL of acetic acid was added slowly to triacetonamine (5.00 g, 32.2 mmol, 1.00 equiv.) dissolved in 19 mL of acetic acid. After stirring for 15 min, a precipitate appeared, and the resulting suspension was stirred for 16 h. Subsequently, the precipitate was filtered off and washed with acetic acid (35 mL), water (35 mL) and diethyl ether (35 mL). Afterward, the crude product was refluxed in 15 mL of ethyl acetate for 30 min, filtered, and washed with 50 mL of ethyl acetate. The obtained solid was dried under vacuum to obtain 3,5-dibromo-2,2,6,6-tetramethyl-piperidin-4-one (5.94 g, 19.0 mmol, 59% yield) as a white solid.

R_f = 0.32 (dichloromethane).

^{1}H NMR (400 MHz, DMSO-d_6 [2.50 ppm], ppm) δ = 5.42 (s, 2H, C*H*), 1.66 (s, 6H, CH_3), 1.33 (s, 6H, CH_3).

Missing signal: Amine proton N*H* (1H) due to H/D exchange.

Impurities: Unknown small impurities between 1.80 and 1.20 ppm.

^{13}C NMR (100 MHz, DMSO-d_6 [39.5 ppm], ppm) δ = 189.2 (C_q), 64.8 (C_q, 2C), 60.6 (*C*H, 2C), 28.2 (*C*H_3, 2C), 22.5 (*C*H_3, 2C).

Impurities: Unknown small impurities between 30.0 and 18.0 ppm.

MS (EI, 70 eV, 130 °C), m/z (%): 315/311/313 (24/12/11) $[M]^+$, 298/300/296 (8/4/4) $[M–CH_3]^+$, 232/234 (16/15) $[M–Br]^+$.

HRMS (EI): *m/z* = calcd. for $C_9H_{15}ON^{79}Br^{81}BR$ $[M]^+$: 312.9494; found 312.9492.

IR (ATR, $\tilde{\nu}$) = 3080 (w), 3034 (w), 2990 (w), 2890 (s), 2856 (w), 2829 (w), 2786 (w), 2691 (s), 2638 (m), 2619 (m), 2554 (m), 2520 (w), 2456 (w), 2411 (w), 2353 (w), 2323 (w), 2288 (w), 2276 (w), 2264 (vw), 1749 (vs), 1715 (w), 1541 (m), 1483 (w), 1456 (w), 1404 (w), 1384 (vs), 1322 (w), 1269 (m), 1254 (s), 1187 (w), 1169 (w), 1163 (w), 1136 (m), 1108 (m), 1037 (m), 925 (m), 899 (w), 880 (w), 815 (w), 800 (w), 779 (w), 677 (w), 636 (vs), 611 (w), 555 (w), 527 (w), 432 (vs), 395 (vs), 382 (m) cm^{-1}.

Additional data supporting the chemical synthesis results is available *via* the Chemotion repository: https://dx.doi.org/10.14272/reaction/SA-FUHFF-UHFFFADPSC-SMSQRKIBWO-UHFFFADPSC-NUHFF-NUHFF-NUHFF-ZZZ

2,2,5,5-Tetramethyl-1*H*-pyrrole-3-carboxamide (**49**)

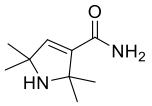

In a 100 mL round bottom flask, 3,5-dibromo-2,2,6,6-tetramethyl-piperidin-4-one (5.50 g, 17.6 mmol, 1.00 equiv.) was added slowly to 45 mL of conc. ammonia. After 15 min, the solid was dissolved completely and the solution was saturated with sodium hydroxide pellets (10.2 g, 255 mmol, 14.5 equiv.). The obtained suspension was stirred for 2 h. Afterward, the solid was filtered off, washed with 55 mL each of aqueous 7M KOH solution and *n*-hexane. The crude product was recrystallized from hot toluene to obtain 2,2,5,5-tetramethyl-1*H*-pyrrole-3-carboxamide (1.02 g, 6.06 mmol, 35% yield) as a colorless solid.

R_f = 0.12 (ethyl acetate).

^{1}H NMR (400 MHz, Chloroform-*d* [7.26 ppm], ppm) δ = 6.15 (s, 1H, C*H*), 5.80 (s, 2H, CONH_2), 1.42 (s, 6H, CH_3), 1.27 (s, 6H, CH_3).

Missing signal: Amin proton N*H* (1H) is missing due to H/D exchange.

^{13}C NMR (100 MHz, Chloroform-*d* [77.2 ppm], ppm) δ = 167.2 (*C*ONH$_2$), 142.3 (*C*H), 142.3 (C_q), 66.9 (C_q), 63.5 (C_q), 30.3 (*C*H$_3$, 2C), 30.2 (*C*H$_3$, 2C).

MS (EI, 70 eV, 80 °C), m/z (%):168 (1) $[M]^+$, 153 (81) $[M–CH_3]^+$, 110 (100) $[M–CH_3 – CONH_2+H]^+$, 95 (11) $[M–2\ CH_3–CONH_2+H]^+$.

HRMS (EI): *m/z* = calcd. for $C_9H_{16}ON_2$ $[M]^+$: 168.1257; found 168.1259.

IR (ATR, $\tilde{\nu}$) = 3347 (w), 3274 (w), 3182 (w), 2956 (w), 2925 (w), 2866 (w), 1663 (vs), 1640 (vs), 1599 (vs), 1470 (w), 1455 (w), 1402 (vs), 1371 (s), 1360 (vs), 1296 (w), 1273 (w), 1220 (w), 1190 (s), 1164 (m), 1136 (w), 1108 (w), 1009 (w), 993 (w), 933 (w), 918 (w), 890 (m), 847 (w), 803 (m), 773 (s), 718 (m), 657 (vs), 640 (vs), 541 (w), 490 (m), 465 (w), 424 (w), 395 (w), 375 (w) cm^{-1}.

Additional data supporting the chemical synthesis results is available *via* the Chemotion repository: https://dx.doi.org/10.14272/reaction/SA-FUHFF-UHFFFADPSC-ACFYUJLIWI-UHFFFADPSC-NUHFF-NUHFF-NUHFF-ZZZ

1-oxidanyl-2,2,5,5-tetramethylpyrrole-3-carboxamide (50)

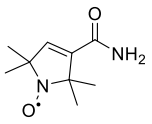

To a suspension of 2,2,5,5-tetramethyl-1*H*-pyrrole-3-carboxamide (800 mg, 4.76 mmol, 1.00 equiv.) in 44 mL of dichloromethane, 3-chlorobenzenecarboperoxoic acid (1.23 g, 7.13 mmol, 1.50 equiv.) was added and the obtained reaction mixture was stirred for 16 h at 21 °C. Afterward, the suspension was washed with aqueous Na_2CO_3 (3 x 40 mL), brine and dried over Na_2SO_4. The solvent was removed under reduced pressure to obtain 1-oxidanyl-2,2,5,5-tetramethylpyrrole-3-carboxamide (602 mg, 3.29 mmol, 69% yield) as a yellow solid.

R_f = 0.69 (ethyl acetate).

MS (EI, 70 eV, 80 °C), m/z (%): 183 (22) $[M]^+$, 153 (100) $[M–2\ CH_3]^+$, 138 (73) $[M–2\ CH_3–O]^+$, 95 (37).

HRMS (EI): *m/z* = calcd. for $C_9H_{15}O_2N_2$ $[M]^+$: 183.1128; found 183.1130.

IR (ATR, $\tilde{\nu}$) = 3349 (m), 3293 (w), 3162 (m), 2973 (w), 2929 (w), 1672 (vs), 1638 (s), 1613 (s), 1463 (m), 1453 (w), 1442 (m), 1429 (w), 1409 (vs), 1367 (s), 1361 (m), 1322 (m), 1271 (w), 1208 (w), 1159 (s), 1126 (w), 1045 (w), 956 (w), 871 (m), 806 (w), 776 (w), 756 (w), 744 (w), 659 (vs), 635 (vs), 613 (vs), 568 (s), 494 (w), 467 (vs), 398 (s), 377 (s) cm^{-1}.

UV-VIS (abs. DCM, 21 °C), λ_{max} = 218 nm.

Additional data supporting the chemical synthesis results is available *via* the Chemotion repository: https://dx.doi.org/10.14272/reaction/SA-FUHFF-UHFFFADPSC-RUEXQFPLRR-UHFFFADPSC-NUHFF-NUHFF-NUHFF-ZZZ

3-Carboxy-2,2,5,5-tetramethylpyrrole-1-oxidanyl (**52**)

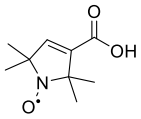

1-Oxidanyl-2,2,5,5-tetramethylpyrrole-3-carboxamide (2.60 g, 14.2 mmol, 1.00 equiv.) was suspended in 10% sodium hydroxide (59.6 g, 53.7 mL, 149 mmol, 10.5 equiv.) and was refluxed for 16 h until no ammonia was released anymore. The reaction mixture was let cool down to 21 °C and was acidified with 2M HCl (20 mL). Subsequently diethyl ether (30 mL) was added, and the aqueous phase was extracted with diethyl ether (2 x 20 mL). The combined organic phase was washed with sat. NaCl solution and dried over Na_2SO_4. The solvent was removed under reduced pressure to obtain 3-Carboxy-2,2,5,5-tetramethylpyrrole-1-oxidanyl (1.35 g, 7.33 mmol, 52% yield) as yellow solid.

R_f = 0.11 (ethyl acetate).

MS (EI, 70 eV, 50 °C), m/z (%):184 (65) $[M]^+$, 154 (100) $[M–2 \times CH_3]^+$, 139 (56) $[M–CO_2H]^+$, 109 (27) $[M–CO_2H–2 \times CH_3]^+$.

HRMS (EI): *m/z* = calcd. for $C_9H_{14}O_3N$ $[M]^+$: 184.0968; found 184.0970.

IR (ATR, $\tilde{\nu}$) = 3090 (w), 2980 (m), 2935 (m), 2750 (w), 1718 (s), 1705 (vs), 1629 (m), 1456 (m), 1428 (m), 1403 (s), 1364 (s), 1356 (m), 1343 (m), 1275 (s), 1236 (s), 1187 (vs), 1164 (vs), 1150 (vs), 1061 (m), 1037 (vs), 952 (m), 909 (m), 897 (w), 882 (m), 864 (m), 825 (m), 765 (vs), 675 (vs), 418 (w) cm^{-1}.

UV-VIS (abs, DCM, 21 °C), λ_{max} = 470, 219 nm.

Additional data supporting the chemical synthesis results is available *via* the Chemotion repository: https://dx.doi.org/10.14272/reaction/SA-FUHFF-UHFFFADPSC-QILCUDCYZV-UHFFFADPSC-NUHFF-NUHFF-NUHFF-ZZZ

RGD-Nitroxide Peptide Synthesis (70)

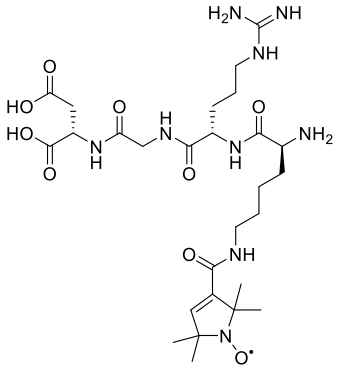

In a fritted syringe, 2-chlorotrityl chloride resin (125 mg, 200 µmol, 1.00 equiv.) was swollen in 3 mL dichloromethane by shaking at 21 °C for at least 30 min. After completion the solvent was removed. The first amino acid (1.60 mmol, 4.00 equiv.) and *N*,*N*-diisopropylethylamine (129 mg, 174 µL, 1.00 mmol, 5.00 equiv.) were dissolved in 2.5 mL *N*,*N*-dimethylformamide and added to the resin. After shaking for 8 h, the solvent was removed, and the resin was washed with *N*,*N*-dimethylformamide, methanol, and dichloromethane. Deprotection of the *N*-Fmoc-protecting group was carried out using a solution of 20% piperidine in *N*,*N*-dimethylformamide. 3 mL were added to the resin, and the mixture was shaken for 5 min. The deprotection cocktail was removed, and the procedure was repeated twice. The resin was washed as described with *N*,*N*-dimethylformamide, methanol, and dichloromethane. The subsequent amino acid (800 µmol, 4.00 equiv.) and O-(7-azabenzotriazol-1-yl)-*N*,*N*,*N*,*N*-tetramethyluronium-hexafluorphosphat (306 mg, 1.60 mmol, 4.00 equiv.) were dissolved in 2.5 mL *N*,*N*-dimethylformamide, added to the loaded resin, and let shaken for 12 h. The resin was washed, deprotected, and additionally washed as described above. Coupling of amino acids (800 µmol, 4.00 equiv.), deprotection, and washing were repeated until the desired peptide was synthesized. After coupling of the last amino acid, removing the *N*-Alloc-protecting group was carried out using tetrakis(triphenylphosphine)palladium (23.1 mg, 20.0 µmol, 0.100 equiv.) and phenyl silane (335 mg, 382 µL, 3.00 mmol, 15.0 equiv.) dissolved in dry dichloromethane (2.5 mL). The mixture was added to the resin and was left shaking for 20 min. The procedure was repeated three times. After washing with dichloromethane, methanol, and *N*,*N*-dimethylformamide, 3-Carboxy-2,2,5,5-tetramethylpyrrolin-1-yloxyl radical (147 mg, 800 µmol, 4.00 equiv.) and HATU (306 mg, 800 µmol, 4.00 equiv.) dissolved in 2.5 mL of *N*,*N*-dimethylformamide were added to the resin, and the mixture was left shaking for 24 h. Subsequently, the *N* terminal Fmoc-protecting group was removed using a solution of 20% piperidine in *N*,*N*-dimethylformamide (3 x 3 mL for 5 min each). The last washing step was followed by washing with dichloromethane (3 x 2.5 mL). Subsequently, 2.5 mL of a solution of 33% hexafluoro isopropanol in dichloromethane was added. The resin was incubated with the cleavage cocktail twice for 1 h. The solvent was collected, and the resin was flushed with dichloromethane five times. The solvent was removed under an air stream resulting in the crude linear precursor. Deprotection of the *N*-Pbf- and *N*-Boc-protecting group was carried out in the

liquid phase. Therefore, the crude peptide was dissolved in 5 mL of 2,2,2-trifluoroacetic acid, phenol, water, and triisopropylsilane (88%:5%:5%:2% (v/v)). The mixture was stirred for 3 h at 21 °C. After completion, the peptide was precipitated with 15 mL of cold diethyl ether, filtered off, and washed with diethyl ether (1 x 10 mL). The desired peptide (49.8 mg, 0.08 mmol, 39%) was isolated as a white solid.

MS (MALDI-TOF), m/z (%): 640 $[M+H]^+$.

Additional data supporting the chemical synthesis results is available *via* the Chemotion repository: https://doi.org/10.14272/reaction/SA-FUHFF-UHFFFADPSC-GXXOJJSMTD-UHFFF

5.2.4 Synthesis Procedures for Chapter 3.4

Methyl 3-azido-4-iodobenzoate (84)

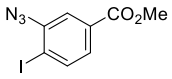

To a solution of methyl 3-amino-4-iodo-benzoate (1.00 g, 3.61 mmol, 1.00 equiv.) in 24 mL of acetonitrile, 4 mL of *N*,*N*-dimethylformamide, and 10% aqueous sulfuric acid (7.08 g, 6.64 mL, 7.22 mmol, 2.00 equiv.) was added dropwise a solution of sodium nitrite (299 mg, 4.33 mmol, 1.20 equiv.) in 4 mL of water at 0 °C. The reaction mixture was stirred at the same temperature for 30 min. Then, a solution of sodium azide (282 mg, 4.33 mmol, 1.20 equiv.) dissolved in 4 mL of water was added dropwise to the mixture at 0 °C. The mixture was allowed to warm to 21 °C and stirred for further 30 min. The resulting mixture was diluted with water and extracted with ethyl acetate (3 x 50 mL). The combined organic phases were washed with brine, dried over Na_2SO_4, and concentrated in vacuo. The residue was purified using flash chromatography on silica gel (cyclohexane/ ethyl acetate 10:1) to obtain methyl 3-azido-4-iodobenzoate (962 mg, 3.17 mmol, 88% yield) as an orange solid.

R_f = 0.47 (cyclohexane/ethyl acetate (8:1)).

^{1}H NMR (400 MHz, Chloroform-*d* [7.26 ppm], ppm) δ = 7.90–7.87 (m, 1H, CH_{ar}), 7.77 (d, *J* = 1.8 Hz, 1H, CH_{ar}), 7.50 (dd, *J* = 8.2 Hz, *J* = 1.8 Hz, 1H, CH_{ar}), 3.96–3.93 (s, 3H, CH_3).

^{13}C NMR (100 MHz, Chloroform-*d* [77.2 ppm], ppm) δ = 165.8 (C_q), 142.4 (C_q), 140.3 (*C*H, C_{ar}), 131.8 (C_q), 126.8 (*C*H, C_{ar}), 118.9 (*C*H, C_{ar}), 94.0 (C_q), 52.6 (*C*H$_3$).

MS (ESI), m/z (%): 304 (100) $[M+H]^+$, 278 (8), 276 (27) $[M–N_2+H]^+$.

HRMS (ESI, DCM): *m/z* = calcd. for $C_{10}H_{10}NO_2$ $[M+H]^+$: 303.9577, found 303.9572.

IR (ATR, ṽ) = 2945 (w), 2111 (vs), 1706 (vs), 1581 (m), 1562 (s), 1472 (m), 1449 (w), 1432 (s), 1408 (w), 1392 (m), 1383 (s), 1307 (s), 1299 (s), 1258 (vs), 1191 (m), 1152 (w), 1142 (w), 1113 (vs), 1018 (vs), 972 (s), 908 (w), 891 (s), 846 (m), 793 (s), 756 (vs), 705 (vs), 650 (m), 555 (w), 527 (s), 482 (w), 445 (w), 426 (m), 384 (m) cm^{-1}.

Additional data supporting the chemical synthesis results is available *via* the Chemotion repository: https://dx.doi.org/10.14272/reaction/SA-FUHFF-UHFFFADPSC-QMAWGTDJFQ-UHFFFADPSC-NUHFF-NUHFF-NUHFF-ZZZ

Methyl 3-amino-4-((4-(methoxycarbonyl)phenyl)ethynyl)benzoate (87)

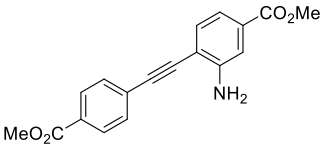

Methyl 3-amino-4-iodo-benzoate (150 mg, 541 µmol, 1.00 equiv.), methyl 4-ethynylbenzoate (104 mg, 650 µmol, 1.20 equiv.), copper(I) iodide (5.16 mg, 27.1 µmol, 0.0500 equiv.) and bis(triphenylphosphine)palladium chloride (19.0 mg, 27.1 µmol, 0.0500 equiv.) and triphenylphosphine (14.2 mg, 54.1 µmol, 0.100 equiv.) were dissolved under an argon atmosphere in 5 mL of dry 1,4-dioxane. The mixture was heated to 60 °C for 16 h. After completion, the mixture was let cool down to 21 °C and was diluted with dichloromethane. The solids were removed by filtration and the residue was purified by flash column chromatography (cyclohexane/ ethyl acetate 4:1) to obtain methyl 3-amino-4-((4-(methoxycarbonyl)phenyl)ethynyl)benzoate (125 mg, 404 µmol, 75% yield) as a yellow solid.

R_f = 0.29 (cyclohexane/ethyl acetate (4:1)).

^{1}H NMR (400 MHz, Dichloromethane-d_2 [5.32 ppm], ppm) δ = 8.07 (d, J = 8.5 Hz, 2H, CH_{ar}), 7.66 (d, J = 8.5 Hz, 2H, CH_{ar}), 7.48–7.46 (m, 1H, CH_{ar}), 7.44 (d, J = 1.5 Hz, 1H, CH_{ar}), 7.39–7.37 (m, 1H, CH_{ar}), 4.52 (br. s, 2H), 3.95 (s, 3H, CH_3), 3.91 (s, 3H, CH_3).

Impurity: Signal at 1.58 ppm due to residues of water.

^{13}C NMR (100 MHz, Dichloromethane-d_2 [53.8 ppm], ppm) δ = 166.5 (C_q), 166.2 (C_q), 148.1 (C_q), 132.2 (*C*H, C_{ar}), 131.5 (C_q), 131.4 (*C*H, 2C, C_{ar}), 130.0 (C_q), 129.5 (*C*H, 2C, C_{ar}), 127.3 (C_q), 118.4 (*C*H ,C_{ar}), 115.0 (*C*H ,C_{ar}), 111.2 (*C*H, C_{ar}), 96.0 (C_q), 88.0 (C_q), 52.1 (*C*H$_3$), 52.1 (*C*H$_3$).

MS (ESI), m/z (%): 310 (13) $[M+H]^+$, 282 (8), 274 (7), 243 (40), 222 (15), 221 (100), 185 (19), 158 (13), 157 (6), 100 (7).

HRMS (ESI, DCM): *m/z* = calcd. for $C_{18}H_{16}NO_4^+$ $[M+H]^+$ 310.1074, found 310.1072.

IR (ATR, ṽ) = 3370 (w), 2956 (w), 2925 (w), 2901 (w), 2877 (w), 2842 (w), 2201 (w), 1721 (vs), 1679 (m), 1613 (s), 1605 (s), 1561 (m), 1513 (w), 1494 (w), 1428 (vs), 1402 (m), 1329 (m), 1305 (s), 1289 (m), 1272 (vs), 1230 (vs), 1191 (s), 1174 (s), 1145 (m), 1103 (vs), 1057 (m), 1014 (m), 986 (w), 973 (m), 950 (m), 926 (w), 914 (w), 881 (m), 857 (s), 840 (w), 810 (m), 793 (w), 759 (vs), 728 (m), 711 (w), 693 (s), 523 (w), 477 (m), 433 (w), 378 (w) cm^{-1}.

UV-VIS (abs., DCM, 21 °C), λ_{max} = 365, 313, 304, 295, 255, 233, 219 nm.

Additional data supporting the chemical synthesis results is available *via* the Chemotion repository: https://dx.doi.org/10.14272/reaction/SA-FUHFF-UHFFFADPSC-ZPVLMZHGEP-UHFFFADPSC-NUHFF-NUHFF-NUHFF-ZZZ

Methyl 3-azido-4-((4-(methoxycarbonyl)phenyl)ethynyl)benzoate (86)

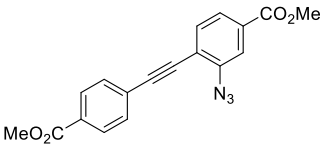

To a solution of methyl 3-amino-4-((4-(methoxycarbonyl)phenyl)ethynyl)benzoate (70.0 mg, 226 µmol, 1.00 equiv.) in 2 mL of acetonitrile, 300 µL of *N*,*N*-dimethylformamide and 700 µL of 10% aqueous H_2SO_4 was added dropwise a solution of $NaNO_2$ (18.7 mg, 272 µmol, 1.20 equiv.) in water (0.3 mL) at 0 °C. The reaction mixture was stirred at the same temperature for 30 min. Then, a solution of sodium azide (17.7 mg, 272 µmol, 1.20 equiv.) in water (0.3 mL) was added dropwise to the mixture at 0 °C. The mixture was allowed to warm to 21 °C and stirred for 1.5 h. The mixture was diluted with water (30 mL) and extracted with ethyl acetate (3 x 20 mL). The combined organic phases were washed with sat. NaCl solution, dried over Na_2SO_4, and concentrated in vacuo. The residue was purified by flash chromatography (cyclohexane/ ethyl acetate 8:1) to obtain methyl 3-azido-4-((4-(methoxycarbonyl)phenyl)ethynyl)benzoate (42.0 mg, 125 µmol, 55% yield) as an off-white solid.

R_f = 0.34 (cyclohexane/ethyl acetate (8:1)).

^{1}H NMR (400 MHz, Chloroform-*d* [7.26 ppm], ppm) δ = 8.07 (d, *J* = 8.5 Hz, 2H, CH_{ar}), 7.84 (d, *J* = 1.3 Hz, 1H, CH_{ar}), 7.82–7.80 (m, 1H, CH_{ar}), 7.66 (d, *J* = 8.6 Hz, 2H, CH_{ar}), 7.60 (d, *J* = 8.0 Hz, 1H, CH_{ar}), 3.97 (s, 3H, CH_3), 3.96 (s, 3H, CH_3)

Impurities: Signals at 1.62 ppm due to water, at 1.26 ppm due to H–grease and at 0.08 ppm due to silicone grease.

^{13}C NMR (100 MHz, Chloroform-*d* [77.2 ppm], ppm) δ = 166.4 (C_q), 165.7 (C_q), 141.5 (C_q), 133.7 (*C*H, C_{ar}), 131.7 (*C*H, 2C, C_{ar}), 131.4 (C_q), 130.2 (C_q), 129.6 (*C*H, 2C, C_{ar}), 127.0 (C_q), 125.6 (*C*H, C_{ar}), 119.8 (*C*H, C_{ar}), 119.2 (C_q), 97.0 (C_q), 87.1 (C_q), 52.6 (CH_3), 52.3 (CH_3)

Impurity: Signal at 29.7 ppm due to H–grease.

MS (ESI), m/z (%): 336 (14) $[M+H]^+$, 308 (8) $[M+H–N2]^+$, 282 (9) $[C_{17}H_{14}O_4]^+$, 222 (14), 221 (100), 177 (5), 165 (7), 122 (8), 120 (7), 115 (6), 109 (5), 105 (25), 100 (14).

HRMS (ESI, DCM): *m/z* = calcd. for $C_{18}H_{14}N_3O_4^+$ $[M+H]^+$ 336.0979, found 336.0975.

IR (ATR, ṽ) = 3061 (w), 2958 (w), 2918 (w), 2873 (w), 2849 (w), 2109 (vs), 2041 (w), 1727 (vs), 1718 (vs), 1630 (vw), 1605 (s), 1558 (m), 1492 (w), 1463 (w), 1441 (s), 1404 (vs), 1375 (w), 1340 (w), 1322 (m), 1307 (m), 1289 (vs), 1282 (vs), 1269 (vs), 1248 (vs), 1196 (s), 1177 (s), 1153 (m), 1142 (s), 1108 (vs), 1084 (s), 1016 (s), 982 (s), 959 (m), 909 (w), 895 (s), 856 (s), 841 (s), 815 (m), 800 (s), 761 (vs), 731 (m), 718 (s), 690 (vs), 654 (m), 633 (w), 586 (w), 523 (m), 490 (w), 475 (m), 452 (m), 397 (m), 381 (w) cm^{-1}.

Additional data supporting the chemical synthesis results is available *via* the Chemotion repository: https://dx.doi.org/10.14272/reaction/SA-FUHFF-UHFFFADPSC-KBIMIOCTDZ-UHFFFADPSC-NUHFF-NUHFF-NUHFF-ZZZ

3-Azido-4-((4-carboxyphenyl)ethynyl)benzoic acid (79)

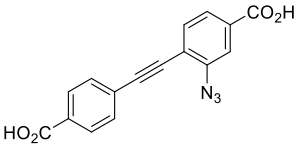

Methyl 3-azido-4-((4-(methoxycarbonyl)phenyl)ethynyl)benzoate (161 mg, 480 µmol, 1.00 equiv.) and lithium hydroxide (230 mg, 9.60 mmol, 20.0 equiv.) were suspended in a mixture of 3 mL of methanol, 3 mL of tetrahydrofuran and 2 mL of water. The obtained suspension was stirred for 4 d at 21 °C. After completion, 1M HCl was added to achieve a pH of 4. Subsequently, ethyl acetate (15 mL) was added, and the phases were separated. The aqueous phase was extracted with ethyl acetate (3 x 10 mL). The combined organic layers were dried over Na_2SO_4. The solvent was removed under reduced pressure to obtain 3-azido-4-((4-carboxyphenyl)ethynyl)benzoic acid (120 mg, 391 µmol, 81% yield) as an off-white solid.

^{1}H NMR (400 MHz, DMSO-d_6 [2.50 ppm], ppm) δ = 8.01–8.00 (m, 2H, CH_{ar}), 7.77–7.73 (m, 3H, CH_{ar}), 7.72–7.69 (m, 2H, CH_{ar}).

Missing signals: COO*H* (2H) due to H/D exchange.

Impurity: unknown impurity at 7.97 ppm.

^{13}C NMR (100 MHz, DMSO-d_6 [39.5 ppm], ppm) δ = 167.1 (C_q), 166.4 (C_q), 141.6 (C_q), 134.2 (*C*H, C_{ar}), 132.9 (C_q), 132.1 (*C*H, 2C, C_{ar}), 131.6 (C_q), 130.1 (CH, 2C, C_{ar}), 126.3 (C_q), 126.0 (*C*H, C_{ar}), 120.3 (*C*H, C_{ar}), 118.1 (C_q), 96.7 (C_q), 87.6 (C_q).

Impurities: unknown impurities at 133.2 and 130.1 ppm.

MS (ESI), m/z (%): 306 (100) $[M-H]^-$.

Unknown adducts 362 (22), 360 (31), 358 (13), 324 (19), 310 (45).

HRMS (ESI, MeCN): *m/z* = calcd. for $C_{16}H_8N_3O_4^-$ $[M–H]^-$: 306.0520, found 306.0523.

IR (ATR, $\tilde{\nu}$) = 3337 (w), 3067 (w), 3050 (w), 2922 (m), 2883 (m), 2853 (m), 2657 (w), 2534 (w), 2529 (w), 2119 (s), 1681 (vs), 1605 (vs), 1551 (m), 1519 (w), 1486 (w), 1421 (vs), 1405 (vs), 1312 (s), 1279 (vs), 1179 (s), 1145 (s), 1123 (s), 1112 (s), 1052 (vs), 1017 (s), 914 (s), 898 (s), 857 (s), 833 (s), 790 (s), 765 (vs), 721 (s), 688 (s), 653 (m), 632 (s), 611 (m), 578 (s), 550 (vs), 520 (vs), 492 (s), 475 (s), 438 (m), 418 (s), 385 (m) cm^{-1}.

Additional data supporting the chemical synthesis results is available *via* the Chemotion repository: https://dx.doi.org/10.14272/reaction/SA-FUHFF-UHFFFADPSC-FDEUJHWKMU-UHFFFADPSC-NUHFF-NUHFF-NUHFF-ZZZ

Methyl 3-amino-4-((trimethylsilyl)ethynyl)benzoate (89)

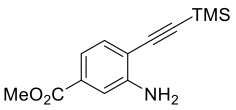

To a round bottom flask was added methyl 3-amino-4-iodo-benzoate (1.75 g, 6.32 mmol, 1.00 equiv.), bis(triphenylphosphine)palladium chloride (222 mg, 316 µmol, 0.0500 equiv.), and copper(I) iodide (60.1 mg, 316 µmol, 0.0500 equiv.). The vessel was sealed with a rubber septum, evacuated and backfilled with argon three times. Subsequently, the solids were dissolved in 15 mL of triethylamine, and trimethylsilyl acetylene (931 mg, 1.31 mL, 9.47 mmol, 1.50 equiv.) was added. The reaction mixture was stirred for 3 h at 60 °C. After completion, the reaction was let cool down to room temperature. Solids were removed by filtration, the solvent was removed under reduced pressure and the resulting crude product was directly purified by flash column chromatography (cyclohexane/ethyl acetate 4:1) to isolate the methyl 3-amino-4-((trimethylsilyl)ethynyl)benzoate (1.51 g, 6.11 mmol, 97% yield) as a yellow solid.

R_f = 0.21 (cyclohexane/ethyl acetate (6:1)).

^{1}H NMR (400 MHz, Chloroform-*d* [7.26 ppm], ppm) δ = 7.39 (d, *J* = 0.6 Hz, 1H, CH_{ar}), 7.35–7.34 (m, 2H, CH_{ar}), 3.90 (s, 3H, CH_3), 0.29 (s, 9H, CH_3).

Missing Signal: Amine protons of N*H*2 (2H) due to H/D exchange.

Impurities: unknown impurities at 7.37 ppm and 7.32 ppm.

^{13}C NMR (100 MHz, Chloroform-*d* [77.2 ppm], ppm) δ = 166.8 (*C*O), 148.1 (C_q), 132.2 (*C*H, C_{ar}), 131.0 (C_q), 118.6 (*C*H, C_{ar}), 114.9 (*C*H, C_{ar}), 112.0 (C_q), 102.7 (C_q), 100.9 (C_q), 52.2 (*C*H_3), 0.0 (*C*H_3, 3C).

MS (ESI), m/z (%): 293 (69) $[M+2\ Na]^+$, 279 (87) $[M+CH_3OH+H]^+$, 274 (93) , 248 (100) $[M+H]^+$, 146 (65), 102 (27).

Unknown adducts at 389 (27) and 297 (42).

HRMS (ESI, DCM): *m/z* = calcd. for $C_{13}H_{18}NO_2Si^+$ $[M+H]^+$: 248.1101, found 248.1093.

IR (ATR, $\tilde{\nu}$) = 3479 (w), 3380 (m), 2951 (w), 2897 (vw), 2145 (w), 1701 (vs), 1618 (m), 1599 (w), 1570 (w), 1558 (w), 1534 (vw), 1499 (w), 1438 (vs), 1429 (s), 1329 (m), 1293 (vs), 1247 (vs), 1211 (s), 1145 (w), 1113 (m), 1067 (w), 996 (w), 915 (w), 904 (w), 837 (vs), 802 (s), 783 (m), 764 (vs), 756 (vs), 730 (s), 696 (m), 667 (s), 622 (m), 598 (w), 581 (w), 565 (w), 540 (m), 520 (w), 511 (w), 496 (s), 439 (m), 416 (m), 404 (m), 392 (m) cm^{-1}.

UV-VIS (abs., DCM, 21 °C), λ_{max} = 349, 282, 273, 241, 217 nm.

Additional data supporting the chemical synthesis results is available *via* the Chemotion repository: https://dx.doi.org/10.14272/reaction/SA-FUHFF-UHFFFADPSC-FXENPAIIAX-UHFFFADPSC-NUHFF-NUHFF-NUHFF-ZZZ.1

Methyl 3-amino-4-ethynyl-benzoate (**90**)

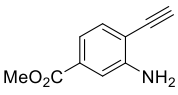

Methyl 3-amino-4-((trimethylsilyl)ethynyl)benzoate (1.50 g, 6.06 mmol, 1.00 equiv.) was dissolved in 15 mL of methanol. Subsequently, K_2CO_3 (1.26 g, 9.10 mmol, 1.50 equiv.) was added and the resulting suspension was stirred at 21 °C for 3 h. After completion, water (50 mL) was added, and the aqueous phase was extracted with dichloromethane (3 x 20 mL). The solvent was removed under reduced pressure and the crude product was purified by column chromatography (cyclohexane/ ethyl acetate 4:1) to obtain methyl 3-amino-4-ethynyl-benzoate (901 mg, 5.14 mmol, 85% yield) as a yellow solid.

R_f = 0.31 (cyclohexane/ethyl acetate (4:1)).

^{1}H NMR (400 MHz, Chloroform-*d* [7.26 ppm], ppm) δ = 7.41 (d, *J* = 0.8 Hz, 1H, CH_{ar}), 7.39 (s, 1H, CH_{ar}), 7.37–7.34 (m, 1H, CH_{ar}), 3.91 (s, 3H, CH_3), 3.54 (s, 1H, C*H*).

Missing signal: Amine protons of NH_2 (2H) due to H/D exchange.

Impurity: Signal at 1.43 ppm due to residues of cyclohexane.

^{13}C NMR (100 MHz, Chloroform-*d* [77.2 ppm], ppm) δ = 166.8 (*C*O), 148.4 (C_q), 132.6 (*C*H, C_{ar}), 131.3 (C_q), 118.6 (*C*H, C_{ar}), 115.1 (*C*H, C_{ar}), 110.8 (C_q), 84.8 (*C*H), 79.9 (C_q), 52.2 (*C*H_3).

MS (ESI), m/z (%): 176 (100) $[M+H]^+$, 139 (8).

Unknown adduct at 195 (26).

HRMS (ESI, DCM): *m/z* = calcd. for $C_{10}H_{10}NO_2^+$ $[M+H]^+$: 176.0706, found 176.0701.

IR (ATR, $\tilde{\nu}$) = 3473 (m), 3376 (s), 3251 (s), 2995 (w), 2951 (w), 2928 (w), 2847 (w), 1708 (vs), 1625 (vs), 1601 (m), 1561 (s), 1502 (s), 1463 (w), 1434 (vs), 1327 (s), 1278 (w), 1241 (vs), 1194 (s), 1139 (s), 1105 (vs), 1062 (m), 982 (m), 956 (m), 938 (m), 878 (s), 837 (m), 830 (m), 796 (m), 759 (vs), 731 (s), 707 (vs), 643 (vs), 592 (s), 578 (s), 543 (m), 531 (m), 503 (s), 484 (vs), 455 (vs), 425 (s), 416 (m), 409 (m), 385 (vs) cm^{-1}.

UV-VIS (abs., DCM, 21 °C), λ_{max} = 345, 273, 266, 237 nm.

Additional data supporting the chemical synthesis results is available *via* the Chemotion repository: https://dx.doi.org/10.14272/reaction/SA-FUHFF-UHFFFADPSC-ILQZKIKAPV-UHFFFADPSC-NUHFF-NUHFF-NUHFF-ZZZ.1

Dimethyl 4,4'-(ethyne-1,2-diyl)bis(3-aminobenzoate) (91)

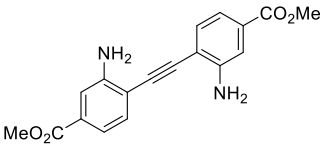

Methyl 3-amino-4-bromo-benzoate (3.74 g, 16.3 mmol, 1.00 equiv.), methyl 3-amino-4-ethynyl-benzoate (3.00 g, 17.1 mmol, 1.05 equiv.), bis(triphenylphosphine)palladium chloride (1.14 g, 1.63 mmol, 0.100 equiv) and copper(I) iodide (310 mg, 1.63 mmol, 0.100 equiv.) were dissolved in 40 mL of triethylamine under an argon atmosphere. The reaction was stirred at 60 °C for 16 h. Afterward, the yellow precipitate was separated by filtration and washed with ethyl acetate (200 mL), water (200 mL) and methanol (50 mL) to obtain dimethyl 4,4'-(ethyne-1,2-diyl)bis(3-aminobenzoate) (3.08 g, 9.50 mmol, 58% yield) as a yellow solid.

R_f = 0.74 (ethyl acetate).

^{1}H NMR (400 MHz, DMSO-d_6 [2.50 ppm], ppm) δ = 7.50 (d, *J* = 7.6 Hz, 2H, CH_{ar}), 7.39 (s, 2H, CH_{ar}), 7.11 (d, *J* = 7.4 Hz, 2H, CH_{ar}), 5.85 (br. s, 4H, NH_2), 3.83 (s, 6H, CH_3).

Impurity: Signal at 3.33 ppm due to residues of water.

^{13}C NMR (100 MHz, DMSO-d_6 [39.5 ppm], ppm) δ = 166.7 (*C*O, 2C), 149.8 (C_q, 2C), 133.0 (*C*H, 2C, C_{ar}), 130.6 (C_q, 2C), 116.4 (*C*H, 2C, C_{ar}), 115.0 (*C*H, 2C, C_{ar}), 110.7 (C_q, 2C), 93.6 (C_q, 2C), 52.5 (*C*H_3, 2C).

MS (ESI), m/z (%): 294 (11) $[M–CH_3O]^+$, 243 (7), 222 (5), 221 (35), 148 (6), 147 (100) $[C_{17}H_{15}N_2O_3]^{2+}$, 122 (8), 102 (13), 100 (9).

Unknown adduct at 355 (3).

HRMS (ESI, MeCN): *m/z* = calcd. for $C_{18}H_{17}N_2O_4$ $[M+H]^+$: 325.1183 , found 325.1176.

IR (ATR, $\tilde{\nu}$) = 3444 (w), 3354 (m), 2956 (w), 1701 (vs), 1622 (s), 1561 (m), 1510 (m), 1438 (s), 1432 (s), 1327 (vs), 1303 (vs), 1271 (m), 1232 (vs), 1194 (s), 1152 (w), 1132 (s), 1103 (vs), 1072 (m), 1000 (w), 979 (m), 955 (w), 933 (w), 919 (w), 884 (s), 836 (m), 813 (m), 790 (w), 762 (vs), 731 (s), 673 (w), 663 (w), 647 (w), 636 (w), 612 (w), 601 (w), 596 (w), 582 (m), 568 (m), 558 (m), 548 (m), 489 (s), 462 (vs), 431 (vs), 409 (s) cm^{-1}.

UV-VIS (abs., DMSO, 21 °C), λ_{max} = 409, 310, 252 nm.

Additional data supporting the chemical synthesis results is available *via* the Chemotion repository: https://dx.doi.org/10.14272/reaction/SA-FUHFF-UHFFFADPSC-XQVYASICMD-UHFFFADPSC-NUHFF-NUHFF-NUHFF-ZZZ.1

Dimethyl 4,4'-(ethyne-1,2-diyl)bis(3-azidobenzoate) (92)

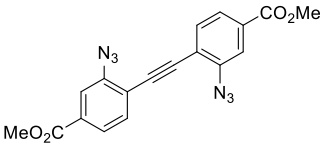

p-Toluenesulfonic acid monohydrate (1.76 g, 9.25 mmol, 6.00 equiv.) was dissolved in 27 mL of acetonitrile at 0 °C. Once dissolved, *tert*-butyl nitrite (954 mg, 1.10 mL, 9.25 mmol, 6.00 equiv.) was added followed by dimethyl 4,4'-(ethyne-1,2-diyl)bis(3-aminobenzoate) (500 mg, 1.54 mmol, 1.00 equiv.) portion-wise. The obtained suspension was stirred at 0 °C for 30 min. Then, a solution of sodium azide (601 mg, 9.25 mmol, 6.00 equiv.) in 2 mL of water was added dropwise to the mixture. The mixture was allowed to warm to 21 °C and was stirred further for 2 h. The solution was diluted with water (50 mL) and extracted with ethyl acetate (3 x 50 mL). The combined organic phases were washed with sat. NaCl solution, dried over Na_2SO_4, and concentrated in vacuo. The residue was purified by column chromatography (cyclohexane/ethyl acetate 9:1) to obtain dimethyl 4,4'-(ethyne-1,2-diyl)bis(3-azidobenzoate) (221 mg, 587 µmol, 38% yield) as a yellow solid.

R_f = 0.31 (cyclohexane/ethyl acetate (9:1)).

^{1}H NMR (400 MHz, Dichloromethane-d_2 [5.32 ppm], ppm) δ = 7.87 (d, J = 1.4 Hz, 2H, CH_{ar}), 7.82 (dd, J = 8.0 Hz, J = 1.5 Hz, 2H, CH_{ar}), 7.65 (d, J = 8.1 Hz, 2H, CH_{ar}), 3.96 (s, 6H, CH_3).

Impurity: Signal at 1.58 ppm due to residues of water.

^{13}C NMR (100 MHz, Dichloromethane-d_2 [53.8 ppm], ppm) δ = 165.4 (*C*O, 2C), 141.7 (C_q, 2C), 133.6 (*C*H, 2C, C_{ar}), 131.8 (C_q, 2C), 125.5 (*C*H, 2C, C_{ar}), 119.7 (*C*H, 2C, C_{ar}), 118.7 (C_q, 2C), 92.5 (C_q, 2C), 52.4 (*C*H_3, 2C).

MS (ESI), m/z (%): 349 (29) $[M+H–N_2]^+$, 321 (11) $[M+H–2\ N_2]^+$, 294 (7), 282 (5), 222 (15), 221 (100), 165 (6), 147 (21), 123 (5), 122 (7), 102 (14), 100 (8).

HRMS (ESI, DCM): *m/z* = calcd. for $C_{18}H_{13}N_4O_4^+$ $[M+H–N_2]^+$ 349.0931, found 349.0921.

IR (ATR, ṽ) = 3064 (w), 3009 (w), 2956 (w), 2109 (vs), 2101 (vs), 2013 (w), 1730 (vs), 1686 (w), 1602 (m), 1558 (m), 1514 (w), 1443 (m), 1408 (vs), 1327 (m), 1289 (vs), 1269 (vs), 1248 (vs), 1194 (s), 1149 (vs), 1122 (vs), 1088 (s), 986 (s), 897 (vs), 847 (w), 836 (s), 798 (s), 756 (vs), 720 (s), 659 (s), 639 (m), 602 (w), 586 (w), 569 (w), 543 (w), 530 (m), 507 (w), 465 (m), 435 (w), 411 (s), 391 (w) cm^{-1}.

UV-VIS (abs., DMSO, 21 °C), λ_{max} = 360, 346, 310, 257, 217 nm.

Additional data supporting the chemical synthesis results is available *via* the Chemotion repository: https://dx.doi.org/10.14272/reaction/SA-FUHFF-UHFFFADPSC-GBYBCSVIRP-UHFFFADPSC-NUHFF-NUHFF-NUHFF-ZZZ

4,4'-(Ethyne-1,2-diyl)bis(3-azidobenzoic acid) (**80**)

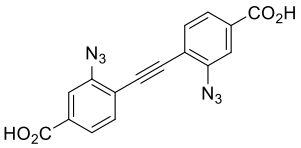

Dimethyl 4,4'-(ethyne-1,2-diyl)bis(3-azidobenzoate) (500 mg, 1.33 mmol, 1.00 equiv.) and lithium hydroxide (636 mg, 26.6 mmol, 20.0 equiv.) were stirred at 21 °C for 4 d in 20 mL of methanol, 30 mL of tetrahydrofuran and water 10 mL of water. After completion, 1M HCl was added to acidify the reactions mixture. Ethyl acetate (50 mL) was added, and the phases were separated. The aqueous phase was extracted with ethyl acetate (3 x 20 mL). The combined organic layers were dried over Na_2SO_4. the solvent was removed under reduced pressure to obtain 4,4'-(ethyne-1,2-diyl)bis(3-azidobenzoic acid) (353 mg, 1.01 mmol, 76% yield) as a dark yellow solid.

^{1}H NMR (400 MHz, DMSO-d_6 [2.50 ppm], ppm) δ = 7.77–7.69 (m, 6H; CH_{ar}).

Missing signals: COO*H* (2H) due to H/D exchange.

Impurity: Signal at 3.34 ppm due to residues of water.

^{13}C NMR (100 MHz, DMSO-d_6 [39.5 ppm], ppm) δ = 166.4 (C_q, 2C), 141.6 (C_q, 2C), 134.1 (*C*H, 2C, C_{ar}), 133.1 (C_q, 2C), 126.1 (*C*H, 2C, C_{ar}), 120.3 (*C*H, 2C, C_{ar}), 117.8 (C_q, 2C), 92.7 (C_q, 2C).

MS (ESI), m/z (%): 347 (49) $[M–H]^-$, 173 (12) $[M–2\ H]^-$, 171 (16), 169 (10), 155 (8), 113 (100).

Unknown adducts at 383 (6) and 371 (8).

HRMS (ESI, MeOH): *m/z* = calcd. for $C_{16}H_7N_6O_4^-$ $[M-H]^-$: 347.0534, found: 347.0531.

IR (ATR, $\tilde{\nu}$) = 2978 (vw), 2857 (vw), 2653 (vw), 2524 (vw), 2123 (vs), 1691 (vs), 1606 (m), 1551 (m), 1421 (vs), 1405 (vs), 1339 (w), 1290 (vs), 1251 (vs), 1150 (m), 1127 (w), 1088 (m), 913 (m), 835 (w), 761 (vs), 693 (m), 638 (w), 568 (w), 518 (m), 465 (w), 413 (w) cm^{-1}.

UV-VIS (abs., DMSO, 21 °C), λmax = 345, 311, 256 nm.

Additional data supporting the chemical synthesis results is available *via* the Chemotion repository: https://dx.doi.org/10.14272/reaction/SA-FUHFF-UHFFFADPSC-SFAKHHLHLL-UHFFFADPSC-NUHFF-NUHFF-NUHFF-ZZZ

5.2.5 Synthesis Procedures for Chapter 3.5

4-(2-Phenylethynyl)phenol (100)

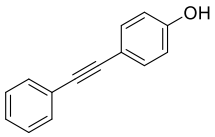

A vial was charged with 4-iodophenol (500 mg, 2.27 mmol, 1.00 equiv.), bis(triphenylphosphine)palladium chloride (31.9 mg, 45.5 µmol, 0.0200 equiv.), triphenylphosphine (11.9 mg, 45.5 µmol, 0.0200 equiv.) and copper(I) iodide (8.66 mg, 45.5 µmol, 0.0200 equiv.). Subsequently, the flask was evacuated and refiled with argon, the procedure was repeated three times. The solids were dissolved in 3 ml of dry tetrahydrofuran and 2 mL of triethylamine. After complete dissolution ethynylbenzene (279 mg, 300 µL, 2.73 mmol, 1.20 equiv.) was added and the mixture was stirred for 24 h at 60 °C. After completion the reaction was allowed to cool to 21 °C, and water was added. The mixture was extracted with ethyl acetate (3 x 30 mL), and the obtained organic phase was washed with water (3 x 30 mL) and dried over Na_2SO_4. The crude product was purified by column chromatography (cyclohexane/ ethyl acetate 9:1) to obtain 4-(2-phenylethynyl)phenol (275 mg, 1.42 mmol, 62% yield) as a light yellow solid.

R_f = 0.21 (cyclohexane/ethyl acetate (8:1)).

^{1}H NMR (400 MHz, Chloroform-*d* [7.26 ppm], ppm) δ = 7.45–7.40 (m, 2H, CH_{ar}), 7.36–7.32 (m, 2H, CH_{ar}), 7.29–7.20 (m, 3H, CH_{ar}), 6.73–6.70 (m, 2H, CH_{ar}), 5.12 (br. s, 1H, O*H*) Impurity: Signals at 4.12 ppm, 2.05 ppm and 1.26 ppm due to residues of ethyl acetate.

^{13}C NMR (100 MHz, Chloroform-*d* [77.2 ppm], ppm) δ = 155.6 (C_q), 133.3 (*C*H, 2C, C_{ar}), 131.5 (*C*H, 2C, C_{ar}), 128.4 (*C*H, 2C, C_{ar}), 128.1 (*C*H, C_{ar}), 123.5 (C_q), 115.7 (C_q), 115.6 (*C*H, 2C, C_{ar}), 89.3 (C_q), 88.1 (C_q).

MS (EI, 70 eV, 60 °C), m/z (%): 194 (100) $[M]^+$.

HRMS (EI): *m/z* = calcd. for $C_{14}H_{10}O$ $[M]^+$: 194.0726; found 194.0727.

IR (ATR, $\tilde{\nu}$) = 3398 (m), 3391 (m), 3383 (m), 3377 (m), 3344 (m), 3306 (m), 1606 (m), 1588 (m), 1509 (vs), 1435 (s), 1368 (m), 1350 (m), 1238 (vs), 1173 (m), 1166 (m), 1137 (m), 1101 (s), 1069 (m), 1023 (m), 1014 (m), 999 (w), 912 (m), 832 (vs), 798 (m), 748 (vs), 686 (vs), 662 (m), 647 (m), 629 (w), 622 (w), 602 (w), 595 (w), 582 (m), 548 (m), 537 (m), 517 (vs), 499 (vs), 475 (vs), 443 (s), 422 (s), 412 (s), 402 (s), 390 (s) cm^{-1}.

UV-VIS (abs., DCM, 21 °C), λ_{max} = 306, 288, 218 nm.

Additional data supporting the chemical synthesis results is available *via* the Chemotion repository: https://dx.doi.org/10.14272/reaction/SA-FUHFF-UHFFFADPSC-NVUNTCDLAQ-UHFFFADPSC-NUHFF-NUHFF-NUHFF-ZZZ

Methyl 4-(2-phenylethynyl)benzoate (**102**)

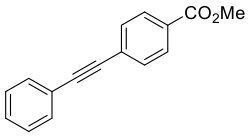

A round bottom flask was charged with methyl 4-iodanylbenzoate (500 mg, 1.85 mmol, 1.00 equiv.), copper(I) iodide (7.05 mg, 37.0 µmol, 0.02 equiv.), bis(triphenylphosphine)palladium chloride (26.5 mg, 37.0 µmol, 0.02 equiv.) and triphenylphosphine (4.62 mg, 17.6 µmol, 0.01 equiv.). Subsequently, the flask was evacuated and refilled with argon; the procedure was repeated three times. The solids were dissolved in 7 ml of dry tetrahydrofuran and 3 mL of triethylamine. After complete, dissolution ethynylbenzene (198 mg, 213 µL, 1.94 mmol, 1.05 equiv.) was added and the mixture was stirred for 24 h at 60 °C. Afterward, the reaction was let cool down to 21 °C. The mixture was extracted with ethyl acetate (3 x 20 mL), the obtained organic phase was washed with water (3 x 20 mL) and dried over Na_2SO_4. The solvent was removed under reduced pressure and the crude product was purified by column chromatography (cyclohexane/ ethyl acetate 20:1) to isolate methyl 4-(2-phenylethynyl)benzoate (359 mg, 1.52 mmol, 82% yield) as a light yellow solid.

R_f = 0.11 (cyclohexane/ethyl acetate (20:1)).

^{1}H NMR (400 MHz, Chloroform-*d* [7.26 ppm], ppm) δ = 8.03–8.01 (m, 2H, CH_{ar}), 7.60–7.58 (m, 2H, CH_{ar}), 7.56–7.53 (m, 2H, CH_{ar}), 7.38–7.36 (m, 3H, CH_{ar}), 3.93 (s, 3H, CH_3).

Impurities: Signals at 3.12 and 1.43 ppm due to residues of triethylamine and signal at 1.61 ppm due to water.

^{13}C NMR (100 MHz, Chloroform-*d* [77.2 ppm], ppm) δ = 166.6 (*C*O), 131.7 (*C*H, 2C, C_{ar}), 131.5 (*C*H, 2C, C_{ar}), 129.5 (*C*H, 2C, C_{ar}), 129.5 (C_q), 128.8 (*C*H, C_{ar}), 128.4 (*C*H, 2C, C_{ar}), 128.0 (C_q), 122.7 (C_q), 92.4 (C_q), 88.6 (C_q), 52.2 (CH_3).

Impurities: Signals at 45.8 and 8.63 ppm due to residues of triethylamine.

MS (EI, 70 eV, 70 °C), m/z (%): 236 (100) $[M]^+$, 205 (68) $[M–C_{15}H_9O]^+$, 203 (11), 202 (53), 200 (9), 178 (7), 177 (16) $[C_{14}H_9]^+$, 176 (35), 151 (15), 150 (7).

HRMS (EI): *m/z* = calcd. for $C_{16}H_{12}O_2$ $[M]^+$: 236.0832; found 236.0830.

IR (ATR, ṽ) = 3996 (w), 3077 (w), 3055 (w), 3031 (w), 3021 (w), 2995 (w), 2945 (w), 2846 (w), 2214 (w), 1708 (vs), 1679 (m), 1672 (m), 1656 (w), 1649 (w), 1639 (w), 1602 (m), 1594 (m), 1571 (w), 1560 (w), 1555 (w), 1485 (m), 1455 (w), 1435 (s), 1405 (m), 1375 (w), 1309 (m), 1275 (vs), 1254 (s), 1191 (m), 1173 (s), 1160 (m), 1139 (m), 1106 (vs), 1098 (vs), 1071 (s), 1027 (m), 1014 (m), 996 (m), 959 (m), 925 (m), 887 (m), 854 (s), 816 (m), 759 (vs), 721 (s), 690 (vs), 640 (m), 620 (m), 601 (m), 589 (m), 574 (w), 561 (w), 540 (s), 516 (vs), 493 (s), 466 (m), 449 (s), 422 (m), 401 (m), 392 (m), 381 (m) cm^{-1}.

UV-VIS (abs., DCM, 21 °C), λ_{max} = 316, 299, 219 nm.

Additional data supporting the chemical synthesis results is available *via* the Chemotion repository: https://dx.doi.org/10.14272/reaction/SA-FUHFF-UHFFFADPSC-IOMGFEKBYS-UHFFFADPSC-NUHFF-NUHFF-NUHFF-ZZZ

1-(4-Hydroxyphenyl)-2-phenylethane-1,2-dione (103)

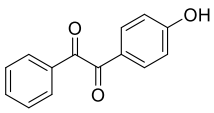

4-(2-phenylethynyl) phenol (210 mg, 1.03 mmol, 1.00 equiv.) and palladium dichloride (7.67 mg, 43.2 µmol, 0.0400 equiv.) were dissolved in dimethyl sulfoxide (10 mL), and the resulting solution was stirred at 140 °C for 3 h. Afterward, water was added to the mixture and the obtained mixture was extracted with ethyl acetate (3 x 15 mL), the combined organic phases were washed with saturated NH_4Cl (10 mL) solution and dried over Na_2SO_4. The solvent was evaporated, and the crude product was purified by column chromatography (cyclohexane/ ethyl acetate 20:1–2:1) to obtain 1-(4-hydroxyphenyl)-2-phenylethane-1,2-dione (201 mg, 888 µmol, 82% yield) as an orange solid.

R_f = 0.27 (cyclohexane/ethyl acetate (2:1)).

^{1}H NMR (400 MHz, Chloroform-*d* [7.26 ppm], ppm) δ = 7.96–7.94 (m, 2H, CH_{ar}), 7.87–7.84 (m, 2H, CH_{ar}), 7.67–7.63 (m, 1H, CH_{ar}), 7.50 (d, *J* = 15.5 Hz, 2H, CH_{ar}), 6.94 (s, 1H, O*H*), 6.91–6.88 (m, 2H, CH_{ar}).

Impurities: Signals at 1.43 ppm due to residues of cyclohexane and at 1.26 ppm due to H-grease.

^{13}C NMR (100 MHz, Chloroform-*d* [77.2 ppm], ppm) δ = 195.4 (*C*O), 193.7 (*C*O), 162.3 (C_q), 135.1 (*C*H, C_{ar}), 133.0 (C_q), 132.8 (*C*H, 2C, C_{ar}), 130.0 (*C*H, 2C, C_{ar}), 129.1 (*C*H, 2C, C_{ar}), 125.8 (C_q), 116.2 (*C*H, 2C, C_{ar}).

Impurities: Signals at 26.9 ppm due to residues of cyclohexane and at 29.7 ppm due to H-grease.

MS (EI, 70 eV, 130 °C), m/z (%): 226 (5) $[M]^+$, 121 (89) $[C_7H_5O_2]^+$, 105 (12) $[C_7H_5O]^+$, 93 (100) $[C_6H_5O]^+$, 77 (55) $[C_6H_5]^+$, 65 (65) $[C_5H_5]^+$, 51 (21) $[C_4H_4]^+$.

HRMS (EI): *m/z* = calcd. for $C_{14}H_{10}O_3$ $[M]^+$: 226.0624; found 226.0623.

IR (ATR, $\tilde{\nu}$) = 3381 (s), 1673 (s), 1647 (m), 1595 (vs), 1561 (vs), 1516 (s), 1493 (w), 1446 (w), 1323 (m), 1302 (s), 1261 (w), 1205 (vs), 1159 (vs), 1108 (s), 1074 (m), 1047 (m), 1021 (w), 1009 (w), 997 (w), 967 (w), 955 (w), 938 (w), 878 (vs), 844 (s), 833 (m), 815 (w), 793 (m), 764 (s), 718 (vs), 701 (s), 679 (s), 637 (vs), 608 (vs), 509 (s), 463 (s), 452 (m), 438 (m), 422 (w), 402 (m), 397 (m), 378 (w) cm^{-1}.

UV-VIS (abs., DMSO, 21 °C), λ_{max} = 300 nm.

Additional data supporting the chemical synthesis results is available *via* the Chemotion repository: https://dx.doi.org/10.14272/reaction/SA-FUHFF-UHFFFADPSC-IVUXDMQTCN-UHFFFADPSC-NUHFF-NUHFF-NUHFF-ZZZ.1

4-(1,2-Dioxo-2-phenylethyl)benzoic acid methyl ester (104)

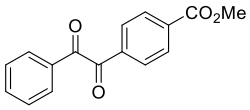

4-(2-Phenylethynyl)benzoic acid methyl ester (429 mg, 1.82 mmol, 1.00 equiv.) and palladium dichloride (16.1 mg, 90.8 µmol, 0.0500 equiv.) were dissolved in 10 mL of dimethyl sulfoxide. and the resulting solution was stirred at 140 °C for 3 h. Afterward, water was added, and the aqueous layer was extracted with ethyl acetate (3 x 15 mL). The combined organic phases were washed with saturated NH_4Cl (10 mL) solution and dried over Na_2SO_4. The solvent was evaporated, and the crude product was purified by column chromatography (cyclohexane/ ethyl acetate 10:1) to obtain 4-(1,2-dioxo-2-phenylethyl)benzoic acid methyl ester (413 mg, 1.54 mmol, 85% yield) as a yellow solid.

R_f = 0.13 (cyclohexane/ethyl acetate (10:1)).

^{1}H NMR (500 MHz, Chloroform-*d* [7.26 ppm], ppm) δ = 8.16 (d, *J* = 8.2 Hz, 2H, *C*H$_{ar}$), 8.04 (d, *J* = 8.2 Hz, 2H, *C*H$_{ar}$), 7.97 (d, *J* = 7.3 Hz, 2H, *C*H$_{ar}$), 7.68 (t, *J* = 7.5 Hz, 1H, *C*H$_{ar}$), 7.52 (t, *J* = 7.8 Hz, 2H, *C*H$_{ar}$), 3.95 (s, 3H, *C*H$_{ar}$)

Impurities: Signals at 1.63 ppm due to residues of water and at 1.42 ppm due to cyclohexane.

^{13}C NMR (125 MHz, Chloroform-*d* [77.2 ppm], ppm) δ = 193.8 (*C*O), 193.7 (*C*O), 165.9 (*C*OOCH$_3$), 136.0 (C_q), 135.3 (C_q), 135.2 (*C*H, C$_{ar}$), 132.7 (C_q), 130.1 (*C*H, 2C, C$_{ar}$), 130.0 (*C*H, 2C, C$_{ar}$), 129.8 (*C*H, 2C, C$_{ar}$), 129.1 (*C*H, 2C, C$_{ar}$), 52.6 (*C*H$_3$).

Impurity: Signal at 26.9 ppm due to residues of cyclohexane.

MS (EI, 70 eV, 70 °C), m/z (%): 269 (2) $[M+H]^+$, 268 (11) $[M]^+$, 237 (5) $[M–CH_3O]^+$, 164 (12) $[CH_8O_3]^+$, 163 (55) $[C_9H_7O_3]^+$, 135 (9) $[M+2\ H]^+$, 133 (9) $[C_8H_5O_2]^+$, 106 (8) $[C_7H_6O]^+$, 105 (100) $[C_7H_5O]^+$, 77 (23) $[C_6H_5]^+$.

HRMS (EI): *m/z* = calcd. for $C_{16}H_{12}O_4$ $[M]^+$: 268.0730; found 268.0731.

IR (ATR, $\tilde{\nu}$) = 3057 (w), 2962 (w), 2922 (w), 1720 (vs), 1672 (vs), 1662 (vs), 1609 (w), 1596 (m), 1582 (w), 1568 (w), 1500 (w), 1451 (m), 1435 (s), 1407 (m), 1319 (w), 1282 (vs), 1205 (vs), 1190 (s), 1180 (vs), 1116 (m), 1103 (vs), 1050 (w), 1024 (w), 1016 (m), 1000 (w), 980 (w), 969 (w), 950 (m), 931 (w), 882 (s), 857 (s), 826 (s), 795 (s), 782 (s), 735 (vs), 718 (vs), 703 (vs), 679 (vs), 659 (vs), 628 (s), 613 (m), 579 (w), 534 (m), 469 (m), 441 (w), 426 (m), 399 (w) cm^{-1}.

UV-VIS (abs., DMSO, 21 °C), λ_{max} = 265 nm.

Additional data supporting the chemical synthesis results is available *via* the Chemotion repository: https://dx.doi.org/10.14272/reaction/SA-FUHFF-UHFFFADPSC-ASOBFLCMBL-UHFFFADPSC-NUHFF-NUHFF-NUHFF-ZZZ

4-(2-Oxo-2-phenyl-acetyl)benzoic acid (**105**)

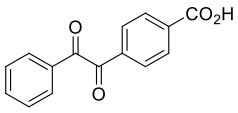

Methyl 4-(2-oxo-2-phenyl-acetyl)benzoate (250 mg, 932 µmol, 1.00 equiv.) was dissolved in 11 mL of acetic acid. To this suspension a mixture of H_2SO_4 (7.31 g, 3.97 mL, 74.6 mmol, 80.0 equiv.) and water (1.01 g, 1.01 mL, 55.9 mmol, 60.0 equiv.) was slowly added. The reaction mixture was heated to 80 °C and was stirred for 16 h. The mixture was diluted with water (4.00 mL) and was let cool down to 21 °C. The precipitate was filtered off and washed with water (3 x 20 mL) and dried at 70 °C under high vacuum to obtain 4-(2-oxo-2-phenyl-acetyl)benzoic acid (206 mg, 810 µmol, 87% yield) as a light yellow solid.

^{1}H NMR (400 MHz, DMSO-d_6 [2.50 ppm], ppm) δ = 8.16–8.14 (m, 2H, CH_{ar}), 8.07–8.04 (m, 2H, CH_{ar}), 7.98–7.95 (m, 2H, CH_{ar}), 7.85–7.80 (m, 1H, CH_{ar}), 7.67–7.63 (m, 2H, CH_{ar}).

Missing signal: COO*H* (1H) due to H/D exchange.

Impurity: Impurity at 3.34 ppm due to residues of water.

^{13}C NMR (100 MHz, DMSO-d_6 [39.5 ppm], ppm) δ = 194.6 (C_q), 194.6 (C_q), 166.8 (*C*OOH), 136.8 (C_q), 136.2 (*C*H, C_{ar}), 135.6 (C_q), 132.5 (*C*H, 1C, C_{ar}), 130.6 (*C*H, 2C, C_{ar}), 130.4 (*C*H, 2C, C_{ar}), 130.3 (*C*H, 2C, C_{ar}), 130.0 (*C*H, 2C, C_{ar}).

MS (ESI), m/z (%): 255 (100) $[M+H]^+$, 221 (27), 163 (37), 149 (19) $[C_8H_5O_3]^+$, 100 (19) Unknown adducts at 282 (42) and 256 (16).

HRMS (ESI, MeCN): *m/z* = calcd. for $C_{15}H_{11}O_4^+$ $[M]^+$: 255.0652, found 255.0650.

IR (ATR, ṽ) = 3057 (w), 2956 (w), 2874 (w), 2844 (w), 2815 (w), 2723 (w), 2670 (w), 2632 (w), 2606 (w), 2551 (w), 1686 (vs), 1660 (vs), 1608 (m), 1596 (m), 1582 (m), 1570 (m), 1504 (m), 1452 (w), 1425 (s), 1407 (m), 1373 (w), 1320 (m), 1315 (m), 1293 (vs), 1204 (vs), 1177 (vs), 1128 (s), 1118 (s), 1096 (m), 1071 (w), 1017 (w), 1000 (w), 987 (w), 970 (w), 929 (m), 895 (w), 884 (vs), 858 (vs), 817 (m), 790 (s), 782 (vs), 728 (vs), 721 (vs), 696 (vs), 676 (vs), 659 (vs), 628 (s), 615 (m), 547 (s), 523 (s), 475 (s), 445 (w), 425 (w), 414 (w), 398 (w), 377 (w) cm^{-1};

UV-VIS (abs., DMSO, 21 °C), λ_{max} = 264 nm.

Additional data supporting the chemical synthesis results is available *via* the Chemotion repository: https://dx.doi.org/10.14272/reaction/SA-FUHFF-UHFFFADPSC-IVUXDMQTCN-UHFFFADPSC-NUHFF-NUHFF-NUHFF-ZZZ.1

Methyl 4-[1-hydroxy-2-(4-methoxycarbonylphenyl)-2-oxo-ethyl]benzoate (107)

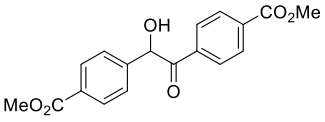

Potassium cyanide (59.5 mg, 914 µmol, 0.300 equiv.) was added to a solution of methyl 4-formylbenzoate (500 mg, 3.05 mmol, 1.00 equiv.) in 2 mL of abs. ethanol and 600 µL of water. The reaction mixture was stirred at 30 °C for 15 min. After 5 min a voluminous precipitate could be observed. After completion the solid was filtered, washed with water and dried under reduced pressure to obtain methyl 4-[1-hydroxy-2-(4-methoxycarbonylphenyl)-2-oxo-ethyl]benzoate (289 mg, 880 µmol, 58% yield) as a colorless solid.

^{1}H NMR (400 MHz, Chloroform-d [7.26 ppm], ppm) δ = 8.06–8.04 (m, 2H, C*H*$_{ar}$), 8.00–7.97 (m, 2H, C*H*$_{ar}$), 7.93–7.91 (m, 2H, C*H*$_{ar}$), 7.40 (m, 2H, C*H*$_{ar}$), 6.01 (d, *J* = 5.9 Hz, 1H, C*H*), 4.52 (d, *J* = 5.9 Hz, 1H, O*H*), 3.91 (s, 3H, C*H*$_3$), 3.88 (s, 3H, C*H*$_3$).

^{13}C NMR (100 MHz, Chloroform-d [77.2 ppm], ppm) δ = 198.2 (C_q), 166.4 (COOCH$_3$), 165.7 (COOCH$_3$), 143.0 (C_q), 136.6 (C_q), 134.7 (C_q), 130.5 (C_q), 130.5 (CH, 2C, C_{ar}), 129.9 (CH, 2C, C_{ar}), 128.9 (CH, 2C, C_{ar}), 127.8 (CH, 2C, C_{ar}), 76.2 (CH), 52.6 (CH$_3$), 52.2 (CH$_3$).

MS (FAB, 3-NBA), m/z (%): 329 (22) $[M]^+$, 307 (36), 155 (31), 154 (100), 138 (35), 137 (76), 136 (65).

HRMS (FAB): *m/z* = calcd. for $C_{18}H_{17}O_6$ $[M]^+$: 329.1020; found 329.1020.

IR (ATR, ṽ) = 3463 (w), 3432 (w), 2955 (vw), 1720 (vs), 1679 (s), 1609 (w), 1572 (vw), 1438 (m), 1415 (w), 1405 (w), 1387 (w), 1312 (w), 1276 (vs), 1247 (s), 1186 (m), 1109 (vs), 1095 (vs), 1018 (w), 983 (m), 963 (m), 881 (w), 863 (w), 849 (w), 836 (w), 815 (m), 766 (s), 721 (vs), 703 (m), 688 (w), 636 (w), 615 (m), 586 (vw), 537 (m), 493 (w), 484 (w), 455 (w), 445 (w), 438 (w), 428 (w), 407 (w), 388 (w), 377 (w) cm^{-1}.

Additional data supporting the chemical synthesis results is available *via* the Chemotion repository: https://dx.doi.org/10.14272/reaction/SA-FUHFF-UHFFFADPSC-XFRIKHRKYH-UHFFFADPSC-NUHFF-NUHFF-NUHFF-ZZZ.1

Methyl 4-[2-(4-methoxycarbonylphenyl)-2-oxo-acetyl]benzoate (**108**)

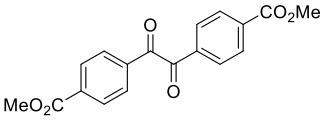

Hydrobromic acid (3.54 g, 2.37 mL, 21.0 mmol, 12.0 equiv.) was added to a solution of methyl 4-[1-hydroxy-2-(4-methoxycarbonylphenyl)-2-oxo-ethyl]benzoate (574 mg, 1.75 mmol, 1.00 equiv.) in 8 mL of dimethyl sulfoxide under stirring. The reaction mixture was heated to 60 °C for 24 h. Subsequently, water (10 mL) was added, and the obtained yellow colored precipitate was filtered off and washed with water (3 x 10 mL) and dried under vacuum. Methyl 4-[2-(4-methoxycarbonylphenyl)-2-oxo-acetyl]benzoate (481 mg, 1.47 mmol, 84% yield) was isolated as a yellow powder.

^{1}H NMR (400 MHz, Chloroform-*d*, ppm) δ = 8.19–8.17 (m, 4H, $C_{ar}H$), 8.06–8.04 (m, 4H, $C_{ar}H$), 3.99 (s, 6H, CH_3).

^{13}C NMR (100 MHz, Chloroform-*d*, ppm) δ = 192.9 (C_q, 2C), 165.8 (COOCH$_3$, 2C), 135.8 (C_q, 2C), 135.6 (C_q, 2C), 130.2 (CH, 4C, C_{ar}), 129.9 (CH, 4C, C_{ar}), 52.7 (CH$_3$, 2C).

MS (EI, 70 eV, 120 °C), m/z (%):326 (3) $[M]^+$, 295 (4) $[C_{17}H_{11}O_5]^+$, 163 (100) $[C_9H_7O_3]^+$, 135 (11), 120 (4), 104 (7), 103 (7).

HRMS (EI): *m/z* = calcd. for $C_{18}H_{14}O_6$ $[M]^+$: 326.0785; found 326.0784.

IR (ATR, ṽ) = 2962 (w), 1718 (vs), 1664 (vs), 1609 (w), 1570 (w), 1502 (w), 1448 (w), 1435 (m), 1407 (m), 1282 (vs), 1203 (vs), 1188 (vs), 1174 (m), 1103 (vs), 1014 (m), 950 (m), 890 (m), 860 (m), 820 (m), 792 (w), 782 (m), 731 (vs), 713 (vs), 684 (m), 674 (m), 629 (w), 534 (w), 475 (w), 460 (w), 448 (w) cm^{-1};

UV-VIS (abs., DCM, 21 °C), λ_{max} = 271 nm.

Additional data supporting the chemical synthesis results is available *via* the Chemotion repository: https://dx.doi.org/10.14272/reaction/SA-FUHFF-UHFFFADPSC-PCLYIKBMKK-UHFFFADPSC-NUHFF-NUHFF-NUHFF-ZZZ.1

4-[2-(4-Carboxyphenyl)-2-oxo-acetyl]benzoic acid (**109**)

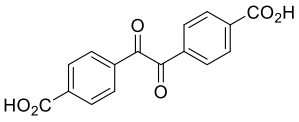

Methyl 4-[2-(4-methoxycarbonylphenyl)-2-oxo-acetyl]benzoate (200 mg, 613 µmol, 1.00 equiv.) was added to acetic acid (14.7 g, 14.0 mL, 245 mmol, 400 equiv.). After suspending in a mixture of 1.40 ml of water and 5.60 mL of H_2SO_4 the mixture was refluxed for 10 h. Subsequently 25 mL of water was added, and the mixture was cooled on ice. The obtained precipitate was filtered and washed with water (3 x 15 mL). The solid was dried under vacuum to obtain 4-[2-(4-carboxyphenyl)-2-oxo-acetyl]benzoic acid (170 mg, 570 µmol, 93% yield) as a yellow solid.

^{1}H NMR (400 MHz, DMSO-d_6 [2.50 ppm], ppm) δ = 8.16–8.14 (m, 4H, CH_{ar}), 8.09–8.07 (m, 4H, CH_{ar}).

Missing signals: COOH (2H) due to H/D exchange.

^{13}C NMR (100 MHz, DMSO-d_6 [39.5 ppm], ppm) δ = 193.8 (*C*O, 2C), 166.8 (*C*OOH, 2C), 136.9 (C_q, 2C), 135.5 (C_q 2C), 130.5 (*C*H, 4C, C_{ar}), 130.5 (*C*H, 4C, C_{ar}).

MS (ESI), m/z (%): 297 (24) $[M–H]^-$, 227 (11), 168 (21), 127 (5), 113 (100)

Unknown adduct at 395 (12).

HRMS (ESI, DMF): *m/z* calcd. for $C_{16}H_9O_6^-$ $[M-H]^-$: 297.0405, found: 297.0402.

IR (ATR, ṽ) = 3347 (w), 3279 (w), 3272 (w), 3180 (m), 3080 (w), 3072 (w), 2956 (w), 2924 (w), 2866 (w), 1663 (vs), 1640 (vs), 1599 (vs), 1470 (w), 1455 (w), 1401 (vs), 1371 (s), 1360 (vs), 1296 (w), 1273 (w), 1218 (w), 1190 (s), 1164 (m), 1136 (w), 1108 (w), 993 (w), 933 (w), 916 (w), 890 (m), 847 (w), 805 (w), 773 (s), 718 (w), 657 (vs), 637 (vs), 541 (w), 489 (w), 424 (w) cm^{-1}.

UV-VIS (abs., DMSO, 21 °C), λ_{max} = 269, 249, 247 nm.

Additional data supporting the chemical synthesis results is available *via* the Chemotion repository: https://dx.doi.org/10.14272/reaction/SA-FUHFF-UHFFFADPSC-BQDSQOCMNS-UHFFFADPSC-NUHFF-NUHFF-NUHFF-ZZZ.1

5.3 Crystallographic Data

The crystal structure in this chapter was measured by Dr. Olaf Fuhr from the at the Institute of Nanotechnology at Karlsruhe Institute of Technology.

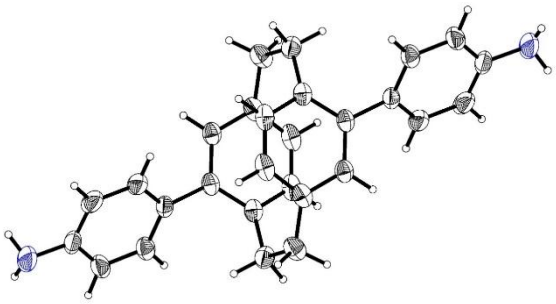

Figure 51: ORTEP plot of the molecular structure of monomer ***p*PCP-PA** (**18**) (ellipsoids with 50% probability).

Table 3: Crystallographic data and refinement details for ***p*PCP-PA** (**18**).

Identification code	*p*PCP-PA
Empirical formula	$C_{28}H_{26}N_2$
Formula weight	390.51
Temperature/K	180
Crystal system	monoclinic
Space group	$P2_1/c$
a/Å	9.2928(5)
b/Å	9.8811(4)
c/Å	11.0801(6)
α/°	90
β/°	96.282(4)
γ/°	90
Volume/Å^3	1011.30(9)
Z	2
ρ_{calc}g/cm^3	1.282
μ/mm^{-1}	0.367
F(000)	416.0
Crystal size/mm^3	0.12 × 0.1 × 0.04
Radiation	Ga Kα (λ = 1.34143)
2Θ range for data collection/°	8.328 to 124.984
Index ranges	$-12 \leq h \leq 11$, $-13 \leq k \leq 5$, $-13 \leq l \leq 14$
Reflections collected	9119
Independent reflections	2417 [R_{int} = 0.0144, R_{sigma} = 0.0117]
Ind. reflections with I≥2σ (I)	2059
Data/restraints/parameters	2417/0/137
Goodness-of-fit on F^2	1.084

Final R indexes [I≥2σ (I)]	R_1 = 0.0420, wR_2 = 0.1192
Final R indexes [all data]	R_1 = 0.0485, wR_2 = 0.1243
Largest diff. peak/hole / e Å^{-3}	0.25/–0.23
CCDC number	2329941

6 List of Abbreviations

1PA	one-photon absorption
2D	two-dimensional
2PA	two-photon absorption
2SA	two-step absorption
3D	three-dimensional
AA	alkoxyamine
AcOH	acetic acid
AI	artificial intelligence
Alloc	allyloxy carbonyl
AM	additive manufacturing
APH	Institute of Applied Physics
ASTM	American Society for Testing and Materials
BDBA	1,4-benzenediboronic acid
BDC	1,4-benzene dicarboxylate
BET	BRUNAUER-EMMETT-TELLER
BJT	binder jetting
Boc	*tert*-butyloxycarbonyl
BP	benzophenone
BPDC	4,4'-biphenyl dicarboxylate
BTB	1,3,5-benzenetribenzoate
BTT	4,4',4"-benzene-1,3,5-trityltris(ethyne-2,1-diyl)tribenzaldehyde
BZ	benzil
CAD	computer-aided design
CCS	carbon capture and storage
CuAAC	copper-catalyzed azide-alkyne cycloaddition
CVD	chemical vapor deposition
CW	continuous wave
DCM	dichloromethane
DED	direct energy deposition
DIPEA	diisopropylethylamine
DLP	digital light processing
DLW	direct laser writing

DMD	digital mircomirror device
DMF	dimethylformamide
DMM	dimethoxymethane
DNA	deoxyribonucleic acid
DOE	department of energy
EA	elemental analysis
EDC	1-ethyl-3(3-dimethylaminopropyl)carbodiimide
EPOX	3,4-epoxycyclohexylmethyl-3,4-epoxycyclohexanecarboxylate
EPR	electron paramagnetic resonance
FDM	fused deposition molding
Fmoc	fluorenylmethoxy carbonyl
FT-IR	fourier-transform infared
GPC	gel permeation chromatography
HATU	*O*-(7-azabenzotriazol-1-yl)-*N*,*N*,*N*,*N*-tetramethyluronium-hexafluorophosphate
HCP	hyper-crosslinked polymer
HFIP	hexafluoro isopropanol
HFPTP	2,3,6,7,14,15-hexakis(4'-formylphenyl)triptycene
HHTP	2,3,6,7,10,11-hexahydroxytriphenylene
IAST	ideal adsorbed solution theory
IFG	Institute of Functional Interfaces
IJP	inkjet printing
KIT	Karlsruher Institute of Technology
LbL	layer-by-layer
LPE	liquid phase epitaxy
*m*CPBA	*meta*-chlorperoxybenzoic acid
ML	machine learning
MOF	metal-organic framework
MOF NP	metal-organic framework nanoparticle
n-BuLi	*n*-butyllithium
NER	nitroxide-exchange reaction
NLDFT	non-linear density functional theory
NMP	nitroxide-mediated polymerization
NMR	nuclear magnetic resonance
PAF	porous aromatic framework

Pbf	2,2,4,7-pentamethyl dihydrobenzofurane-5-sulfonyl
PCP	[2.2]paracyclophane
PETA	pentaerythritol triacrylate
PI	photoinitiator
PIM	polymer of intrinsic microporosity
PLA	polylactic acid
POCl3	phosphorus oxychloride
PPN	porous polymer network
PSM	post-synthetic modification
PU	polyurethane
PVC	poly(vinyl chloride)
QST	heats of adsorption
RNA	ribonucleic acid
SA	surface area
SAM	self-assembled monolayer
SBU	secondary building unit
SEM	scanning electron microscopy
SLA	stereolithography
SPEGA	PEO-methyl-*p*-vinylbenzyl-ether
SSH	substrate-seeded heteroepitaxy
SURMOF	surface-mounted metal-organic framework
TA	terephtalaldehyde
TAM	tetrakis(4-aminophenyl)methane
TAPP	5,10,15,20-tetrakis(4-aminophenyl)porphyrine
TB	TRÖGERs Base
TBC	terphenyl dicarboxylate
TEGDMA	triethylene glycol dimethyl acrylate
TEMPO	2,2,6,6-tetramethylpiperidine-1-oxyl
TFA	trifluoroacetic acid
TFPA	tris(4-formylphenyl)amine
TFPB	1,3,5-tris(4-formylphenyl)benzene
TFTA	1,3,5-tris(4-formylphenyl)triazine
TGA	thermogravimetric analysis
THF	tetrahydrofurane

TIPS	triisopropylsilane
TLC	thin-layer chromatography
ToF-SIMS	time-of-flight ion mass spectrometry
TP	1,3,5-triformylphloroglucinol
UV	ultraviolet
VPP	vat photopolymerization
XRD	x-ray diffraction

7 Bibliography

[1] A. Jonsson, T. Bjorklund, A. M. Tillman, *The International Journal of Life Cycle Assessment* **1998**, *3*, 216-224.

[2] L. Zhang, *IEEE Consumer Electronics Magazine* **2014**, *3*, 44-48.

[3] M. Choudhury, H. S. Bindra, K. Singh, A. K. Singh, R. Nayak, *Polymers for Advanced Technologies* **2022**, *33*, 1997-2024.

[4] S. F. Liu, Z. W. Hou, L. Lin, Z. Li, H. B. Sun, *Advanced Functional Materials* **2023**, *33*, 2211280.

[5] P. Cheng, Y. Peng, S. Li, Y. Rao, A. Le Duigou, K. Wang, S. Ahzi, *Composites Part B: Engineering* **2023**, *250*, 110450.

[6] T. A. Makal, J.-R. Li, W. Lu, H.-C. Zhou, *Chemical Society Reviews* **2012**, *41*, 7761-7779.

[7] E. I. Knerelman, Y. A. Karozina, I. G. Shunina, I. V. Sedov, *Petroleum Chemistry* **2022**, *62*, 561-582.

[8] R. E. Morris, P. S. Wheatley, *Angewandte Chemie International Edition* **2008**, *47*, 4966-4981.

[9] P. Horcajada, T. Chalati, C. Serre, B. Gillet, C. Sebrie, T. Baati, J. F. Eubank, D. Heurtaux, P. Clayette, C. Kreuz, J.-S. Chang, Y. K. Hwang, V. Marsaud, P.-N. Bories, L. Cynober, S. Gil, G. Férey, P. Couvreur, R. Gref, *Nature Materials* **2010**, *9*, 172-178.

[10] M. Arruebo, *WIREs Nanomedicine and Nanobiotechnology* **2012**, *4*, 16-30.

[11] N. Singh, S. Son, J. An, I. Kim, M. Choi, N. Kong, W. Tao, J. S. Kim, *Chemical Society Reviews* **2021**, *50*, 12883-12896.

[12] Y. Tang, A. Varyambath, Y. Ding, B. Chen, X. Huang, Y. Zhang, D.-G. Yu, I. Kim, W. Song, *Biomaterials Science* **2022**, *10*, 5369-5390.

[13] C. Barner-Kowollik, M. Bastmeyer, E. Blasco, G. Delaittre, P. Müller, B. Richter, M. Wegener, *Angewandte Chemie International Edition* **2017**, *56*, 15828-15845.

[14] M. Kadic, G. W. Milton, M. Van Hecke, M. Wegener, *Nature Reviews Physics* **2019**, *1*, 198-210.

[15] E. Dogan, A. Bhusal, B. Cecen, A. K. Miri, *Applied Materials Today* **2020**, *20*, 100752.

[16] R. L. Siegelman, E. J. Kim, J. R. Long, *Nat Mater* **2021**, *20*, 1060-1072.

[17] Umweltbundesamt. *Carbon Capture and Storage*; 28.02.2024. Available from: https://www.umweltbundesamt.de/themen/wasser/gewaesser/grundwasser/nutzung-belastungen/carbon-capture-storage#grundlegende-informationen [Accessed: January 30, 2025].

[18] G. Singh, J. Lee, A. Karakoti, R. Bahadur, J. Yi, D. Zhao, K. Albahily, A. Vinu, *Chemical Society Reviews* **2020**, *49*, 4360-4404.

[19] Z. Moussa, M. Hmadeh, M. G. Abiad, O. H. Dib, D. Patra, *Food Chemistry* **2016**, *212*, 485-494.

[20] J. Juan-Alcañiz, J. Gascon, F. Kapteijn, *Journal of Materials Chemistry* **2012**, *22*, 10102.

[21] S. S. Nadar, L. Vaidya, V. K. Rathod, *International Journal of Biological Macromolecules* **2020**, *149*, 861-876.

[22] C. Wang, K. Liao, *ACS Applied Materials & Interfaces* **2021**, *13*, 56752-56776.

[23] S. A. Polash, A. Poddar, F. Ahmady, G. Kannourakis, A. Jayachandran, R. Shukla, *ACS Applied Bio Materials* **2024**, *7*, 7635-7645.

[24] S. A. Polash, S. Pyreddy, A. N. Abraham, S. Mahasivam, V. Bansal, L. Varadi, G. Bryant, R. Shukla, *Materials Advances* **2023**, *4*, 4761-4774.

[25] K. Lu, T. Aung, N. Guo, R. Weichselbaum, W. Lin, *Advanced Materials* **2018**, *30*, 1707634.

[26] W. Zhang, C. Liu, Z. Liu, C. Zhao, J. Zhu, J. Ren, X. Qu, *ACS Nano* **2022**, *16*, 20975-20984.

[27] P.-H. Tong, L. Zhu, Y. Zang, J. Li, X.-P. He, T. D. James, *Chemical Communications* **2021**, *57*, 12098-12110.

[28] A. Bieniek, A. P. Terzyk, M. Wiśniewski, K. Roszek, P. Kowalczyk, L. Sarkisov, S. Keskin, K. Kaneko, *Progress in Materials Science* **2021**, *117*, 100743.

[29] M. X. Wu, Y. W. Yang, *Advanced Materials* **2017**, *29*, 1606134.

[30] J. Yang, Y. W. Yang, *Small* **2020**, *16*, 1906846.

[31] S. Rojas, A. Arenas-Vivo, P. Horcajada, *Coordination Chemistry Reviews* **2019**, *388*, 202-226.

[32] S. Feng, X. Zhang, D. Shi, Z. Wang, *Frontiers of Chemical Science and Engineering* **2021**, *15*, 221-237.

[33] Y. Wang, M. Zeng, T. Fan, M. Jia, R. Yin, J. Xue, L. Xian, P. Fan, M. Zhan, *International Journal of Nanomedicine* **2024**, *Volume 19*, 5523-5544.

[34] M. P. Abuçafy, R. C. G. Frem, G. Polinario, F. R. Pavan, H. Zhao, A. Mielcarek, C. Boissiere, C. Serre, L. A. Chiavacci, *International Journal of Molecular Sciences* **2022**, *23*, 7670.

[35] C. R. Quijia, C. Lima, C. Silva, R. C. Alves, R. Frem, M. Chorilli, *Journal of Drug Delivery Science and Technology* **2021**, *61*, 102217.

[36] B. Singco, L.-H. Liu, Y.-T. Chen, Y.-H. Shih, H.-Y. Huang, C.-H. Lin, *Microporous and Mesoporous Materials* **2016**, *223*, 254-260.

[37] R. Freund, O. Zaremba, G. Arnauts, R. Ameloot, G. Skorupskii, M. Dinca, A. Bavykina, J. Gascon, A. Ejsmont, J. Goscianska, M. Kalmutzki, U. Lachelt, E. Ploetz, C. S. Diercks, S. Wuttke, *Angew Chem Int Ed Engl* **2021**, *60*, 23975-24001.

[38] A. U. Czaja, N. Trukhan, U. Müller, *Chemical Society Reviews* **2009**, *38*, 1284.

[39] U. Mueller, M. Schubert, F. Teich, H. Puetter, K. Schierle-Arndt, J. Pastré, *J. Mater. Chem.* **2006**, *16*, 626-636.

[40] O. Shekhah, *Materials* **2010**, *3*, 1302-1315.

[41] L. Heinke, M. Tu, S. Wannapaiboon, R. A. Fischer, C. Wöll, *Microporous and Mesoporous Materials* **2015**, *216*, 200-215.

[42] O. Shekhah, J. Liu, R. A. Fischer, C. Wöll, *Chemical Society Reviews* **2011**, *40*, 1081.

[43] A. K. Hussein, E. Yousif, M. K. Rasheed, G. I. Edo, M. Bufaroosha, H. Umar, *Polymer-Plastics Technology and Materials* **2024**, 1-40.

[44] H. W. Engels, H. G. Pirkl, R. Albers, R. W. Albach, J. Krause, A. Hoffmann, H. Casselmann, J. Dormish, *Angewandte Chemie International Edition* **2013**, *52*, 9422-9441.

[45] R. Aksakal, C. Mertens, M. Soete, N. Badi, F. Du Prez, *Advanced Science* **2021**, *8*, 2004038.

[46] S. C. Tan, B. C. Yiap, *BioMed Research International* **2009**, *2009*, 1-10.

[47] V. M. Yashchuk, V. Y. Kudrya, *Methods and Applications in Fluorescence* **2017**, *5*, 014001.

[48] H. Mutlu, J. F. Lutz, *Angewandte Chemie International Edition* **2014**, *53*, 13010-13019.

[49] R. Gheorghita, L. Anchidin-Norocel, R. Filip, M. Dimian, M. Covasa, *Polymers* **2021**, *13*, 2729.

[50] M. Flórez, P. Cazón, M. Vázquez, *Polymers* **2023**, *15*, 641.

[51] N. B. McKeown, P. M. Budd, K. J. Msayib, B. S. Ghanem, H. J. Kingston, C. E. Tattershall, S. Makhseed, K. J. Reynolds, D. Fritsch, *Chemistry – A European Journal* **2005**, *11*, 2610-2620.

[52] P. Kaur, J. T. Hupp, S. T. Nguyen, *ACS Catalysis* **2011**, *1*, 819-835.

[53] Z. Zhang, Z. Liu, C. Xue, H. Chen, X. Han, Y. Ren, *Communications Chemistry* **2023**, *6*.

[54] X. Feng, X. Ding, D. Jiang, *Chem Soc Rev* **2012**, *41*, 6010-6022.

[55] K. T. Tan, S. Ghosh, Z. Wang, F. Wen, D. Rodríguez-San-Miguel, J. Feng, N. Huang, W. Wang, F. Zamora, X. Feng, A. Thomas, D. Jiang, *Nature Reviews Methods Primers* **2023**, *3*.

[56] B. F. Hoskins, R. Robson, *Journal of the American Chemical Society* **1989**, *111*, 5962-5964.

[57] O. M. Yaghi, G. Li, H. Li, *Nature* **1995**, *378*, 703-706.

[58] D. J. Tranchemontagne, J. L. Mendoza-Cortés, M. O'Keeffe, O. M. Yaghi, *Chemical Society Reviews* **2009**, *38*, 1257.

[59] J. R. Holst, A. I. Cooper, *Advanced Materials* **2010**, *22*, 5212-5216.

[60] L. Zhu, X.-Q. Liu, H.-L. Jiang, L.-B. Sun, *Chemical Reviews* **2017**, *117*, 8129-8176.

[61] P. Kumar, A. Deep, K.-H. Kim, *TrAC Trends in Analytical Chemistry* **2015**, *73*, 39-53.

[62] D. Yang, Y. Chen, Z. Su, X. Zhang, W. Zhang, K. Srinivas, *Coordination Chemistry Reviews* **2021**, *428*, 213619.

[63] Q. Shang, T. Zeng, K. Gao, N. Liu, Q. Cheng, G. Liao, Z. Pan, H. Zhou, *New Journal of Chemistry* **2019**, *43*, 16595-16603.

[64] S. Sharma, S. Dutta, G. K. Dam, S. K. Ghosh, *Chemistry – An Asian Journal* **2021**, *16*, 2569-2587.

[65] D. Zhao, D. J. Timmons, D. Yuan, H.-C. Zhou, *Accounts of Chemical Research* **2011**, *44*, 123-133.

[66] L. K. Macreadie, K. B. Idrees, C. S. Smoljan, O. K. Farha, *Angewandte Chemie* **2023**, *135*.

[67] O. M. Yaghi, M. O'Keeffe, N. W. Ockwig, H. K. Chae, M. Eddaoudi, J. Kim, *Nature* **2003**, *423*, 705-714.

[68] S. J. Garibay, S. M. Cohen, *Chemical Communications* **2010**, *46*, 7700.

[69] M. T. Wharmby, J. P. S. Mowat, S. P. Thompson, P. A. Wright, *Journal of the American Chemical Society* **2011**, *133*, 1266-1269.

[70] C. McKinstry, R. J. Cathcart, E. J. Cussen, A. J. Fletcher, S. V. Patwardhan, J. Sefcik, *Chemical Engineering Journal* **2016**, *285*, 718-725.

[71] N. Al Amery, H. R. Abid, S. Al-Saadi, S. Wang, S. Liu, *Materials Today Chemistry* **2020**, *17*, 100343.

[72] N. A. Khan, S. H. Jhung, *Coordination Chemistry Reviews* **2015**, *285*, 11-23.

[73] X. Wu, Z. Bao, B. Yuan, J. Wang, Y. Sun, H. Luo, S. Deng, *Microporous and Mesoporous Materials* **2013**, *180*, 114-122.

[74] I. Pakamorė, J. Rousseau, C. Rousseau, E. Monflier, P. Á. Szilágyi, *Green Chemistry* **2018**, *20*, 5292-5298.

[75] D. J. Tranchemontagne, J. R. Hunt, O. M. Yaghi, *Tetrahedron* **2008**, *64*, 8553-8557.

[76] S. Mandal, S. Natarajan, P. Mani, A. Pankajakshan, *Advanced Functional Materials* **2021**, *31*, 2006291.

[77] K. K. Tanabe, S. M. Cohen, *Chem. Soc. Rev.* **2011**, *40*, 498-519.

[78] Z. Wang, S. M. Cohen, *Chemical Society Reviews* **2009**, *38*, 1315.

[79] J. Winarta, B. Shan, S. M. McIntyre, L. Ye, C. Wang, J. Liu, B. Mu, *Crystal Growth & Design* **2020**, *20*, 1347-1362.

[80] T. Loiseau, C. Serre, C. Huguenard, G. Fink, F. Taulelle, M. Henry, T. Bataille, G. Férey, *Chemistry – A European Journal* **2004**, *10*, 1373-1382.

[81] H. Wu, T. Yildirim, W. Zhou, *The Journal of Physical Chemistry Letters* **2013**, *4*, 925-930.

[82] M. Ding, X. Cai, H.-L. Jiang, *Chemical Science* **2019**, *10*, 10209-10230.

[83] J. H. Cavka, S. Jakobsen, U. Olsbye, N. Guillou, C. Lamberti, S. Bordiga, K. P. Lillerud, *Journal of the American Chemical Society* **2008**, *130*, 13850-13851.

[84] J. Liu, C. Wöll, *Chemical Society Reviews* **2017**, *46*, 5730-5770.

[85] O. Shekhah, R. Swaidan, Y. Belmabkhout, M. Du Plessis, T. Jacobs, L. J. Barbour, I. Pinnau, M. Eddaoudi, *Chemical Communications* **2014**, *50*, 2089.

[86] O. Shekhah, H. Wang, S. Kowarik, F. Schreiber, M. Paulus, M. Tolan, C. Sternemann, F. Evers, D. Zacher, R. A. Fischer, C. Wöll, *Journal of the American Chemical Society* **2007**, *129*, 15118-15119.

[87] J.-L. Zhuang, A. Terfort, C. Wöll, *Coordination Chemistry Reviews* **2016**, *307*, 391-424.

[88] A. Hozumi, Y. Yokogawa, T. Kameyama, H. Sugimura, K. Hayashi, H. Shirayama, O. Takai, *Journal of Vacuum Science & Technology A: Vacuum, Surfaces, and Films* **2001**, *19*, 1812-1816.

[89] F. Schreiber, *Progress in Surface Science* **2000**, *65*, 151-257.

[90] A. Ulman, *Chemical Reviews* **1996**, *96*, 1533-1554.

[91] L. Heinke, C. Wöll, *Advanced Materials* **2019**, *31*, 1806324.

[92] Y.-H. Xiao, Z.-G. Gu, J. Zhang, *Nanoscale* **2020**, *12*, 12712-12730.

[93] O. Shekhah, H. Wang, M. Paradinas, C. Ocal, B. Schüpbach, A. Terfort, D. Zacher, R. A. Fischer, C. Wöll, *Nature Materials* **2009**, *8*, 481-484.

[94] M. Gupta, J. J. Vittal, *Coordination Chemistry Reviews* **2021**, *435*, 213789.

[95] H. Li, M. Eddaoudi, T. L. Groy, O. M. Yaghi, *Journal of the American Chemical Society* **1998**, *120*, 8571-8572.

[96] A. Nefedov, C. Li, K. Müller, A. B. Kanj, L. Heinke, C. Luo, K. Chen, F. Radu, E. Golias, W. Kuch, C. Wöll, *Physical Review B* **2023**, *107*, 054433.

[97] H. Gliemann, C. Wöll, *Materials Today* **2012**, *15*, 110-116.

[98] E. Biemmi, S. Christian, N. Stock, T. Bein, *Microporous and Mesoporous Materials* **2009**, *117*, 111-117.

[99] Y. Luo, S. Bag, O. Zaremba, A. Cierpka, J. Andreo, S. Wuttke, P. Friederich, M. Tsotsalas, *Angewandte Chemie International Edition* **2022**, *61*.

[100] Z. Han, Y. Yang, J. Rushlow, J. Huo, Z. Liu, Y.-C. Hsu, R. Yin, M. Wang, R. Liang, K.-Y. Wang, H.-C. Zhou, *Chemical Society Reviews* **2025**, *54*, 367-395.

[101] N. Rabiee, *Clinical and Translational Discovery* **2023**, *3*.

[102] C. Pettinari, F. Marchetti, N. Mosca, G. Tosi, A. Drozdov, *Polymer International* **2017**, *66*, 731-744.

[103] BASF. *BASF becomes first company to successful produce metal-organic frameworks on a commercial scale for carbon capture*; 2023. Available from: https://www.basf.com/global/en/media/news-releases/2023/10/p-23-327 [Accessed: 01 Febuary, 2025].

[104] *Nature Chemistry* **2016**, *8*, 987-987.

[105] Y. Li, R. T. Yang, *Langmuir* **2007**, *23*, 12937-12944.

[106] I. Spanopoulos, C. Tsangarakis, E. Klontzas, E. Tylianakis, G. Froudakis, K. Adil, Y. Belmabkhout, M. Eddaoudi, P. N. Trikalitis, *Journal of the American Chemical Society* **2016**, *138*, 1568-1574.

[107] H. R. Abid, A. Hanif, A. Keshavarz, J. Shang, S. Iglauer, *Energy & Fuels* **2023**, *37*, 7260-7267.

[108] S. Keskin, S. Kızılel, *Industrial & Engineering Chemistry Research* **2011**, *50*, 1799-1812.

[109] I. Wagner, S. Spiegel, J. Brückel, M. Schwotzer, A. Welle, M. H. Stenzel, S. Bräse, S. Begum, M. Tsotsalas, *Macromolecular Materials and Engineering* **2023**, *308*.

[110] S. Begum, Z. Hassan, S. Bräse, C. Wöll, M. Tsotsalas, *Accounts of Chemical Research* **2019**, *52*, 1598-1610.

[111] I. Abánades Lázaro, R. S. Forgan, *Coordination Chemistry Reviews* **2019**, *380*, 230-259.

[112] H. D. Lawson, S. P. Walton, C. Chan, *ACS Applied Materials & Interfaces* **2021**, *13*, 7004-7020.

[113] P. Wiśniewska, J. Haponiuk, M. R. Saeb, N. Rabiee, S. A. Bencherif, *Chemical Engineering Journal* **2023**, *471*, 144400.

[114] Y. He, W. Zhang, T. Guo, G. Zhang, W. Qin, L. Zhang, C. Wang, W. Zhu, M. Yang, X. Hu, V. Singh, L. Wu, R. Gref, J. Zhang, *Acta Pharmaceutica Sinica B* **2019**, *9*, 97-106.

[115] S.-Y. Ding, W. Wang, *Chem. Soc. Rev.* **2013**, *42*, 548-568.

[116] X. Zhao, P. Pachfule, A. Thomas, *Chemical Society Reviews* **2021**, *50*, 6871-6913.

[117] P. Katekomol, J. Roeser, M. Bojdys, J. Weber, A. Thomas, *Chemistry of Materials* **2013**, *25*, 1542-1548.

[118] S. Y. Ding, W. Wang, *Chem Soc Rev* **2013**, *42*, 548-568.

[119] K. Geng, T. He, R. Liu, S. Dalapati, K. T. Tan, Z. Li, S. Tao, Y. Gong, Q. Jiang, D. Jiang, *Chemical Reviews* **2020**, *120*, 8814-8933.

[120] A. P. CôTé, A. I. Benin, N. W. Ockwig, M. O'Keeffe, A. J. Matzger, O. M. Yaghi, *Science* **2005**, *310*, 1166-1170.

[121] H. M. El-Kaderi, J. R. Hunt, J. L. Mendoza-CortéS, A. P. CôTé, R. E. Taylor, M. O'Keeffe, O. M. Yaghi, *Science* **2007**, *316*, 268-272.

[122] F. Zhao, M. An, N. Wang, X. Yin, *Chemistry – A European Journal* **2024**.

[123] Y. Yin, Y. Zhang, X. Zhou, B. Gui, W. Wang, W. Jiang, Y.-B. Zhang, J. Sun, C. Wang, *Science* **2024**, *386*, 693-696.

[124] P. Kuhn, M. Antonietti, A. Thomas, *Angewandte Chemie International Edition* **2008**, *47*, 3450-3453.

[125] Z. Qian, Z. J. Wang, K. A. I. Zhang, *Chemistry of Materials* **2021**, *33*, 1909-1926.

[126] L. Liao, M. Li, Y. Yin, J. Chen, Q. Zhong, R. Du, S. Liu, Y. He, W. Fu, F. Zeng, *ACS Omega* **2023**, *8*, 4527-4542.

[127] J. Wang, S. Zhuang, *Coordination Chemistry Reviews* **2019**, *400*, 213046.

[128] F. J. Uribe-Romo, J. R. Hunt, H. Furukawa, C. Klöck, M. O'Keeffe, O. M. Yaghi, *J. Am. Chem. Soc.* **2009**, *131*, 4570-4571.

[129] X. Liu, D. Huang, C. Lai, G. Zeng, L. Qin, H. Wang, H. Yi, B. Li, S. Liu, M. Zhang, R. Deng, Y. Fu, L. Li, W. Xue, S. Chen, *Chemical Society Reviews* **2019**, *48*, 5266-5302.

[130] S. Kandambeth, A. Mallick, B. Lukose, M. V. Mane, T. Heine, R. Banerjee, *Journal of the American Chemical Society* **2012**, *134*, 19524-19527.

[131] Y. Zhao, S. Das, T. Sekine, H. Mabuchi, T. Irie, J. Sakai, D. Wen, W. Zhu, T. Ben, Y. Negishi, *Angewandte Chemie International Edition* **2023**, *62*.

[132] T. D. Bennett, F.-X. Coudert, S. L. James, A. I. Cooper, *Nature Materials* **2021**, *20*, 1179-1187.

[133] P. M. Budd, B. S. Ghanem, S. Makhseed, N. B. McKeown, K. J. Msayib, C. E. Tattershall, *Chemical Communications* **2004**, 230.

[134] N. B. McKeown, *ISRN Materials Science* **2012**, *2012*, 1-16.

[135] N. B. McKeown, *Polymer* **2020**, *202*, 122736.

[136] N. B. McKeown, P. M. Budd, *Chemical Society Reviews* **2006**, *35*, 675.

[137] A. Del Regno, A. Gonciaruk, L. Leay, M. Carta, M. Croad, R. Malpass-Evans, N. B. McKeown, F. R. Siperstein, *Industrial & Engineering Chemistry Research* **2013**, *52*, 16939-16950.

[138] J. Tröger, *Journal für Praktische Chemie* **1887**, *36*, 225-245.

[139] M. Spielman, *Journal of the American Chemical Society* **1935**, *57*, 583-585.

[140] V. Prelog, P. Wieland, *Helvetica Chimica Acta* **1944**, *27*, 1127-1134.

[141] B. Dolenský, J. Elguero, V. Král, C. Pardo, M. Valík, in *Advances in Heterocyclic Chemistry, Vol. 93* (Ed.: A. R. Katritzky), Academic Press, **2007**, pp. 1-56.

[142] P. Niu, C. Shi, J. Jiao, W. Xie, H. Qiu, Z. Yang, J. Jiang, L. Wang, *Chemical Communications* **2023**, *59*, 10960-10963.

[143] C. Shi, G. Xu, H. Qiu, Y. Li, X. Lu, J. Jiang, L. Wang, *Chemical Communications* **2025**.

[144] M. Carta, R. Malpass-Evans, M. Croad, Y. Rogan, M. Lee, I. Rose, N. B. McKeown, *Polym. Chem.* **2014**, *5*, 5267-5272.

[145] M. Carta, R. Malpass-Evans, M. Croad, Y. Rogan, J. C. Jansen, P. Bernardo, F. Bazzarelli, N. B. McKeown, *Science* **2013**, *339*, 303-307.

[146] B. Comesaña-Gándara, J. Chen, C. G. Bezzu, M. Carta, I. Rose, M.-C. Ferrari, E. Esposito, A. Fuoco, J. C. Jansen, N. B. McKeown, *Energy & Environmental Science* **2019**, *12*, 2733-2740.

[147] Z. Chang, D.-S. Zhang, Q. Chen, X.-H. Bu, *Physical Chemistry Chemical Physics* **2013**, *15*, 5430.

[148] Z. Wang, S. Yuan, A. Mason, B. Reprogle, D.-J. Liu, L. Yu, *Macromolecules* **2012**, *45*, 7413-7419.

[149] P. Bains, P. Psarras, J. Wilcox, *Progress in Energy and Combustion Science* **2017**, *63*, 146-172.

[150] B. Dziejarski, J. Serafin, K. Andersson, R. Krzyżyńska, *Materials Today Sustainability* **2023**, *24*, 100483.

[151] M.-X. Wu, Y.-W. Yang, *Chinese Chemical Letters* **2017**, *28*, 1135-1143.

[152] Q. Xu, B. Xin, J. Wei, Y. Ma, Z. Qing, C. Feng, S. Yi, N. Li, K. Li, F. Wang, J. Zhao, L. Yang, L. Yao, W. Jiang, Y. Dai, Z. Dai, *Journal of Materials Chemistry A* **2023**, *11*, 15600-15634.

[153] P. Pandey, R. S. Chauhan, *Progress in Polymer Science* **2001**, *26*, 853-893.

[154] Y. Li, J. Brückel, M. Jereb, A. Zupanc, S. P. Hirvonen, S. Hietala, M. Kemell, Y. Wu, O. Fuhr, R. D. Jansen-Van Vuuren, M. Carta, S. Bräse, *Advanced Functional Materials* **2024**, *34*.

[155] M. Saleh, H. M. Lee, K. C. Kemp, K. S. Kim, *ACS Applied Materials & Interfaces* **2014**, *6*, 7325-7333.

[156] N. Merukan Chola, P. Gajera, H. Kulkarni, G. Kumar, R. Parmar, R. K. Nagarale, G. Sethia, *ACS Omega* **2023**, *8*, 24761-24772.

[157] J. J. Beaman, D. L. Bourell, C. C. Seepersad, D. Kovar, *Journal of Manufacturing Science and Engineering* **2020**, *142*, 1-50.

[158] K. V. Wong, A. Hernandez, *ISRN Mechanical Engineering* **2012**, *2012*, 1-10.

[159] T. D. Ngo, A. Kashani, G. Imbalzano, K. T. Q. Nguyen, D. Hui, *Composites Part B: Engineering* **2018**, *143*, 172-196.

[160] J. Huang, Q. Qin, J. Wang, *Processes* **2020**, *8*, 1138.

[161] F. P. W. Melchels, J. Feijen, D. W. Grijpma, *Biomaterials* **2010**, *31*, 6121-6130.

[162] A. Awad, F. Fina, A. Goyanes, S. Gaisford, A. W. Basit, *International Journal of Pharmaceutics* **2020**, *586*, 119594.

[163] S. Subedi, S. Liu, W. Wang, S. M. A. Naser Shovon, X. Chen, H. O. T. Ware, *npj Advanced Manufacturing* **2024**, *1*.

[164] K. Rajan, M. Samykano, K. Kadirgama, W. S. W. Harun, M. M. Rahman, *The International Journal of Advanced Manufacturing Technology* **2022**, *120*, 1531-1570.

[165] A. Selimis, V. Mironov, M. Farsari, *Microelectronic Engineering* **2015**, *132*, 83-89.

[166] A. Balena, M. Bianco, F. Pisanello, M. De Vittorio, *Advanced Functional Materials* **2023**, *33*, 2211773.

[167] M. Layani, X. Wang, S. Magdassi, *Advanced Materials* **2018**, *30*, 1706344.

[168] M. Shah, A. Ullah, K. Azher, A. U. Rehman, W. Juan, N. Aktürk, C. S. Tüfekci, M. U. Salamci, *RSC Advances* **2023**, *13*, 1456-1496.

[169] S. Dadashi-Silab, C. Aydogan, Y. Yagci, *Polymer Chemistry* **2015**, *6*, 6595-6615.

[170] M. V. Tsurkan, C. Jungnickel, M. Schlierf, C. Werner, *Journal of the American Chemical Society* **2017**, *139*, 10184-10187.

[171] B. Tarek Benkhaled, K. Belkhir, T. Brossier, C. Chatard, A. Graillot, B. Lonetti, A.-F. Mingotaud, S. Catrouillet, S. Blanquer, V. Lapinte, *European Polymer Journal* **2022**, *179*, 111570.

[172] H. A. Houck, P. Müller, M. Wegener, C. Barner-Kowollik, F. E. Du Prez, E. Blasco, *Advanced Materials* **2020**, *32*, 2003060.

[173] A. Bagheri, J. Jin, *ACS Applied Polymer Materials* **2019**, *1*, 593-611.

[174] Z. Zhao, X. Tian, X. Song, *Journal of Materials Chemistry C* **2020**, *8*, 13896-13917.

[175] T. G. Michael, R. Markus, P. Joern, S. Helmut, *Optical Engineering* **1994**, *33*, 3556-3566.

[176] M. Göppert-Mayer, *Annalen der Physik* **1931**, *401*, 273-294.

[177] M. Pawlicki, H. A. Collins, R. G. Denning, H. L. Anderson, *Angewandte Chemie International Edition* **2009**, *48*, 3244-3266.

[178] D. M. Zuev, A. K. Nguyen, V. I. Putlyaev, R. J. Narayan, *Bioprinting* **2020**, *20*, e00090.

[179] M. Rumi, J. W. Perry, *Adv. Opt. Photon.* **2010**, *2*, 451-518.

[180] S. Maruo, O. Nakamura, S. Kawata, *Opt. Lett.* **1997**, *22*, 132-134.

[181] T. Abele, T. Messer, K. Jahnke, M. Hippler, M. Bastmeyer, M. Wegener, K. Göpfrich, *Advanced Materials* **2022**, *34*, 2106709.

[182] M. Deubel, G. Von Freymann, M. Wegener, S. Pereira, K. Busch, C. M. Soukoulis, *Nature Materials* **2004**, *3*, 444-447.

[183] P. Somers, A. Münchinger, S. Maruo, C. Moser, X. Xu, M. Wegener, *Nature Reviews Physics* **2023**, *6*, 99-113.

[184] V. Hahn, T. Messer, N. M. Bojanowski, E. R. Curticean, I. Wacker, R. R. Schröder, E. Blasco, M. Wegener, *Nature Photonics* **2021**, *15*, 932-938.

[185] S. C. Gauci, A. Vranic, E. Blasco, S. Bräse, M. Wegener, C. Barner-Kowollik, *Advanced Materials* **2024**, *36*.

[186] V. Hahn, N. M. Bojanowski, P. Rietz, F. Feist, M. Kozlowska, W. Wenzel, E. Blasco, S. Bräse, C. Barner-Kowollik, M. Wegener, *ACS Photonics* **2023**, *10*, 24-33.

[187] V. Hahn, P. Rietz, F. Hermann, P. Müller, C. Barner-Kowollik, T. Schlöder, W. Wenzel, E. Blasco, M. Wegener, *Nature Photonics* **2022**, *16*, 784-791.

[188] M. L. Birsa, H. Hopf, P. G. Jones, L. G. Sarbu, L. G. Bahrin, *Materials* **2023**, *16*, 4051.

[189] E. Elacqua, T. Friščić, L. R. Macgillivray, *Israel Journal of Chemistry* **2012**, *52*, 53-59.

[190] H. Hopf, *Angewandte Chemie International Edition* **2008**, *47*, 9808-9812.

[191] H. Maeda, R. Inoue, A. Saeki, Y. Morisaki, *Polymer Journal* **2023**, *55*, 537-545.

[192] M. Carta, M. Croad, R. Malpass-Evans, J. C. Jansen, P. Bernardo, G. Clarizia, K. Friess, M. Lanč, N. B. McKeown, *Advanced Materials* **2014**, *26*, 3526-3531.

[193] G. Cheng, B. Bonillo, R. S. Sprick, D. J. Adams, T. Hasell, A. I. Cooper, *Advanced Functional Materials* **2014**, *24*, 5219-5224.

[194] A. R. Antonangelo, N. Hawkins, M. Carta, *Current Opinion in Chemical Engineering* **2022**, *35*, 100766.

[195] R. Konaka, K. Kuruma, S. Terabe, *Journal of the American Chemical Society* **1968**, *90*, 1801-1806.

[196] C. Braun, S. Bräse, L. L. Schafer, *European Journal of Organic Chemistry* **2017**, *2017*, 1760-1764.

[197] J. Byun, S.-H. Je, H. A. Patel, A. Coskun, C. T. Yavuz, *Journal of Materials Chemistry A* **2014**, *2*, 12507.

[198] V. Kumar, S. Chatterjee, P. Sharma, S. Chakrabarty, C. V. Avadhani, S. Sivaram, *Journal of Polymer Science Part A: Polymer Chemistry* **2018**, *56*, 1046-1057.

[199] H. Becker G. O., W. Berger, G. Domschke, E. Fanghänel, J. Faust, M. Fischer, F. Gentz, K. Gewald, G. Reiner, R. Mayer, K. Müller, D. Pavel, H. Schmidt, K. Schollberg, K. Schwetlick, E. Seiler, G. Zeppenfeld, *Organikum, 22. Auflage*, Wiley-VCH, **2004**.

[200] M. Murai, T. Ogita, K. Takai, *Chemical Communications* **2019**, *55*, 2332-2335.

[201] B. Li, L. Gao, F. Bian, W. Yu, *Tetrahedron Letters* **2013**, *54*, 1063-1066.

[202] H. J. Reich, D. J. Cram, *Journal of the American Chemical Society* **1969**, *91*, 3527-3533.

[203] A. F. Littke, C. Dai, G. C. Fu, *Journal of the American Chemical Society* **2000**, *122*, 4020-4028.

[204] C. Braun, E. Spuling, N. B. Heine, M. Cakici, M. Nieger, S. Bräse, *Advanced Synthesis & Catalysis* **2016**, *358*, 1664-1670.

[205] O. R. P. David, *Tetrahedron* **2012**, *68*, 8977-8993.

[206] K. A. Cychosz, M. Thommes, *Engineering* **2018**, *4*, 559-566.

[207] A. Sayari, Y. Belmabkhout, R. Serna-Guerrero, *Chemical Engineering Journal* **2011**, *171*, 760-774.

[208] D. Aaron, C. Tsouris, *Separation Science and Technology* **2005**, *40*, 321-348.

[209] A. Jana, A. Modi, *Carbon Capture Science & Technology* **2024**, *11*, 100204.

[210] N. Hedin, L. Andersson, L. Bergström, J. Yan, *Applied Energy* **2013**, *104*, 418-433.

[211] C. Xu, N. Hedin, *Journal of Materials Chemistry A* **2013**, *1*, 3406.

[212] L. W. Bruch, *Surface Science* **1983**, *125*, 194-217.

[213] P. J. Waller, F. Gándara, O. M. Yaghi, *Accounts of Chemical Research* **2015**, *48*, 3053-3063.

[214] W. Huang, Y. Jiang, X. Li, X. Li, J. Wang, Q. Wu, X. Liu, *ACS Applied Materials & Interfaces* **2013**, *5*, 8845-8849.

[215] M. S. Lohse, T. Bein, *Advanced Functional Materials* **2018**, *28*.

[216] M. Liu, L. Guo, S. Jin, B. Tan, *Journal of Materials Chemistry A* **2019**, *7*, 5153-5172.

[217] C. Qian, L. Feng, W. L. Teo, J. Liu, W. Zhou, D. Wang, Y. Zhao, *Nat Rev Chem* **2022**, *6*, 881-898.

[218] H. Zhuang, C. Guo, J. Huang, L. Wang, Z. Zheng, H. N. Wang, Y. Chen, Y. Q. Lan, *Angewandte Chemie International Edition* **2024**, *63*.

[219] W. Gong, H. Xie, K. B. Idrees, F. A. Son, Z. Chen, F. Sha, Y. Liu, Y. Cui, O. K. Farha, *Journal of the American Chemical Society* **2022**, *144*, 1826-1834.

[220] H. Jiang, W. Zhang, B. Hou, Y. Liu, Y. Cui, *CCS Chemistry* **2023**, *5*, 1635-1643.

[221] Z. Shan, M. Wu, Z. Gu, Y. Nishiyama, G. Zhang, *Chemical Communications* **2021**, *57*, 9236-9239.

[222] K. Cai, W. Wang, J. Zhang, L. Chen, L. Wang, X. Zhu, Z. Yu, Z. Wu, H. Zhou, *Journal of Materials Chemistry A* **2022**, *10*, 7165-7172.

[223] X. Li, Q. Su, Z. Liu, K. Luo, G. Li, Q. Wu, *Chemical Research in Chinese Universities* **2020**, *36*, 1017-1023.

[224] J. Li, J. Wang, Z. Wu, S. Tao, D. Jiang, *Angewandte Chemie International Edition* **2021**, *60*, 12918-12923.

[225] L. Grunenberg, G. Savasci, M. W. Terban, V. Duppel, I. Moudrakovski, M. Etter, R. E. Dinnebier, C. Ochsenfeld, B. V. Lotsch, *Journal of the American Chemical Society* **2021**, *143*, 3430-3438.

[226] Y. Peng, W. K. Wong, Z. Hu, Y. Cheng, D. Yuan, S. A. Khan, D. Zhao, *Chemistry of Materials* **2016**, *28*, 5095-5101.

[227] E. Nipperts, Karlsruher Institute of Technology **2024**.

[228] G. Wang, X. Zhang, J. Geng, K. Li, D. Ding, K. Y. Pu, L. Cai, Y. H. Lai, B. Liu, *Chemistry – A European Journal* **2012**, *18*, 9705-9713.

[229] T. Mallegol, S. Gmouh, M. A. A. Meziane, M. Blanchard-Desce, O. Mongin, *Synthesis* **2005**, *2005*, 1771-1774.

[230] T. He, Z. Huang, S. Yuan, X.-L. Lv, X.-J. Kong, X. Zou, H.-C. Zhou, J.-R. Li, *Journal of the American Chemical Society* **2020**, *142*, 13491-13499.

[231] F. Meng, S. Bi, Z. Sun, B. Jiang, D. Wu, J. S. Chen, F. Zhang, *Angewandte Chemie International Edition* **2021**, *60*, 13614-13620.

[232] S. B. Kalidindi, C. Wiktor, A. Ramakrishnan, J. Weßing, A. Schneemann, G. Van Tendeloo, R. A. Fischer, *Chem. Commun.* **2013**, *49*, 463-465.

[233] J. Xiao, J. Chen, J. Liu, H. Ihara, H. Qiu, *Green Energy & Environment* **2023**, *8*, 1596-1618.

[234] Donald L. Pavia, Gary M. Lampman, George S. Kritz, J. R. Vyvyan, *Introduction to Spectroscopy, Fifth Edition*, CENGAGE Learning, **2015**.

[235] Manfre Hesse, Herbert Meier, B. Zeeh, *Spektroskopische Methoden in der organischen Chemie, 7te Auflage*, Thieme, **2005**.

[236] X. Wang, X. Hu, Y. Shao, L. Peng, Q. Zhang, T. Zhou, Y. Xiang, N. Ye, *Microchimica Acta* **2019**, *186*.

[237] R.-W. Tsai, J.-S. Chang, R.-M. Wu, D.-J. Lee, *Materials Letters* **2023**, *351*, 135059.

[238] A. Rajasekharan Sujatha, A. Anil, P. Deni Raju, C. Veettil Suneesh, *Chemistry – An Asian Journal* **2025**.

[239] B. P. Biswal, S. Kandambeth, S. Chandra, D. B. Shinde, S. Bera, S. Karak, B. Garai, U. K. Kharul, R. Banerjee, *Journal of Materials Chemistry A* **2015**, *3*, 23664-23669.

[240] C. Sun, D. Sheng, B. Wang, X. Feng, *Angewandte Chemie* **2023**, *135*.

[241] Y. Ge, H. Zhou, Y. Ji, L. Ding, Y. Cheng, R. Wang, S. Yang, Y. Liu, X. Wu, Y. Li, *The Journal of Physical Chemistry C* **2018**, *122*, 27495-27506.

[242] H. Furukawa, K. E. Cordova, M. O'Keeffe, O. M. Yaghi, *Science* **2013**, *341*, 1230444.

[243] S. Mallakpour, E. Nikkhoo, C. M. Hussain, *Coordination Chemistry Reviews* **2022**, *451*, 214262.

[244] S. Wang, C. M. McGuirk, A. D'Aquino, J. A. Mason, C. A. Mirkin, *Advanced Materials* **2018**, *30*, 1800202.

[245] E. Ploetz, H. Engelke, U. Lächelt, S. Wuttke, *Advanced Functional Materials* **2020**, *30*, 1909062.

[246] S. Spiegel, I. Wagner, S. Begum, M. Schwotzer, I. Wessely, S. Bräse, M. Tsotsalas, *Langmuir* **2022**, *38*, 6531-6538.

[247] A. Giannoulis, K. Ackermann, A. Bogdanov, D. B. Cordes, C. Higgins, J. Ward, A. M. Z. Slawin, J. E. Taylor, B. E. Bode, *Organic & Biomolecular Chemistry* **2023**, *21*, 375-385.

[248] S. Sato, M. Tsunoda, M. Suzuki, M. Kutsuna, K. Takido-uchi, M. Shindo, H. Mizuguchi, H. Obara, H. Ohya, *Spectrochimica Acta Part A: Molecular and Biomolecular Spectroscopy* **2009**, *71*, 2030-2039.

[249] A. Nakagawa, Y. Hisamatsu, S. Moromizato, M. Kohno, S. Aoki, *Inorganic Chemistry* **2014**, *53*, 409-422.

[250] R. Krzyminiewski, T. Kubiak, B. Dobosz, G. Schroeder, J. Kurczewska, *Current Applied Physics* **2014**, *14*, 798-804.

[251] S. Bräse, C. Gil, K. Knepper, V. Zimmermann, *Angewandte Chemie International Edition* **2005**, *44*, 5188-5240.

[252] T. J. Deming, *Chemical Reviews* **2016**, *116*, 786-808.

[253] H. G. Lee, G. Lautrette, B. L. Pentelute, S. L. Buchwald, *Angewandte Chemie International Edition* **2017**, *56*, 3177-3181.

[254] E. Ruoslahti, M. D. Pierschbacher, *Science* **1987**, *238*, 491-497.

[255] Y. Sun, C. Kang, F. Liu, Y. Zhou, L. Luo, H. Qiao, *Drug Development Research* **2017**, *78*, 283-291.

[256] M. Pavone, M. Biczysko, N. Rega, V. Barone, *The Journal of Physical Chemistry B* **2010**, *114*, 11509-11514.

[257] M. S. Wagner, D. G. Castner, *Langmuir* **2001**, *17*, 4649-4660.

[258] J. Song, X. Yu, A. Nefedov, P. G. Weidler, S. Grosjean, S. Bräse, Y. Wang, C. Wöll, *Angewandte Chemie International Edition* **2023**, *62*.

[259] V. I. Isaeva, L. M. Kustov, *Petroleum Chemistry* **2010**, *50*, 167-180.

[260] S. Yuan, L. Feng, K. Wang, J. Pang, M. Bosch, C. Lollar, Y. Sun, J. Qin, X. Yang, P. Zhang, Q. Wang, L. Zou, Y. Zhang, L. Zhang, Y. Fang, J. Li, H. C. Zhou, *Advanced Materials* **2018**, *30*, 1704303.

[261] M. Bosch, M. Zhang, H.-C. Zhou, *Advances in Chemistry* **2014**, *2014*, 1-8.

[262] L. Feng, K.-Y. Wang, G. S. Day, M. R. Ryder, H.-C. Zhou, *Chemical Reviews* **2020**, *120*, 13087-13133.

[263] R. J. Kuppler, D. J. Timmons, Q.-R. Fang, J.-R. Li, T. A. Makal, M. D. Young, D. Yuan, D. Zhao, W. Zhuang, H.-C. Zhou, *Coordination Chemistry Reviews* **2009**, *253*, 3042-3066.

[264] P. Sivaguru, Y. Ning, X. Bi, *Chemical Reviews* **2021**, *121*, 4253-4307.

[265] J. Mieres-Pérez, E. Mendez-Vega, K. Velappan, W. Sander, *The Journal of Organic Chemistry* **2015**, *80*, 11926-11931.

[266] R. S. Gomes, G. A. M. Jardim, R. L. de Carvalho, M. H. Araujo, E. N. da Silva Júnior, *Tetrahedron* **2019**, *75*, 3697-3712.

[267] D. Castelvecchi, H. Ledford, *Nature* **2022**, *610*, 242-243.

[268] F. Mohajer, M. M. Heravi, V. Zadsirjan, N. Poormohammad, *RSC Advances* **2021**, *11*, 6885-6925.

[269] C. Bednarek, I. Wehl, N. Jung, U. Schepers, S. Bräse, *Chemical Reviews* **2020**, *120*, 4301-4354.

[270] J. E. Leffler, R. D. Temple, *Journal of the American Chemical Society* **1967**, *89*, 5235-5246.

[271] Z. Zuo, X. Liu, X. Qian, T. Zeng, N. Sang, H. Liu, Y. Zhou, L. Tao, X. Zhou, N. Su, Y. Yu, Q. Chen, Y. Luo, Y. Zhao, *Journal of Medicinal Chemistry* **2020**, *63*, 7633-7652.

[272] M. S. Maier, K. Hüll, M. Reynders, B. S. Matsuura, P. Leippe, T. Ko, L. Schäffer, D. Trauner, *Journal of the American Chemical Society* **2019**, *141*, 17295-17304.

[273] M. Sheng, D. Frurip, D. Gorman, *Journal of Loss Prevention in the Process Industries* **2015**, *38*, 114-118.

[274] V. D. Filimonov, M. Trusova, P. Postnikov, E. A. Krasnokutskaya, Y. M. Lee, H. Y. Hwang, H. Kim, K.-W. Chi, *Organic Letters* **2008**, *10*, 3961-3964.

[275] P. Mainik, C. A. Spiegel, E. Blasco, *Advanced Materials* **2024**, *36*.

[276] G. de Miguel, G. Vicidomini, B. Harke, A. Diaspro, in *Three-Dimensional Microfabrication Using Two-photon Polymerization* (Ed.: T. Baldacchini), William Andrew Publishing, Oxford, **2016**, pp. 190-220.

[277] H. Ding, M. Dong, Q. Zheng, Z. L. Wu, *Molecular Systems Design & Engineering* **2022**, *7*, 1017-1029.

[278] A. Amini, R. M. Guijt, T. Themelis, J. De Vos, S. Eeltink, *Journal of Chromatography A* **2023**, *1692*, 463842.

[279] A. Grzybowski, K. Pietrzak, *Clinics in Dermatology* **2013**, *31*, 221-225.

[280] S. O'Halloran, A. Pandit, A. Heise, A. Kellett, *Advanced Science* **2023**, *10*, 2204072.

[281] N. M. Bojanowski, A. Vranic, V. Hahn, P. Rietz, T. Messer, J. Brückel, C. Barner-Kowollik, E. Blasco, S. Bräse, M. Wegener, *Advanced Functional Materials* **2023**, *33*, 2212482.

[282] E. Blasco, M. Wegener, C. Barner-Kowollik, *Advanced Materials* **2017**, *29*, 1604005.

[283] N. Phetrak, T. Rukkijakan, J. Sirijaraensre, S. Prabpai, P. Kongsaeree, C. Klinchan, P. Chuawong, *The Journal of Organic Chemistry* **2013**, *78*, 12703-12709.

[284] K.-W. Chi, M. S. Yusubov, V. D. Filimonov, *Synthetic Communications* **1994**, *24*, 2119-2122.

[285] V. Medabalmi, K. Ramanujam, *Journal of The Electrochemical Society* **2017**, *164*, A1720.

[286] H. Li, K. Wang, Y. Sun, C. T. Lollar, J. Li, H.-C. Zhou, *Materials Today* **2018**, *21*, 108-121.

[287] J. M. Lee, A. I. Cooper, *Chem Rev* **2020**, *120*, 2171-2214.

[288] N. M. Bojanowski, A. Vranic, V. Hahn, P. Rietz, T. Messer, J. Brückel, C. Barner-Kowollik, E. Blasco, S. Bräse, M. Wegener, *Advanced Functional Materials* **2022**, 2212482.

[289] Z. Liu, F. Wang, X. Chen, *Drug Development Research* **2008**, *69*, 329-339.

[290] L. Van Gerven, J. Talpe, A. Van Itterbeek, *Physica* **1967**, *33*, 207-211.

[291] A. L. Myers, J. M. Prausnitz, *AIChE Journal* **1965**, *11*, 121-127.

[292] S. Lee, J. H. Lee, J. Kim, *Korean Journal of Chemical Engineering* **2018**, *35*, 214-221.

[293] O. V. Dolomanov, L. J. Bourhis, R. J. Gildea, J. A. K. Howard, H. Puschmann, *Journal of Applied Crystallography* **2009**, *42*, 339-341.

[294] G. M. Sheldrick, *Acta Crystallographica Section C Structural Chemistry* **2015**, *71*, 3-8.

[295] G. M. Sheldrick, *Acta Crystallographica Section A Foundations and Advances* **2015**, *71*, 3-8.

8 Appendix

8.1 Acknowledgements

Zuallererst möchte ich Prof. Dr. Stefan Bräse, meinen aufrichtigen Dank für seine unschätzbare Anleitung und Unterstützung während meiner Promotion aussprechen. In den vergangenen Jahren habe ich nicht nur ein tieferes Verständnis der Chemie entwickeln können, sondern auch Fähigkeiten in Selbstorganisation, Mitarbeiterführung und dem Umgang mit professionellen Beziehungen entwickelt. Sein Vertrauen in meine Arbeit und die Freiheit, meine Forschung eigenständig durchzuführen, schufen die perfekte Umgebung für meine persönliche und wissenschaftliche Weiterentwicklung.

Prof. Dr. Christof Wöll danke ich herzlich für die Übernahme des Koreferats dieser Dissertation.

Mein weiterer Dank gilt meinen Kooperationspartnern. Dr. Mariolino Carta (Universität Swansea), Anže Zupanc (Universität Ljubljana) und Ilona Wagner (Karlsruher Institut für Technologie) danke ich für die Durchführung wichtiger Messungen im Rahmen dieser Arbeit. Ana Fingolo danke ich für die Durchführung und Bereitstellung der Pulver-XRD-Daten. Der Arbeitsgruppe WEGENER und insbesondere Aleksandra Vranic danke ich für die 3D-Laser-Nanoprinting-Experimente, die zum Erfolg meiner Arbeit maßgeblich beigetragen haben.

Ich möchte allen Mitarbeitern des IOC, einschließlich Dr. Andreas Rapp, Dr. Norbert Foitzik, Karolin Kohnle, Angelika Mösle, Lara Hirsch, Despina Savvidou, Richard von Budberg und Christoph Götz, für den analytischen Service danken und dafür, dass Sie das Institut am Laufen halten. Zuletzt gilt mein großer Dank Dr. Olaf Fuhr für die Messung und Analyse der Einkristalle.

Ein herzliches Dankeschön geht an Dr. Nicole Jung und Dr. Christin Bednarek für die wissenschaftliche und organisatorische Unterstützung sowie an Janine Bolz, Christiane Lampert und Sabine Ghironi für ihre freundliche Art, ihre außergewöhnliche administrative und organisatorische Unterstützung und die angenehme Art und Weise, mit der sie die Gruppe am Laufen halten.

Mein tiefster Dank gilt Patrick Kern, Aleksandra Vranic und Clara Adam, die den Hauptteil dieser Arbeit gelesen und korrigiert haben und die mich während des Schreibprozesses tatkräftig unterstützt haben. Ebenso möchte ich Eileen List und Leon Bartlewski für die Zeit

danken, die sie sich genommen haben, um verschiedene Abschnitte dieser Dissertation Korrektur zu lesen. Eure Anmerkungen und das Feedback waren von unschätzbarem Wert.

Insbesondere möchte ich mich bei Clara bedanken, die mich drei Jahre lang, als Laborpartnerin begleitet hat. Obwohl wir doch so unterschiedlich sind, haben wir uns in vielen Bereichen hervorragend ergänzt und waren über die Jahre hinweg eine Konstante im MZE. Danke für so manchen Ratschlag, den ich mir zu Herzen genommen habe und der mir geholfen hat mich im Laufe dieser Promotion persönlich weiterzuentwickeln.

Zudem möchte ich mich bei all meinen neu gewonnenen Freunden bedanken. Ein herzliches Dankeschön geht an die CW-Gang: Jonas, Luis, Emma und Sven, die mich seit Beginn meines Studiums begleitet haben und zu engen Freunden geworden sind. Ebenso danke ich allen Ausdauersportlern und angehenden Marathonläufern: Danke Ali, Patrick, Bohn, Häcker und Simon für die zahlreichen gemeinsamen Trainingseinheiten. In diesem Zusammenhang möchte ich mich besonders bei meinem Trainings- und Laufpartner sowie unvergleichlichen Coach Leon bedanken, der nicht nur meinen Universitätsalltag bereichert, sondern auch die „Track Tuesday“- und Mittwochmorgen-Technik-Swolf-Einheiten erträglicher gemacht hat.

Ich möchte mich bei allen Studierenden bedanken, die wesentlich zum Gelingen dieser Arbeit beigetragen haben: Haopu Su, Zeinab Haidar und Nipperts Eric, ich danke euch für euren tatkräftigen Einsatz. Die Betreuung eurer Bachelor- und Vertieferarbeiten hat mir geholfen, mich persönlich weiterzuentwickeln, und die Zusammenarbeit mit euch hat mir viel Freude bereitet.

Meiner Familie und meinen Freunden möchte ich für ihre unermüdliche Unterstützung danken. Danke das ihr ohne Hinterfragen immer hinter mir steht. Ihr hattet stets ein offenes Ohr für meine Anliegen und Probleme und eure Unterstützung war entscheidend für den erfolgreichen Abschluss dieser Arbeit.

Zu guter Letzt danke ich Eileen, die es nicht immer leicht mit mir hatte. Danke, dass du meine Launen in schwierigen Zeiten ertragen hast und mich an so manchen Tiefpunkten wieder aufgebaut hast, danke das du mir den Rücken freihältst und mich so akzeptierst wie ich bin. In all den Jahren warst und bist du die wichtigste Unterstützung für mich und dir gehört mein größter Dank.

8.2 List of Publications

[1] **J. Brückel**, Y. Matt, L. Schmidt, C. M. Mattern, U. Schepers, S. Leopold, M. Calkovsky, D. Gerthsen, S. Bräse, Azide Thermolysis Frameworks: Self-inflating, Porous, and Lightweight Materials, *ChemNanoMat* **2023**, *10*.

[2] I. Wagner, S. Spiegel, **J. Brückel**, M. Schwotzer, A. Welle, M. H. Stenzel, S. Bräse, S. Begum, M. Tsotsalas, Biofunctionalization of Metal-Organic Framework Nanoparticles *via* Combined Nitroxide-Mediated Polymerization and Nitroxide-Exchange Reaction, *Macromolecular Materials and Engineering* **2023**, *308*.

[3] C. N. Herlan, A. Sonnefeld, T. Gloge, **J. Brückel**, L. C. Schlee, C. Muhle-Goll, M. Nieger, S. Bräse, Macrocyclic Tetramers - Structural Investigation of Peptide-Peptoid Hybrids, *Molecules* **2021**, *26*, 4548.

[4] Y. Li, **J. Brückel**, M. Jereb, A. Zupanc, S. P. Hirvonen, S. Hietala, M. Kemell, Y. Wu, O. Fuhr, R. D. Jansen-Van Vuuren, M. Carta, S. Bräse, Polymers of Intrinsic Microporosity Containing [2.2]Paracyclophane Moieties Synthesis and Gas Sorption Properties, *Advanced Functional Materials* **2024**, *34*.

[5] N. M. Bojanowski, A. Vranic, V. Hahn, P. Rietz, T. Messer, **J. Brückel**, C. Barner-Kowollik, E. Blasco, S. Bräse, M. Wegener, Search for Alternative Two-Step-Absorption Photoinitiators for 3D Laser Nanoprinting, *Advanced Functional Materials* **2022**, 2212482.

[6] D. Schmidt, P. Gartner, I. Berezkin, J. Rudat, M. Bilger, T. Grünert, N. Zimmerer, P. Quarz, P. Scharfer, **J. Brückel**, A. P. Jung, P. Singh, P. Pooja, B. Meier, M. Stahlberger, W. Schabel, S. Bräse, G. Lanza, A. Nesterov-Mueller, Selective Peptide Binders to the Perfluorinated Sulfonic Acid Ionomer Nafion, *Advanced Functional Materials* **2024**, *34*.

[7] X. Qiu, **J. Brückel**, C. Zippel, M. Nieger, F. Biedermann, S. Bräse, Tris(4-azidophenyl)methanol - A Novel and Multifunctional Thiol Protecting Group, *RSC Advances* **2023**, *13*, 2483-2486.